

Doctorate Dissertation

博士論文

A Study of Nature and Origins of the X-ray Background below about 2 keV

(2 keV 以下の帯域における X 線背景放射の性質と起源に関する研究)

A Dissertation Submitted for Degree of Doctor of Philosophy

December 2018

平成 30 年 12 月 博士 (理学) 申請

Department of Physics, Graduate School of Science, The University of Tokyo

東京大学大学院 理学系研究科  
物理学専攻

Takahiro Kikuchi

菊地 貴大

# Acknowledgement

My seven years in ISAS/JAXA are divided into the first five years and after two years. In the former five years, I devoted to the study of new readout techniques for a detector. In the next two years, I have studied the topic of this thesis, the X-ray background. I thought about withdrawing from graduate school since I was told that the readout study was not appropriate for the degree of Ph.D. But I chose to continue to study something new. And at last, I have written this thesis. The new topic, the X-ray background, was new fields for me. Therefore, many people have helped me to complete this thesis. I have appreciated those who supported my challenge.

I want to express special appreciation to my advisor Professor Kazuhisa Mitsuda. What I keep in my mind is that he taught me the fun and importance to study the new topic, the X-ray background. I also want to thank Professor Noriko Y. Yamasaki and Dr. Ryo Yamamoto. For seven years, the three people have given me helpful advice, however, I could not understand their suggestion due to my lack of knowledge. Nevertheless, they have continued to advise me even today. Thanks to their help, I completed this thesis.

I would like to appreciate the thesis committee members, Professor Masato Takita, Professor Akito Kusaka, Professor Masahiro Takada, Professor Takanori Yoshikoshi and Professor Wataru Ootani for the comments and suggestions which improved my thesis surprisingly.

Thanks to the standard analysis tool distributed by Dr. Steven Snowden and Dr. Kuntz, I learned how to analyze the data. The two people kindly answered my e-mail about the data analysis. Then, I have constructed my analysis methods. If it were not for their help, I could not analyze the data.

I also thanks to lab mates, Dr. Norio Sekiya, Dr. Kazuhisa Sakai, Kenichiro Nagayoshi, Dr. Tasuku Hayashi, Dr. Haruka Muramatsu, Masatoshi Hoshino, Yuuki Nakashima, Keisei Maehisa, Takahiro Nakayama, Ryohei Konno, Ryota Takaku, Dr. Tomotake Matsumura, Dr. hiroaki Imada and Dr. Shu Koyama. I will not forget the days spent with them.

My father and mother always have supported me mentally and financially even today. I am overwhelmed with gratitude for their support. Without their help, I could not complete this thesis. I much appreciate their kindness.

This work was supported by Research Fellowships for Young Scientists DC2.

# Abstract

The  $92.7 \pm 13.3\%$  of the X-ray background in the energy band of 2-8 keV has been spatially resolved into point sources, which are mainly active galactic nuclei (AGNs), by the deep observations by the *Chandra* X-ray observatory. The energy spectrum of the X-ray background in 2-8 keV can be well represented by a simple power-law function, and the spectrum can also be explained by a sum of various types of the AGN spectra. The X-ray background emission in 2-8 keV is likely to be resolved entirely into point sources in the future.

On the other hand, the X-ray background below 2 keV may consist of components of various hierarchical origins. Warm-Hot Intergalactic Medium (WHIM) is one of such examples and arises from the large-scale structure formation of the Universe. This emission can contribute  $\sim 20\%$  of the X-ray background in 0.5-1 keV. In this thesis, we try to make a breakdown of the X-ray background below 2 keV. One of the key issues is to estimate the contribution of the unresolved sources contributing in 2-8 keV, because we do not know their spectra below 2 keV. In this thesis, we thus excluded the spatially resolved sources as much as possible from the X-ray background. The Chandra Deep Field - South (CDF-S) is the best direction for this purpose.

Removal of point sources was tried for *Chandra* data itself. However, *Chandra* spectra below 1 keV are not very suited for this analysis since the *Chandra* effective area rapidly drops below 1 keV. On the other hand, *XMM-Newton* has a large effective area even below 1 keV. We thus considered that the *XMM-Newton* data in the CDF-S direction was the best for this purpose.

The soft proton contamination (SPC) is known to be a severe problem for the studies with *XMM-Newton* of the X-ray background emission because the SPC spectral model is still unclear below 2 keV. Nevertheless, the SPC has dominated the X-ray background emission below 2 keV. Thus, we excluded the time intervals contaminated by the soft protons. As a result, we obtained reliable spectra in this field without the soft proton contamination for the first time.

The surface brightness in 0.5-1 keV showed significant time variation which is related to the solar activity. We determined the surface brightness after removal of the point sources detected by *Chandra* to be  $(3.19 \pm 0.10_{-0.61}^{+0.25}) \times 10^{-12} \text{ erg cm}^{-2} \text{ s}^{-1} \text{ deg}^{-2}$  in 0.5-1 keV for the time intervals of the low solar activity. Thus, we measured the surface brightness of the X-ray background emission in the solar minimum period without spatially resolved point sources, in 0.5-1 keV. For *Chandra*, the surface brightness without spatially resolved point sources was only found for the time period of high solar activity in the literature. If we compare our surface brightness for high solar activity, the value is consistent with that of *Chandra*. Then, we successfully separated the OVII line and the OVIII line for the first time in the X-ray background spectrum without spatially resolved point sources, which was not possible with the *Chandra* data. The surface brightnesses of the OVII line and the OVIII line were  $(0.98 \pm 0.17 \pm 0.07) \times 10^{-12} \text{ erg cm}^{-2} \text{ s}^{-1} \text{ deg}^{-2}$  and  $(0.28 \pm 0.10 \pm 0.02) \times 10^{-12} \text{ erg cm}^{-2} \text{ s}^{-1} \text{ deg}^{-2}$ , respectively. These errors are the statistical  $1.6\sigma$  error (90% confidence level) and the systematic error. The detection significance of the OVIII line was  $3.4 (= 0.28 / (0.10 / 1.6 + 0.02))\sigma$ .

To make a breakdown of the X-ray background emission without spatially resolved point sources in 0.5-1 keV, we estimated the surface brightnesses of the thermal emission other than OVII and OVIII, and the contribution of the unresolved point sources which were not resolved in 2-8 keV. This is the first quantitative breakdown of the X-ray background emission in 0.5-1 keV, taking various systematic errors into account. Then, we estimated the possible surface-brightness range of the yet-unknown components. As we found no significant evidence for the yet-unknown components, we set a  $1.6\sigma$  statistical + systematic upper limit of  $2.3 \times 10^{-12} \text{ erg cm}^{-2} \text{ s}^{-1} \text{ deg}^{-2}$ . The upper limit was roughly 70% of the observed X-ray background, and it did not contradict the expected surface brightness of the WHIM from the cosmological simulations.

# Contents

|  |           |
|--|-----------|
| <b>Acknowledgement</b>   | <b>i</b>  |
| <b>Abstract</b>  | <b>ii</b> |
| <b>Chapter 1 Introduction</b>  | <b>1</b>  |
| <b>Chapter 2 Review</b>  | <b>3</b>  |
| 2.1 The X-ray background . . . . .   | 3         |
| 2.2 Spectrum and intensity above 2 keV . . . . .   | 3         |
| 2.3 Spectrum and intensity below 2 keV . . . . .   | 4         |
| 2.4 Resolving X-ray background intensity above 2 keV into point sources . . . . .                                      | 5         |
| 2.4.1 Chandra Deep Field . . . . .   | 5         |
| 2.4.2 Spectra of Resolved point sources and Resolved Fraction . . . . .  | 7         |
| 2.4.2.1 log $N$ -log $S$ relation and modeling it . . . . .  | 7         |
| 2.4.3 Comparison of energy spectra between X-ray background and X-rays from the AGNs . . . . .                         | 7         |
| 2.5 Origins of X-ray background below 2 keV . . . . .  | 8         |
| 2.5.1 Rosat All Sky Survey (RASS) . . . . .  | 8         |
| 2.5.2 Charge-exchange process . . . . .  | 9         |
| 2.5.2.1 Geo-coronal Solar Wind Charge eXchange (SWCX) . . . . .  | 9         |
| 2.5.2.2 Heliospheric SWCX . . . . .  | 9         |
| 2.5.3 X-ray background below $\sim 0.3$ keV (1/4 keV band) and Local Hot Bubble (LHB) . . . . .                        | 10        |
| 2.5.4 Hot plasma in Galactic halo . . . . .  | 10        |
| 2.5.4.1 Line-of-sight extension of hot plasma in Galactic halo . . . . .   | 11        |
| 2.6 Possible origins of unknown X-ray background components below 2 keV and their searches . . . . .                   | 12        |
| 2.6.1 Two possible additional origins of extragalactic emission . . . . .  | 12        |
| 2.6.1.1 X-ray observation of Warm Hot Intergalactic Medium (WHIM) . . . . .  | 13        |
| 2.6.1.2 Cosmic re-ionization by X-ray heating . . . . .  | 13        |
| 2.6.1.3 Constraining possible origins of unresolved X-ray background below 2 keV with spatial power spectrum . . . . . | 13        |
| 2.7 Summary of this Review . . . . .   | 14        |
| <b>Chapter 3 Strategy for anatomy of the X-ray background in soft X-ray band</b>                                       | <b>30</b> |
| 3.1 Uncertainties in estimating spectral components . . . . .  | 30        |
| 3.2 Combining <i>XMM-Newton</i> and <i>Chandra</i> data . . . . .  | 31        |
| 3.3 Difficulty of using <i>XMM-Newton</i> data . . . . .   | 31        |
| 3.4 Our strategy . . . . .   | 32        |
| <b>Chapter 4 Instruments</b>   | <b>33</b> |
| 4.1 The <i>XMM-Newton</i> observatory . . . . .  | 33        |
| 4.1.1 Design structure of telescope and Point Spread Function (PSF) . . . . .  | 34        |
| 4.1.2 Metal Oxide Semi-conductor (MOS) detector onboard <i>XMM-Newton</i> . . . . .                                    | 36        |
| 4.1.2.1 Detector assembly . . . . .  | 36        |
| 4.1.2.2 Filters of the MOS camera . . . . .  | 37        |
| 4.1.2.3 Response of the MOS detector . . . . .   | 38        |
| 4.1.2.4 Pattern IDs and FLAG . . . . .   | 38        |
| 4.1.2.5 Time degradation . . . . .   | 39        |

|                  |  |           |
|------------------|--|-----------|
| 4.2              | Instrumental background, non X-ray background, soft proton contamination . . . . .   | 40        |
| 4.2.1            | Instrumental lines . . . . .   | 40        |
| 4.2.2            | Anomalous and anonymous CCD chips . . . . .  | 41        |
| 4.2.3            | Soft Proton Contamination (SPC) . . . . .  | 41        |
| 4.2.4            | Non X-ray Background (NXB) and Residual Soft Proton Contamination (RSPC) . . . . .   | 42        |
| 4.2.5            | Spatial distribution of NXB and RSPC . . . . .   | 43        |
| 4.2.6            | Systematic errors on NXB estimation . . . . .  | 43        |
| <b>Chapter 5</b> | <b>Analysis 1: Data reduction</b>  | <b>45</b> |
| 5.1              | Overview . . . . .   | 45        |
| 5.2              | Archive data . . . . .   | 46        |
| 5.3              | Standard event screening . . . . .   | 48        |
| 5.3.1            | Screening with event grade . . . . .   | 48        |
| 5.3.2            | Exclusion of anomalous CCD Chips . . . . .   | 48        |
| 5.4              | Extracting overlapping region with <i>Chandra</i> and <i>XMM-Newton</i> , and detector areas of in and out of fields of view . . . . .       | 51        |
| 5.5              | Removal of time intervals contaminated with soft protons . . . . .   | 52        |
| 5.5.1            | short time scales . . . . .  | 53        |
| 5.5.2            | Long time scales . . . . .   | 55        |
| 5.5.3            | Confirmation of soft proton removal . . . . .  | 58        |
| 5.6              | Long-term variations in the soft band . . . . .  | 58        |
| 5.7              | Sky region free from <i>Chandra</i> point sources . . . . .  | 61        |
| 5.7.1            | <i>Chandra</i> point-source list . . . . .   | 61        |
| 5.7.2            | Overview of point-source mask . . . . .  | 61        |
| 5.7.3            | <i>XMM-Newton</i> simulation images of resolved point sources . . . . .  | 61        |
| 5.7.4            | Comparisons of simulation image and the <i>XMM-Newton</i> real image . . . . .   | 64        |
| 5.7.5            | Determination of point-source mask . . . . .   | 65        |
| <b>Chapter 6</b> | <b>Analysis 2: Estimation of non X-ray background and Response functions</b>   | <b>71</b> |
| 6.1              | Spectral fits . . . . .  | 71        |
| 6.2              | Non X-ray background . . . . .   | 72        |
| 6.2.1            | Treatment of instrumental lines . . . . .  | 73        |
| 6.2.2            | NXB estimation considering count rate between inFOV and outFOV, and energy dependence of count-rate ratio between inFOV and outFOV . . . . . | 73        |
| 6.3              | Effective area . . . . .   | 74        |
| 6.3.1            | Calculating effective area using arfgen . . . . .  | 76        |
| 6.3.2            | Comparison of effective area between without and with Delta-Function approximation of the PSF . . . . .                                      | 77        |
| 6.4              | Pulse height redistribution matrix . . . . .   | 78        |
| <b>Chapter 7</b> | <b>Surface brightnesses in two energy bands and of O lines and other remaining emission</b>  | <b>86</b> |
| 7.1              | X-ray background spectrum with <i>Chandra</i> resolved point sources . . . . .   | 86        |
| 7.1.1            | Spectral models and fitting results . . . . .  | 87        |
| 7.2              | X-ray background spectrum without <i>Chandra</i> resolved point sources . . . . .  | 91        |
| 7.2.1            | Spectral models and fitting results . . . . .  | 91        |
| 7.3              | Components of Soft X-ray Diffuse Background . . . . .  | 91        |
| <b>Chapter 8</b> | <b>Discussion</b>  | <b>99</b> |
| 8.1              | Summary of Results . . . . .   | 99        |
| 8.2              | Comparison with previous studies . . . . .   | 99        |
| 8.2.1            | Figure of Merit . . . . .  | 99        |
| 8.2.2            | Spectra without point sources in 2-8 keV . . . . .   | 99        |
| 8.2.3            | Spectra without point sources below 2 keV . . . . .  | 100       |
| 8.3              | Total surface brightness of X-ray background in 0.5-1 keV . . . . .  | 101       |
| 8.3.1            | Treatment of surface brightness in 0.4-0.5 keV . . . . .   | 101       |
| 8.3.2            | Total surface brightness in 0.5-1 keV . . . . .  | 104       |

|                   |   |            |
|-------------------|---|------------|
| 8.3.3             | Thermal hot plasma emission other than OVII and OVIII emission lines . . . . .                      | 104        |
| 8.3.4             | Surface brightness of unresolved point sources which were not resolved by <i>Chandra</i> in 2-8 keV | 104        |
| 8.3.5             | Break down of X-ray background without resolved point sources in 0.5-1 keV . . . . .                | 105        |
| 8.3.6             | Comparisons with pre-expectation prior to the analysis in 0.5-1 keV . . . . .                       | 106        |
| 8.3.7             | Comparisons with WHIM and re-ionizing photons . . . . .   | 108        |
| 8.3.8             | Possible further improvements . . . . .   | 109        |
| <b>Chapter 9</b>  | <b>Summary and Conclusions</b>  | <b>110</b> |
| <b>Appendix A</b> | <b>Figures employed to eliminate bad data</b>   | <b>113</b> |
| A.1               | All of out of FOV spectra for all ObsIDs to determine the anomalously bright CCD chips . . . . .    | 113        |
| A.2               | Light curve and good time interval . . . . .  | 128        |
| A.3               | Observed images in 0.4-1 keV and region for extracting spectrum for MOS2 . . . . .                  | 140        |
| <b>Appendix B</b> | <b>Examination of soft proton contamination in X-ray background</b>                                 | <b>144</b> |
| <b>Appendix C</b> | <b>Estimation of conceivable residual soft proton contamination by Monte Carlo simulation</b>       | <b>148</b> |
| C.1               | Example of observed time variability in count rate . . . . .  | 148        |
| C.2               | Model of the time variable components . . . . .   | 148        |
| C.3               | Example of simulated flare . . . . .  | 149        |
| C.4               | Difference between true Poisson average and fit average . . . . .                                   | 149        |
| C.5               | Residual soft proton contamination (RSPC) as a function of amplitude and duration . . . . .         | 149        |
| C.6               | Amounts of conceivable residual soft proton contamination . . . . .                                 | 150        |
| C.7               | Influence of conceivable residual soft proton contamination on X-ray background . . . . .           | 150        |

# List of Figures

|     |   |   |
|-----|---|---|
| 2.1 | The X-ray background spectra observed with different instruments cited from Revnivtsev et al. (2003). RXTE/PCA spectrum is expressed by a photon index $\Gamma = 1.42 \pm 0.02$ and a normalization $9.8 \pm 0.3$ photon/s/cm <sup>2</sup> /keV/str. Although obtained over a similarly large solid angle of the sky, the normalization is slightly higher than that by HEAO-1 A2. . . . .  | 4 |
| 2.2 | X-ray background spectra from 3 keV to 1 MeV observed with the HEAO-1 observatory (Boldt, E. 1992, in Proceedings of the International Workshop on the X-Ray Background, edited by X. Barcons and A. Fabian (Cambridge University Press, Cambridge), p. 115). Above 20 keV, the spectrum falls more rapidly than the simple power law, 1.4, in 2-10 keV. The spectrum in the 2-100 keV band can be approximated with a power-law function multiplied with an exponential one. . . . .   | 5 |
| 2.3 | X-ray spectrum of high-latitude $\sim 1$ steradian sky centered at $l$ (galactic longitude) = $90^\circ$ , $b$ (galactic latitude) = $+60^\circ$ obtained with the XQC instrument (an X-ray micro calorimeter spectrometer) onboard a sounding rocket (a), and simulated spectrum for thermal emission (b). The emission components of the X-ray background inferred from the XQC spectrum and previous spectra obtained with <i>ROSAT</i> , <i>Chandra</i> and other instruments. The blue filled circles and diamonds are the total intensity of the X-ray background at several energies, and the solid curves show the X-ray background above $\sim 1.5$ keV and their extensions to the lower energy range based on the X-ray spectra of point sources resolved in the X-ray background (see Section 2.4), while the red and pink vertical bars denote the thermal emission intensity from the emission lines resolved with XQC. The difference between the vertical pink bars and yellow and green solid curves indicates an existence of unknown emission below 1 keV. Both Figures cited from McCammon et al. (2002). . . . . | 6 |

|      |   |    |
|------|---|----|
| 2.16 | Soft X-ray diffuse background observed by <i>XMM-Newton</i> (Henley & Shelton (2013)) together with that observed by <i>Suzaku</i> . Orange cross is derived from <i>Suzaku</i> results (Yoshino et al. (2009)) while black cross observed by <i>XMM-Newton</i> (Henley & Shelton (2013)). Filled black triangle from <i>XMM-Newton</i> should be compared with orange crossed from <i>Suzaku</i> . The emission measures observed by <i>Suzaku</i> and <i>XMM-Newton</i> are consistent with each other. . . . .   | 11 |
| 2.4  | Previous deep surveys (a) in 0.5-2 keV and (b) in 2-10 keV (Brandt & Alexander (2015)). The blue filled circles are the <i>Chandra</i> survey and the green filled circles are the <i>XMM-Newton</i> survey. For comparison purpose, a few surveys from previous X-ray missions are shown in the red filled circle. The solid circles around filled circle indicate serendipitous surveys. The vertical dotted line shows the solid angle for all sky. . . . .  | 15 |
| 2.5  | Total spectra for resolved sources in the CDF-S (Hickox & Markevitch (2006)). The resolved source positions are cited from Alexander et al. (2003). Their fitting model is a single power-law spectrum. Photon index is a $1.47 \pm 0.04$ and normalization is $6.78 \pm 0.18$ photons $\text{cm}^{-2} \text{s}^{-1} \text{keV}^{-1} \text{str}^{-1}$ at 1 keV.   | 16 |
| 2.6  | $\log N$ - $\log S$ plot determined in the 4 Msec the CDF-S region (Lehmer et al. (2012)), (a) for 0.5-2 keV and (b) for 2-8 keV. The black filled circles are the observed data, which are classified by the AGNs, Galaxies and Stars by the follow-up observation of the other wavelengths. The blue open triangles are the AGNs, the red open squares are Galaxies and the green open stars are Stars. The green, blue and red dashed lines are the best-fit $\log N$ - $\log S$ function. The black solid line is sum of the dashed lines. The <i>Chandra</i> detection efficiency is taken into account in the data. . . . .   | 16 |
| 2.7  | Synthesized the AGN spectra based on the models reproduced by model A and model B (for detail see text) v.s. the observed spectra cited from Gilli et al. (2001). The data in 3–40 keV and 15–100 keV are from the A2 HED and A4 LED detectors on board HEAO–1, respectively. . . . .   | 17 |
| 2.8  | All sky images taken by ROSAT (Snowden et al. (1997)). The maps excluded point sources s, in reference to their own survey catalogue (RASS-I). The catalogue covers over 90% of all sky. The intervals when background enhancements above $5\sigma$ are excluded and the period when the particle background was unpredictable are also excluded. Mean free path of photo-absorption in the 1/4 keV band (ROSAT R1+R2 band $\sim 0.1 - 0.3$ keV (a)) is $\sim 100$ pc. While the photons in the 3/4 keV band are absorbed by only the Galactic plane. In the 3/4 keV band (ROSAT R4+R5 band $\sim 0.5 - 0.9$ keV: (b)), the most prominent features is the Loop I associated with North Polar Spur, the Eridanus enhancement and the Cygnus super bubble. The R6+R7 band is shown in (c). . . . . | 18 |
| 2.9  | 3D map for dense gas (Lallement et al. (2003)) obtained by using the equivalent width of the NaI Fraunhofer D1 and D2 absorption lines of the stars whose distances are measured by the astrometry missions, <i>Hipparcos</i> and GAIA. These Figures are sliced maps for (a) galactic planes, (b) meridian planes and for (c) rotation planes. Dots denotes stellar targets. . . . .   | 19 |
| 2.10 | (a): Explanation of charge exchange interaction H and He with solar-wind ion (e.g., $\text{O}^{7+}$ ) (Cravens (2002)). (b): Soft X-ray image of Comet Hyakutake taken by ROSAT. The soft X-ray on the surface toward the Sun is stronger than opposite surface, because the moving comet gathers neutrals in front of itself. . . . .  | 20 |
| 2.11 | Example of theoretically calculated SWCX spectra in line unit (photons/ $\text{cm}^2/\text{s}/\text{str}$ ) (Koutroumpa et al. (2009)). The OVII line consists of the forbidden ( $2^3S_1 \rightarrow 1^1S_0$ ) line 561.1 eV, the inter-combination ( $2^3P_1 \rightarrow 1^1S_0$ ) line 568.7 eV and the resonance ( $2^1P_1 \rightarrow 1^1S_0$ ) line 574.0 eV. . . . .   | 21 |
| 2.12 | Configuration for observing enhanced SWCX emission in direction with high Helium density (Yoshitake et al. (2012)) (a). The helium focusing cone caused by the Sun's gravitational attraction is shown in green. The Sun is moving in the opposite direction to the He flow. The molecular cloud (MBM16) blocks the distant source emission. An interaction between the solar wind and the dense neutral He atoms induces SWCX. Red and blue filled circles and squares are observed results and dashed lines are expected value by simulations provided by Koutroumpa (b). Possible origin for offset $\sim 2$ L.U. is distant plasma, which means local hot bubble and galactic halo. . . . .   | 22 |
| 2.13 | (a): C-band ( $\sim 0.2$ - $0.3$ keV) counting rate obtained with the Wisconsin sounding rocket all sky survey, plotted as a function of total Galactic Hydrogen column density ( $N_{\text{H}}$ ). (b): B-band ( $\sim 0.1$ - $0.2$ keV) to C-band count rate ratio, plotted as a function of $N_{\text{H}}$ . The ratio of the transmissions of $N_{\text{H}}$ in the B band to the C band is plotted with a dashed curve which is very different from the observation. Thus, it can not be due to the Galactic absorption although the C-band intensity shows anti-correlation with $N_{\text{H}}$ (McCammon & Sanders (1990)). . . . .  | 23 |

|      |  |    |
|------|--|----|
| 2.14 | ROSAT counting rates in the direction of the MBM-12 molecular cloud ( $\sim 100$ pc) is plotted as functions of $100 \mu\text{m}$ far infrared intensity ( $I_{100}$ ). Three panels are for different energy bands, (a) ROSAT R1+R2 (1/4 keV) band, (b) R4+R5 (3/4 keV band), and (c) R6+R7 (1.5 keV) band. The $100 \mu\text{m}$ intensity is known to show correlation with the total (atomic + molecule + dust) H column density; $N_{\text{H}}(10^{20} \text{ cm}^{-2}) = 1.4 I_{100}(\text{MJy sr}^{-1}) + 0.15$ . These Figures are cited from Snowden et al. (1993). . . . .   | 24 |
| 2.15 | Relation between OVII surface brightness and OVIII surface brightness relation (Yoshino et al. (2009)). There are 14 observations along with the linear line to investigate the Galactic hot plasma emission in high Galactic latitude. Errors are at 90% confidence level. . . . .  | 25 |
| 2.17 | (a): ROSAT X-ray map centered at LMC X-3. Two squares show the Suzaku filed of view ( $20' \times 20'$ ). (b): Observed <i>Suzaku</i> spectrum in the vicinity of LMC X-3 and the best fit model functions convolved with the instrumental response functions. The X-ray background components in the model components are also separately shown. (c): <i>Chandra</i> spectra of LMC X-3. Only the narrow wavelength ranges including NeIX or OVII lines are shown. From Yao et al. (2009). . . . .  | 26 |
| 2.18 | (a): $\chi^2$ contour maps of spectral parameters of the combined emission and absorption fits to the LMC X-3 data. From Yao et al. (2009). (b): $\chi^2$ contour maps of spectral parameters of the combined emission and absorption fits to the Mkn 421. From Sakai et al. (2014). . . . .   | 27 |
| 2.19 | Evolution of Universe. Neutral hydrogen is re-ionized after dark ages. Initial the AGNs, Galaxies and Warm Hot Intergalactic Medium contributes to the X-ray background. Resolved X-ray sources are not included in the X-ray background. . . . .  | 27 |
| 2.20 | Extra-galactic contribution to the unresolved X-ray background (Fialkov et al. (2017)). Red dash, red solid, green solid are the different type of models to simulate X-ray heating. Gray shaded area is the different simulation considered by Dijkstra et al. (2012). Fialkov et al. (2017) calibrate the X-ray background in the 0.5-2 keV band to $0.251 \times 10^{-12} [\text{erg cm}^{-2} \text{ s}^{-1} \text{ deg}^{-2}]$ derived from Cappelluti et al. (2012a). The black solid line is average intensity. Black crosses are the observed data cited from McCammon et al. (2002). The normalization of the black cross is rescaled at the horizontal bar at 1 keV. Black dots is best-fit spectra index derived from Hickox & Markevitch (2006), photon index 1.5. The normalization is also re-scaled at horizontal bar. . . . . | 28 |
| 2.21 | Brightness temperature of Global 21cm line (Fialkov et al. (2017)). The dashed and solid lines are calculated by different X-ray heating efficiency. X-ray heating efficiency for the dashed line is based on nearby galaxies. The solid lines are based on observed and the rescaled X-ray background Cappelluti et al. (2012a). . . . .  | 28 |
| 2.22 | $\log N$ - $\log S$ plot in 0.5-2 keV used to reproduce spatial fluctuation of observed unresolved X-ray background (Cappelluti et al. (2012b)), for the AGNs (green), Galaxies (blue) and for the sum of the AGN and galaxies (black-shaded). The black shade area means uncertainty due to count-rate to flux conversion. The red shaded area is the $\log N$ - $\log S$ measured by Lehmer et al. (2012) in the CDFS 4 Msec observation. The lower red line expresses contribution of the mini-Quasars. The cyan shaded area is expected counts from the another fluctuation analysis (Miyaji and Griffiths (2002)). The inset shows the contribution of mini-Quasars and the blue triangle means the expected number of the AGNs at the 4 Msec CDFS flux limit, red square is the observed number counts of quasi-stars. . . .           | 29 |
| 2.23 | A schematic view of our understanding on the origins of the X-ray background. . . . .  | 29 |
| 3.1  | Contents of the X-ray background inferred from previous experiments. The abscissa of all panels is X-ray energy, while the ordinate expresses the percentage of energy intensity of different components of the corresponding energy band. Plot (a) is based on McCammon et al. (2002) and Hickox & Markevitch (2006), respectively. Plot (b) assumes the percentage of (a) but the thermal emission was modified by using the <i>XMM-Newton</i> observations of CDF-S direction (Henley & Shelton (2013)). As a result, the total intensity for this plot is not 100%. Plot (c) shows the expected percentages of components if we remove the contribution from all the resolved point sources of this direction. . . .   | 31 |
| 4.1  | The <i>XMM-Newton</i> observatory. The original figure is cited from Jansen et al. (2001). . . . .   | 33 |
| 4.2  | Comparison of non X-ray background among representative instruments. The Xray background (shown in yellow) is just a power-law with photon index is 1.4. . . . .   | 34 |
| 4.3  | Light path in the <i>XMM-Newton</i> telescope with an EPIC camera (cited from ESA homepage). . . .   | 35 |
| 4.4  | (a): A front end view of the EPIC mirror module containing the 58 co-axial mirrors shells and spider support structure used to hold the shells. (b): The PSF of the EPIC camera when observing severely pile up source GX 33904. These figures are cited from Read et al. (2011). . . . .  | 35 |

|      |   |    |
|------|---|----|
| 4.5  | Width of two spokes (Read et al. (2011)). The black horizontal dashed line means not a spoked line which is calculated so as the red area becomes the same as the green shaded area. . . . .  | 35 |
| 4.6  | Very bright source observed by the EPIC camera at off axis angle $\sim 4$ arcmin (left). Equivalent the PSF model at a similar off-axis angle (right). In the two Figures, 16 spokes can be seen. The observed spokes are reproduced well by the equivalent the PSF module (Read et al. (2011)). . . . .  | 36 |
| 4.7  | Encircled Energy Fraction (EEF) calculated using parameters stored in the calibration database. At around $\sim 1$ arcmin, EEF is almost 90%. . . . .   | 36 |
| 4.8  | MOS CCDs mounted in the cryostat with their flexible PCB links (Turner et al. (2001)). The central CCD chip camera located 4.5 mm lower than the outer six CCD chips due to the difference in focal length of the telescope. As the operating temperature is $\sim 170$ K, the radiator is very important. . .  | 37 |
| 4.9  | Filter Wheels for the MOS camera (Turner et al. (2001)). Thin1, Thin2, Thick, and Medium filters block UV. . . . .  | 37 |
| 4.10 | (a): Quantum efficiency curve based on synchrotron measurement and celestial source measurement. (b): Response of the MOS detector at 800 eV. (c): Filter transmission, thin (black), medium (red), thick (green) filters. These figures are cited from Turner et al. (2001). . . . .   | 38 |
| 4.11 | Pattern identifiers for CCD events. The red pixel is the center pixel with the signal is above a threshold. The red one is the largest signal in a $3 \times 3$ pixel matrix. The green pixels have also signals above a threshold. The white pixel has a signal below the threshold. . . . .   | 39 |
| 4.12 | Time degradation for the EPIC the MOS FWHM cited from technical notes XMM-SOC-CAL-TN-0018. Energy resolution for pn camera (upper), for the MOS1 (middle) and for the MOS2 (lower). In this thesis, we do not use the pn detector. . . . .  | 40 |
| 4.13 | Spatial distribution of instrumental lines of the MOS detectors. These instrumental lines are corresponding to Al (1.49 keV), Si(1.74 keV), Au (2.12, 9.71 and 11.4 keV) and a sum of Fe (6.4 keV) and Cr (5.4 keV). . . . .  | 40 |
| 4.14 | (a): Typical anomalous image appearing in the MOS2/chip5. (b): Typical anomalous (green) and anonymous (blue) spectra. (c): The anonymous state whose color represents positions within a chip. These figures are cited from Kuntz & Snowden (2008). . . . .  | 41 |
| 4.15 | (a): Soft proton contributions (Turner et al. (2001)) (including vignetting effect) for a period when the soft proton contamination occurred. (b): A period without soft proton contamination. Faint point-like sources can be seen in (b), while they are masked by SPC in (a). . . . .  | 42 |
| 4.16 | (a): Long time variability for the NXB. Correlation between sunspot numbers and count rates in the particle detector. (b): The red curve represents the sunspot numbers. The black data points indicate count rates in the particle detector. The NXB count rates in 7.5-11.8 keV as a function of revolutions of <i>XMM-Newton</i> . (c): The NXB count rates in 7.5-11.8 keV as a function of count rate in the particle detector (8-40 MeV) for protons on board <i>XMM-Newton</i> . HES0 in the right figure is the count rate in the high energy particle unit on board <i>XMM-Newton</i> . The NXB dominates the most events detected by the MOS cameras in 7.5-11.5 keV. These figures are cited from Gastaldello et al. (2017). . . . . | 43 |
| 4.17 | (left): Image for the spatial distribution of the NXB. (right): Image for the spatial distribution of the NXB the RSPC. These figures are cited from Marelli et al. (2017). . . . .   | 43 |
| 4.18 | Differential count rate (inFOV minus outFOV) in the Filter Wheel Closed data (Salveti et al. (2017)). The blue shaded area indicates a significant offset which one should take into account as a systematic error, when necessary. . . . .   | 44 |
| 5.1  | Exposure of each selected observation IDs. The dashed line represents a 10 ksec threshold for the data selection. At last, we selected 33 observation IDs. Total exposure is 3.6 Msec . . . . .   | 48 |
| 5.2  | Softness ratio (ratio of count rate in 0.4-0.8 keV to that in 2.5-5 keV) as a function of counting rate in 0.3-10 keV excluding the 1.2-2.5 keV band for the outFOV pixels of the MOS1. Energy range, 1.2-2.5 keV, where instrumental lines are dominant is not included in the analysis. One data point corresponds to one ObsID. The Chips indicated in red are excluded from further analysis. . . . .   | 49 |
| 5.3  | Same as the previous figure for the MOS2 . . . . .  | 50 |
| 5.4  | Count rate of Chip1 for both (a) the MOS1 and (b) the MOS2. . . . .   | 51 |

- 5.5 (upper): Time variation of count rates (light curve) in actual observation in the energy range of 5-10 keV. The accepted time bins are shown in green. (middle): Number of occurrence of time bins ( $D(n)$ ) as a function of number of counts per 350 sec. Results of model fits to the histogram are shown with blue and red curves, (lower): Blue curve is for the initial model of the iteration, while red curve for the converged model. Cumulative probability ( $P_c(n, D(n))$ ) for obtaining the number of occurrence of time bins larger than  $D(n)$  and the product of the two probabilities in the successive two bins,  $P_c(n, D(n))P_c(n+1, D(n+1))$ . The red horizontal dotted broken corresponds to  $P_{Th} = 0.05$  according to Equation (5.11). . . . . 52
- 5.6 Two different Poisson statistics involved in the present analysis. The number of occurrence of time bins ( $D(n)$ ) in a given count bin ( $n$ ) obeys a Poisson distribution as a function of  $n$  as an illustrated in the left. On the other hand, if we focus on one count bin, the number of occurrence time bins fluctuates according to Poisson statistics as illustrated in the right. The mean value ( $\mu$ ) of the distribution can be estimated from the model fit of the distribution in the left. We denote the effective number of count bins as  $u$  where the distribution is regarded as a Poisson distribution in the count range. . . . . 54
- 5.7 Long time variation in 2-5 keV (a) for the MOS1 and (b) for the MOS2. (upper): Event rate of the MOS detectors in 2-5 keV for inFOV (overlapping region with Chandra observation) and for outFOV (non X-ray exposed region). (middle) Ratio of count rates of inFOV to outFOV regions in the 10-11 keV range. (lower): Background subtracted inFOV count rate in 2-5 keV (red data points). Another estimation of the same quantity without correction of  $r_{ID}$  is shown with blue data points for comparison. . . . . 57
- 5.8 Occurrence histogram of  $s_{ID}$  (see Equation (5.17)), for the MOS1 and the MOS2 separately. Histogram of deviation from the average normalized to with statistical fluctuation of each ObsIDs. The MOS1 and the MOS2 are shown separately. The best fit Gaussian function is shown with horizontal bars connected with a dotted broken line. Distribution of the MOS1 is more extended than the Gaussian function. . . . . 58
- 5.9 Same as Figure 5.8 for the MOS1. We remove the highest  $s_{ID}$  bin containing three occurrences in Figure 5.8 and recalculate the histogram and fit it with a Gaussian. . . . . 59
- 5.10 Long-term variability of count rate, (a) for the MOS1 and (b) for the MOS2, as a function of ObsID. (upper): Count rate of the MOS detector in the 0.4-1 keV range. The blue circle represents an inFOV count rate ( $R_{inFOV}$ ), while the orange circle represents an outFOV count rate ( $R_{outFOV}$ ). We see constant count rate of the  $R_{inFOV}$ . On the other hand, the count rate of  $R_{outFOV}$  suddenly goes up between 0108062301 and 0555780101 and stay higher after 0555780101. (middle): Ratio,  $r_{ID}$  in Equation 5.14 in the 10-11 keV range. (lower): The blue circle is  $R_{inFOV} - R_{outFOV}$  and the red circle is  $R_{inFOV} - r_{ID}R_{outFOV}$  . . . . . 60
- 5.11 Flow chart for making simulation image. The name of a tool is expressed by black bold characters.  $V_{pq}$  indicates a simulation image.  $N_{conv}$  is a conversion factor for calculating pixel length,  $L$ .  $M_k$  and  $R_k$  are a spectral model and a response for a point source, respectively. . . . . 63
- 5.12 *XMM-Newton* simulation images of point sources in the CDF-S catalogue in Luo et al. (2017), (a) for the 0.4-1 keV band and (b) for the 2-8 keV band, respectively. These images are for the MOS1 in Observation ID:0604960101. The radius of the image is 9.5 arcmin and the spatial resolution is 2.5 arcsec/pixel. Underbar is in a unit of cts/s. Entire size is  $37.5 \times 37.5$  arcmin<sup>2</sup>. We calculated these images in the sky coordinate system. . . . . 64
- 5.13 Comparison between (a) simulation image and (b) actual *XMM-Newton* real image within *Chandra* and *XMM-Newton* overlapping region indicated inside a white circle. We show the simulation image including 10 bright sources in the CDF-S. Note that the vertical color scale bar shows the surface brightness only around these point sources. The yellow region is not related to the vertical color scale bar. . . . . 67
- 5.14 Comparison between observed fluxes and the CDF-S catalogue fluxes. Errors are  $1.6\sigma$  single parameter errors. The sources,  $k = 2, 6$  and  $8$  are employed, as they are isolated and inside the overlapping region between *XMM-Newton* and *Chandra*. . . . . 68
- 5.15 Expected statistical error ( $\delta_{stat}$ ) and spill over of point sources in the background spectrum ( $\delta_{PS}$ ) as a function of factor  $b$  which determines the threshold of the point sources mask (see Equation 5.24). We calculated  $\delta_{stat}$  and  $\delta_{PS}$  for an ObsID, 0604960101, and we scaled  $\delta_{stat}$  for all ObsIDs by  $\sqrt{T_1/T_{all}} = 0.035$ , where  $T_1$  and  $T_{all}$  are the exposure times of the ObsID and all ObsIDs, respectively. . . . . 68

|      |  |    |
|------|--|----|
| 5.16 | <i>XMM-Newton</i> real images after the mask was applied step by step for ObsID=0604960101. The color bar is in unit of cts/s. From top-left, (top-left), (top-right), (middle-left), (middle-right), (bottom-left), (bottom-right), we set $b$ to 8, 4, 2, 1.7, 1, 0.8, respectively. . . . .   | 70 |
| 6.1  | (upper): All of the detected events in the MOS2 when the filter wheel is closed. The extended source analysis team of <i>XMM-Newton</i> proved this data. Blue points are count rates inside the field of view ( $R_{\text{FWCinFOV}}$ ). Orange points are count rates outside the field of view ( $R_{\text{FWCoutFOV}}$ ). This data detected from 2001 to 2017. (lower): The total exposure is 1.9 Msec. Events detected in all chips are stacked. Black points are the ratio ( $b(E)$ ) of the count rate of inside to outside. . . . .   | 74 |
| 6.8  | Comparison of calculated effective area between without and with Delta-Function approximation of the PSF as a function of Channel (5eV/ch). . . . .  | 78 |
| 6.9  | One column of the pulse height redistribution matrix, which shows the PHA response to the MOS2 for monochromatic X-rays of 0.56 keV. This is calculated for ObsID 0555780101. The input X-ray energy corresponds to the OVII line. There is a significant low energy tail which is a feature of the <i>XMM-Newton</i> MOS detectors. The FWHM is 25 ch. It is equivalent corresponding to 125 eV. . . . .  | 79 |
| 6.2  | In field of view spectrum in the CDF-S <i>Chandra</i> overlapping region with resolved point sources ( $C_{\text{inFOV}}$ ) (blue), estimated the NXB spectrum ( $C_{\text{NXB}}$ ) (orange) and corrected the NXB spectrum ( $C'_{\text{NXB}}$ ) (green) for all ObsIDs from 0555780101 to 0604961801. The panel (a) and (b) show the spectra for the 0.4-2 keV energy range and for the 2-9 keV energy range of <i>XMM-Newton</i> , respectively, while the panel (c) shows a close-up view from 9 to 12 keV. The abscissa is linearly plotted with the channel number where one channel corresponds to 5 eV. The NXB correction factor $r'$ is determined by using the spectrum in 10-11 keV (ch 2000 to 2200). Note that strong instrumental lines in ch 280 (Al), ch 340 (Si) and ch 420 (Au) are very different between orange and blue spectra. The energy ranges at and near the instrumental emission lines must be excluded from the spectral analysis. . . . .    | 80 |
| 6.3  | In field of view spectrum in the CDF-S <i>Chandra</i> overlapping region without resolved point sources ( $C_{\text{inFOV}}$ ) (blue), estimated the NXB spectrum ( $C_{\text{NXB}}$ ) (orange) and corrected the NXB spectrum ( $C'_{\text{NXB}}$ ) (green) for all ObsIDs from 0555780101 to 0604961801. The panel (a) and (b) show the spectra for the 0.4-2 keV energy range and for the 2-9 keV energy range of <i>XMM-Newton</i> , respectively, while the panel (c) shows a close-up view from 9 to 12 keV. The abscissa is linearly plotted with the channel number where one channel corresponds to 5 eV. The NXB correction factor $r'$ is determined by using the spectrum in 10-11 keV (ch 2000 to 2200). Note that strong instrumental lines in ch 280 (Al), ch 340 (Si) and ch 420 (Au) are very different between orange and blue spectra. The energy ranges at and near the instrumental emission lines must be excluded from the spectral analysis. . . . . | 81 |
| 6.4  | The box samples used to determine the mesh size and determination method. . . . .  | 82 |
| 6.5  | Effective area calculated with <b>arfgen</b> for box 0 shown in Figure 6.4 plotted as a function of mesh sizes for different energies (a). Derivative of the effective area as a function of mesh size (b). . . . .  | 83 |
| 6.6  | (a): Same as Figure 6.5 (a) but with best-fit parabolic model functions. (b): Relative difference in the effective ( $S'_0 - S'_{\text{arf}}(m)$ )/ $S'_{\text{arf}}(m)$ for the box 0 shown in Figure 6.4 as a function of $E$ , where $S'_{\text{arf}}$ is the effective area calculated by <b>arfgen</b> , the best fit $S'_{\text{palabora}}$ and $S'_0$ are defined in Equation 6.33, for various mesh sizes $m$ . . . . .  | 84 |
| 6.7  | (a): Relative difference in the effective ( $S'_0 - S'_{\text{arf}}(m)$ )/ $S'_{\text{arf}}(m)$ for the box 9 shown in Figure 6.4 as a function of $E$ , where $S'_{\text{arf}}$ is the effective area calculated by <b>arfgen</b> , the best fit $S'_{\text{palabora}}$ and $S'_0$ are defined in Equation 6.33. (b): The ratio of $S'_0/S'_{\text{arf}}(m)$ as a function of $E$ , where $S'_{\text{arf}}$ is the effective area calculated by <b>arfgen</b> , $S'_{\text{palabora}}$ and $S'_0$ are defined in Equation 6.33 for various mesh sizes $m$ . . . . .   | 85 |
| 7.1  | NXB-subtracted MOS2 spectra of the CDF-S overlapping region with point sources. The spectra with different colors show uncertainties of the NXB. The spectrum with $n_b = 0$ is plotted in blue, while those for $n_b = \pm 1$ and $n_b = \pm 2$ are plotted in red and green, respectively, where for the definition of $n_b$ , see Subsection 6.2.2. In the energy range 1.3-2.4 keV, the NXB is not properly subtracted because of position dependence of instrumental emission lines. . . . .  | 87 |
| 7.2  | Fitting results of the X-ray background with <i>Chandra</i> resolved point sources without considering systematic uncertainty of the NXB (for the definition of $n_b = 0$ , see Subsection 6.2.2). The best fit models (defined in Equation 7.8) are plotted in the dashed lines. . . . .  | 89 |
| 7.3  | Fitting results of the X-ray background with <i>Chandra</i> resolved point sources without considering systematic uncertainty of the NXB (for the definition of $n_b = 0$ , see Equation 6.19 in Subsection 6.2.2). The best fit models (defined in Equation 7.10) are plotted in the dashed lines. . . . .  | 91 |

|      |  |     |
|------|--|-----|
| 7.4  | Fitting results of the X-ray background with <i>Chandra</i> resolved point sources considering systematic uncertainty of the NXB (for the definition of $n_b = \pm 2$ , see Subsection 6.2.2). The best fit models (defined in Equation 7.10) are plotted in the dashed lines. . . . .   | 94  |
| 7.5  | NXB-subtracted MOS2 spectra of the CDF-S overlapping region with resolved point sources. The spectra with different colors show uncertainties of the NXB. The spectrum with $n_b = 0$ is plotted in blue, while those for $n_b = \pm 1$ and $n_b = \pm 2$ are plotted in red and green, respectively, where for the definition of $n_b$ , see Subsection 6.2.2. In the energy range 1.3-2.4 keV, the NXB is not properly subtracted because of position dependence of instrumental emission lines. . . . . | 95  |
| 7.6  | Fitting results of the X-ray background without <i>Chandra</i> resolved point sources without considering systematic uncertainty of the NXB (for the definition of $n_b = 0$ , see Subsection 6.2.2). The best fit models (defined in Equation 7.8) are plotted in the dashed lines. . . . .   | 96  |
| 7.7  | Fitting results of the X-ray background without <i>Chandra</i> resolved point sources without considering systematic uncertainty of the NXB (for the definition of $n_b = 0$ , see Equation 6.19 in Subsection 6.2.2). The best fit models (defined in Equation 7.12) are plotted in the dashed lines. . . . .   | 96  |
| 7.8  | Fitting results of the X-ray background without <i>Chandra</i> resolved point sources considering systematic uncertainty of the NXB (for the definition of $n_b = \pm 2$ , see Subsection 6.2.2). The best fit models (defined in Equation 7.10) are plotted in the dashed lines. . . . .  | 97  |
| 7.9  | Surface brightnesses in two energy bands, 0.4-1 keV (top panels) and 2-8 keV (bottom panels) before (left panels) and after (right panels) <i>Chandra</i> resolved point sources removal. The contributions of emission components are also shown. The errors quoted are for statistical errors at 90% ( $1.6\sigma$ ) confidence and systematic error. The systematic errors are calculated in Table 7.5 and Table 7.6. . .   | 98  |
| 8.1  | Figure of Merits (FoM) below 1 keV. Red curve indicates the <i>XMM-Newton</i> MOS2 detector. Blue curve shows the <i>Chandra</i> ACIS-I. . . . .   | 100 |
| 8.2  | Spectrum in the solar maximum epoch observed by the MOS2. . . . .  | 101 |
| 8.3  | Two spectra without resolved point sources (a) in CDF-N and (b) in the CDF-S observed by <i>Chandra</i> cited from Hickox & Markevitch (2006). Fitting models for these spectra are a simple power-law model and a thermal emission model (APEC). These models convolve the response of <i>Chandra</i> . The OVII plus OVIII emission lines are not separated in 0.5-0.7 keV. . . . .  | 102 |
| 8.4  | Comparison between two spectra below 1 keV. This work is indicated by the blue crosses with error bars. which is the same as Figure 7.7. The <i>Chandra</i> spectrum in the CDF-S is indicated by the black crosses cited from Hickox & Markevitch (2006). This work separates the OVIII line from the OVII line. . . . .  | 103 |
| 8.5  | Intensity ratio of solar wind emission lines to the OVII emission line as a function of ion temperature. The ratios of C+N emission lines to OVII, and of OVIII to OVII are calculated using the simulation code by Smith et al. (2012). . . . .   | 103 |
| 8.6  | Relation between power-law index and point-source flux determined by <i>Chandra</i> in the two energy bands, 0.5-2 keV and 2-8 keV cited from Luo et al. (2017). . . . .   | 105 |
| 8.7  | Contents of the X-ray background in 0.5-1 keV based on previous observations ((a) and (a')) and based on this work ((A), (B) and (C)). The panel (a) is the same as Figure 3.1 (c), while the OVII line intensity is corrected to the value obtained with this work in the panel (a'). The (A), (B) and (C) panels show the estimation based on this work. . . . .   | 108 |
| A.1  | Out field of view spectra for MOS1 (blue) and for MOS2 (orange) for 0108060401. . . . .  | 113 |
| A.2  | Same as the previous figure but for 0108060501 . . . . .   | 114 |
| A.3  | Same as the previous figure but for 0108060601 . . . . .   | 114 |
| A.4  | Same as the previous figure but for 0108060701 . . . . .   | 115 |
| A.5  | Same as the previous figure but for 0108061801 . . . . .   | 115 |
| A.6  | Same as the previous figure but for 0108062301 . . . . .   | 116 |
| A.7  | Same as the previous figure but for 0555780101 . . . . .   | 116 |
| A.8  | Same as the previous figure but for 0555780201 . . . . .   | 117 |
| A.9  | Same as the previous figure but for 0555780301 . . . . .   | 117 |
| A.10 | Same as the previous figure but for 0555780401 . . . . .   | 118 |
| A.11 | Same as the previous figure but for 0555780501 . . . . .   | 118 |
| A.12 | Same as the previous figure but for 0555780601 . . . . .   | 119 |
| A.13 | Same as the previous figure but for 0555780701 . . . . .   | 119 |
| A.14 | Same as the previous figure but for 0555780801 . . . . .   | 120 |

|      |   |     |
|------|---|-----|
| A.15 | Same as the previous figure but for 0555780901 . . . . .  | 120 |
| A.16 | Same as the previous figure but for 0555781001 . . . . .  | 121 |
| A.17 | Same as the previous figure but for 0555782301 . . . . .  | 121 |
| A.18 | Same as the previous figure but for 0604960201 . . . . .  | 122 |
| A.19 | Same as the previous figure but for 0604960301 . . . . .  | 122 |
| A.20 | Same as the previous figure but for 0604960401 . . . . .  | 123 |
| A.21 | Same as the previous figure but for 0604960501 . . . . .  | 123 |
| A.22 | Same as the previous figure but for 0604960601 . . . . .  | 124 |
| A.23 | Same as the previous figure but for 0604960701 . . . . .  | 124 |
| A.24 | Same as the previous figure but for 0604960801 . . . . .  | 125 |
| A.25 | Same as the previous figure but for 0604960901 . . . . .  | 125 |
| A.26 | Same as the previous figure but for 0604961001 . . . . .  | 126 |
| A.27 | Same as the previous figure but for 0604961101 . . . . .  | 126 |
| A.28 | Same as the previous figure but for 0604961201 . . . . .  | 127 |
| A.29 | Same as the previous figure but for 0604961301 . . . . .  | 127 |
| A.30 | Same as the previous figure but for 0604961801 . . . . .  | 128 |
| A.31 | The left figures are for MOS1 and the right figures are for MOS2, respectively, for different ObsIDs (a), (b) and (c). (upper): Time variation of count rates (light curve) in actual observation in the energy range of 5-10 keV. The accepted time bins are shown in green. (middle): Number of occurrence of time bins ( $D(n)$ ) as a function of number of counts per 350 sec. Results of model fits to the histogram are shown with blue and red curves, Blue curve is for the initial model of the iteration, while red curve for the converged model. (lower): Cumulative probability ( $P_c(n, D(n))$ ) for obtaining the number of occurrence of time bins larger than $D(n)$ and the product of the two probabilities in the successive two bins, $P_c(n, D(n))P_c(n+1, D(n+1))$ . The red horizontal dotted broken corresponds to $P_{Th} = 0.05$ according to Equation (5.11). . . . . | 129 |
| A.32 | Same as the previous figure for different ObsIDs . . . . .  | 130 |
| A.33 | Same as the previous figure for different ObsIDs . . . . .  | 131 |
| A.34 | Same as the previous figure for different ObsIDs . . . . .  | 132 |
| A.35 | Same as the previous figure for different ObsIDs . . . . .  | 133 |
| A.36 | Same as the previous figure for different ObsIDs . . . . .  | 134 |
| A.37 | Same as the previous figure for different ObsIDs . . . . .  | 135 |
| A.38 | Same as the previous figure for different ObsIDs . . . . .  | 136 |
| A.39 | Same as the previous figure for different ObsIDs . . . . .  | 137 |
| A.40 | Same as the previous figure for different ObsIDs . . . . .  | 138 |
| A.41 | Same as the previous figure for different ObsIDs . . . . .  | 139 |
| A.42 | The observed image (left) and exposure map (right) by MOS2 in 0.4-1 keV for different ObsIDs from (a) to (f). The green boxes indicate point-source free regions used to extract spectrum for MOS2. The red circle indicates the overlapping region between <i>XMM-Newton</i> and <i>Chandra</i> . The radius is 9.54 arcmin. The green boxes are regions used to extract the spectra. . . . .  | 140 |
| A.43 | The observed images and exposure maps by MOS2 in 0.4-1 keV for different ObsIDs from (a) to (f). . . . .  | 141 |
| A.44 | The observed images and exposure maps by MOS2 in 0.4-1 keV for different ObsIDs from (a) to (f). . . . .  | 142 |
| A.45 | The observed images and exposure maps by MOS2 in 0.4-1 keV for different ObsIDs from (a) to (g). . . . .  | 143 |
| B.1  | Fit results for the MOS1 spectra, with the $r$ (see definition Subsection 6.2.2) correction before soft-proton removal (before filtering short-term variation) (a), after soft-proton removal (after filtering short-term variation) (b). The best fit parameters are shown in Table B.1. . . . .   | 146 |
| B.2  | Same as the previous Figure B.1 for the MOS2. . . . .   | 147 |
| C.1  | Example of light curve observed by <i>XMM-Newton</i> and close-up view of the time variable component. . . . .  | 148 |
| C.2  | Model of the time variable components which we call a flare. The amplitude and duration are treated as variable parameters. The rise time and the fall time are fixed at 100 sec. This flare is assumed to occur once in one observation ( $\sim 100$ ksec) randomly. . . . .   | 149 |

- C.3 Example of the simulation results for the strong amplitude ( $4\sigma$ ) and the long duration flare. The flare is assumed to be once in one observation ( $\sim 100$  ksec). Simulated light curve (upper). The x-axis is in a unit of sec and the time bins are 350 sec. The black points are reproduced by the Poisson distribution while the red points are reproduced by the flares and the Poisson distribution. The green points are good time intervals. The inset shows the contamination rate. The number of occurrence of time bins ( $D_{\text{sim}}(n)$ ) for the simulated light curve (middle). The black histogram is the Poisson distribution corresponds to the upper black light curve. Average of the Poisson distribution is 0.2 cts/s which is the same as observed count rate in 5-10 keV. Then, the center of the histogram of the Poisson distribution ( $\mu_{\text{true}}$ ) became 70 cts in the simulation. The solid red curve is the Poisson distribution determined by fit with a given range. The inset shows the fit range and the average of the Poisson distribution determined by fit ( $\mu_{\text{fit}}$ ). Cumulative probability ( $P_c(n, D_{\text{sim}}(n))$ ) for obtaining the number of occurrence of time bins larger than  $D_{\text{sim}}(n)$  (Equation (5.6)) and the product of the two probabilities in the successive two bins,  $P_c(n, D(n))P_c(n+1, D_{\text{sim}}(n+1))$ . The green horizontal dotted broken line corresponds to threshold probability ( $P_{\text{Th}}$  see Equation (5.11)) (lower). . . . . 152
- C.4 Difference between  $\mu_{\text{true}}$  and  $\mu_{\text{fit}}$ . The  $\mu_{\text{true}}$  is 70 [cts]. Colors indicate the different amplitude of flares. 153
- C.5 Contamination rate as a function of amplitudes and durations. . . . . 154
- C.6 Power-law index in 2-5 keV v.s. the contamination rate in 5-10 keV. The fit results (blue open circle) accommodated the canonical value (dashed line) if the soft proton contamination was less than 23%. 155
- C.7 Simulated spectrum and best fit models. Red crosses indicate the simulated spectrum by using the simulation model which included the residual soft proton contamination and the X-ray background. Dashed curved means fit model assumed only the X-ray background . . . . . 155
- C.8 Difference of the surface brightness due to the residual soft proton contamination between the simulation parameters and the best fit parameters for the OVII emission line (a) and for the OVIII emission line (b). The plot (c) indicates the relationship between the OVII emission line and the OVIII emission line. The orange and green lines are the simulation parameters. . . . . 156

# Chapter 1

## Introduction

The X-ray background is a sum of all the X-rays coming from the sky except for those resolved into individual X-ray sources. Therefore, the X-ray background may carry various information along with a line of sight. The character of the X-ray background will be dependent on the sensitivity to detect individual sources. The X-ray background was first discovered by Giacconi et al. (1962), when they first discovered the X-rays from an extra-solar object later named Sco X-1 with a sounding rocket experiment. In the same experiment, they found that X-ray emission was coming from all the directions the rocket payload had scanned. Since then, the X-ray background has been studied extensively.

The X-ray background in the 2-8 keV energy band is now considered to be a sum of individual faint point sources. *Chandra* observatory resolved  $92.7 \pm 13.3\%$  of the X-ray background emission in 2-8 keV into point sources (Luo et al. (2017)). It is likely that with instruments with better spatial resolution and larger detection effective area, the rest of the X-ray background will be resolved into active galactic nuclei and galaxies in the future.

The same point sources are likely to contribute to the X-ray background in nearby energy bands. However, it has been already since 1970's that there has existed excess emission in 0.5-2 keV over a simple extrapolation of the 2-8 keV background (e.g. Bowyer et al. (1968)). A fraction of the excess emission exists in a form of emission lines such as OVII (0.56 keV) and OVIII (0.65 keV) (McCammon et al. (2002)). The present understanding is that a part of OVII emission line is from the Heliosphere originating from solar wind charge exchange (SWCX) induced X-ray emission and that the most of remaining OVII and most of OVIII emission lines are from the hot gas in the halo of our Galaxy (e.g. Yoshino et al. (2009)). Emission from the local hot bubble surrounding solar system also makes a small contribution to OVII.

Although we have identified the possible origins of the rest of the X-ray background in the 0.5-2 keV band, It is still not sure whether all the rest of the X-ray background in the 0.5-2 keV range can be explained with point sources, emission from the Heliosphere, (the local bubble), and the halo of our galaxy. This ambiguity arises mainly from the fact that we do not know the spectral shape of the point sources in this energy range. We also have ambiguity in the continuum emission of the thermal emission, because we do not know the metal (elements heavier than He) abundance of the hot plasma in the Galactic halo.

A few other emission components are suggested to contribute the rest of the X-ray background in 0.5-2 keV; e.g., emission from the warm hot intergalactic medium, the relic of re-ionization photons of the Universe. To measure those emission intensities is related to the fundamental questions of astronomy and astrophysics, i.e., how the structures of the Universe was formed from the initial fluctuation imprinted in the 3 K emission.

One of the promising approaches to reduce the uncertainty of the point source spectra is to remove the point sources in the X-ray background as much as possible. This was tried by Hickox & Markevitch (2006) using the *Chandra* observing two directions, CDF-S (Chandra Deep Field - South) and CDF-N (CDF - North). However, the statistical significance of the resultant spectra was not very high, so they could not constrain the surface brightness of possible unknown emission components. The *XMM-Newton* has a much larger detection effective area than that of *Chandra*. The spatial resolution is not so good as *Chandra* (1 arcsec). However, the half power diameter of the X-ray telescope is 15 arcsec, and it seems to be possible to remove *Chandra* point sources from the spectrum. However, it is known that *XMM-Newton* has a few difficulties in this kind of study. The most significant one is the contamination by soft protons, which *Chandra* does not suffer from.

In this thesis, we investigated the nature and the origins of the rest of the X-ray background in 0.4-1 keV using the *XMM-Newton* observation data of CDF-S. In this study, we utilize the point source list from *Chandra*, which contains more than 1000 point sources. We develop a new method to remove soft proton contamination using temporal variations and obtain reliable spectra for both point sources and point sources.

This thesis is organized in the following way. In Chapter 2, we review the previous studies of the X-ray background with emphasis on the soft energy band. In Chapter 3, we consider our strategy to understand the X-ray background and make crude estimations of the surface brightness break down. In Chapter 4, we review the instruments on *XMM-Newton* and their performance. Then, in Chapter 5 to Chapter 7, we analyze the data. Chapter 5 is devoted to data screening and extraction of X-ray events. Then, in Chapter 6, we prepare data necessary to conduct spectral fits. In Chapter 5, we perform spectral fits and estimate the surface brightnesses, In Chapter 8, we discuss the implications of the results. Various systematic errors are estimated in Chapter 5, Chapter 6, Chapter 7 and Chapter 8. And finally, we summarize the results in Chapter 9. Details of the plots used in the data reduction are shown in Appendix A. The spectra out of field of view (FOV) are summarized for reference in Appendix A.1. The observed light curves and good intervals used in the analysis for each observation in FOV are shown in Appendix A.2. The observed images in the 0.4-1 keV band and the regions excluding point sources to extract the spectrum without point source are listed in Appendix A.3. An examination of the soft proton contamination in the X-ray background is summarized in Appendix B. Details of a Monte Carlo simulation for estimating the conceivable soft proton contamination are summarized in Appendix C. Throughout this thesis, all error ranges state corresponding to 90% ( $1.6\sigma$ ) confidence levels, and vertical error bars in the figures indicate  $1\sigma$  levels.

# Chapter 2

## Review

### 2.1 The X-ray background

In 1962, Giacconi et al. (1962) discovered X-rays from an extra-solar object (later named Sco X-1) for the first time with a sounding rocket experiment (Giacconi & Gursky (1965)). In the same experiment, they also discovered that X-ray emission was coming from all the directions the rocket payload had scanned. This is also the first discovery of the X-ray background emission.

It is not very straight forward to define the X-ray background. In this thesis, we refer to the X-ray background as an X-ray emission which cannot be resolved into individual X-ray sources. According to this definition, the intensity and the contents of the X-ray background are not uniquely defined as the X-ray background will be dependent on the sensitivity of observation to resolve individual sources. One may claim that this is not a good definition. However, we consider that this is the most important nature of the X-ray background and that this is the major reason why we study it. Namely, by improving observations and/or analyses, we may be able to find new unknown emission component, i.e., the X-ray background without point source individual sources.

In this chapter, we will review the previous studies of the X-ray background and some theoretical predictions of emission components of the X-ray background. Subsequently, we will discuss the origins of the X-ray background above 2 keV and below 2 keV separately because of their difference in spectral features leading to possibly different origins.

### 2.2 Spectrum and intensity above 2 keV

In Figure 2.1, we show the X-ray background spectra measured by different instruments (Revnivtsev et al. (2003)). The point sources flux threshold of these instruments is slightly different from one another, but it is around  $1 \times 10^{-12}$  erg s<sup>-1</sup> cm<sup>-2</sup> in the 2-10 keV band.

All the observed spectra in the energy band shown Figure 2.1 can be represented by a single power-law function

$$\frac{dN(E)}{dE} = NE^{-\Gamma}, \quad (2.1)$$

where  $N$  is a number of photons after correcting for galactic absorption,  $E$  is the energy of a photon and  $\Gamma$  is a photon spectral index. All the previous studies show the photon index,  $\Gamma$ , to be approximately 1.4 (Kushino et al. (2002), Revnivtsev et al. (2003)). On the other hand, the normalizations in Figure 2.1 are different among the different instruments. This can be partly due to the difference in the threshold of point-source detection but also can be due to calibration problems among different instruments.

In the higher energy range (Figure 2.2), 20 keV, the spectrum starts to decrease more rapidly than the power law and can be described with an equation,

$$\frac{dN(E)}{dE} = NE^{-\Gamma} \exp(-E/E_e), \quad (2.2)$$

where the e-folding energy,  $E_e$ , is 40 keV. As we will see in Section 2.4, presently more than  $92.7 \pm 13.3\%$  of the X-ray background in the 2-8 keV band is resolved into individual point sources. It is expected that all the X-ray background in this energy range will be resolved into individual point sources by instruments with a higher spatial resolution and a higher sensitivity.

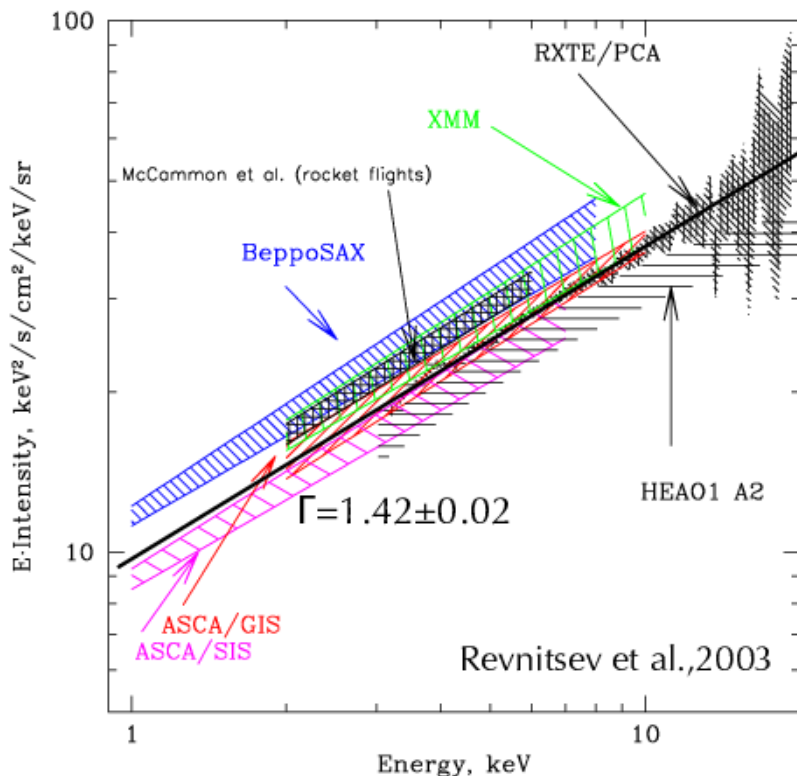


Figure 2.1: The X-ray background spectra observed with different instruments cited from Revnitsev et al. (2003). RXTE/PCA spectrum is expressed by a photon index  $\Gamma = 1.42 \pm 0.02$  and a normalization  $9.8 \pm 0.3$  photon/s/cm<sup>2</sup>/keV/str. Although obtained over a similarly large solid angle of the sky, the normalization is slightly higher than that by HEAO-1 A2.

### 2.3 Spectrum and intensity below 2 keV

It was already noted in late 1960's with sounding rocket experiments that the X-ray background below 1 keV shows a large excess compared to a simple extrapolation of the X-ray background spectrum observed above 2 keV (Bowyer et al. (1968)). From early proportional-counter experiments, the emission spectrum was suggested to be a temperature of the thermal emission  $\sim 0.1$  keV, and hot plasma in the vicinity of the solar system was suggested as the origin (e.g., Tanaka & Bleeker (1977)).

We had to wait for another thirty years approximately to obtain firm evidence for the thermal emission. McCammon et al. (2002) clearly detected emission lines from highly ionized C (CVI) and O (OVII and OVIII) (Figure 2.3(a)), using a microcalorimeter spectrometer with a superior energy resolution from 5 to 12 eV FWHM (full width at half maximum). They extrapolated the X-ray background from 2 to 8 keV to the lower energy band using the spectra of point sources resolved in the X-ray background (see Section 2.4) and concluded that 42 % of the total X-ray background in ROSAT R4 band ( $\sim 0.5$  to 0.9 keV) is from thermal emission at  $z < 0.1$  and 38 % from the point sources which comprises the X-ray background in 2-10 keV. Origin of the remaining 20 % of the X-ray background is unknown and they suggested spatially diffuse extragalactic emission. However, the spectral shape in the 0.5-1 keV range of unresolved point-source contributing to 2-8 keV is yet unknown. Thus, we consider that there are large uncertainties in their extrapolation of the 2-8 keV background spectrum. We only know, on the other hand, the hardness ratio of the resolved point-source determined by typically the ratio between the 2-7 keV and the 0.5-2 keV intensities (see Section 2.4.2). Then, the simple power law shapes of the resolved sources are known. We need furthermore study to measure the intensity of the diffuse extragalactic emission.

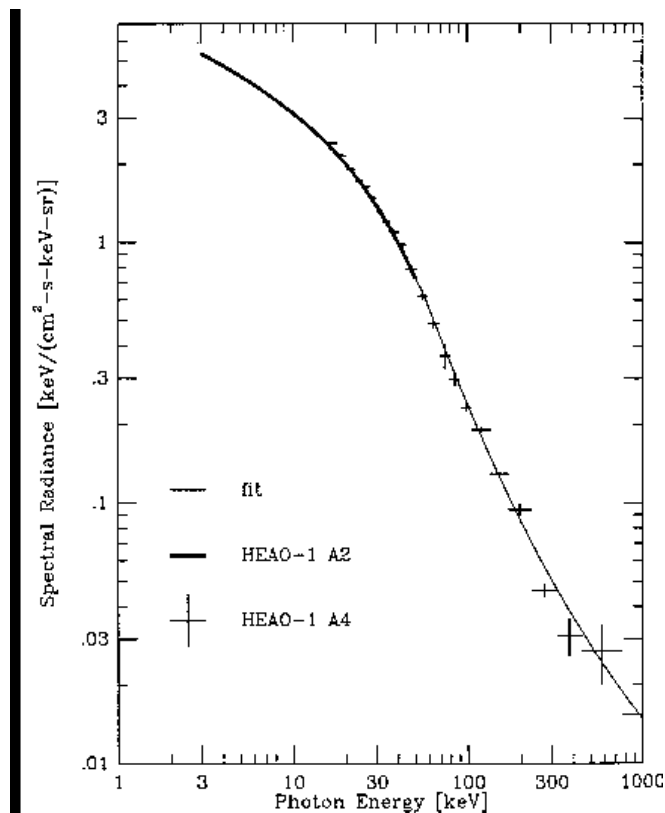


Figure 2.2: X-ray background spectra from 3 keV to 1 MeV observed with the HEAO-1 observatory (Boldt, E. 1992, in Proceedings of the International Workshop on the X-Ray Background, edited by X. Barcons and A. Fabian (Cambridge University Press, Cambridge), p. 115). Above 20 keV, the spectrum falls more rapidly than the simple power law, 1.4, in 2-10 keV. The spectrum in the 2-100 keV band can be approximated with a power-law function multiplied with an exponential one.

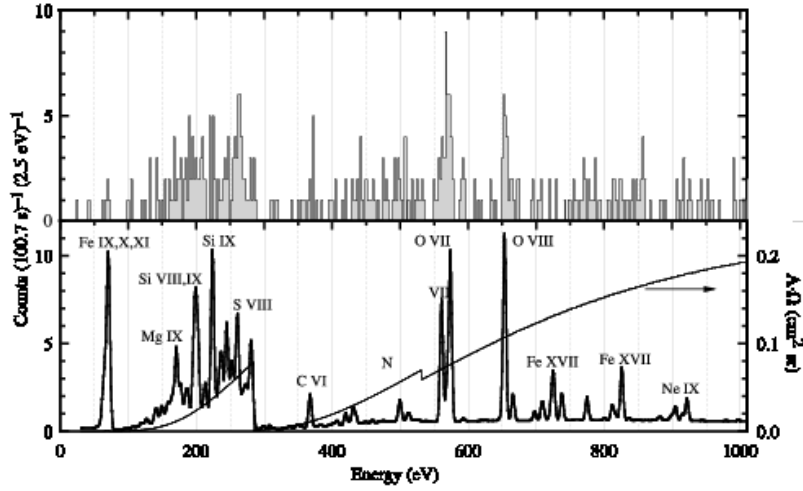
## 2.4 Resolving X-ray background intensity above 2 keV into point sources

The unresolved faint X-ray sources, if they exist, can contribute a certain fraction of the X-ray background. Thus, we can resolve (a part of) the X-ray background into individual sources by observing with instruments with lower detection flux limits. Many point sources surveys have been conducted for this purpose. The previous whole sky surveys and deep surveys are summarized in Figure 2.4 (Brandt & Alexander (2015)). The 3XMM and XMM-XXL surveys with low sensitivity covered most of the whole sky area. In contrast to these observations, the Chandra Deep Field surveys concentrate in a very limited field of view to perform the deepest survey. The flux limit was approximately  $10^{-18}$  ergs $^{-1}$  cm $^{-2}$ . In the appendix, these surveys are tabulated with references. In total, 1008 X-ray sources were detected in 485 arcmin $^2$  field of view of the CDF-S (Luo et al. (2017)). Most of them are considered to be Active Galactic Nuclei (AGNs).

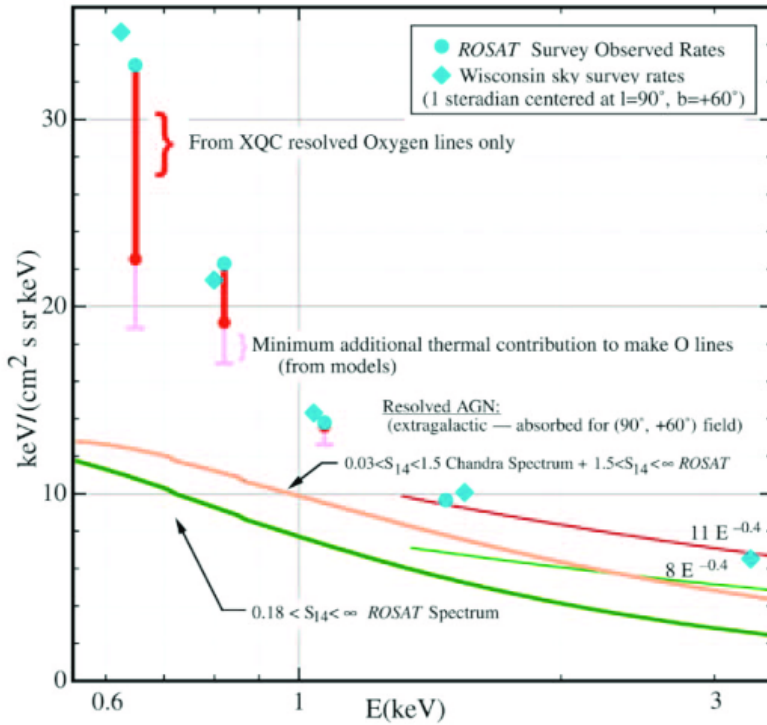
### 2.4.1 Chandra Deep Field

The *Chandra* observation of Chandra Deep Field South is the deepest,  $\sim 7$  Msec, X-ray observation. The sky coverage is 484 arcmin $^2$ , centered at  $\alpha_{J2000} = 03 : 32 : 28.27$ ,  $\delta_{J2000} = -27 : 48 : 21.8$  in the equatorial coordinate system and  $(l, b) = (53.118, -27.806)$  in the galactic coordinate system. As the 7 Msec exposure is not significantly affected by background flares, the total cleaned exposure amounts to 6.7 Msec. Luo et al. (2017) created an image in 0.5-7 keV, with using good grade <sup>1</sup>events. Then, they ran **wavdetect** (Freeman et al. (2002)) to search for X-ray astronomical sources. Finally, 1008 X-ray sources are resolved into discrete sources in the CDF-S. These resolved sources are tabulated in Luo et al. (2017). Positional uncertainty,  $\sigma_{\text{Chandra}}$ , is determined by the following empirical

<sup>1</sup>Standard ASCA grade



(a)



(b)

Figure 2.3: X-ray spectrum of high-latitude  $\sim 1$  steradian sky centered at  $l$ (galactic longitude) =  $90^\circ$ ,  $b$ (galactic latitude) =  $+60^\circ$  obtained with the XQC instrument (an X-ray micro calorimeter spectrometer) onboard a sounding rocket (a), and simulated spectrum for thermal emission (b). The emission components of the X-ray background inferred from the XQC spectrum and previous spectra obtained with *ROSAT*, *Chandra* and other instruments. The blue filled circles and diamonds are the total intensity of the X-ray background at several energies, and the solid curves show the X-ray background above  $\sim 1.5$  keV and their extensions to the lower energy range based on the X-ray spectra of point sources resolved in the X-ray background (see Section 2.4), while the red and pink vertical bars denote the thermal emission intensity from the emission lines resolved with XQC. The difference between the vertical pink bars and yellow and green solid curves indicates an existence of unknown emission below 1 keV. Both Figures cited from McCammon et al. (2002).

equation (Kim et al. (2007)),

$$\log \sigma_{\text{Chandra}} = \alpha_1 \theta + \alpha_2 \log C_{\text{source}} + \alpha_3, \quad (2.3)$$

where  $\alpha_1, \alpha_2, \alpha_3$  are just coefficients,  $\theta$  is an off-axis angle, and  $C_{\text{source}}$  is the total number of detected source photons from a source. Using the *Chandra* observational data combined with the TENNIS data, the positional uncertainty  $\sigma_{\text{Chandra}}$  is estimated to be 0.47 arcsec where  $\alpha_1 = 0.0606$ ,  $\alpha_2 = -0.320$ ,  $\alpha_3 = -0.064$ .

## 2.4.2 Spectra of Resolved point sources and Resolved Fraction

To determine the X-ray intensity corrected for the response function of the *Chandra* telescope and detector, the spectral hardness ratio of 2-7 keV to 0.5-2 keV was calculated. Then, assuming a power-law spectrum with Galactic absorption in the direction, the power-law index of the spectrum was estimated. For the sources detected in only either hard or soft band, the index was assumed to be 1.4. Then, the flux of a point sources in the two bands was calculated. The  $92.7 \pm 13.3\%$  of the X-ray background was resolved into individual point sources in the CDF-S direction, for compared to the whole sky X-ray data provided by Kim et al. (2007).

Dividing the resolved point sources into subgroups according to the X-ray flux, the average spectral index of the point sources was calculated as a function of the X-ray flux. Total spectra for resolved sources in the CDF-S are shown in Figure 2.5.

### 2.4.2.1 log $N$ -log $S$ relation and modeling it

The relation between the number of X-ray sources brighter than a given flux and the flux itself is often plotted in log-log space and called log  $N$ -log  $S$  relation. According to the Bayesian inference in Lehmer et al. (2012), the log  $N$ -log  $S$  relation can be modeled by a sum of log  $N$ -log  $S$  relations of different components represented below,

$$\frac{dN^{\text{AGN}}}{dS} = \begin{cases} K^{\text{AGN}} \left( \frac{S}{S_{\text{ref}}} \right)^{-\beta_1^{\text{AGN}}} & (S \leq f_b^{\text{AGN}}) \\ K^{\text{AGN}} \left( \frac{S_b}{S_{\text{ref}}} \right)^{\beta_2^{\text{AGN}} - \beta_1^{\text{AGN}}} \left( \frac{S}{S_{\text{ref}}} \right)^{-\beta_2^{\text{AGN}}} & (S > f_b^{\text{AGN}}) \end{cases},$$

$$\frac{dN^{\text{Gal}}}{dS} = K^{\text{Gal}} \left( \frac{S}{S_{\text{ref}}} \right)^{-\beta^{\text{Gal}}},$$

$$\frac{dN^{\text{Star}}}{dS} = K^{\text{Star}} \left( \frac{S}{S_{\text{ref}}} \right)^{-\beta^{\text{Star}}},$$

where  $dN/dS$  means differential number counts, the  $S_b$  is break flux point in a broken-power-law  $K$  is a normalization and  $S_{\text{ref}}$  is in a unit of  $10^{-14}$  erg s $^{-1}$  cm $^{-2}$ . Figure 2.6 shows the log  $N$ -log  $S$  relation. Dashed lines show best-fit model functions. Due to the small solid angle of the CDF-S survey, the number of bright normal galaxies appears to drop off at the flux greater than  $4 \times 10^{-16}$  erg s $^{-1}$  cm $^{-2}$  in Figure (a) (0.5-2 keV). However, it is consistent with the best fit model function after the bright end correction to the data. They employed  $(17.3 \pm 2.3) \times 10^{-12}$  [erg cm $^{-2}$  s $^{-1}$  deg $^{-2}$ ] as the total surface brightness of the X-ray background in 2-8 keV. The budget of the X-ray background in 2-8 keV is shown in Table 2.1. Table 2.1 was determined by the 4 Msec *Chandra* observation. The fraction of the X-ray background in 2-8 keV was  $82.4 \pm 13.0\%$ . After the five years, the fraction of the X-ray background in 2-8 keV determined by the 7 Msec *Chandra* observation was the  $92.7 \pm 13.3\%$  (Luo et al. (2017)). Because almost all the resolved sources are the AGNs, Gilli et al. (2001) tested whether the synthesized emission of the AGNs can explain the power-law index 1.4.

### 2.4.3 Comparison of energy spectra between X-ray background and X-rays from the AGNs

The average spectrum of bright the AGNs in the local Universe shows a power-law index of  $\sim 1.8$  in 2-10 keV, which is different from that ( $1.42 \pm 0.02$ ) of the X-ray background. This was recognized as a spectral paradox of the X-ray background in the 1980's. This problem was solved by heavily absorbed X-ray emission from the AGNs, which has a hard spectrum with even a negative photon index in 2-10 keV and shows a peak called a Compton bump at 20 keV. The X-ray background spectrum shows an exponential decay above 20 keV, as we have seen in

Table 2.1: Budgets of the X-ray background in 2-8 keV determined by the 4 Msec *Chandra* observation (Lehmer et al. (2012)).

| Items                      | Number | Total (deg <sup>-2</sup> ) | Fraction (%) |
|----------------------------|--------|----------------------------|--------------|
| All + Bright-end           | -      | -                          | 82.4±13.0    |
| All (AGNs + Galaxy + Star) | 403    | 10495±871                  | 66.3±5.8     |
| AGNs                       | 387    | 9310±776                   | 65.5±5.8     |
| Galaxy                     | 14     | 1142±394                   | 0.8±0.3      |
| Star                       | 2      | 34±32                      | 0.1±0.1      |

Section 2.2. Many authors tried to explain the X-ray background spectrum with a sum of the un-absorbed and the absorbed AGN spectra.

In Gilli et al. (2001), they synthesized the AGN and QSO spectra with two models. They first assumed that local (at  $z = 0$ ) ratio,  $R$ , of unabsorbed the AGNs to absorbed the AGNs was 4. They adopted  $R = 4$  for all the AGNs with different luminosities at  $z = 0$ . Then,  $R$  is assumed to be constant against the redshift  $z$  in the model A while  $R$  is assumed to vary with  $z$  in the model B;

$$R(z) = \begin{cases} 4(1+z)^p & (z < z_{\text{cut}}) \\ R(z_{\text{cut}}) = 10 & (z_{\text{cut}} \geq z) \end{cases}, \quad (2.4)$$

where  $p$  is a constant and  $z_{\text{cut}}$  is the redshift at which the AGNs stop evolving. Absorbing objects in the vicinity of the AGNs have  $\log N_{\text{H}} \leq 24$  and it is assumed to be constant with redshift both in models A and B. The contribution of these the AGNs to the X-ray Background is evaluated by integrating the X-ray luminosity function (XLF). They refer to XLF derived from the 700 the AGN sample observed with ROSAT. The integration starts from  $z = z_{\text{cut}} = 4.6$  to  $z = 0$ . The value of  $p$  was determined from observation of observed the absorbed the AGNs. Figure 2.7 shows the two model spectra together with observed spectra by ASCA, HEAO and ROSAT. We see that the models explain the observed spectra well above 2 keV including the peak at around 20 keV. On the other hand, the models do not reproduce the X-ray background below 2 keV.

## 2.5 Origins of X-ray background below 2 keV

As we have shown in the previous Section, 92.7±13.3 % of the X-ray background in 2-8 keV is resolved into individual point sources. It is likely that all the X-ray background in this energy range has a point-source origin. McCammon et al. (2002) suggested 38 % in the ROSAT R4 band, ~ 0.5 to 0.9 keV. As discussed in Section 2.3, we consider this estimation contains a large uncertainty, because we do not know the spectra of unresolved point sources included in the X-ray background in this energy range, 0.5-1 keV. They also assigned 42 % of the X-ray background in the ROSAT R4 band to the thermal origin from the intensity of the OVII and OVIII emission lines. However, we have to be careful about the thermal-origin interpretation, because now we know a certain fraction of the OVII emission line arises from the non-thermal process, SWCX (Solar Wind Charge Exchange), although these lines are clearly resolved in their experiment. However, these numbers indicate that there is room (20%) for emission whose origins are yet not known.

In this section, we review the studies of the thermal and SWCX origins of the X-ray background. They are related to 42%. In the next section, we will review the studies of emission with unknown origins in X-ray background. It is related to the 20%.

### 2.5.1 Rosat All Sky Survey (RASS)

The German X-ray observatory, ROentgen SATellite (ROSAT), performed an all sky survey in the 0.2 to 2 keV energy band using X-ray mirror optics and position sensitive proportional counters. The energy resolution was only  $E/\Delta E \sim 1$ , thus the X-ray data are often divided into 3 or 6 energy bands (R1, R2, R4, R5, R6, R7). All sky maps of diffuse X-ray background were created, after removing not only the particle background, scattered solar X-rays, and so-called long-term enhancements which were later identified as SWCX from the geo-corona around the but also point sources resolved at the ROSAT all sky survey sensitivity.

Figure 2.8 shows these all sky maps in the energy bands, 1/4 keV (R1+R2), 3/4 keV (R4+R5) and 3/2 keV (R6+R7) cited from Snowden et al. (1997). These maps contain spatially extended individual sources or sky regions,

such as Galactic Center, North Polar Spur, LMC, super nova remnants and super bubbles. In addition, low-intensity X-ray photons are coming from all directions, which are called as the X-ray background.

Assuming the Galactic mean neutral distribution, mean free path for the 1/4 keV band is  $\sim 100$  pc. on the other hand, the emission coming from the high latitude region is not absorbed, in the 3/4 keV band. wavelength. Loop I distribution associated with the North Polar Spur, the Eridanus enhancement and the Cygnus super bubble is consistent with neutral hydrogen distribution observed by 21 cm or other wavelengths. The cavity has been interpreted as a large cavity formed by stellar winds by a series of supernovae.

The existence of a cavity around the solar system is supported by observations by other wavelengths. Lallement et al. (2003) measured the intensities of NaI absorption line in the spectra of about 900 stars within  $\sim 300$  pc whose distance is accurately determined with the Hipparcos satellite (Figure 2.9). The differential absorption strength of a direction gives the density of the neutral medium. They show that the solar system is inside a cavity whose extension is 50 to 150 pc. Lallement (2015) applied the same method to E(B-V) of these stars and obtained similar results.

## 2.5.2 Charge-exchange process

It was not until the discovery of X-ray emission from the comet Hyakutake that we recognized the importance of the charge exchange process in the X-ray line emission. The X-ray intensity of the comet (Figure 2.10 Right) cannot be explained by the reprocessing of the solar X-rays, and the only explanation was the charge exchange process of ions in the solar wind to the neutrals (CO and etc. ) in the vicinities of the comet.



where  $X^{Q+}$ ,  $N$ , and  $h\nu$  are, respectively, an ion in the solar wind, a neutral in the comet, an X-ray photon emitted. An asterisk, “\*”, represent an excitation state of the ion.

### 2.5.2.1 Geo-coronal Solar Wind Charge eXchange (SWCX)

The SWCX emission arises from the low-density neutral matter surrounding the Earth, named Geo-corona. Usually, this emission shows time variation on relatively short time scales (a few tens of minutes to a few hours). Examples are the long-term enhancement observed by ROSAT and the X-ray flares observed in the blank sky region with Suzaku (Fujimoto et al. (2007)).

### 2.5.2.2 Heliospheric SWCX

Cox (1998) suggested that most of the X-ray background below 0.5 keV could be explained by charge exchange between the solar wind and neutrals (mostly H and He) in the interplanetary space, which we call Heliospheric SWCX. Emission from this process contains only lines and no continuum (shown in Figure 2.11), however, detector response broadens the line width. The theoretical X-ray emission derived from charge exchange is shown in Figure 2.11. The OVII triplet lines, however, cannot be distinguished with the current CCD energy resolution. The OVII and OVIII emission lines exist in Heliospherical SWCX spectrum. The OVII and OVIII emission lines can be distinguished with the current CCD resolution with sufficient statistics. Other emission lines below 0.5 keV will look as continuum due to the current CCD energy resolution.

Heliospheric SWCX namely H-SWCX is induced by motion of the solar system in neutral helium medium. The Earth is moving in the H and He neutral medium, H and He are distributed around the Earth similar way as around a comet. Yoshitake et al. (2012) observed the brightening the OVII spectrum in the direction with high He density. (Figure 2.12), furthermore, a significant difference between the direction where the molecular cloud (MBM16) located and the direction which is outside of the molecular cloud. A fraction of the X-ray background emission in the R1+R2 band is also supposed to come from SWCX in the Heliosphere. The constant C-band counting rate against  $N_H$  when  $N_H > 5 \times 10^{20} \text{ cm}^{-2}$  supports this idea as shown in Figure 2.13 (a).

In the next year, Yoshitake et al. (2013) analyzed the in the direction of Lockman Hole observed by Suzaku from 2006 to 2011 in order to check the time variability of the OVII intensity from 2006 to 2011. The intensity from 2006 to 2009 did not show significant time variability within 90% statistical errors. The intensities from 2010 to 2011 was  $2\sim 3$  photons/s/cm<sup>2</sup>/str stronger than those of from 2006 to 2009. Possible candidates which explains this long-term variability is the solar wind associated with solar activities. Based on the sunspot numbers, solar activities were at minimum around December 2008 and then solar cycle 24 began. This paper alerts that the OVII intensity dependent on solar activities.

### 2.5.3 X-ray background below $\sim 0.3$ keV (1/4 keV band) and Local Hot Bubble (LHB)

The photo-absorption coefficient as a function of energy is approximately proportional to  $E^{-7/2}$  where the X-ray photon energy  $E$  is much higher than the absorption edge energy of the element. The neutral gas column density of  $1 \times 10^{21} \text{ cm}^{-2}$  is not transparent for X-ray photons below 0.3 keV. In Figure 2.13 (a), the 0.2-0.3 keV intensity in the X-ray background is plotted as a function of total Galactic neutral column density of the direction. The 0.2-0.3 keV intensity decreases with increasing column density. However, the intensity ratio of the 0.1 - 0.2 keV band to the 0.2 - 0.3 keV band is constant (Figure 2.13 (b)). This is very different from what is expected from the Galactic absorption (the broken curve). Thus, the anti-correlation as shown in Figure 2.13 (a) is not due to the absorption, a large fraction of the X-ray background in 0.1-0.3 keV is not absorbed by the Galactic neutral medium. The anti-correlation is interpreted by the displacement model (Sanders et al. (1977)). In this model, the solar system is surrounded by a hot plasma and the depth of hot plasma along the line of sight is anti-correlated with the total column density of the Galactic neutral medium. The region filled with hot plasma is often called the Local Hot Bubble (LHB).

Figure 2.14 shows an example of shadowing effects using the molecular cloud MBM-12 which is located at a distance of about 100 pc. The X-ray intensities of three energy bands are plotted as a function of 100  $\mu\text{m}$  far infrared intensity ( $I_{100}$ ). It is known that  $I_{100}$  is well correlated with  $N_{\text{H}}$ ;  $N_{\text{H}}(10^{20} \text{ cm}^{-2}) = 1.4 I_{100}(\text{MJy sr}^{-1}) + 0.15$ . X-rays from the source in the three energy band are expected to be blocked if MBM-12 is located between the source and the Earth along the line of sight. In Figure 2.14, we find that a large fraction of the X-ray background in the R4+R5 and the R6+R7 bands are supposed to come from behind the MBM-12. On the other hand, a large fraction of R1+R2 band comes from the front of MBM-12. If the LHB is the source of xrayBkg in the 1/4 keV band, the depth of the local hot bubble along the line of sight must be at most 100 pc distant from the Earth.

### 2.5.4 Hot plasma in Galactic halo

Yoshino et al. (2009) showed the correlation between the OVII and OVIII intensities in the 14 directions toward high latitude, as shown in Figure 2.15. In their paper, the time-dependent geo-coronal SWCX contamination is removed by calculating the solar wind proton flux using the ACE SWEOM and the WNID SWE data. point sources are also excluded.

All data points indicated that an OVII intensity equal to or larger than 2 LU (LU = ph/s/cm<sup>2</sup>/str). And the data points with OVII > 2 LU follow approximately the relation,

$$\text{OVIII intensity} = 0.5 \times (\text{OVII intensity} - 2 [\text{LU}]). \quad (2.7)$$

They discussed that the offset intensity of OVII emission arose from the Heliospheric solar-wind charge-exchange and from the Local Hot Bubble. The excess OVII (2-7 LU) is emission from a more distant place in the galaxy. If we assume collisional-ionized-equilibrium-plasma (CIE) emission, the temperature is estimated to be  $\sim 0.2$  [keV] from the OVII to OVIII ratio. Yoshino et al. (2009) employed a spectral model:

- Solar Wind Charge Exchange (SWCX) + Local Hot Bubble(LHB): As an SWCX model, they assumed thin thermal CIE plasma emission with the solar abundance.
  - Temperature fixed at 0.1 keV.
  - The normalization was fixed to a value to reproduce the 2 LU offset intensity in the OVII emission.
- Galactic disk and halo emission: They assumed thin thermal CIE plasma emission with solar-abundance. It is absorbed by the Galactic neutral hydrogen.
  - Absorption column density was fixed at the value from the HI observations.
  - Temperature of  $\sim 0.2$  keV.
- Unresolved point sources: The two broken-power-law.
  - Break energy fixed at 1.2 keV
  - soft index fixed at 1.52 and 1.96
  - hard index fixed at 1.4
  - Normalization for the soft index 1.52 fixed at  $5.7 \text{ photons cm}^{-2} \text{ s}^{-1} \text{ keV}^{-1} \text{ str}^{-1}$  at 1 keV, while the normalization for 1.96 set to be free.

The spectral shape assuming the two broken-power-law spectra was introduced by introduced by Smith et al. (2007), in order to take into account the fact that some of the point sources resolved by *ROSAT* and *Chandra* below 1 keV showed a steeper spectrum than the average the AGN spectrum in 2-10 keV (the photon index = 1.8), while the other show a flatter spectrum. They also employed a single power-law function to estimate the possible systematic errors introduced by the choice of the spectral model functions.

Henley & Shelton (2013) investigated further the spatial distribution of the galactic halo emission by using the *XMM-Newton* data. Figure 2.16 shows their result, with those from *Suzaku*. The emission measures observed by *Suzaku* and *XMM-Newton* are consistent with each other.

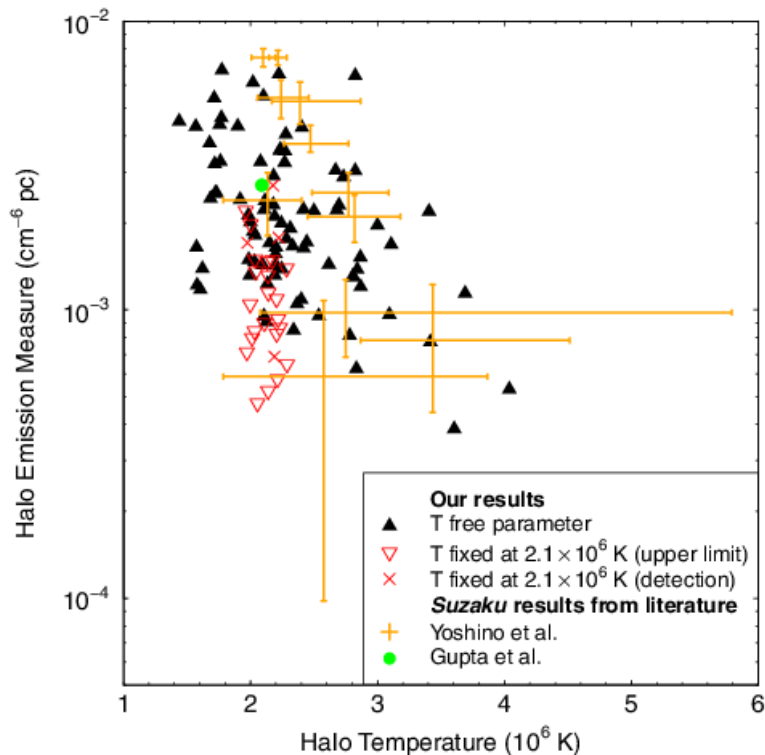


Figure 2.16: Soft X-ray diffuse background observed by *XMM-Newton* (Henley & Shelton (2013)) together with that observed by *Suzaku*. Orange cross is derived from *Suzaku* results (Yoshino et al. (2009)) while black cross observed by *XMM-Newton* (Henley & Shelton (2013)). Filled black triangle from *XMM-Newton* should be compared with orange crossed from *Suzaku*. The emission measures observed by *Suzaku* and *XMM-Newton* are consistent with each other.

#### 2.5.4.1 Line-of-sight extension of hot plasma in Galactic halo

From combined analyses of the absorption lines and emission lines in the approximately same directions, we can constrain the line-of-sight depth of the plasma, since the absorption is approximately  $\propto nL$ , while emission is  $\propto n^2L$ , where  $n$  and  $L$  are, respectively, the density of the plasma and the line-of-sight depth. Yao et al. (2009) used *Chandra* grating spectrum of the X-ray binary source in LMC, LMC X-3 for the absorption and the *Suzaku* CCD spectrum from the two directions close to LMC X-3 for the emission (Figure 2.17 (a)).

The ionization temperature of oxygen inferred from the OVII to OVIII emission ratio is significantly higher than that inferred from the OVII to OVIII absorption ratio. This suggests the temperature gradient ( $10^{5.5\sim 6.5}$  K) along the line of sight: although the emissivity of OVII decreases rapidly below  $10^6$  K, the ionization fraction of OVII stays almost constant down to  $10^{5.5}$  K, while both the emissivity and ionization fraction of OVIII rapidly decreases below  $10^{6.5}$  K. Thus, existence of hot plasma in the temperature range between  $10^{5.5}$  and  $10^6$  K can increase the equivalent width of the OVII absorption line without increasing the emission intensity.

Yao et al. (2009) introduced temperature gradient along the line of sight. Because the dynamical status of the hot plasma in the halo is not known, there is no realistic model based on the physics of the halo. Thus, they

assumed a simple exponential model

$$n = n_0 e^{-\frac{z}{h_n}}, T = T_0 e^{-\frac{z}{h_T}}, \quad (2.8)$$

where the  $z$  is the vertical distance from galactic plane,  $n_0$  and  $T_0$  are the density and temperature at the Galactic plane,  $h_n$  and  $h_T$  are the scale heights of density and temperature, respectively. From these equations, we find

$$n \propto T^{1/\gamma}, \quad (2.9)$$

where  $\gamma = h_T/h_n$ . Thus this model is equivalent to a polytrope model which is widely used to describe the equation of state of self-gravitating gases. In this case, the polytrope index is  $\gamma$ . In (a) of Figure 2.18, the combined fit results of the emission and absorption lines in OVII and OVIII are shown.

In Figure 2.18, we find that the scale heights are within the 1 - 10 kpc range. Hagihara et al. (2011) and Sakai et al. (2014), obtained similar results in the lines of sight of the two active galactic nuclei with 2155-304 and Mkn 421 ((b) of Figure 2.18).

On the other hand, Gupta et al. (2014) obtained quite different results from Sakai et al. (2014) with the same Mkn 421 data. Gupta et al. (2014) considered neither the temperature gradient nor the density the gradient. They assumed the constant temperature although density up to a certain depth and the density was assumed to drop to 0 abruptly. As a result, they required significantly large line of sight depth of 100 kpc to explain the absorption equivalent width.

## 2.6 Possible origins of unknown X-ray background components below 2 keV and their searches

In the soft X-ray band, we can distinguish SWCX and the hot plasma in the Galactic halo by using the OVII and OVIII relation, whereas we cannot separate continuum emission of unresolved point-source and Galactic halo. This is why the major uncertainty in the resolved fraction in 0.5 - 2 keV still exists. On the other hand, in 2-8 keV, we can explain the observed spectrum by using the synthesized the AGN emission. *Chandra* has resolved 92.7% of the X-ray background in 2-8 keV into point sources, residual 7.3% of xrayBkg in 2-8 keV can be explained by extrapolating log  $N$ -log  $S$  plot.

### 2.6.1 Two possible additional origins of extragalactic emission

$\Lambda$ CDM model is now widely believed as a picture of the Universe. Figure 2.19 shows a theoretical picture of the stages in the evolution of the Universe. The afterglow of Big Bang has been confirmed by observing CMB. Brief reviews are given below.

1. First of all, initial fluctuation, possibly quantum fluctuation, takes place, and then the Universe starts to expand exponentially (so-called Inflation). After the Inflation, the temperature of the Universe is approximately  $10^9$  K. Some light nucleus such as Li, Be, B are created in this epoch.
2. In the early Universe, when the temperature of the Universe down to approximately 4000 K, protons and free electrons are combined and changed into neutral hydrogens. Accordingly, the Universe transparent to photons, because these light elements did not affect photons.
3. At  $z \sim 100$ , the temperature of the Universe gets further down to approximately 60 K and more neutral hydrogens are created. Most of the photons interact with the neutral hydrogens.
4. Dark matters are vialized and then, dark matter halos are created. Stars and Galaxies, active galactic nuclei (AGN) are gradually created by the dark halo gravity. In the next phase ( $z \sim 15$ ), these objects emit many photons and these photons make neutrals ionized. As a result, some ionized gases are gradually created (Re-ionization). Finally, at  $z \sim 6$ , Stars, the AGNs and Galaxies are completed.
5. After that large scale structure was gradually created. Baryonic matters which have not been included in a gravitationally bound system follow the large scale structure and expected to form Warm Hot Intergalactic Medium (so-called the WHIM). The large scale structure was forming gradually. Present Universe is accelerated by dark energy.

From the above scenarios, we can consider two major origins of unknown X-ray background components below 2 keV; thermal emission from the WHIM ( $z < 0.3$ ) and the relics of the re-ionized X-ray photons at ( $z \sim 10$ ).

### 2.6.1.1 X-ray observation of Warm Hot Intergalactic Medium (WHIM)

More than half of the baryonic matter in the present Universe has not been observed (so-called missing baryon problems).

In Scenario 5 in Section 2.6.1, the WHIM ( $z < 0.3$ ) contains more than half of Baryonic matter in the present Universe and expected to be in the plasma state. Its temperature is  $10^{5\sim 7}$  K heated up by gravitational heating, however, it is very faint in X-rays, as it is widely distributed along the large scale structure of the Universe. This is why we have not successfully observed the WHIM so far (so-called missing baryon problem see detail Cen & Ostriker (1999)). The equivalent width for the OVII and the OVIII emission lines from CIE plasma is only a few eV.

The wavelength-dispersive high-resolution spectrometers onboard the *Chandra* and *XMM-Newton* observatories are considered to be most sensitive to the WHIM. With these instruments, searches have been performed for absorption lines by the WHIM in the energy spectra of the background the AGN. Fujimoto et al. (2004) are one of the early pioneering works of this study. Nicastro et al. (2005) claimed  $5.8\sigma$  (sum-of-lines significance) detection of two Warm-Hot Intergalactic Medium (WHIM) filaments at  $z > 0$  in the energy spectrum of Mkn 421 observed with *Chandra* transmission gratings. This observation strongly supports the existence of the WHIM. However, it did not measure the strength of the WHIM emission contained in the X-ray background. We can resolve the line-of-sight depth and density of the WHIM if we observe the WHIM emission and the line absorption from the WHIM. We note the wavelength-dispersive high-resolution spectrometers can be only employed to point sources. Measurements of the WHIM emission can reveal the filamentary extended structure of the WHIM.

### 2.6.1.2 Cosmic re-ionization by X-ray heating

The 21 cm global signal and relics of the re-ionized X-ray photons are useful to constrain the nature of high-redshift heating source (Fialkov et al. (2017)). Fialkov et al. (2017) simulated the evolution of the high redshifted Universe in large cosmological volume within  $384 \text{ Mpc}^3$ . They generated a density fluctuation of the early Universe based on the WMAP observation. They employed the unresolved spectrum simulated by Cappelluti et al. (2012b) to set maximum possible X-ray efficiency. They also used the observed intensity of the unresolved X-ray background in the 0.5-2 keV band as measured by *Chandra* (Hickox & Markevitch (2006)). Figure 2.20 shows the simulated extragalactic contribution, together with the observed unresolved X-ray background. Black dotted curve in this figure is best-fit spectral index derived from Hickox & Markevitch (2006). Note that normalization is re-scaled at horizontal bar. The shape of the simulated X-ray background in the 0.5-2 keV band shown in this figure is poorly constrained by observations. The brightness temperature of the global 21cm line is calculated by their simulation. Figure 2.21 shows the temperature of the global 21 cm line as a function of redshift ( $1+z$ ). Different colors represent different X-ray heating models. The brightness temperature gets more than 0 if X-ray heating adequately effects.

### 2.6.1.3 Constraining possible origins of unresolved X-ray background below 2 keV with spatial power spectrum

In Scenario 4 in Subsection 2.6.1, X-ray photons emitted from the AGNs change the HI clouds into HII clouds. Some researchers tried to observe the X-ray emission coming from the re-ionization epoch for constraining the X-ray re-heating. For this purpose, they proposed to utilize the difference in the spatial power spectra of different origins. In the CDF-S region, after excluding resolved point sources, origins of the unresolved spatial power spectra are considered by Galeazzi et al. (2009), Kolodzig et al. (2017), and Cappelluti et al. (2012a). After estimating the spatial power spectrum of the X-ray background without point sources in the 0.5-2 keV band, they tried to reconstruct it with a model function. The model function consists of a sum of components representing shot noise of (nearby) the AGNs and Galaxies, clustering the AGN, clustering Galaxies, the WHIM, and re-ionizing mini-Quasars. The model function of the components were derived from the cosmological  $\Lambda$ CDM simulations. They claimed that the model could reproduce the observed power spectrum well without adjusting any model parameters. Instead, they added model components one by one to the model. They started a model containing only shot noise of the AGNs and Galaxies. This could not reproduce the observed power spectrum and added the model components one by one and reached the model including shot noise of the clustering the AGNs, Galaxies, the WHIM and mini-Quasars.

Their model parameters for the unresolved X-ray background in the 0.5-2 keV band are shown in Table 2.2. The contribution of the components excluding the shot noise, remaining  $\sim 12\%$  of the X-ray background emission are listed in the first column of Table 2.2.

Table 2.2: Components of the X-ray background in 0.5-2 keV (Cappelluti et al. (2012b)).

| Component                | Surface brightness<br>$10^{-13} \text{ erg cm}^{-2} \text{ s}^{-1} \text{ deg}^{-2}$ | Fraction to total <sup>†</sup><br>% | Fraction to unresolved <sup>††</sup><br>% |
|--------------------------|--|-------------------------------------|---|
| Clustering the AGN       | 1.97   | 2.4±0.2                             | 19.3±1.3                                  |
| Clustering Galaxies      | 2.51   | 3.1±0.2                             | 24.6±1.7                                  |
| IGM (WHIM <sup>*</sup> ) | 5.70   | 7.0±0.5                             | 55.9±3.9                                  |
| Re-ionizing mini-Quasars | < 0.35   | < 0.5                               | < 3.4                                     |
| Total                    | 10.18  | 12.4±0.9                            | 100                                       |

<sup>†</sup>Observed total power-law flux in 0.5-2 keV is  $8.15 \pm 0.58 \times 10^{-12} \text{ erg/cm}^2/\text{s/deg}^2$  (Lehmer et al. (2012)).

<sup>††</sup>Simple ratio for each component.

<sup>\*</sup>WHIM is defined to be gas in the region with over density  $< 100$  and with temperature satisfying between  $10^5$  to  $10^6$  K.

Figure 2.22 is the  $\log N$ - $\log S$  function of point sources used by Cappelluti et al. (2012b) to construct Table 2.2. In the model, the main point sources contributing to the 0.5-2 keV background are galaxies in  $S < \sim 5 \times 10^{-16} \text{ erg/s/cm}^2$ .

## 2.7 Summary of this Review

The X-ray background is composed of the following components:

- (a) Faint point sources.

They are Active Galactic nuclei (AGNs), galaxies and stars. In 2-8 keV, about  $92.7 \pm 13.3\%$  of the X-ray background has been resolved into point sources. The total intensity and spectrum in 2-100 keV can be modeled with the AGNs at  $z = 0$  to  $\sim 5$ .

- (b) Emission from the Heliosphere (Heliospheric SWCX).

This is non-thermal emission caused by charge exchange processes between the solar wind and neutrals (mostly H and He) in the interplanetary space. This process is important in the low energy range of the 1/4 keV band. Also, this process contributes a part of the OVII line.

- (c) Thermal emission from the Local Hot Bubble (LHB), which surrounds the solar system.

This emission also contributes mainly to the 1/4 keV energy band. The emission which shows anti-correlation with the total Galactic neutral column density must arise from the LHB.

- (d) Thermal emission from the halo of our Galaxy.

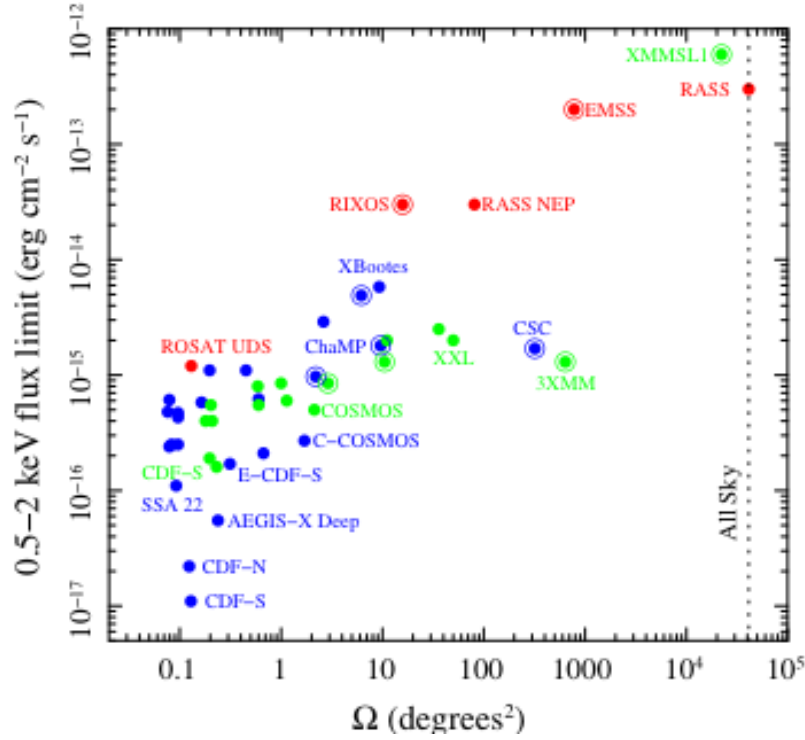
This is the main contributor of the OVII and the OVIII emission lines in the 3/4 keV band. The average temperature of the plasma is  $\sim 0.2$  keV and extended in 1 to 5 kpc scale in the halo of our Galaxy.

- (e) Unknown components in 0.5-2 keV.

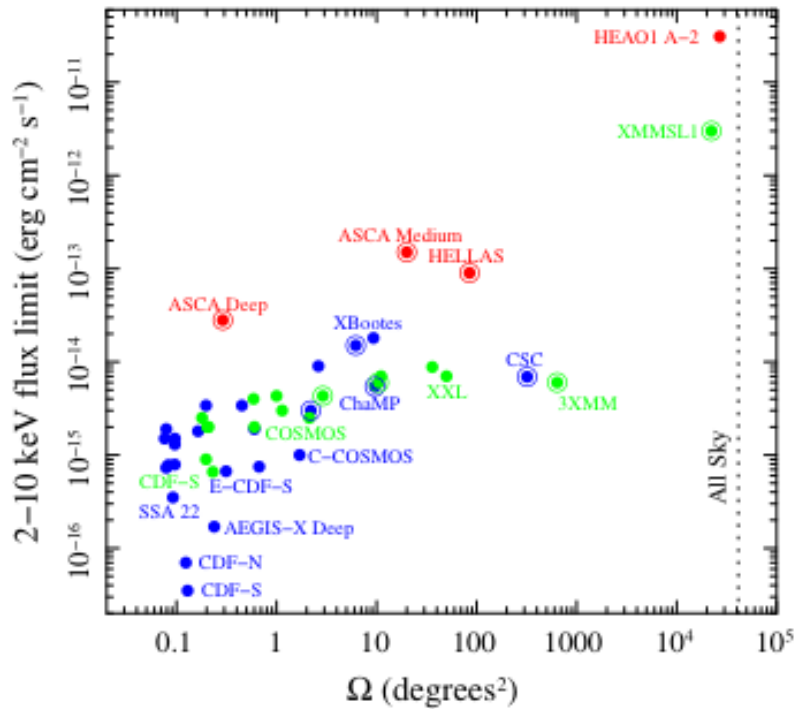
A sum of all the components mentioned above leaves room for unknown emission, whose intensity is about 10 % of the total X-ray background in 0.5-2 keV, and about 20 % in 0.5-1 keV. Two candidates were discussed.

(1) Warm-Hot Intergalactic Medium (WHIM) existing along the filaments of the large-scale structure of the Universe at  $z < 0.3$ . (2) The X-ray emission from the cosmic ionization in the early Universe. The peak of the emission energy was likely at 10-20 keV at  $z = 20$ , while it is expected at 0.5-1 keV at present.

Figure 2.23 shows the components which contribute to the X-ray background and their scales. The main purpose of this thesis is to study the contributions of the above components as much as possible by X-ray spectroscopy using the presently available data. Our interest is in particular in the last item, (e).



(a) In 0.5-2 keV.



(b) In 2-10 keV

Figure 2.4: Previous deep surveys (a) in 0.5-2 keV and (b) in 2-10 keV (Brandt & Alexander (2015)). The blue filled circles are the *Chandra* survey and the green filled circles are the *XMM-Newton* survey. For comparison purpose, a few surveys from previous X-ray missions are shown in the red filled circle. The solid circles around filled circle indicate serendipitous surveys. The vertical dotted line shows the solid angle for all sky.

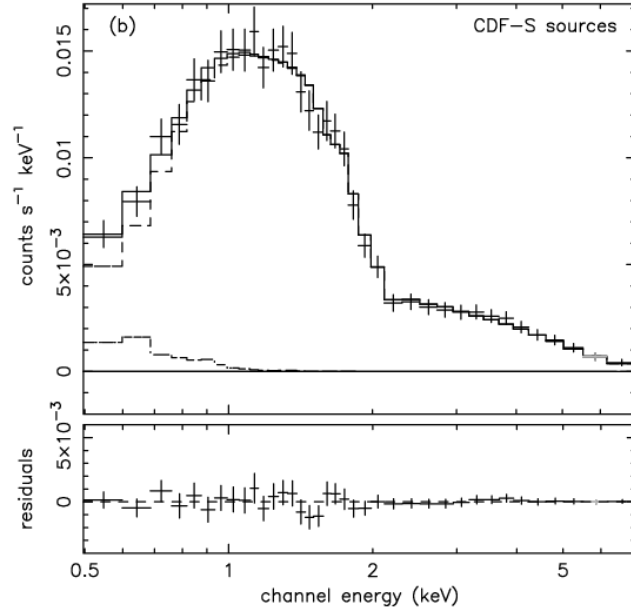


Figure 2.5: Total spectra for resolved sources in the CDF-S (Hickox & Markevitch (2006)). The resolved source positions are cited from Alexander et al. (2003). Their fitting model is a single power-law spectrum. Photon index is a  $1.47 \pm 0.04$  and normalization is  $6.78 \pm 0.18$  photons  $\text{cm}^{-2} \text{s}^{-1} \text{keV}^{-1} \text{str}^{-1}$  at 1 keV.

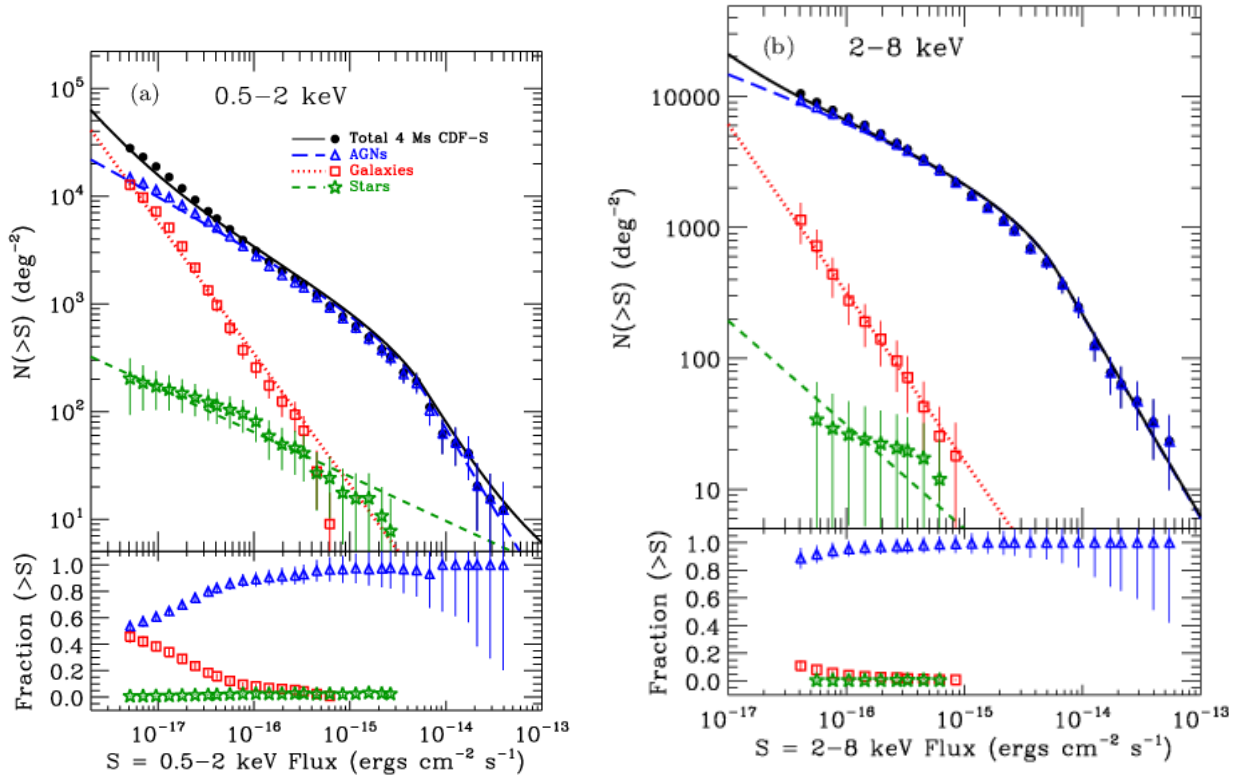


Figure 2.6:  $\log N$ - $\log S$  plot determined in the 4 Msec the CDF-S region (Lehmer et al. (2012)), (a) for 0.5-2 keV and (b) for 2-8 keV. The black filled circles are the observed data, which are classified by the AGNs, Galaxies and Stars by the follow-up observation of the other wavelengths. The blue open triangles are the AGNs, the red open squares are Galaxies and the green open stars are Stars. The green, blue and red dashed lines are the best-fit  $\log N$ - $\log S$  function. The black solid line is sum of the dashed lines. The *Chandra* detection efficiency is taken into account in the data.

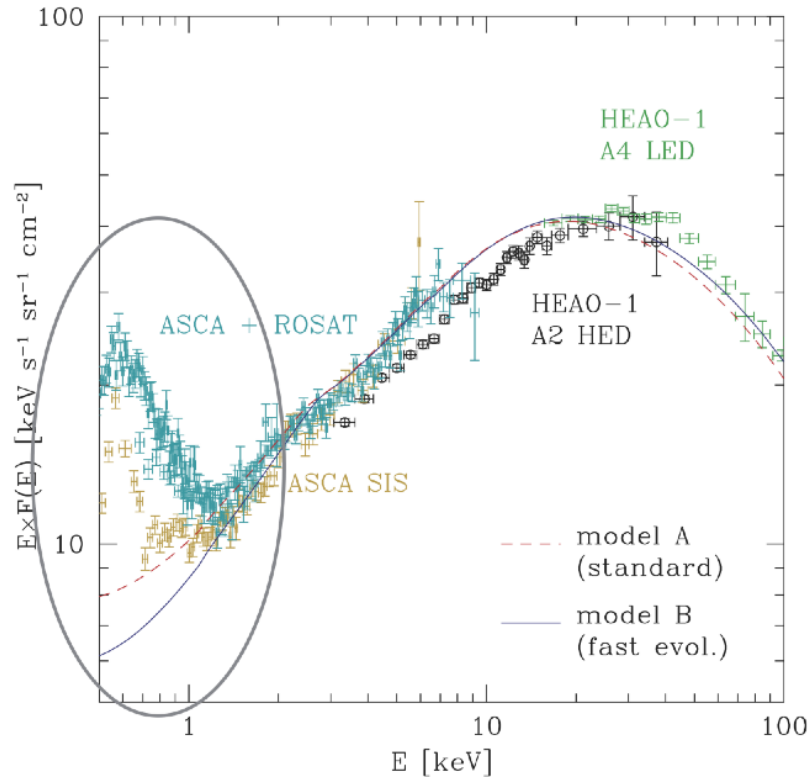
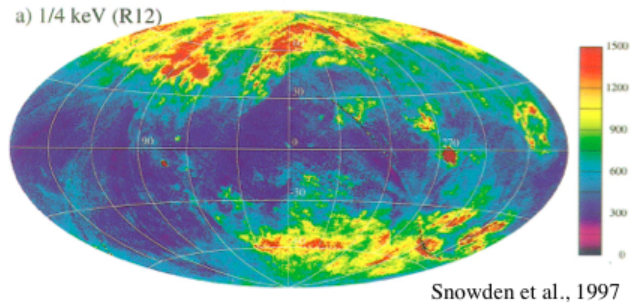
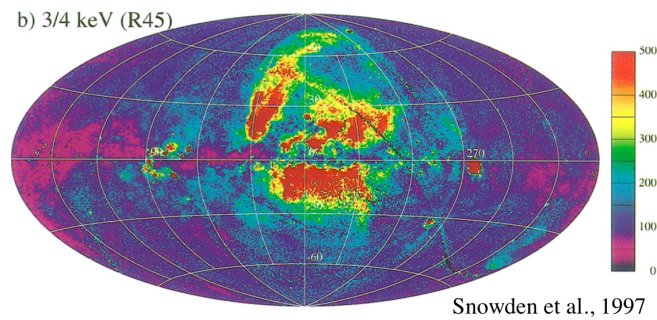


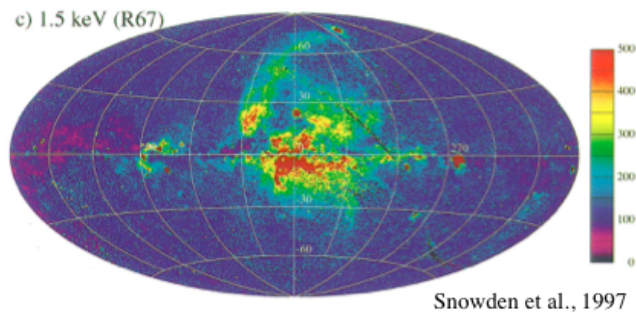
Figure 2.7: Synthesized the AGN spectra based on the models reproduced by model A and model B (for detail see text) v.s. the observed spectra cited from Gilli et al. (2001). The data in 3–40 keV and 15–100 keV are from the A2 HED and A4 LED detectors on board HEAO–1, respectively.



(a)



(b)



(c)

Figure 2.8: All sky images taken by ROSAT (Snowden et al. (1997)). The maps excluded point sources  $s$ , in reference to their own survey catalogue (RASS-I). The catalogue covers over 90% of all sky. The intervals when background enhancements above  $5\sigma$  are excluded and the period when the particle background was unpredictable are also excluded. Mean free path of photo-absorption in the 1/4 keV band (ROSAT R1+R2 band  $\sim 0.1 - 0.3$  keV (a)) is  $\sim 100$  pc. While the photons in the 3/4 keV band are absorbed by only the Galactic plane. In the 3/4 keV band (ROSAT R4+R5 band  $\sim 0.5 - 0.9$  keV: (b)), the most prominent features is the Loop I associated with North Polar Spur, the Eridanus enhancement and the Cygnus super bubble. The R6+R7 band is shown in (c).

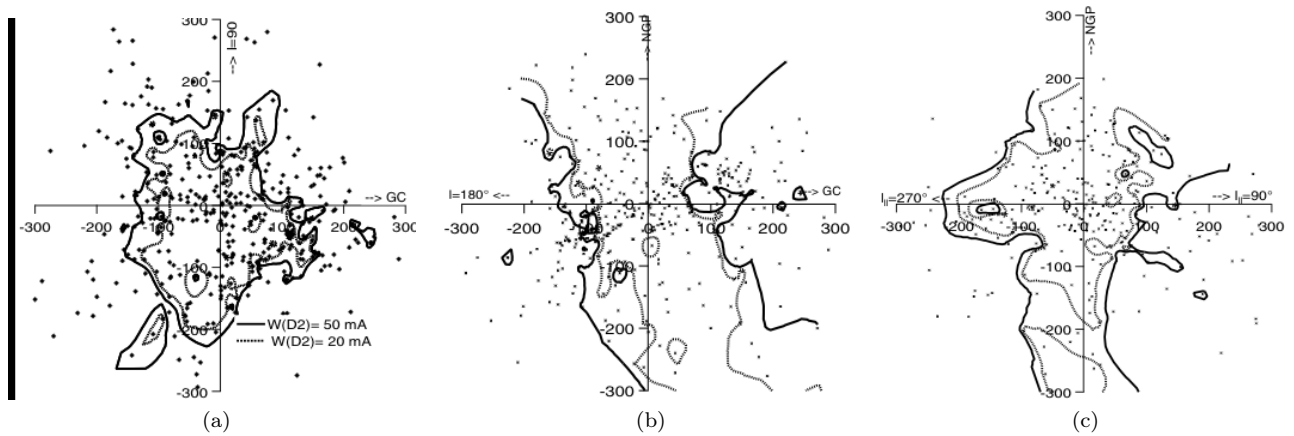
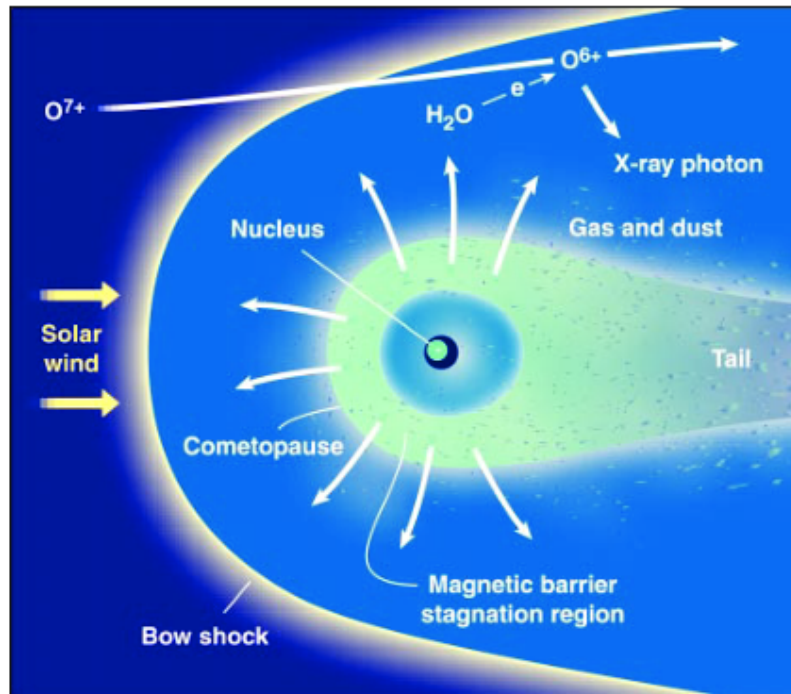
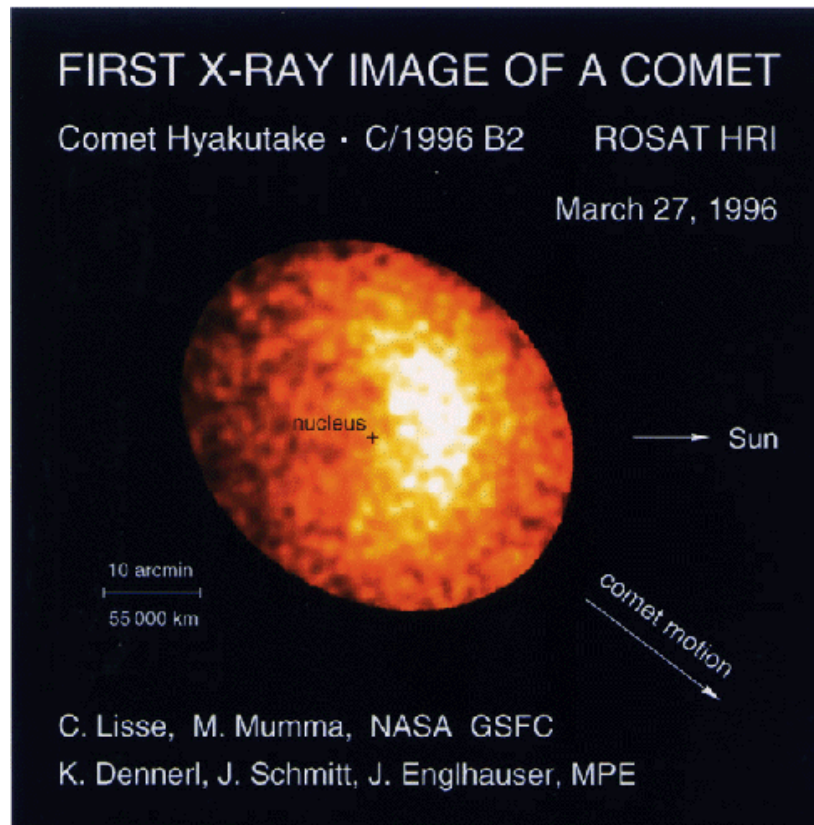


Figure 2.9: 3D map for dense gas (Lallement et al. (2003)) obtained by using the equivalent width of the NaI Fraunhofer D1 and D2 absorption lines of the stars whose distances are measured by the astrometry missions, *Hipparcos* and GAIA. These Figures are sliced maps for (a) galactic planes, (b) meridian planes and for (c) rotation planes. Dots denotes stellar targets.



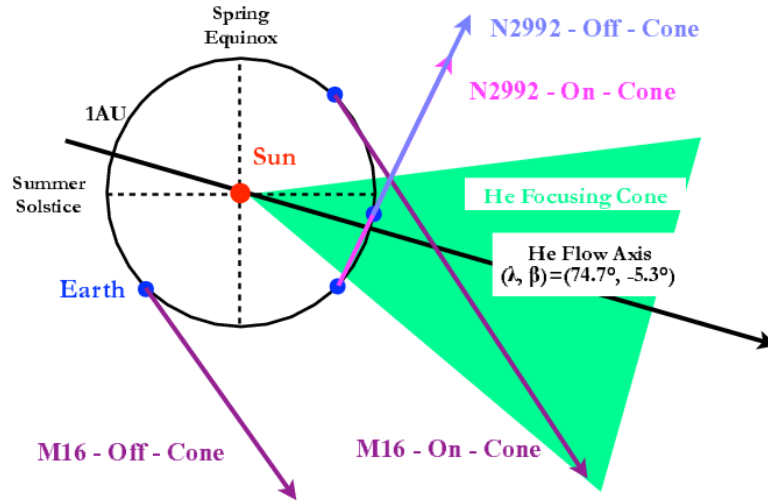
(a)



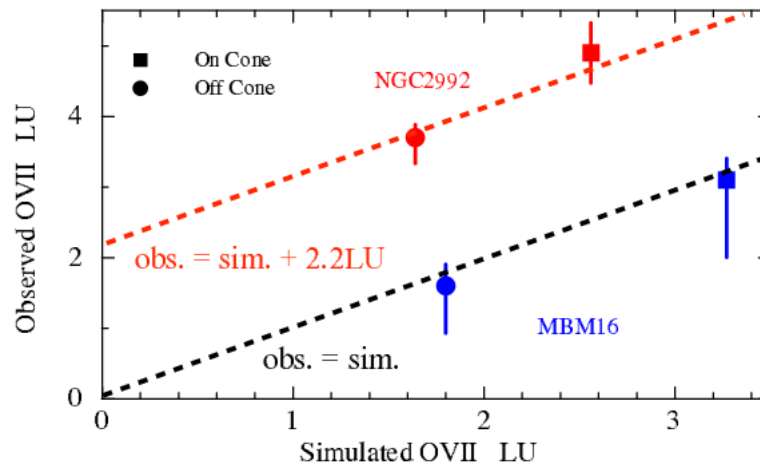
(b)

Figure 2.10: (a): Explanation of charge exchange interaction H and He with solar-wind ion (e.g.,  $O^{7+}$ ) (Cravens (2002)). (b): Soft X-ray image of Comet Hyakutake taken by ROSAT. The soft X-ray on the surface toward the Sun is stronger than opposite surface, because the moving comet gathers neutrals in front of itself.





(a)



(b)

Figure 2.12: Configuration for observing enhanced SWCX emission in direction with high Helium density (Yoshitake et al. (2012)) (a). The helium focusing cone caused by the Sun's gravitational attraction is shown in green. The Sun is moving in the opposite direction to the He flow. The molecular cloud (MBM16) blocks the distant source emission. An interaction between the solar wind and the dense neutral He atoms induces SWCX. Red and blue filled circles and squares are observed results and dashed lines are expected value by simulations provided by Koutroumpa (b). Possible origin for offset  $\sim 2$  L.U. is distant plasma, which means local hot bubble and galactic halo.

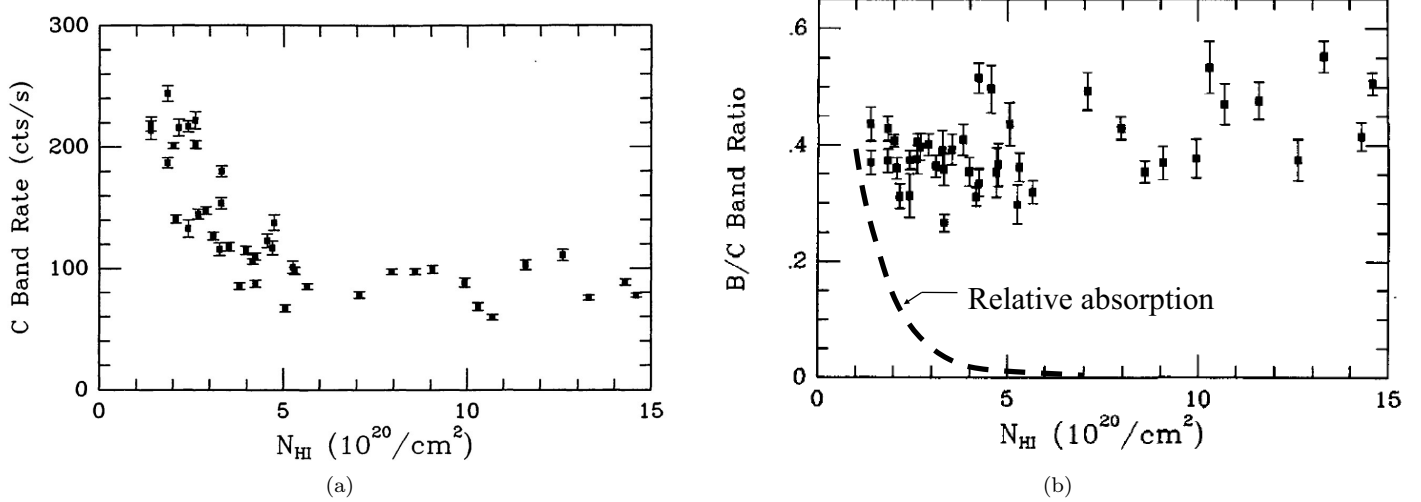


Figure 2.13: (a): C-band ( $\sim 0.2\text{-}0.3$  keV) counting rate obtained with the Wisconsin sounding rocket all sky survey, plotted as a function of total Galactic Hydrogen column density ( $N_{\text{H}}$ ). (b): B-band ( $\sim 0.1\text{-}0.2$  keV) to C-band count rate ratio, plotted as a function of  $N_{\text{H}}$ . The ratio of the transmissions of  $N_{\text{H}}$  in the B band to the C band is plotted with a dashed curve which is very different from the observation. Thus, it can not be due to the Galactic absorption although the C-band intensity shows anti-correlation with  $N_{\text{H}}$  (McCammon & Sanders (1990)).

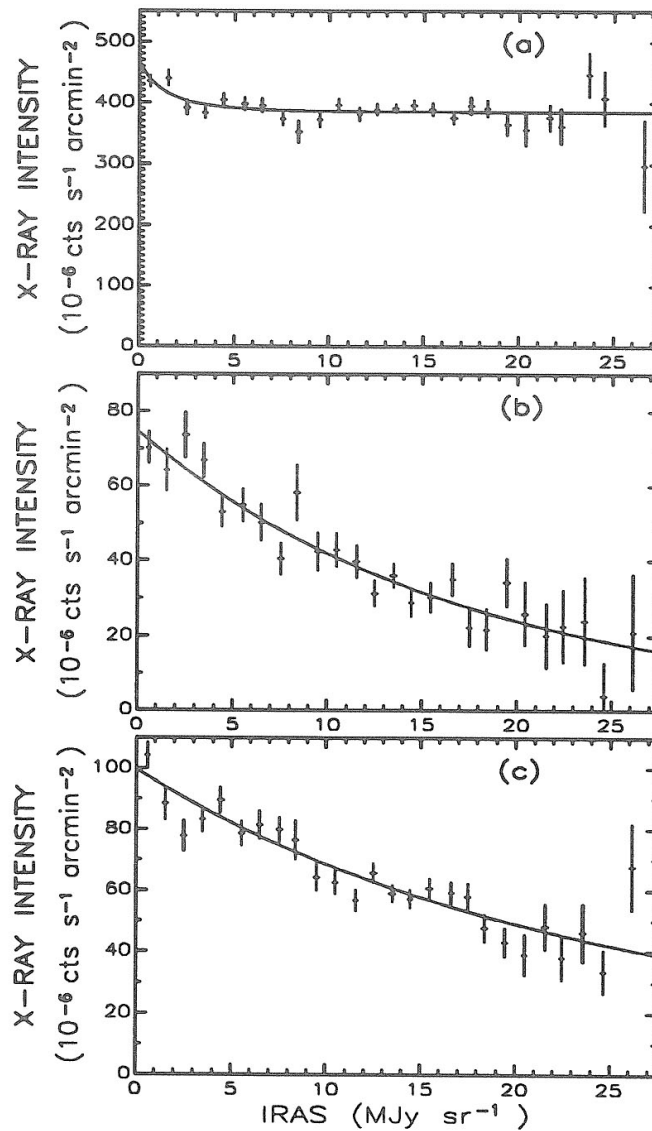


Figure 2.14: ROSAT counting rates in the direction of the MBM-12 molecular cloud ( $\sim 100$  pc) is plotted as functions of  $100 \mu\text{m}$  far infrared intensity ( $I_{100}$ ). Three panels are for different energy bands, (a) ROSAT R1+R2 (1/4 keV) band, (b) R4+R5 (3/4 keV) band, and (c) R6+R7 (1.5 keV) band. The  $100 \mu\text{m}$  intensity is known to show correlation with the total (atomic + molecule + dust) H column density;  $N_{\text{H}}(10^{20} \text{ cm}^{-2}) = 1.4 I_{100}(MJy \text{ sr}^{-1}) + 0.15$ . These Figures are cited from Snowden et al. (1993).

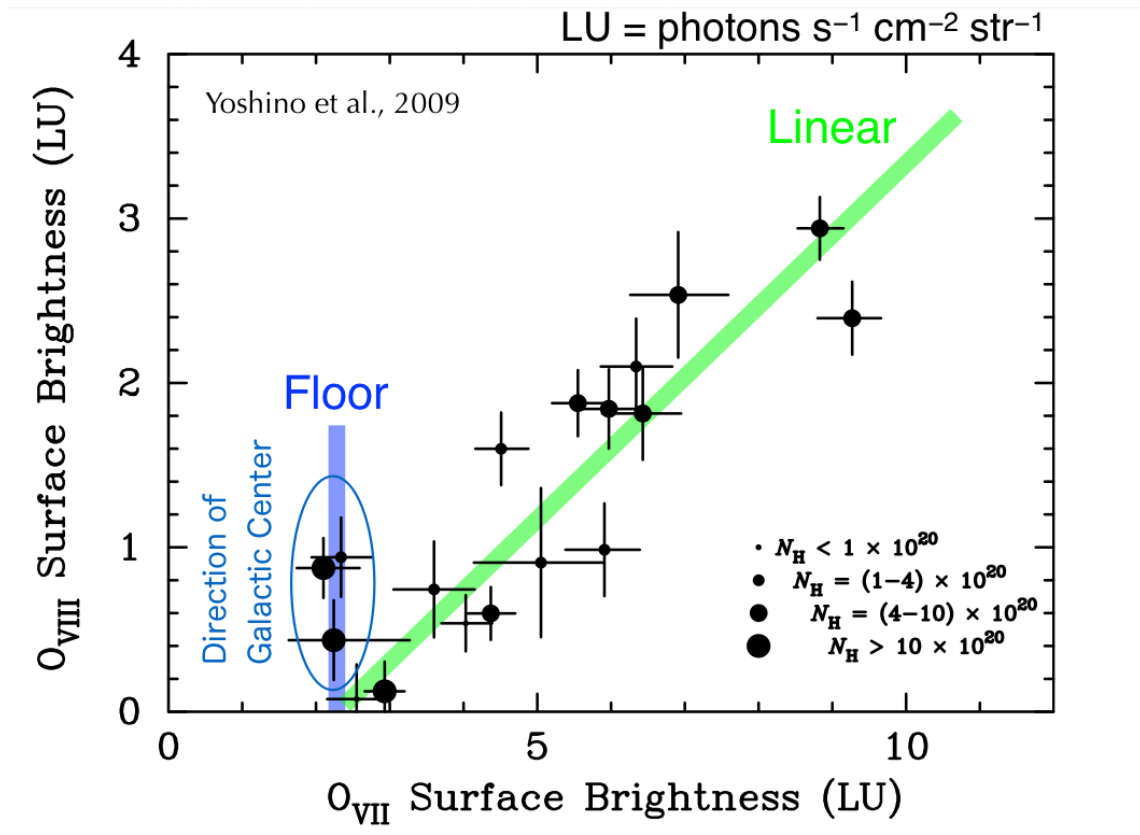


Figure 2.15: Relation between OVII surface brightness and OVIII surface brightness relation (Yoshino et al. (2009)). There are 14 observations along with the linear line to investigate the Galactic hot plasma emission in high Galactic latitude. Errors are at 90% confidence level.

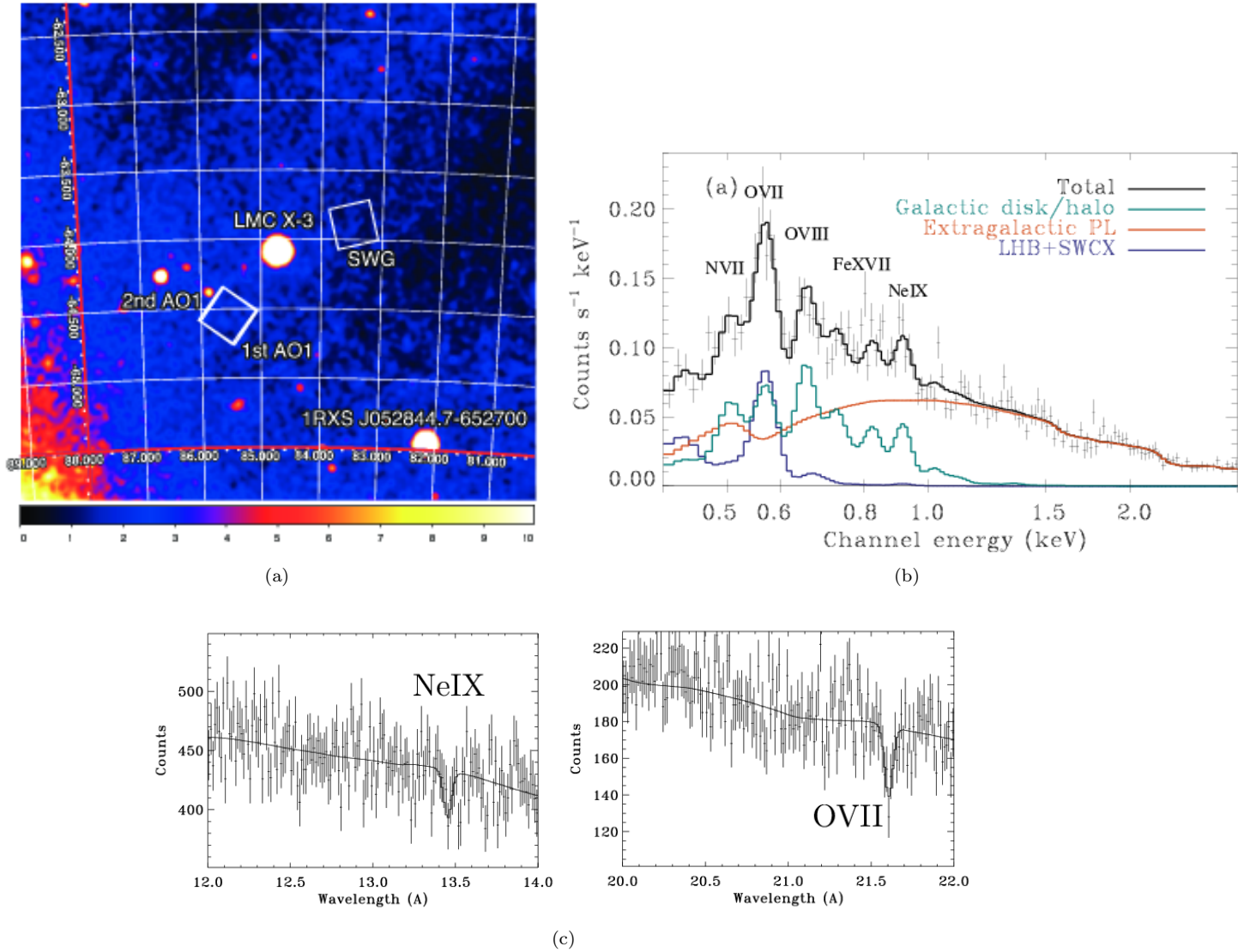


Figure 2.17: (a): ROSAT X-ray map centered at LMC X-3. Two squares show the Suzaku filed of view ( $20' \times 20'$ ). (b): Observed *Suzaku* spectrum in the vicinity of LMC X-3 and the best fit model functions convolved with the instrumental response functions. The X-ray background components in the model components are also separately shown. (c): *Chandra* spectra of LMC X-3. Only the narrow wavelength ranges including NeIX or OVII lines are shown. From Yao et al. (2009).

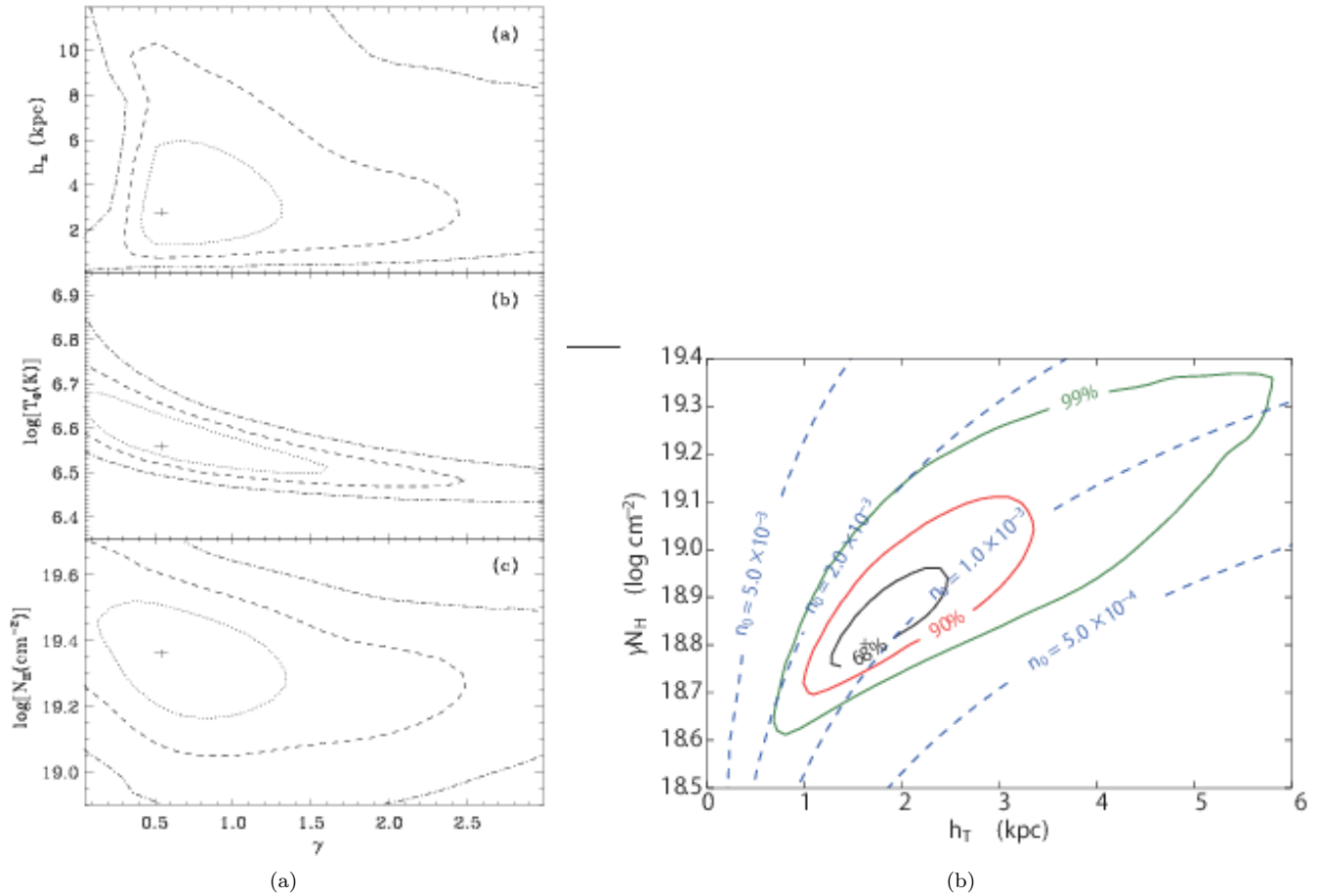


Figure 2.18: (a):  $\chi^2$  contour maps of spectral parameters of the combined emission and absorption fits to the LMC X-3 data. From Yao et al. (2009). (b):  $\chi^2$  contour maps of spectral parameters of the combined emission and absorption fits to the Mkn 421. From Sakai et al. (2014).

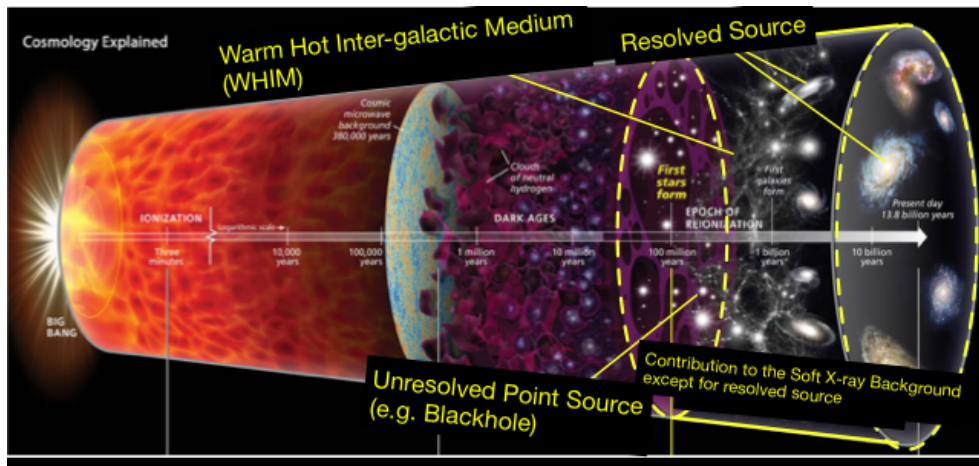


Figure 2.19: Evolution of Universe . Neutral hydrogen is re-ionized after dark ages. Initial the AGNs, Galaxies and Warm Hot Intergalactic Medium contributes to the X-ray background . Resolved X-ray sources are not included in the X-ray background.

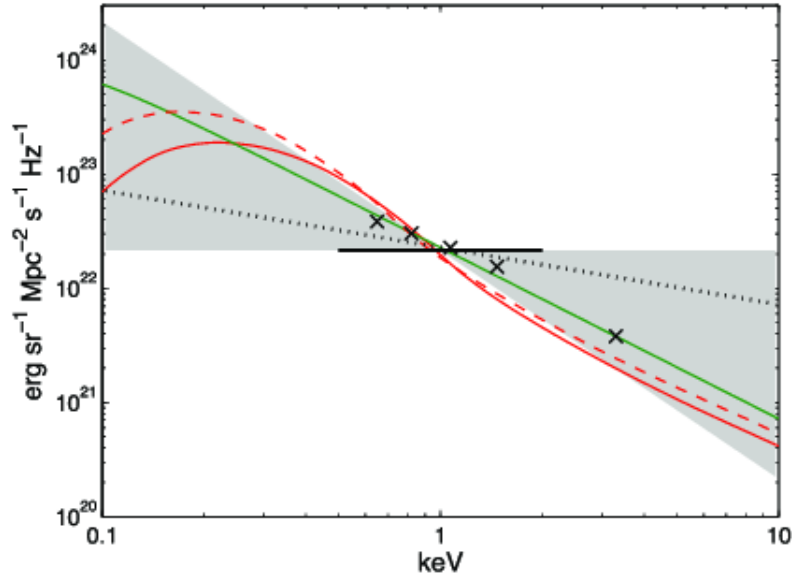


Figure 2.20: Extra-galactic contribution to the unresolved X-ray background (Fialkov et al. (2017)). Red dash, red solid, green solid are the different type of models to simulate X-ray heating. Gray shaded area is the different simulation considered by Dijkstra et al. (2012). Fialkov et al. (2017) calibrate the X-ray background in the 0.5-2 keV band to  $0.251 \times 10^{-12} [\text{erg cm}^{-2} \text{s}^{-1} \text{deg}^{-2}]$  derived from Cappelluti et al. (2012a). The black solid line is average intensity. Black crosses are the observed data cited from McCammon et al. (2002). The normalization of the black cross is rescaled at the horizontal bar at 1 keV. Black dots is best-fit spectra index derived from Hickox & Markevitch (2006), photon index 1.5. The normalization is also re-scaled at horizontal bar.

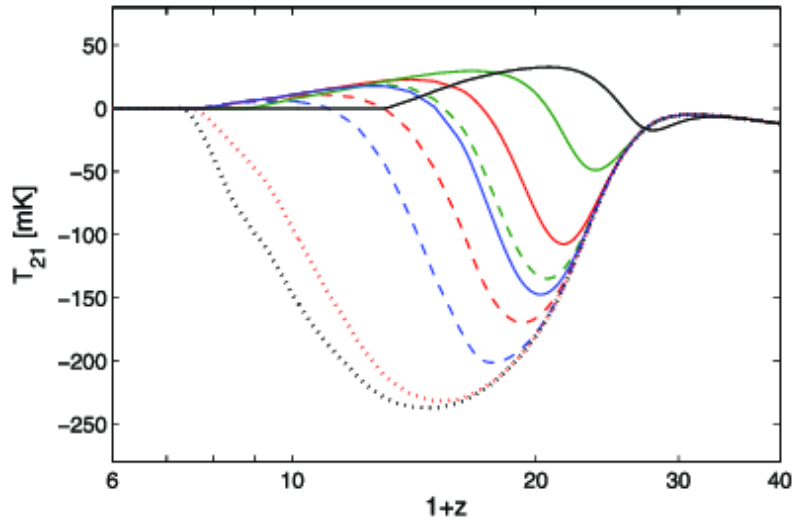


Figure 2.21: Brightness temperature of Global 21cm line (Fialkov et al. (2017)). The dashed and solid lines are calculated by different X-ray heating efficiency. X-ray heating efficiency for the dashed line is based on nearby galaxies. The solid lines are based on observed and the rescaled X-ray background Cappelluti et al. (2012a).

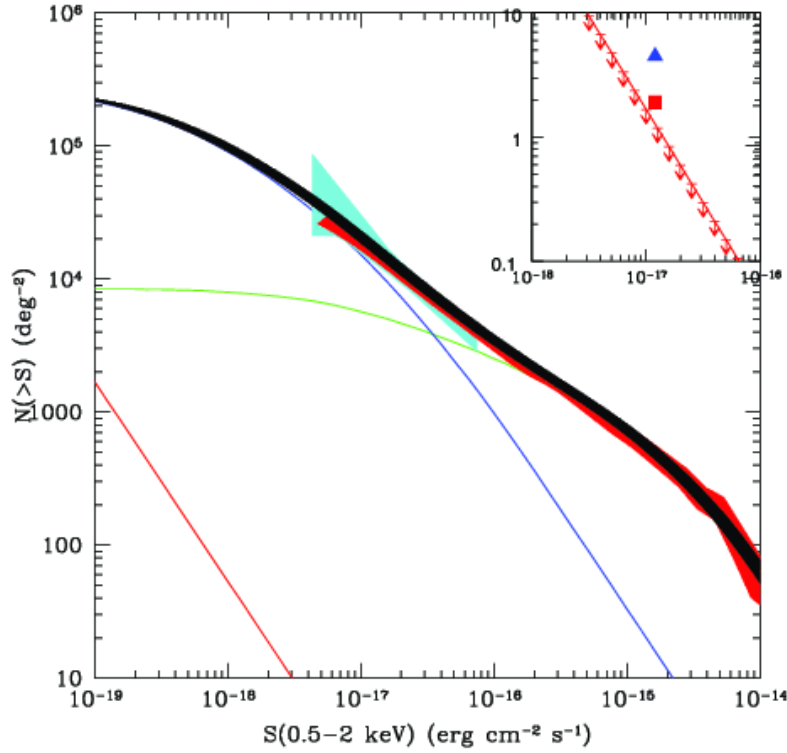


Figure 2.22:  $\log N$ - $\log S$  plot in 0.5-2 keV used to reproduce spatial fluctuation of observed unresolved X-ray background (Cappelluti et al. (2012b)), for the AGNs (green), Galaxies (blue) and for the sum of the AGN and galaxies (black-shaded). The black shade area means uncertainty due to count-rate to flux conversion. The red shaded area is the  $\log N$ - $\log S$  measured by Lehmer et al. (2012) in the CDFS 4 Msec observation. The lower red line expresses contribution of the mini-Quasars. The cyan shaded area is expected counts from the another fluctuation analysis (Miyaji and Griffiths (2002)). The inset shows the contribution of mini-Quasars and the blue triangle means the expected number of the AGNs at the 4 Msec CDFS flux limit, red square is the observed number counts of quasi-stars.

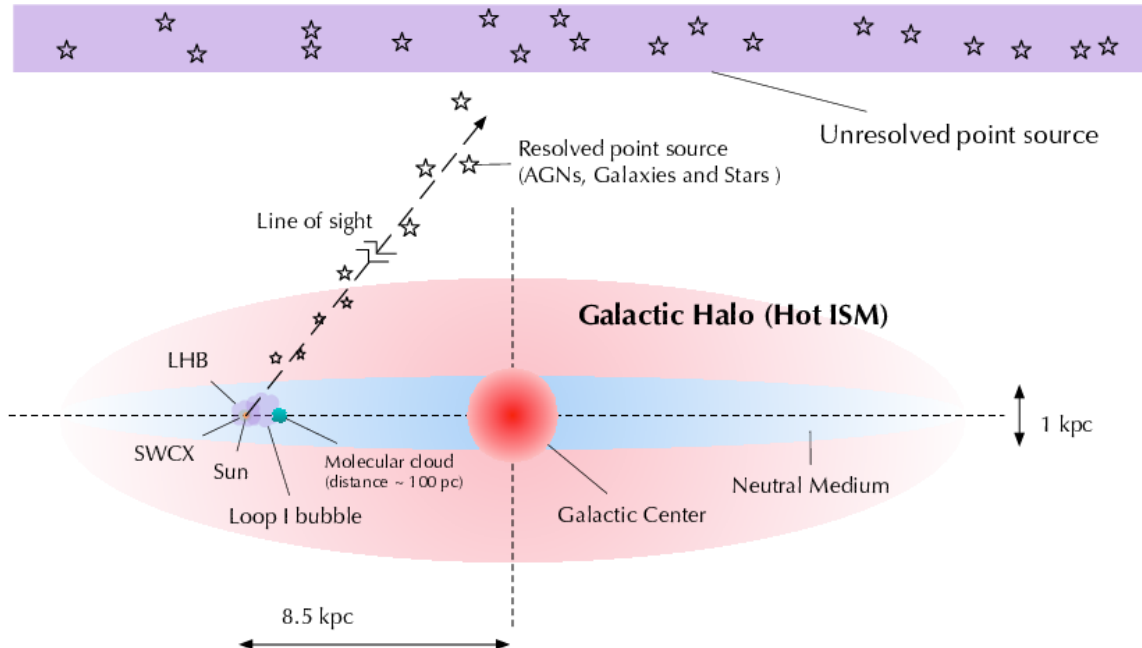


Figure 2.23: A schematic view of our understanding on the origins of the X-ray background.

## Chapter 3

# Strategy for anatomy of the X-ray background in soft X-ray band

### 3.1 Uncertainties in estimating spectral components

In the previous Chapter, we reviewed the present understandings of the X-ray background in the energy range of 0.5-8 keV. In Figure 3.1 (a), we show the present understandings schematically. In 2-8 keV,  $92.7 \pm 13.3\%$  were resolved into point sources in CDF-S. It is likely all the background in this band will be resolved into point sources with higher sensitivity instruments. We paint the contribution of point sources in the 2-8 keV band with blue color. Below 2 keV, excess emission becomes more significant in 0.5-1 keV than in 1-2 keV which indicated in red, white and orange in Figure 3.1 (a). Figure 3.1 (a) shows the components of 0.5-1 keV emission according to McCammon et al. (2002). The red box indicates the energy fluxes of the OVII and the OVIII emission lines. The orange boxes indicates thermal emission other than the OVII and the OVIII lines. According to McCammon et al. (2002), the strength of the orange component is likely to be close to the maximum value. One of the goals of the present thesis is to measure the ratio indicated in the white box (20%) i.e., an unknown component in Figure 3.1 (a). The largest uncertainty in the estimation of the rate (20%) takes place from the extrapolation of the blue box from 2-8 keV to 0.5-1 keV. Yoshino et al. (2009) analyzed X-ray background spectra in 14 different directions in 0.5 to 5 keV obtained with Suzaku XIS (X-ray CCD camera). They tried two different model spectra for estimating the contributions from the unresolved point sources. Independent two broken-power-law spectra model and a single power-law spectrum model. In the former model, the resultant spectrum becomes steep below about 1.2 keV than above 2 keV. Such a model was employed because the average spectrum of nearby active galactic nuclei (AGNs) shows a steeper spectrum below 1 keV, and thus the spectrum of the sum of the unresolved point sources is likely to have steeper spectrum below 2 keV. Yoshino et al. (2009) found both models represent the observed spectra equally well and the best-fit parameters of Galactic halo plasma are consistent with each other for the two models. By assuming a steeper spectrum below about 1.2 keV for the unresolved point sources, we can reduce the intensity of the unknown emission, and we can even make it zero.

We consider that we can reduce this uncertainty by removing point sources as much as possible in the X-ray spectrum. For the CDF-S region, the highest fraction of point sources has been resolved. Therefore CDF-S is the best candidate direction for this study. In Figure 3.1 (b), the blue boxes are the contribution of the resolved and the unresolved sources. The fraction of  $92.7 \pm 13.3\%$  is cited from Luo et al. (2017). In Figure 3.1 (a), we illustrate the breakdown of the X-ray background for CDF-S direction in 0.5-1 keV without resolved point source. In this plot, we assumed we can remove the same fraction of point sources in the 0.5-1 keV band as in the 2-8 keV band. The OVII surface brightness is known to show spatial variation. We used Henley & Shelton (2013) to estimate the OVII emission intensity of this direction. They analyzed the *XMM-Newton* data in the CDF-S direction, and determined the spectral parameters of the emission from Galactic halo. We calculate the OVII line intensity from the parameters to obtain 4.4 LU of the Galactic halo origin. However, we expect additional OVII emission from the Heliospheric SWCX to the observation. Since the observations were made in a low solar activity period, we expect additional 2 LU (SWCX) to 4.4 LU. Then the remaining thermal emission was simply scaled, shown in Figure 3.1 (b) from (a). If the contribution of the unresolved point sources is reduced to only 7 % from 38 %, the uncertainty in spectral shape will give much smaller effect in estimating the fractions of the remaining component.

Moreover, by analyzing the average spectra of the resolved point sources, sorted with their intensities will tell us the spectrum of faint sources. Using this information we can constrain the spectral shape of the remaining point

sources in 0.5-1 keV.

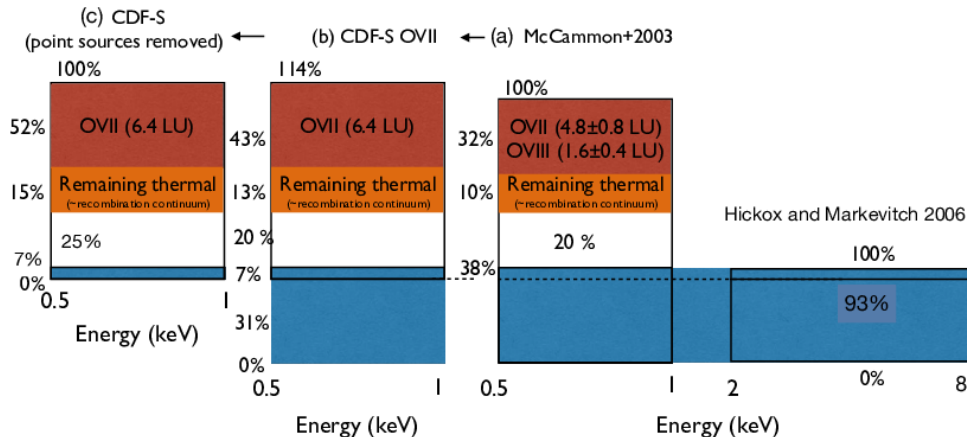


Figure 3.1: Contents of the X-ray background inferred from previous experiments. The abscissa of all panels is X-ray energy, while the ordinate expresses the percentage of energy intensity of different components of the corresponding energy band. Plot (a) is based on McCammon et al. (2002) and Hickox & Markevitch (2006), respectively. Plot (b) assumes the percentage of (a) but the thermal emission was modified by using the *XMM-Newton* observations of CDF-S direction (Henley & Shelton (2013)). As a result, the total intensity for this plot is not 100%. Plot (c) shows the expected percentages of components if we remove the contribution from all the resolved point sources of this direction.

### 3.2 Combining *XMM-Newton* and *Chandra* data

Hickox & Markevitch (2006) already removed point sources for the *Chandra* data of 1 Msec and 2 Msec CDF-S and CDF-N observations and estimated the spectrum of the remaining emission. However, the statistics of the spectrum without resolved point sources is poor, and it is not possible to distinguish between existence and non-existence of the unknown component. Low counting statistics is due to the relatively small X-ray collecting area of *Chandra*. The *XMM-Newton* observatory has the largest collecting area and performed 3.6 Msec observation of CDF-S. We thus consider that the combination of the two instruments will give us the best results. Namely, in the CDF-S direction, we remove point sources from the *XMM-Newton* data using the point source list of *Chandra* observatory.

The drawback of using *XMM-Newton* is its high non X-ray background. This problem will be discussed in the next section in detail. The *Suzaku* observatory has the lowest non X-ray background. However, the spatial resolution is too poor for this analysis. X-ray images of point sources will have a spatial extension because of the point spread function (PSF) of the X-ray collecting mirrors. Thus when we remove point sources we need to remove an area which covers the extent of the PSF. Because *Suzaku*'s PSF is large, no usable detector area will remain after removing point sources. Moreover, *Suzaku* did not observe in the CDF-S direction.

Although the PSF of the *XMM-Newton* mirrors is not good, we expect there remains a sufficient detector area with which we can perform spectral studies of the X-ray background without point sources.

### 3.3 Difficulty of using *XMM-Newton* data

Both *XMM-Newton* and *Chandra* are in a long elliptical orbit. Therefore both observatories are expected to have higher background than *Suzaku* which is in a low Earth orbit. However, *XMM-Newton* frequently has a higher non X-ray background than *Chandra*. There are different background components in *XMM-Newton*, but the most notorious one is soft protons. The exact cause is not known, however, it is generally believed low-energy protons drifting in the orbit are collected by the X-ray optics to the detector. Only *XMM-Newton* suffer from this background.

Ranalli et al. (2013) analyzed the *XMM-Newton* CDF-S data. Solar protons often create flare-like time events. They claimed “However, there is also a quiescent component of soft proton background, with much smaller brightness, that may occur for the entire length of an observation, and for which the standard recipe of identifying and excluding high-background periods is not applicable or which may remain even after the flares are excluded.” Thus, in the analysis of the X-ray background spectrum of *XMM-Newton*, a spectral model which represents soft protons

are often introduced. However, as the intensity and spectral shape of soft protons are both unknown, spectral analysis of the X-ray background becomes very difficult.

### 3.4 Our strategy

We consider that the combination of the *XMM-Newton* and the *Chandra* data will give the best result for measuring the different spectral components in the soft X-ray background. Then, the most serious problem in this approach seems to be the soft proton background.

Previous studies of soft proton background were for the relatively short time duration of a few hundred seconds. Although the time variation of soft protons has the hardest spectral index around the time scale. However, there seems to be much longer time scale variations. Since *XMM-Newton* observations in CDF-S direction consists of 33 sequences of observations. We consider that comparing the counting rates or spectra among the different sequences will tell us time variation of the soft proton background on longer time scales.

- (1) We utilize the *Chandra* point source list of the CDF-S point-source list, for the point source study and the remaining diffuse emission.
- (2) The spectrum of the faintest class of point sources will be used to estimate the spectrum of the unresolved point sources contained in the spectrum without resolved point source.
- (3) The intensities of point source removed and non-removed spectra in different energy bands will be compared.
- (4) The spectrum without point sources will be studied using the information obtained in (2).

# Chapter 4

## Instruments

### 4.1 The *XMM-Newton* observatory

*XMM-Newton* of European Space Agency (ESA) shown in Figure 4.1 was launched on December 10, 1999. We compared three representative instruments, *XMM-Newton*, *Chandra* and *Suzaku* for X-rays at 1 keV. Features of *XMM-Newton* are wide field of view, large effective area and good Half Power Diameter (HPD), as shown in Table 4.1. On the other hand, the count rate of the Non X-ray-Background (NXB) of *XMM-Newton* is higher than in *Suzaku*, because of the orbit and focal length (shown in Figure 4.2). We present a review of the telescope and European Photon Imaging Camera (EPIC) on board *XMM-Newton*.

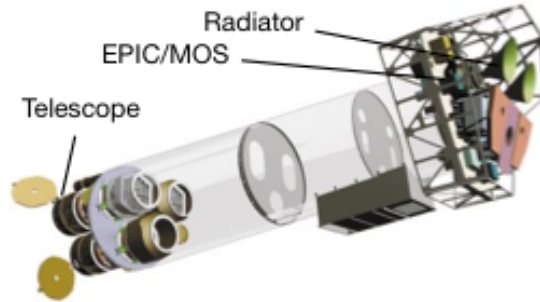


Figure 4.1: The *XMM-Newton* observatory. The original figure is cited from Jansen et al. (2001).

Table 4.1: Comparison among three recent instruments.

|                                 |                        | Chandra/ACIS | XMM-Newton/MOS | Suzaku/XIS |
|---------------------------------|------------------------|--------------|----------------|------------|
| HPD                             | [arcsec]               | 6            | 15             | 120        |
| FOV                             | [arcmin <sup>2</sup> ] | 17 × 17      | 33 × 33        | 18 × 18    |
| Effective Area (On-axis) @1 keV | [cm <sup>2</sup> ]     | 340          | 460            | 350        |
| Exposure of CDF-S               | [Msec]                 | 7            | 3.2            | 0          |
| Focal length                    | [m]                    | 10           | 7.5            | 4.5        |
| $E/\Delta E$ @1 keV             | [-]                    | 20 (BI)      | 20 (FI)        | 20 (BI)    |
| Perigee                         | [km]                   | 16000        | 7000           | 550        |
| Apogee                          | [km]                   | 133000       | 11400          | 550        |
| Period                          | [hour]                 | 48           | 64             | 1.7        |

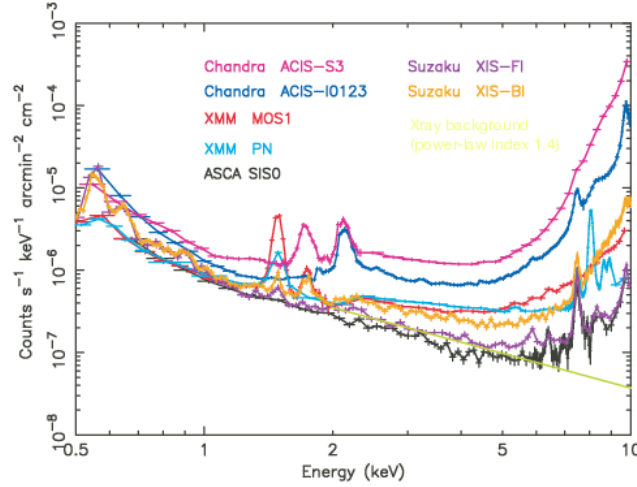


Figure 4.2: Comparison of non X-ray background among representative instruments. The Xray background (shown in yellow) is just a power-law with photon index is 1.4.

#### 4.1.1 Design structure of telescope and Point Spread Function (PSF)

For an extended source analysis, the PSF wing is very important because of spill out from point sources. We show a brief review described in mainly Read et al. (2011). The light path of X-rays shown in Figure 4.3 and a mirror collection module is shown in Figure 4.4. The core of the PSF is narrow and varies little over a wide energy range. the PSF has a little energy dependence above 5 keV. According to Read et al. (2011), the PSF,  $f_{\text{PSF}}$ , is represented by the equation below,

$$f_{\text{PSF}}(r) = \frac{A}{\left(1 + \left(\frac{r}{r_{\text{core}}}\right)^2\right)^\alpha} + Be^{-4 \log 2(r/r_{\text{FWHM}})^2}, \quad (4.1)$$

$$r(x, y, \theta) = \sqrt{[(x \cos \theta + y \sin \theta)]^2 + [(y \sin \theta - x \cos \theta)]^2} / (1 - \epsilon)^2, \quad (4.2)$$

where the  $r_{\text{core}}$  is a core radius,  $\alpha$  is a slope of King profile, and  $r_{\text{FWHM}}$  is full width at half maximum of the Gaussian profile. The first term,  $A / \left(1 + (r/r_{\text{core}})^2\right)^\alpha$ , is called King profile and the second term,  $Be^{-4 \log 2(r/r_{\text{FWHM}})^2}$ , is Gaussian core model, where  $(x, y)$  means detector coordinate,  $\theta$  is rotation angle and the  $\epsilon$  means ellipticity. These parameters are stored in a calibration database (so-called Current Calibration Files: CCFs) as a function of off-axis angle,  $\phi$ . The  $\epsilon$  is  $\sim 0$  on-axis and  $\sim 0.6$  at far off-axis. An encircled energy fraction (EEF) is defined by integrating the PSF as follows,

$$f_{\text{EEF}}(r) = \int_0^r f_{\text{PSF}}(r) 2\pi r dr. \quad (4.3)$$

Parameters for the PSF stored in CCFs are defined so that the encircled energy fraction is the same as the spoked image. Figure 4.5 shows a calculation algorithm for spokes. The black horizontal dashed line means not a spoked line is calculated so as the red area becomes the same as the green shaded area. Figure 4.6 compares the parametrized the PSF function with the observed image. We checked EEF on axis by using stored parameters in the calibration data base. In addition, We are sure that the PSF wing is almost less than 1 % at 3 arcmin below 5 keV, although 1.6 % at 8.5 keV as shown in Table 4.2.

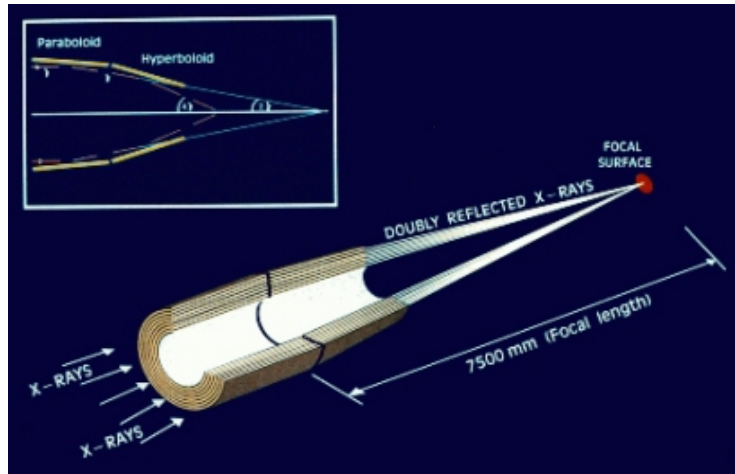


Figure 4.3: Light path in the *XMM-Newton* telescope with an EPIC camera (cited from ESA homepage).

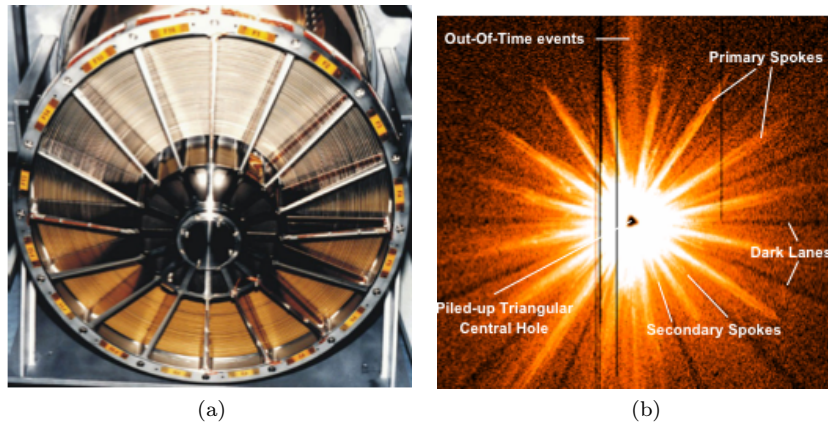


Figure 4.4: (a): A front end view of the EPIC mirror module containing the 58 co-axial mirrors shells and spider support structure used to hold the shells. (b): The PSF of the EPIC camera when observing severely pile up source GX 33904. These figures are cited from Read et al. (2011)

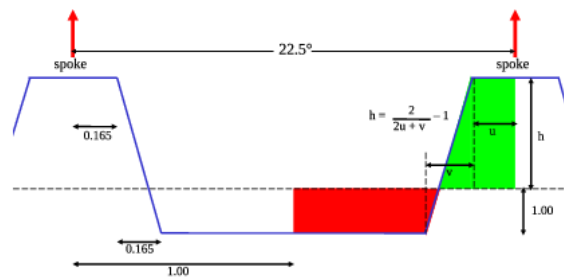


Figure 4.5: Width of two spokes (Read et al. (2011)). The black horizontal dashed line means not a spoked line which is calculated so as the red area becomes the same as the green shaded area.

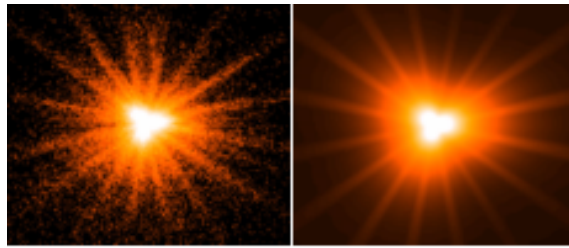


Figure 4.6: Very bright source observed by the EPIC camera at off axis angle  $\sim 4$  arcmin (left). Equivalent the PSF model at a similar off-axis angle (right). In the two Figures, 16 spokes can be seen. The observed spokes are reproduced well by the equivalent the PSF module (Read et al. (2011)).

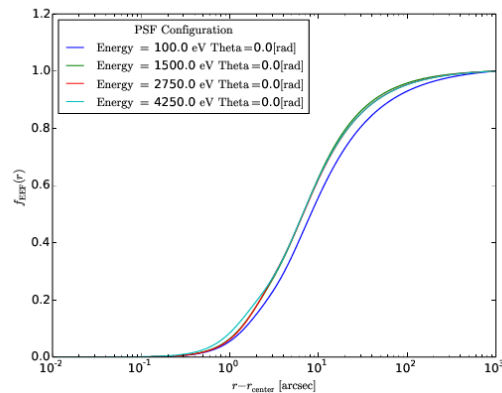


Figure 4.7: Encircled Energy Fraction (EEF) calculated using parameters stored in the calibration database. At around  $\sim 1$  arcmin, EEF is almost 90%.

Table 4.2: On axis the PSF wing at different energies.

| On axis EEF at 3 arcmin |                                 |
|-------------------------|---------------------------------|
| Energy [keV]            | (normalized at 12.5 arcmin) [%] |
| 0.5                     | 99.3                            |
| 1.5                     | 99.5                            |
| 2.5                     | 99.4                            |
| 3.5                     | 99.3                            |
| 4.5                     | 99.2                            |
| 8.5                     | 98.4                            |

## 4.1.2 Metal Oxide Semi-conductor (MOS) detector onboard *XMM-Newton*

There are two Metal Oxide Semi-conductor (MOS) detectors on board *XMM-Newton*, called the MOS1 and the MOS2 located on the focal plane. In this Section, we briefly review the MOS1 and the MOS2, referring to Turner et al. (2001).

### 4.1.2.1 Detector assembly

The size of an actual pixel is  $40\mu\text{m} \times 40\mu\text{m}$  and the pixel covers  $1.1 \text{ arcsec} \times 1.1 \text{ arcsec}$  of a field of view and 15 pixels cover the mirror half power diameter (HPD) of 15 arcsec. There are equivalent two the MOS detectors. As shown in Figure 4.8, the MOS detector is composed of 7 CCD chips. The central CCD is at the focal point on the optical axis of the telescope, while the other six chips are set closer to the mirror by a 4.5 mm to follow approximately the focal plane curvature and to improve the focus for off-axis sources. The gaps around the central CCD chips in the MOS camera are covered by the six CCD chips. Note that the basic readout speed of the MOS CCDs is 2.6 sec.

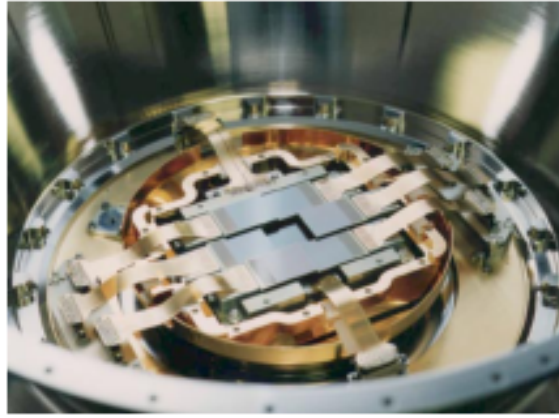


Figure 4.8: MOS CCDs mounted in the cryostat with their flexible PCB links (Turner et al. (2001)). The central CCD chip camera located 4.5 mm lower than the outer six CCD chips due to the difference in focal length of the telescope. As the operating temperature is  $\sim 170$  K, the radiator is very important.

#### 4.1.2.2 Filters of the MOS camera

The EPIC CCD cameras, the MOS1 and MOS2, onboard XMM-Newton are equipped with a filter wheel system with 6 different filter setups shown in Figure 4.9,

- Closed (1.05 mm Al)
- Thin1 (40 nm Al + 160 nm polyamide)
- Thin2 (40 nm Al + 160 nm polyamide)
- Medium (80 nm Al + 160 nm polyamide)
- Thick (45 nm Sn + 55 nm Al + 330 nm polypropylene + 55 nm Al)
- Open

The filter wheel is located between the telescope and the detector. At filter wheel closed (FWC), the count rate is dominated by internal instrumental background and it can be modeled.

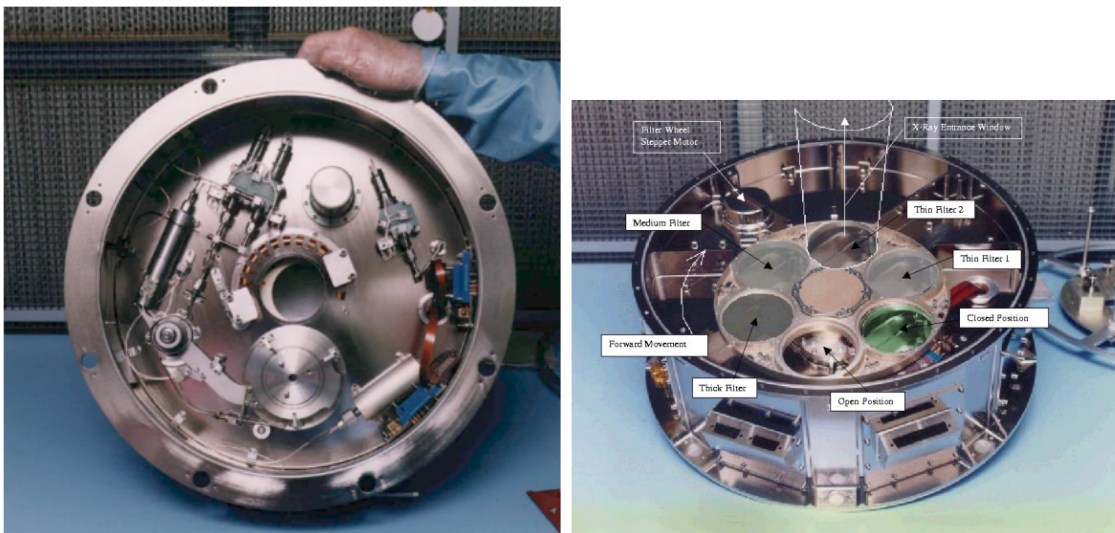


Figure 4.9: Filter Wheels for the MOS camera (Turner et al. (2001)). Thin1, Thin2, Thick, and Medium filters block UV.

### 4.1.2.3 Response of the MOS detector

Detector response of the MOS is shown in Figure 4.10. We can see energy resolution  $\sim 40$  eV at 800 eV in Figure 4.10 (b). The detection mechanism of the CCD camera is a photo absorption<sup>1</sup>. A cluster of many hot electrons is called an electron cloud. The electron cloud is read out by bucket brigade along with the CCD line. Therefore, one bad pixel often disables all the pixels along the line.

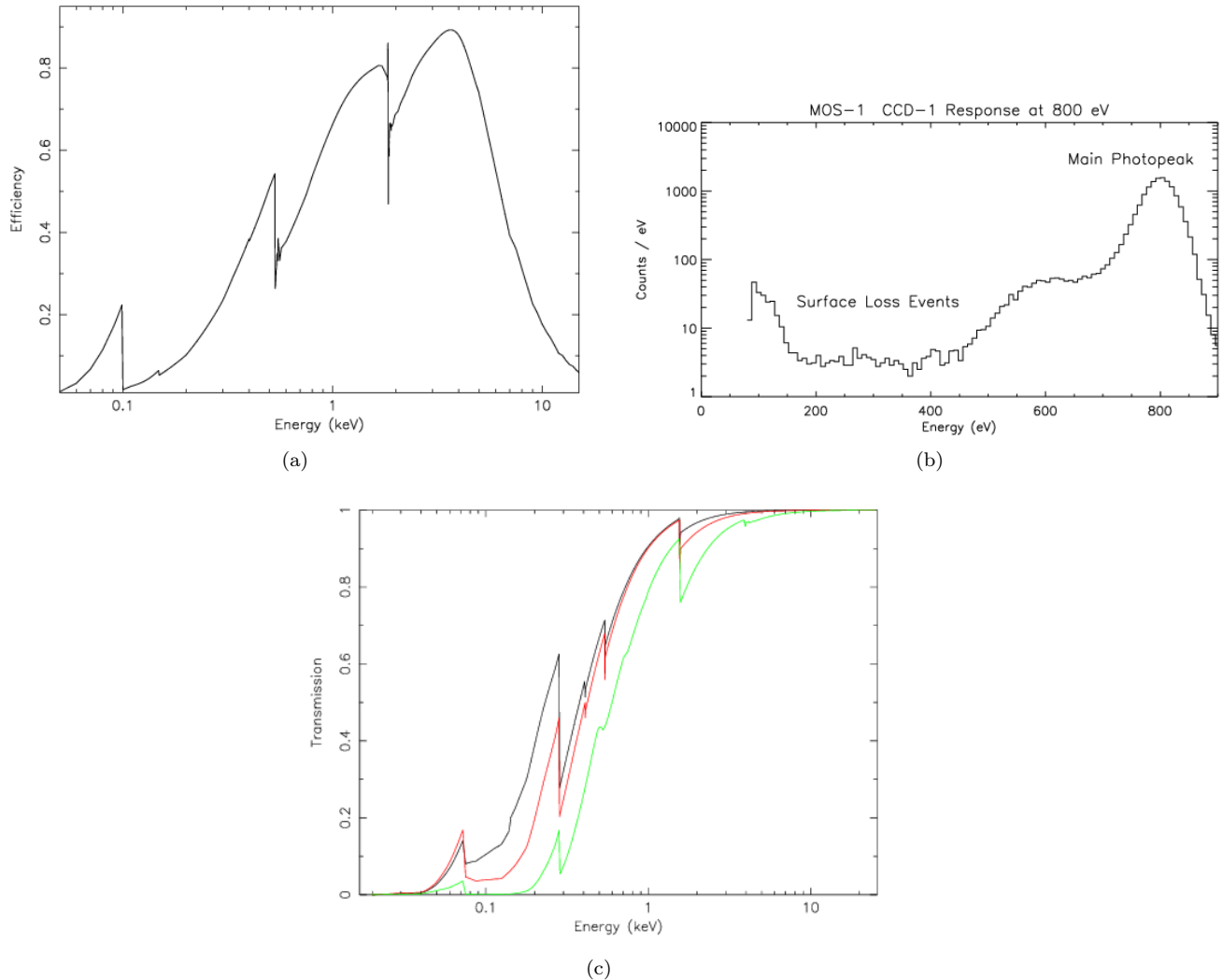


Figure 4.10: (a): Quantum efficiency curve based on synchrotron measurement and celestial source measurement. (b): Response of the MOS detector at 800 eV. (c): Filter transmission, thin (black), medium (red), thick (green) filters. These figures are cited from Turner et al. (2001).

### 4.1.2.4 Pattern IDs and FLAG

Event patterns recognized by analogue electronics are shown in Figure 4.11. As described in Turner et al. (2001), Patterns from zero to twelve are recognized as an X-ray event, while the remaining ones are not. According to their report, that the remaining patterns are due to cosmic rays and also to deeply interacting energetic X-rays. The FLAG defines the quality of an event. The best quality which corresponds to FLAG equal. 0 means that the event does not cross on the edge of CCD and bad pixels are not located nearby (shown in Table 4.3).

<sup>1</sup>Electron inside an atom are changed into hot electrons by incident X-rays.

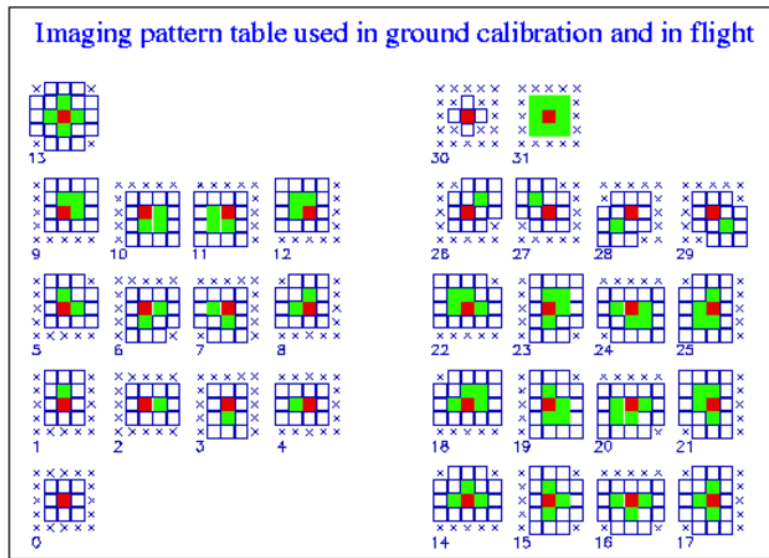


Figure 4.11: Pattern identifiers for CCD events. The red pixel is the center pixel with the signal is above a threshold. The red one is the largest signal in a  $3 \times 3$  pixel matrix. The green pixels have also signals above a threshold. The white pixel has a signal below the threshold.

Table 4.3: Quality FLAG of detected events

| bit | Meaning                 |
|-----|-------------------------|
| 0   | Best quality            |
| 1   | INVALID PATTERN         |
| 2   | CLOSE TO CCD WINDOW     |
| 5   | CLOSE TO ONBOARD BADPIX |
| 6   | CLOSE TO BRIGHTPIX      |
| 8   | CLOSE TO DEADPIX        |
| 16  | OUT OF FOV              |
| 19  | COSMIC RAY              |
| 21  | ON BADPIX               |
| 22  | SECONDARY               |
| 23  | TRAILING                |

#### 4.1.2.5 Time degradation

Long term observation of Chandra Deep Field South is mainly divided into 3 terms. The first term from revolution 289 (2001-07-27) to 389 (2002-01-23), second term is from 1570 (2008-07-05) to 1672 (2009-01-24) and third term is from 1764 (2009-07-05) to 1867 (2010-02-17). Therefore, we carefully checked the time degradation of energy resolution of the MOS cameras. Figure 4.12 shows time degradation of the MOS1 and the MOS2 for a long period cited from technical notes. Center energy of the Al line is 1.4 keV. After 2003, we can see it is almost linearly degraded.

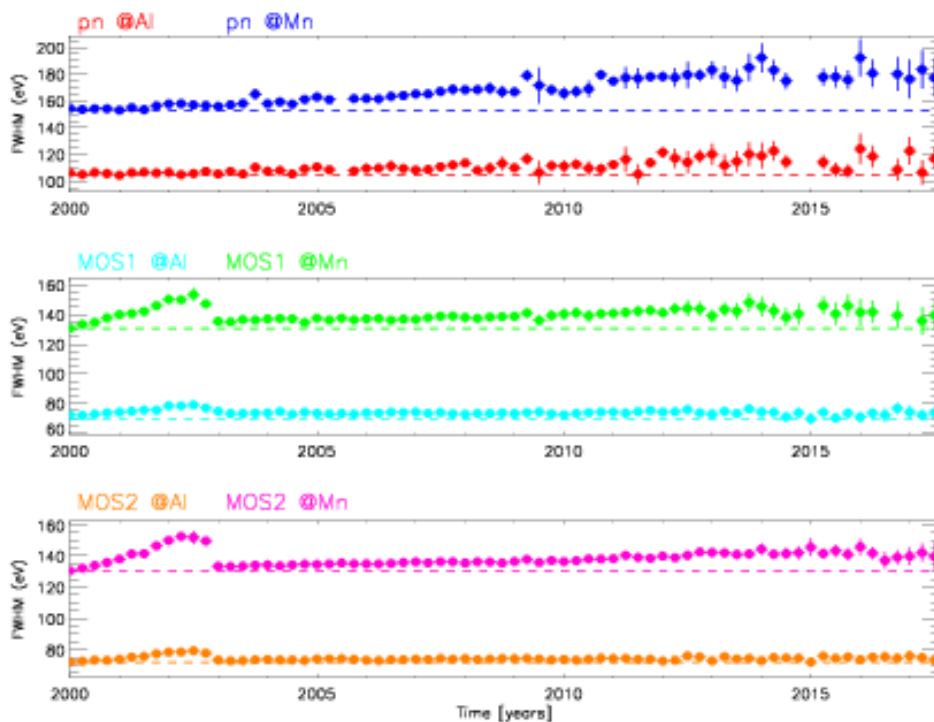


Figure 4.12: Time degradation for the EPIC the MOS FWHM cited from technical notes XMM-SOC-CAL-TN-0018. Energy resolution for pn camera (upper), for the MOS1 (middle) and for the MOS2 (lower). In this thesis, we do not use the pn detector.

## 4.2 Instrumental background, non X-ray background, soft proton contamination

### 4.2.1 Instrumental lines

Some instrumental lines, Si ( $\sim 1.4$  keV), Al ( $\sim 1.7$  keV), Au ( $\sim 2.2$  keV), Fe and Cr ( $5 \sim 7$  keV) exist in 0.5-8 keV. Si and Al lines are the strongest among them in 1.2-2.0 keV. Figure 4.13 shows filter-wheel-closed images in narrow energy bands. We see these lines are not spatially uniform. The Si and Al lines are stronger than the others. We note that the Au lines inside the field of view are stronger than outside the field of view.

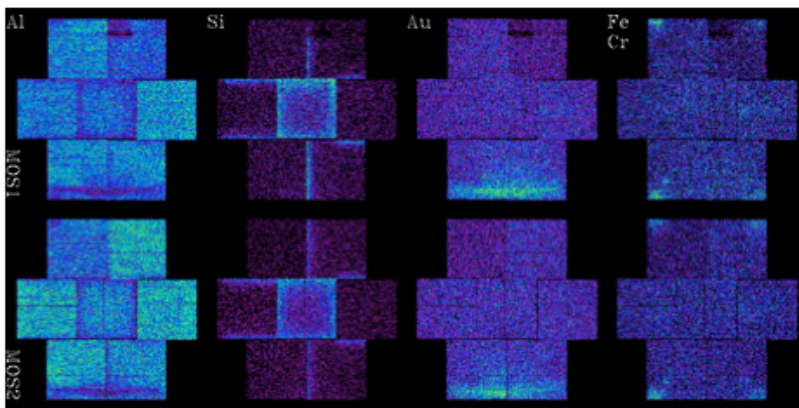


Figure 4.13: Spatial distribution of instrumental lines of the MOS detectors. These instrumental lines are corresponding to Al (1.49 keV), Si(1.74 keV), Au (2.12, 9.71 and 11.4 keV) and a sum of Fe (6.4 keV) and Cr (5.4 keV).

### 4.2.2 Anomalous and anonymous CCD chips

Anomalous and anonymous chip are defined in Kuntz & Snowden (2008). Figure 4.14 (a), (b) and (c) shows a typical anomalous and anonymous chip and its spectra. The noise count rate in the anonymous chip has a dependence on position within the chip. The reason is still unclear. They can empirically found the anonymous and anomalous states with using hardness-ratio v.s. full band count-rate, chip by chip. The criteria are tabulated in Table 1 (Kuntz & Snowden (2008)).

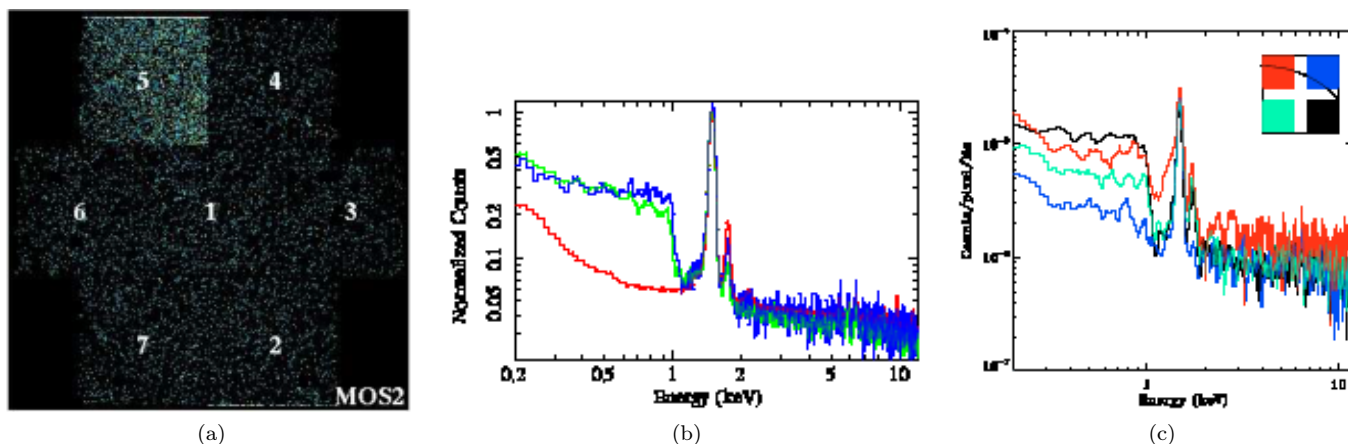


Figure 4.14: (a): Typical anomalous image appearing in the MOS2/chip5. (b): Typical anomalous (green) and anonymous (blue) spectra. (c): The anonymous state whose color represents positions within a chip. These figures are cited from Kuntz & Snowden (2008).

### 4.2.3 Soft Proton Contamination (SPC)

Solar wind protons flux affected by the geomagnetic field in the Earth and the interplanetary magnetic field enter into the telescope and interact with a CCD camera. Features of the SPC are as following:

- Short time variability as well as long term variability
- Empirically, approximately 50% of an observation period is contaminated by SPC

Figure 4.15 shows an image obtained when the soft proton contamination occurring. The central centered chip is terribly affected by SPC because of vignetting. This means that the telescope gathers SPC, unfortunately. The SPC is observed by only *XMM-Newton* as a significant problem, but it does not affect *Chandra*. We do not know the reason yet.

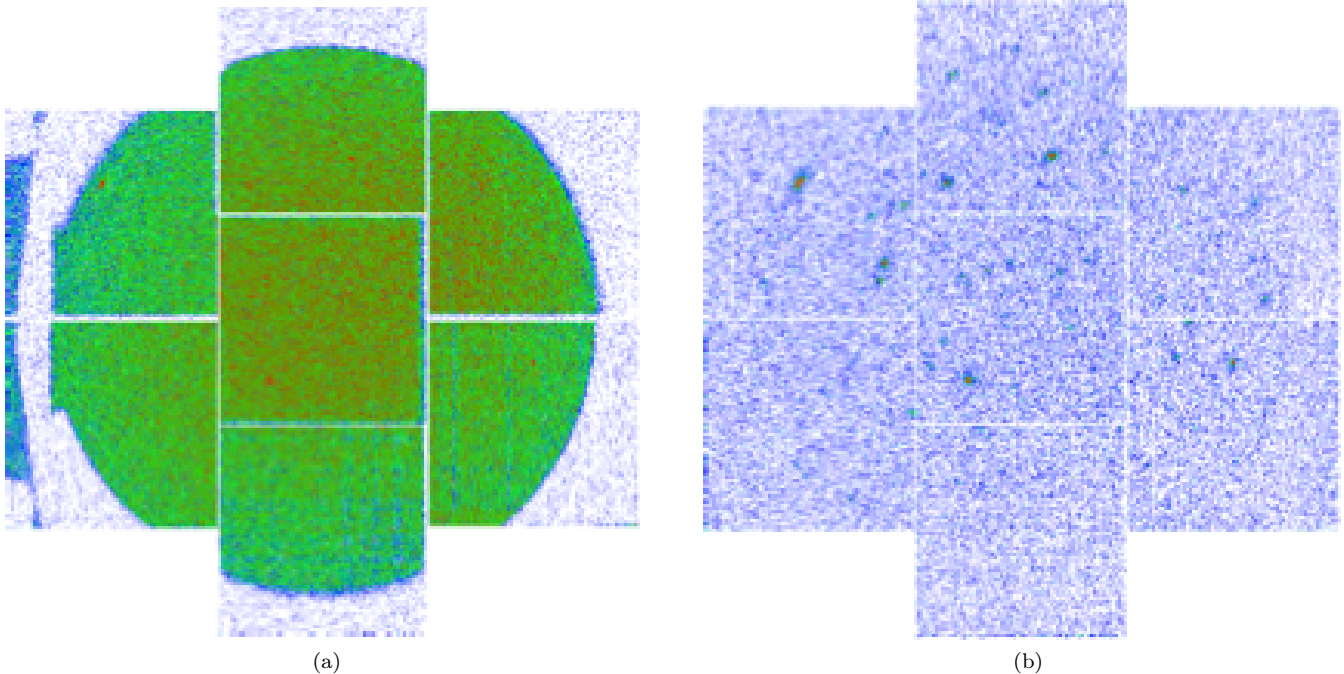


Figure 4.15: (a): Soft proton contributions (Turner et al. (2001)) (including vignetting effect) for a period when the soft proton contamination occurred. (b): A period without soft proton contamination. Faint point-like sources can be seen in (b), while they are masked by SPC in (a).

#### 4.2.4 Non X-ray Background (NXB) and Residual Soft Proton Contamination (RSPC)

Series of papers on analysis of the blank sky data by *XMM-Newton* for future X-ray mission, ATHENA, were published by Marelli et al. (2017), Salvetti et al. (2017), Ghizzardi et al. (2017) and Gastaldello et al. (2017). These papers analyzed the 100 Msec data. The X-ray sources listed in 3XMM catalogue are removed, residual source contribution become less than 0.5% of the X-ray background emission. Gastaldello et al. (2017) pointed out the long-term variable component in the non X-ray background (NXB). The time scale of the NB variability is longer than a typical observation period. In this case, the NXB cannot be excluded by light-curve analysis. There are two methods for estimating the NXB. One of them employs the CCD data in the corner unexposed region. The other uses the Filter Wheel Closed (FWC) data.

Basically, their paper tried to reproduce the NXB by the former method. An advantage lies in this method is that the NXB data are taken from at the same time when observation have done. In this case, FWC data is often used for correction of the spatial distribution of the NXB. According to their papers, the cosmic ray particle has two kinds of energy, either  $\sim 100$  keV or 1-10 MeV. The former particles causing a temporally rapid variable flare can be almost excluded by the light curve reduction, where the remaining background is called residual soft proton contamination (RSPC). The latter particles are expected to make constant detector noise which is irreducible background (NXB).

In Gastaldello et al. (2017), the NXB is separated into particle and the electronic noise component. The electronic noise component is important at low energies, mainly below 0.4 keV. Although a high energy particle ( $E > \text{a few MeV}$ ) generates a signal which is mostly discarded by the pattern IDs, the remaining events represent a serious component of the NXB. The NXB count rates are correlated with the count rate in the particle detector (8-40 MeV) for protons on board *XMM-Newton* as shown in Figure 4.16 (c). We also see that correlation between sunspot numbers and count rates in the particle detector in Figure 4.16 (a). Furthermore, the NXB count rates show correlation with revolutions of *XMM-Newton* as shown in (b) as well.

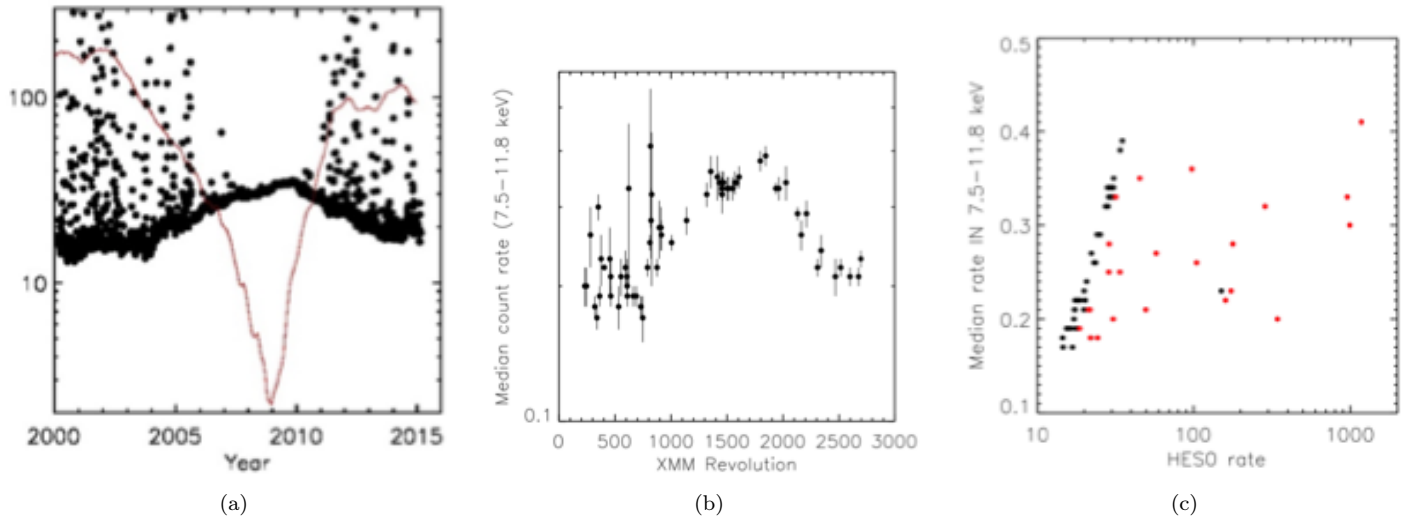


Figure 4.16: (a): Long time variability for the NXB. Correlation between sunspot numbers and count rates in the particle detector. (b): The red curve represents the sunspot numbers. The black data points indicate count rates in the particle detector. The NXB count rates in 7.5-11.8 keV as a function of revolutions of *XMM-Newton*. (c): The NXB count rates in 7.5-11.8 keV as a function of count rate in the particle detector (8-40 MeV) for protons on board *XMM-Newton*. HES0 in the right figure is the count rate in the high energy particle unit on board *XMM-Newton*. The NXB dominates the most events detected by the MOS cameras in 7.5-11.5 keV. These figures are cited from Gastaldello et al. (2017).

#### 4.2.5 Spatial distribution of NXB and RSPC

Figure 4.17 shows images for the spatial distribution of the NXB and the RSPC. These images represent the exposed region (inFOV) and the unexposed corner region (outFOV), respectively. We see non-uniform distribution for the RSPC in right while the NXB in left shows a relatively uniform spatial distribution. The soft proton flare events are affected by vignetting because the particles have a few hundreds of keV energy.

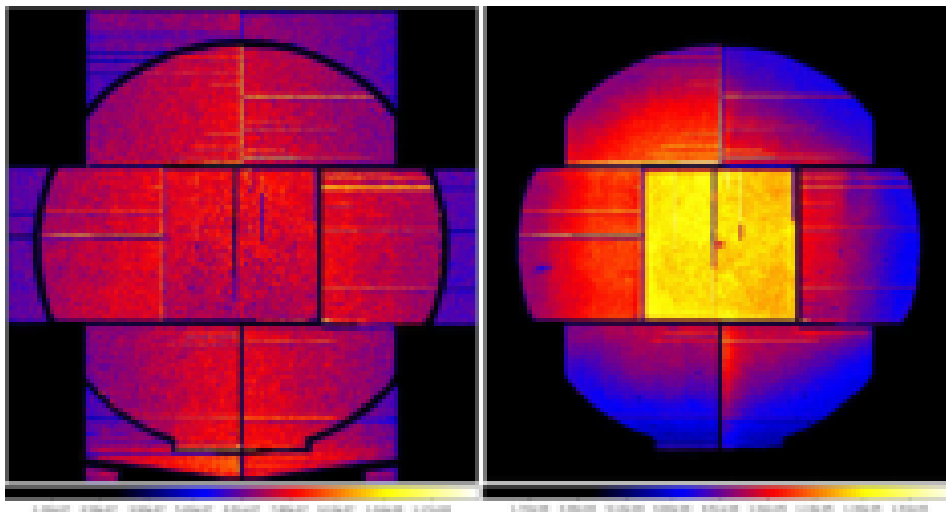


Figure 4.17: (left): Image for the spatial distribution of the NXB. (right): Image for the spatial distribution of the NXB the RSPC. These figures are cited from Marelli et al. (2017).

#### 4.2.6 Systematic errors on NXB estimation

Salveti et al. (2017) characterized a cumulative distribution of the count rates in the exposed pixel region (inFOV). After removing SPC, they calculated the difference between the inFOV count rate and the outFOV count rate

(inFOV count rate minus outFOV count rate) and found a significant excess. The significant offset indicated by the blue shaded area is in Figure 4.18. We take this systematic error into account if necessary.

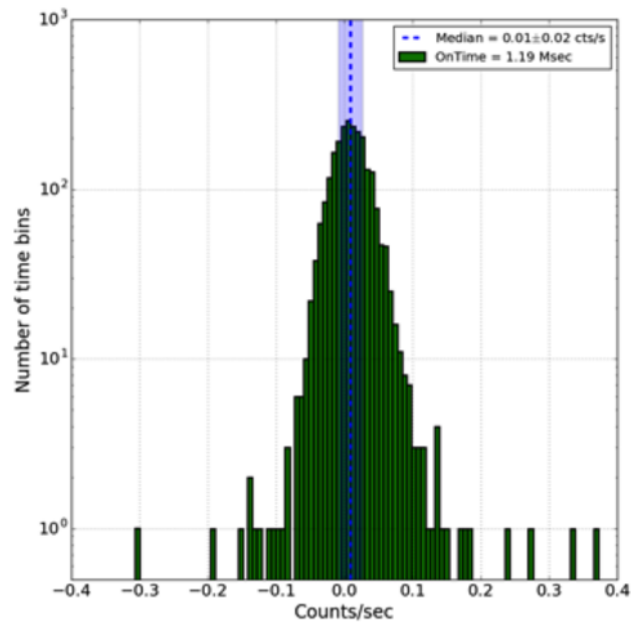


Figure 4.18: Differential count rate (inFOV minus outFOV) in the Filter Wheel Closed data (Salveti et al. (2017)). The blue shaded area indicates a significant offset which one should take into account as a systematic error, when necessary.

# Chapter 5

## Analysis 1: Data reduction

### 5.1 Overview

All the *XMM-Newton* data we use in this thesis are in the XMM-Newton archive system. We can extract them from (<http://nxsas.esac.esa.int/nxsas-web/#search>). The data are reformatted from the original telemetry data to the standard FITS (Flexible Image Transport System) binary-table, where the raw telemetry data have already been converted to physical values using the calibration database. The X-ray data in the FITS files are essentially photon-by-photon data. Namely, all the X-ray events, although in reality some of them can be non X-ray background events, are listed in the FITS binary Table. Each event contains the following information: time, pulse invariant (PI) value which is an energy equivalent value converted from the pulse height of CCD, event grade flag, CCD Chip number, detector X and Y coordinates, sky X and Y coordinates. The flow of the data reduction from the original FITS data to X-ray spectra is described as:

- (1) Standard screening
- (2) Extraction of events in the overlapping region
- (3) Soft proton contamination removal: short time scales
- (4) Soft proton contamination removal: long time scales
- (5) Determination of the Chandra-point-source free sky region, and the sky region for point sources
- (6) Extraction of events from the sky region we would like to analyze

To analyze the spectra, we employ a forward method, i.e. spectral fitting of the data with a model convolved with the telescope and detector response functions. For this purpose, we need further steps:

- (7) Estimation of non X-ray background spectrum for diffuse emission or estimation of diffuse X-ray + non X-ray background spectrum for point sources.
- (8) Estimation of effective-area as a function of energy: the FITS file containing the effective area is called an arf file in X-ray astronomy.
- (9) Prepare a pulse height re-distribution matrix, which is often called response matrix from the calibration database.
- (10) Spectral fits using maximum likelihood method.

In this Chapter, we will describe steps (1)-(6) and the next chapter will be devoted to steps (7)-(10).

In steps (1)-(6), four different filters (or data screenings) are applied to the original event file. First, standard data screening criteria (exclusion of anomalous Chips and event grade screening) are applied (1). Then we extract events from the sky region where the *Chandra* and *XMM-Newton* observatories are overlapped (2). Then in steps (3) and (4), we remove time intervals for which the data are suspected to be contaminated with soft protons. For this removal, we introduced a new method, which utilizes the characteristics of the present X-ray data; the surface brightness should not show intrinsic time variations except for those of SWCX. The method was successful and we obtained for the first time reliable soft-proton free X-ray background spectrum with XMM-Newton. We may have

removed enhancements of SWCX as well. This is acceptable for the present study. In order to confirm successful removal, we need to employ spectral fits to the data. Thus, we will describe the confirmation later at the end of the next chapter, Chapter 6.

In step (5), we determined the sky region for which the emission from the point sources detected by the *Chandra* observatory is negligibly small. The half power radius of the point spread function of the X-ray mirrors is 15 arc seconds. The image is extending to virtually infinite radius although the surface brightness becomes very small at large radii. In order to obtain the best photon statistics, we need to determine the exclusion radii of point sources depending on the brightnesses of the sources.

From the event files obtained from step (6), we further select events in the sky region we would like to analyze. Then, we can create a spectrum from the filtered event file. We used the software package, SAS version 16.1.0 for the data reduction.

## 5.2 Archive data

We searched data sets to find region in the *XMM-Newton* archive which contains the center of the CDF-S, (RA, DEC) = (53.1178, -27.806), is within the field of view of *XMM-Newton*. Each dataset is identified by the observation identifier (ObsID). Selected data are tabulated in Table 5.1. The selected data are identified by observation identifier (hereafter ObsID). Exposures of each selected data sets are plotted in Figure 5.1. We selected 33 ObsID whose exposure time exceeds 10 ksec. The total exposure amounts to 3.6 Msec. We first run a SAS software, **emchain**, to produce initial calibrated event files. A current calibration file (CCF) is downloaded from ESAS ftp server <sup>1</sup>. After masking flaring periods, the total exposure, 3.6 Msec, is reduced to 2.4 Msec by **emchain**. The quiet level of **emchain** is 0.8 cts/ks/arcmin<sup>2</sup> above 14 keV. We applied following event selection, FLAG=0 and PATTERN<=12. This criterion cannot exclude anomalously bright CCD chips.

---

<sup>1</sup>xmm.esac.esa.int

Table 5.1: Log of observation with *XMM-Newton* for the selected observation IDs.

| ObsID       | Target            | RA(J2000)      | DEC(J2000)     | Rev                 | Start Date          | End Date            |
|-------------|-------------------|----------------|----------------|---------------------|---------------------|---------------------|
| 0108060401  | AXAF Ultra Deep F | 3h 32m 26.70s  | -27d 48' 20.0" | 299                 | 2001-07-27 09:03:09 | 2001-07-27 22:54:55 |
| 0108060501  |                   | 3h 32m 29.29s  | -27d 48' 40.0" | 299                 | 2001-07-27 23:42:55 | 2001-07-28 17:34:02 |
| 0108060601  |                   | 3h 32m 27.99s  | -27d 48' 50.0" | 384                 | 2002-01-13 13:48:44 | 2002-01-14 07:57:22 |
| 0108060701  |                   | 3h 32m 26.70s  | -27d 48' 40.0" | 385                 | 2002-01-14 17:47:17 | 2002-01-15 19:54:18 |
| 0108061601# |                   | 3h 32m 26.70s  | -27d 48' 20.0" | 299                 | 2001-07-27 02:03:20 | 2001-07-27 04:44:57 |
| 0108061701# |                   | 3h 32m 26.70s  | -27d 48' 40.0" | 385                 | 2002-01-14 16:49:21 | 2002-01-14 17:41:23 |
| 0108061801  |                   | 3h 32m 27.99s  | -27d 48' 30.0" | 386                 | 2002-01-16 17:24:02 | 2002-01-17 10:54:20 |
| 0108061901  |                   | 3h 32m 27.99s  | -27d 48' 10.0" | 386                 | 2002-01-17 16:38:43 | 2002-01-18 07:42:21 |
| 0108062001# |                   | 3h 32m 27.99s  | -27d 48' 30.0" | 386                 | 2002-01-16 16:26:50 | 2002-01-16 17:22:11 |
| 0108062101  |                   | 3h 32m 29.29s  | -27d 48' 20.0" | 388                 | 2002-01-20 17:08:24 | 2002-01-21 10:23:43 |
| 0108062201# |                   | 3h 32m 29.29s  | -27d 48' 20.0" | 388                 | 2002-01-20 16:14:36 | 2002-01-20 17:06:34 |
| 0108062301  |                   | 3h 32m 27.99s  | -27d 48' 10.0" | 389                 | 2002-01-23 00:23:50 | 2002-01-24 01:00:50 |
| 0555780101  |                   | CDF5           | 3h 32m 42.29s  | -27d 45' 05.0"      | 1570                | 2008-07-05 05:22:38 |
| 0555780201  | 3h 32m 42.29s     |                | -27d 45' 35.0" | 1571                | 2008-07-07 05:22:24 | 2008-07-08 18:26:00 |
| 0555780301  | 3h 32m 39.99s     |                | -27d 45' 35.0" | 1572                | 2008-07-09 07:55:06 | 2008-07-10 18:18:37 |
| 0555780401  | 3h 32m 39.99s     |                | -27d 45' 05.0" | 1573                | 2008-07-11 08:01:48 | 2008-07-12 18:09:11 |
| 0555780501  | 3h 32m 25.00s     |                | -27d 49' 25.0" | 1663                | 2009-01-06 20:57:27 | 2009-01-08 04:20:51 |
| 0555780601  | 3h 32m 25.00s     |                | -27d 49' 55.0" | 1665                | 2009-01-10 19:11:41 | 2009-01-12 04:05:14 |
| 0555780701  | 3h 32m 25.00s     |                | -27d 50' 25.0" | 1666                | 2009-01-12 18:59:31 | 2009-01-14 03:53:06 |
| 0555780801  | 3h 32m 22.70s     |                | -27d 49' 25.0" | 1668                | 2009-01-16 18:24:02 | 2009-01-18 03:59:21 |
| 0555780901  | 3h 32m 22.70s     |                | -27d 49' 55.0" | 1669                | 2009-01-18 18:16:08 | 2009-01-20 04:01:26 |
| 0555781001  | 3h 32m 22.70s     |                | -27d 50' 25.0" | 1671                | 2009-01-22 18:39:27 | 2009-01-24 05:36:20 |
| 0555781101# | 3h 32m 42.29s     |                | -27d 45' 05.0" | 1570                | 2008-07-06 18:40:00 | 2008-07-06 19:22:12 |
| 0555781201# | 3h 32m 42.29s     |                | -27d 45' 35.0" | 1571                | 2008-07-08 18:44:02 | 2008-07-08 19:27:40 |
| 0555781501# | 3h 32m 39.99s     |                | -27d 45' 35.0" | 1572                | 2008-07-10 18:36:43 | 2008-07-10 19:16:14 |
| 0555781601# | 3h 32m 39.99s     |                | -27d 45' 05.0" | 1573                | 2008-07-12 18:29:12 | 2008-07-12 19:08:05 |
| 0555781701# | 3h 32m 25.00s     |                | -27d 49' 25.0" | 1663                | 2009-01-06 17:02:58 | 2009-01-06 18:58:09 |
| 0555781901# | 3h 32m 25.00s     |                | -27d 50' 25.0" | 1666                | 2009-01-12 16:37:31 | 2009-01-12 18:34:36 |
| 0555782001# | 3h 32m 22.70s     |                | -27d 49' 25.0" | 1668                | 2009-01-16 16:21:14 | 2009-01-16 18:05:11 |
| 0555782101# | 3h 32m 22.70s     |                | -27d 49' 55.0" | 1669                | 2009-01-18 16:13:20 | 2009-01-18 17:57:17 |
| 0555782201# | 3h 32m 22.70s     |                | -27d 50' 25.0" | 1671                | 2009-01-22 15:58:10 | 2009-01-22 18:18:40 |
| 0555782301  | 3h 32m 22.70s     |                | -27d 50' 25.0" | 1672                | 2009-01-24 18:34:13 | 2009-01-26 05:29:27 |
| 0555782401# | 3h 32m 22.70s     |                | -27d 50' 25.0" | 1672                | 2009-01-24 15:50:13 | 2009-01-24 18:12:22 |
| 0604960101  | 3h 32m 42.29s     |                | -27d 45' 35.0" | 1764                | 2009-07-27 04:00:26 | 2009-07-28 15:57:45 |
| 0604960201  | 3h 32m 39.99s     |                | -27d 45' 35.0" | 1759                | 2009-07-17 07:59:05 | 2009-07-18 17:37:19 |
| 0604960301  | 3h 32m 42.29s     |                | -27d 46' 09.0" | 1753                | 2009-07-05 08:07:59 | 2009-07-06 18:06:21 |
| 0604960401  | 3h 32m 39.99s     |                | -27d 46' 07.0" | 1765                | 2009-07-29 04:07:27 | 2009-07-30 17:19:22 |
| 0604960501  | 3h 32m 25.00s     |                | -27d 49' 25.0" | 1852                | 2010-01-18 18:13:38 | 2010-01-19 07:16:41 |
| 0604960601  | 3h 32m 25.00s     |                | -27d 49' 55.0" | 1856                | 2010-01-26 17:48:13 | 2010-01-28 04:35:05 |
| 0604960701  | 3h 32m 22.70s     |                | -27d 49' 25.0" | 1849                | 2010-01-12 18:39:40 | 2010-01-14 04:13:19 |
| 0604960801  | 3h 32m 25.00s     |                | -27d 50' 31.0" | 1861                | 2010-02-05 17:12:18 | 2010-02-07 02:50:25 |
| 0604960901  | 3h 32m 22.59s     |                | -27d 50' 34.7" | 1864                | 2010-02-11 16:36:42 | 2010-02-13 03:25:46 |
| 0604961001  | 3h 32m 22.70s     |                | -27d 49' 55.0" | 1865                | 2010-02-13 16:27:56 | 2010-02-15 02:29:51 |
| 0604961101  | 3h 32m 25.00s     |                | -27d 48' 52.3" | 1845                | 2010-01-04 18:54:02 | 2010-01-06 04:27:39 |
| 0604961201  | 3h 32m 22.30s     |                | -27d 48' 52.3" | 1847                | 2010-01-08 18:45:45 | 2010-01-10 04:17:43 |
| 0604961301  | 3h 32m 25.00s     | -27d 49' 25.0" | 1852           | 2010-01-19 22:44:43 | 2010-01-20 04:50:03 |                     |
| 0604961801  | 3h 32m 22.70s     | -27d 49' 55.0" | 1867           | 2010-02-17 15:59:48 | 2010-02-19 02:43:50 |                     |

Observation which has duration less than 10 ksec are excluded and marked "#".

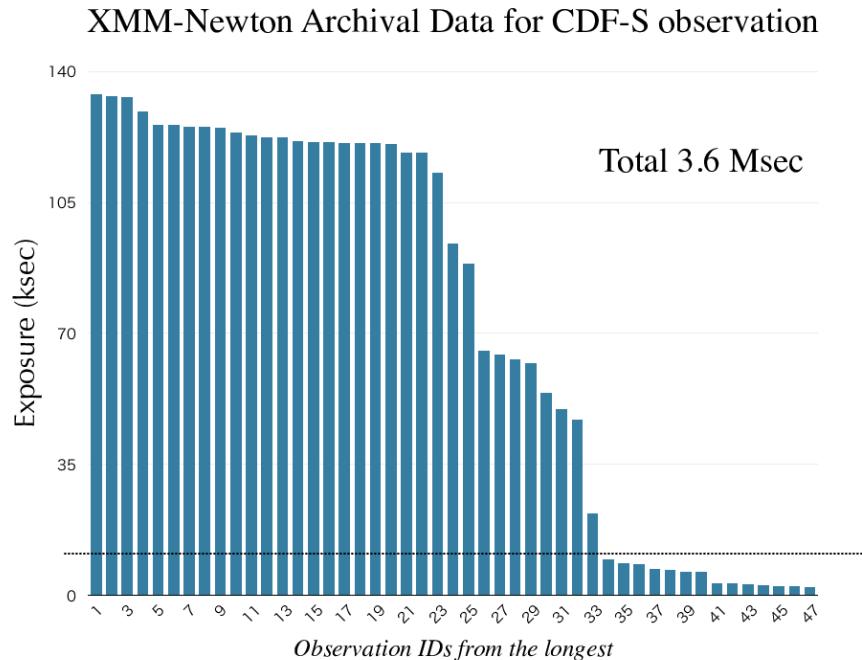


Figure 5.1: Exposure of each selected observation IDs. The dashed line represents a 10 ksec threshold for the data selection. At last, we selected 33 observation IDs. Total exposure is 3.6 Msec

## 5.3 Standard event screening

### 5.3.1 Screening with event grade

We accepted events with  $PATTERN \leq 12$  and  $FLAG = 0$ . The charge-split pixel patterns are shown in Figure 4.11.  $PATTERN \leq 12$  means that charge splitting within  $2 \times 2$  pixels is accepted. Meaning of the quality flag is tabulated in Table 4.3.  $FLAG = 0$  represents the best quality. It is not recommended that we should not use events with the other flags in the standard *XMM-Newton* analysis.

### 5.3.2 Exclusion of anomalous CCD Chips

*XMM-Newton* has two MOS detectors, MOS1 and MOS2. Each the MOS detectors consist of 7 CCD chips. A whole CCD chip occasionally goes into an unusual state for a long duration. Such a CCD chip is called anomalous CCD chip (Section 4.2.2). We need to find out anomalous CCD chips and to discard an event affected by anomalous CCD chips, when the anomalous chips are defined ObsID by ObsIDs. In Chapter 4 (Section 4.2.2), a different pixel may become anomalous when the chip becomes anomalous. This is the reason why we excluded the whole anomalous chips in our analysis ObsID by ObsID.

Among the seven CCD chips, six chips from Chip2 to Chip7, have pixel region which is not exposed to the telescope fields of view. While Chip1 is always exposed to the field of view. For Chip2 to Chip7, we can utilize these outside field of view pixels (outFOV) to identify anomalous CCD chips. The outFOV region is tabulated in Table 3 in Kuntz & Snowden (2008). We followed Table 1 in Kuntz & Snowden (2008) for the criterion about the anomalous chips. According to the criterion, the plot of softness ratio v.s. full band count rate is essential. We show the plots for the MOS1 and the MOS2 in Figure 5.2 and Figure 5.3, respectively. The red crosses indicate the anomalous chips. We excluded these anomalous chips. On the other hand, we cannot apply this method for Chip1. We made the same plots for Chip1 because the anonymous chips show a high softness ratio as shown in Figure 5.2 and Figure 5.3. Figure 5.4 shows the count rates of Chip1 in the MOS1 and the MOS2. The full-band rates ( $\geq 2.0 \times 10^{-9}$  [cts/s/pixel]) is linearly proportional to soft-band rates. This is why we decided to use all of the pixels in Chip1. The spectra in outFOV regions are in Appendix A.1.

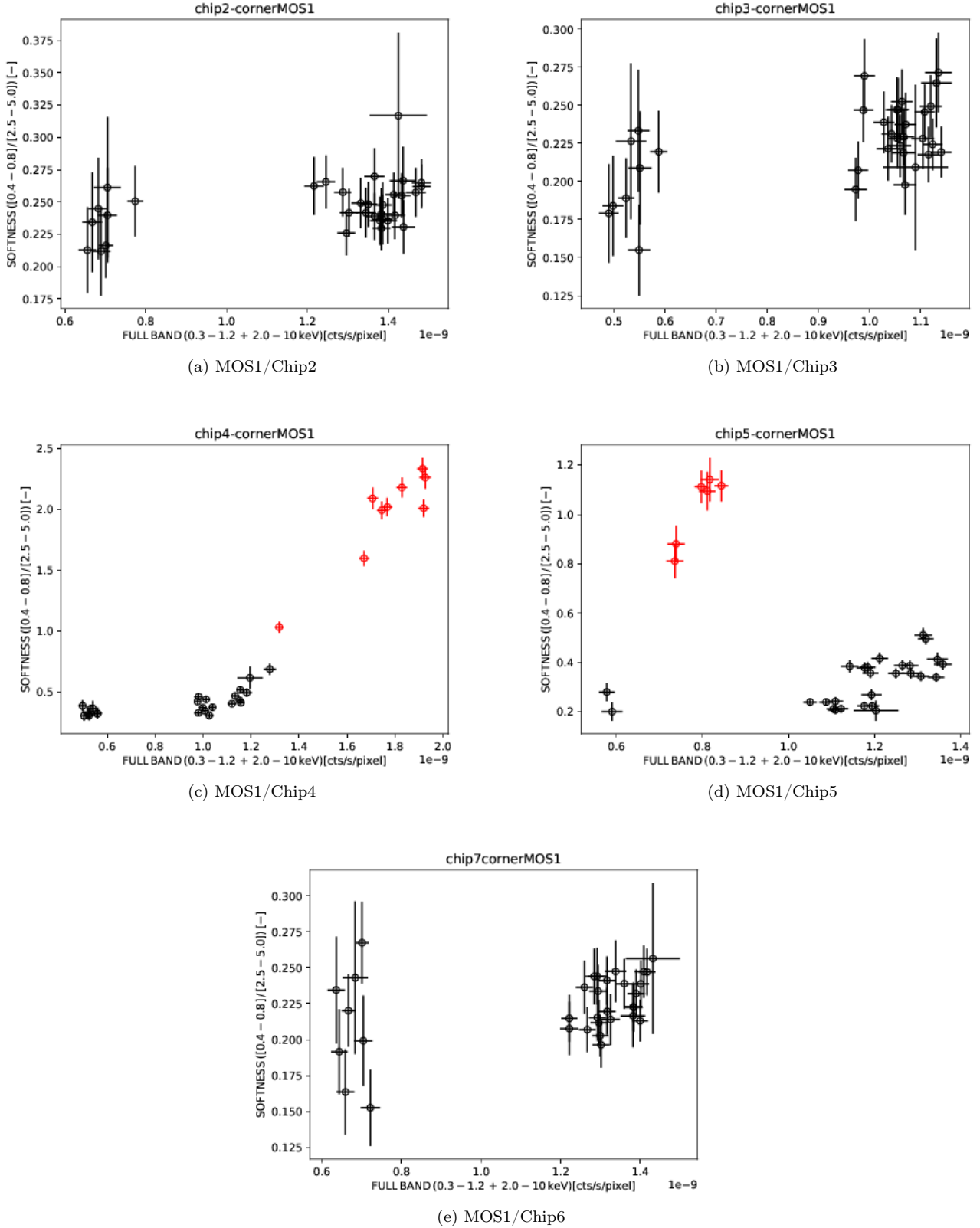


Figure 5.2: Softness ratio (ratio of count rate in 0.4–0.8 keV to that in 2.5–5 keV) as a function of counting rate in 0.3–10 keV excluding the 1.2–2.5 keV band for the outFOV pixels of the MOS1. Energy range, 1.2–2.5 keV, where instrumental lines are dominant is not included in the analysis. One data point corresponds to one ObsID. The Chips indicated in red are excluded from further analysis.

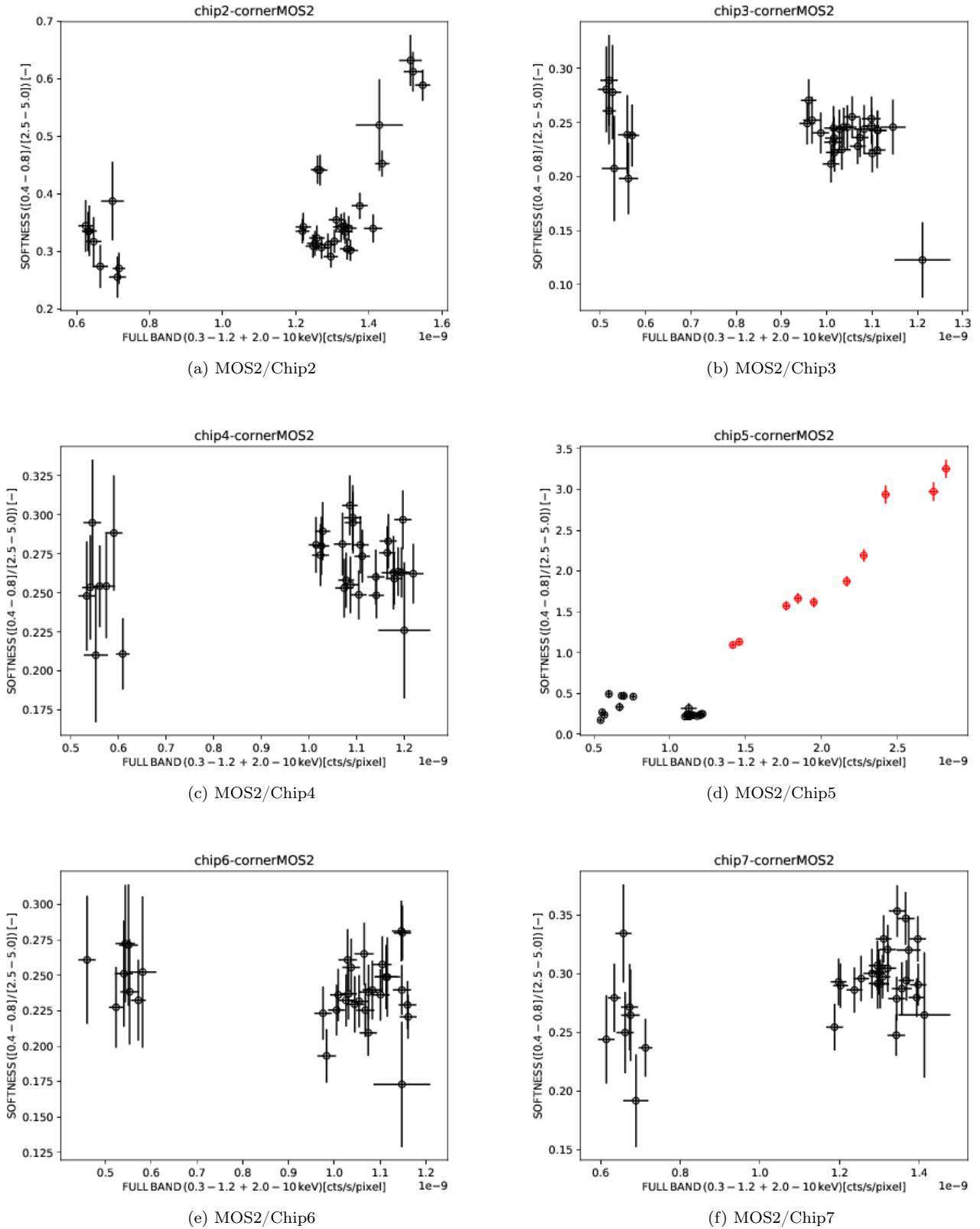
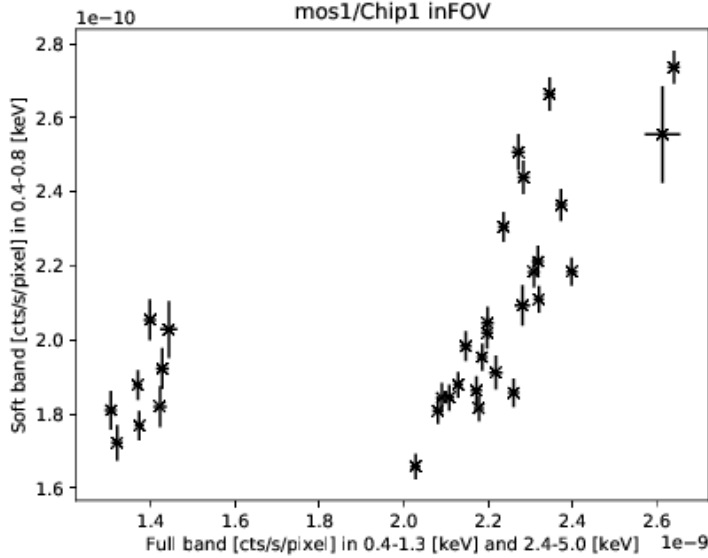
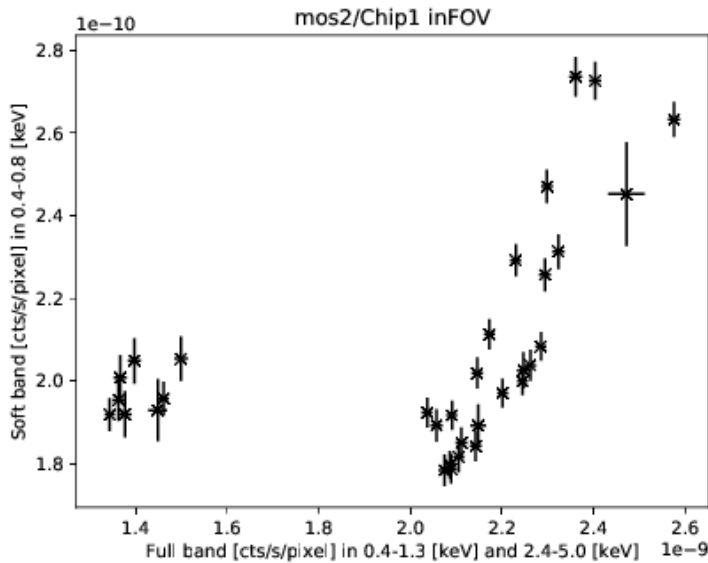


Figure 5.3: Same as the previous figure for the MOS2



(a) MOS1/Chip1



(b) MOS2/Chip1

Figure 5.4: Count rate of Chip1 for both (a) the MOS1 and (b) the MOS2.

## 5.4 Extracting overlapping region with *Chandra* and *XMM-Newton*, and detector areas of in and out of fields of view

The roll angles of *Chandra* were allowed to vary in order to obtain more uniform sensitivity across the field of view. As a result, the total area of the *Chandra* observation is 484.2 arcmin<sup>2</sup> centered at (RA, DEC) = (53.1178, -27.806). We note the field of view of the *Chandra* CCD camera is 285 arcmin<sup>2</sup>. The survey solid angle as a function of vignettted exposure of *Chandra* shows that the 285 arcmin<sup>2</sup> corresponds to roughly 50% of the total exposure. Thus, we selected the 285 arcmin<sup>2</sup> for our observation.

Following an analysis tool, **backscale**, which is an *XMM-Newton* data analysis tool for spatially diffuse emission, we define virtual pixels whose size is (0.05 arcsec)<sup>2</sup>/pixel, which are finer than the actual CCD pixels (1.1 arcsec)<sup>2</sup>/pixel.

## 5.5 Removal of time intervals contaminated with soft protons

As described in Chapter 4 (Section 4.2.3), *XMM-Newton* often suffers from occasional enhancements of soft protons, whose time scale is hundreds of sec to several ksec or possibly be even longer. This enhancement is considered to be due to soft protons with even  $\sim 100$  keV from the Sun. Low energy protons are focused by the X-ray mirror of *XMM-Newton*, and detected by the CCDs. The energy deposited on the CCD pixels is quite uniform over one CCD Chip. Therefore, when we analyze a point source, the soft proton can be removed by subtracting the background spectrum created from events located near the point sources in the same time interval as the point source. This is not applicable to the X-ray background spectrum.

The previous studies have shown that the soft proton spectrum above 2 keV corresponding to the X-ray background can be well approximated with a power-law function and that power-law index is usually smaller than 1.4, although it varies from time to time (e.g. Henley & Shelton (2013) and Snowden et al. (2008)). Therefore the spectrum is flatter than the X-ray background above 2 keV. However, the soft proton spectrum corresponding to the X-ray background below 2 keV is still unknown. Accordingly, modeling of the X-ray background below 2 keV is difficult. Therefore, we remove time intervals contaminated with soft protons.

In the upper panel of Figure 5.5, we show an example of the count time histories in the 5-10 keV band. The time span of the figure is for the whole time span of one ObsID, and the X-ray counts are accumulated in 350-s time bins. We find significant time variations which are not random in time. The number of occurrence of time bins is plotted as a function of counts in the time bins is plotted in the middle panel of Figure 5.5. The enhancement is clearly beyond the Poisson counting statistics.

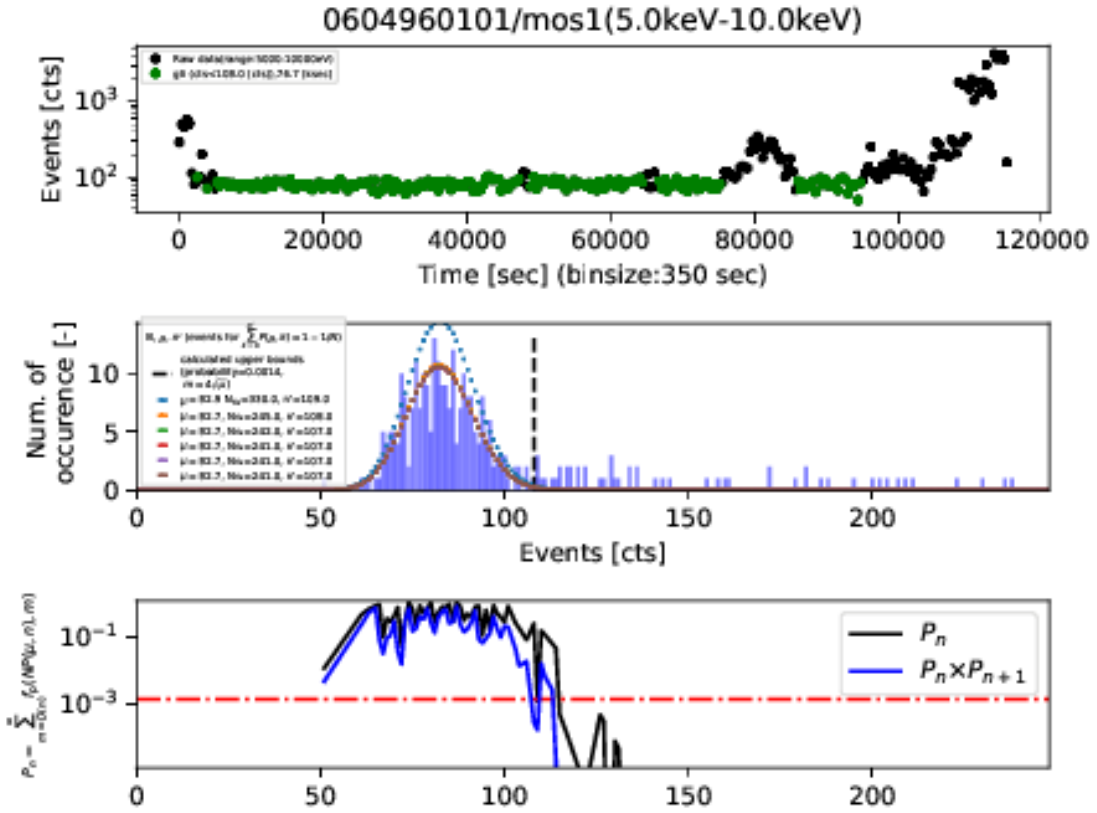


Figure 5.5: (upper): Time variation of count rates (light curve) in actual observation in the energy range of 5-10 keV. The accepted time bins are shown in green. (middle): Number of occurrence of time bins ( $D(n)$ ) as a function of number of counts per 350 sec. Results of model fits to the histogram are shown with blue and red curves, (lower): Blue curve is for the initial model of the iteration, while red curve for the converged model. Cumulative probability ( $P_c(n, D(n))$ ) for obtaining the number of occurrence of time bins larger than  $D(n)$  and the product of the two probabilities in the successive two bins,  $P_c(n, D(n))P_c(n+1, D(n+1))$ . The red horizontal dotted broken corresponds to  $P_{\text{Th}} = 0.05$  according to Equation (5.11).

### 5.5.1 short time scales

We try to discard time intervals when the short time-scale soft proton contaminations exist.

**Detection of contaminated time intervals** We would like to set a threshold in the middle panel of Figure 5.5 and to remove time intervals which contain counts larger than or equal to the threshold. The threshold can be determined by comparing the histograms with the Poisson distribution. For that purpose, we fitted the histogram with a Poisson function. However, we found the result is dependent on the number of counts in a time bin  $T$ . We divided a one ObsID into  $NT$  time bins. Thus, we iterated the fitting process to determine the fitting range  $n_t$  which is the number of counts in the time bin  $T$  where  $t$  is the number of iteration. Therefore, the count range of the  $t$ -th iteration is  $[0, n_t]$ . In the  $t$ -th iteration, we minimize the quantity,

$$L_t = \sum_{n=0}^{n_t} [D(n) - \Lambda_t P(\mu_t, n)]^2, \quad (5.1)$$

where  $n$  is a number of counts per time bin  $T$ ,  $D(n)$  is the number of occurrence of time bins which count  $n$ ,  $\mu_t$  is the average count in the time bin  $T$ ,  $P(\mu, n)$  is a Poisson distribution and  $\Lambda_t$  is a normalization of the Poisson distribution. We fix  $\Lambda_t$  to the value given by

$$\Lambda_t = \sum_{n=0}^{n_t} D(n), \quad (5.2)$$

and we set only  $\mu_t$  as a free parameter of the fit. Two Equations (5.1) and (5.2) are not consistent with each other because

$$\sum_{n=0}^{n_t} \Lambda_t P(\mu, n) < \Lambda_t. \quad (5.3)$$

However, because the number of occurrence of time bins is an integer, two equations are approximately consistent, if

$$\Lambda_t - \sum_{n=0}^{n_t} \Lambda_t P(\mu, n) \leq 1. \quad (5.4)$$

Thus in the next step, we find the upper range for the next iteration which satisfies

$$\sum_{n=0}^{n_{t+1}} D(n) \left[ 1 - \sum_{n=0}^{n_{t+1}} P(\mu_t, n) \right] = 1. \quad (5.5)$$

We iterate this procedure starting from an arbitrary initial value of  $n_1$  until  $n_{t+1} = n_t$ . Hereafter, we denote the converged values of  $\Lambda_t$  and  $\mu_t$  as  $\Lambda_0$  and  $\mu_0$ , respectively.

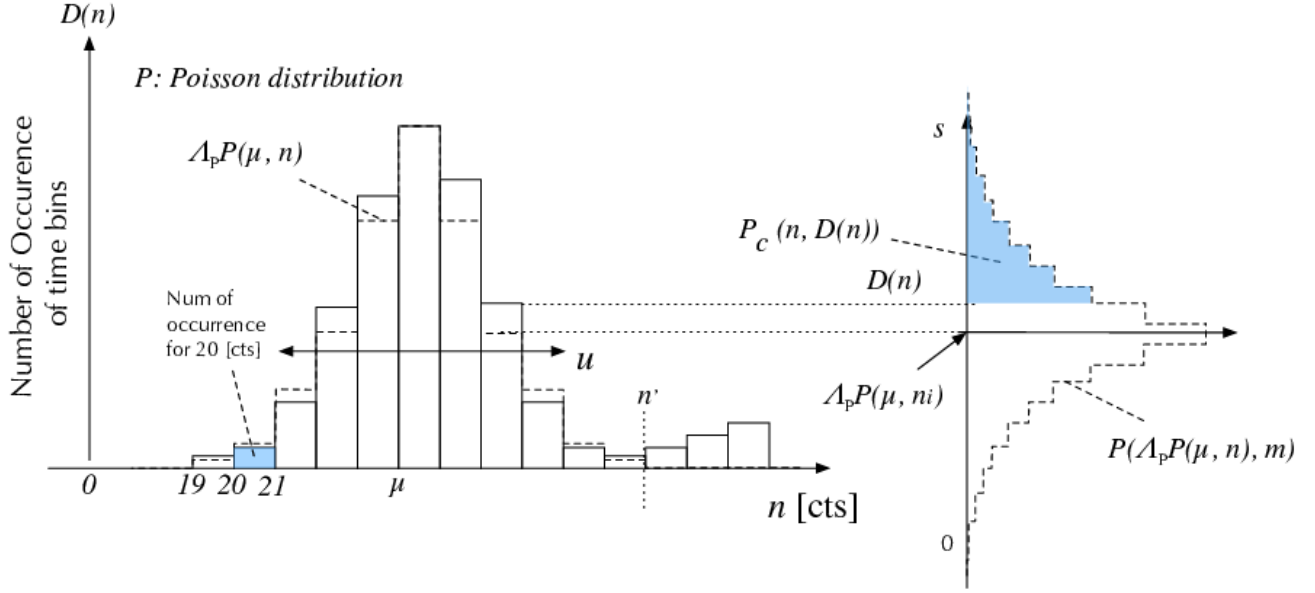


Figure 5.6: Two different Poisson statistics involved in the present analysis. The number of occurrence of time bins ( $D(n)$ ) in a given count bin ( $n$ ) obeys a Poisson distribution as a function of  $n$  as an illustrated in the left. On the other hand, if we focus on one count bin, the number of occurrence time bins fluctuates according to Poisson statistics as illustrated in the right. The mean value ( $\mu$ ) of the distribution can be estimated from the model fit of the distribution in the left. We denote the effective number of count bins as  $u$  where the distribution is regarded as a Poisson distribution in the count range.

We now have expected values of the number of occurrence of time bins for all count bins per  $T$  bins in the middle panel of Figure 5.5. Each number of occurrence of time bins also fluctuates according to a Poisson distribution (see the illustration in Figure 5.6). The probability of obtaining  $s$  occurrences at the  $n$ -th bin will be  $P(\Lambda_0 P(\mu_0, n), s)$ . Then the probability for obtaining the number of occurrence of time bins larger than  $D(n)$  is

$$P_c(n, D(n)) = \sum_{s=D(n)}^{\infty} P(\Lambda P(\mu, n), s). \quad (5.6)$$

If  $P_c(n, D(n))$  is a small number such as 0.01, we may consider that  $D(n)$  is an unusual number obtaining only 1% probability. However, before concluding this probability is unusual, we need to consider the so-called Look Elsewhere Effect (LEE). In Figure 5.5 (middle), we have a number of independent event count bins (samples). If we denote the effective number of count bins as  $u$  where the distribution is regarded as a Poisson distribution in the count range. The probability ( $P_S(n)$ ) that the number of occurrence of time bins in the bin  $n$  greater than  $D(n)$  in the effective number of count bins  $u$  is equal to 1 or greater than 1.

$$P_S(n) = 1 - \{1 - P_c(n, D(n))\}^u. \quad (5.7)$$

We define a threshold probability  $P_{Th}$  and if

$$P_S(n) < P_{Th} \quad (5.8)$$

we may consider that  $D(n)$  is too large and it is likely that something other than Poisson fluctuation, namely soft protons, contributes to the counts.

We can also consider a pair probability. The probability ( $P_P(n)$ ) that the number of occurrence of time bins in the bin  $n$  equal to  $D(n)$  or greater than  $D(n)$  and the time number of occurrence of time bins in the bin  $n+1$  equal to  $D(n+1)$  or greater than  $D(n+1)$  in the effective number of count bins  $u-1$  is equal to 1 or greater than 1. The probability at any pairs of Figure 5.5 (lower) will be

$$P_P(n, n+1) = 1 - \{1 - P_c(n, D(n))P_c(n+1, D(n+1))\}^{u-1}. \quad (5.9)$$

We can also set a criterion,

$$P_P(n, n+1) < P_{Th} \quad (5.10)$$

to find out the possible contribution of soft protons. This equation is re-written as

$$P_c(n, D(n))P_c(n+1, D(n+1)) < 1 - (1 - P_{Th})^{1/(u-1)}. \quad (5.11)$$

**Exclusion of contaminated time intervals** To estimate the probability as described in the previous Subsection, we need to determine the effective number of count bins,  $u$ . In addition, there are two other parameters we must decide, the threshold probability,  $P_{\text{Th}}$ , and the duration of a time bin to accumulate counts,  $T$ . Strictly, we need to perform simulations to determine  $u$ . However, the choice of  $P_{\text{Th}}$  is strongly coupled with  $u$ . Thus we first set the value of  $u$  at each iteration satisfying  $u_t = 4\sqrt{\mu_t - 1}$ . For  $t = 1$ , we do not have a value from the previous iteration, thus we set  $u_1$  manually reading from the shape of the plot in the middle panel of Figure 5.5. Then we determined the value of  $P_{\text{Th}}$  on a trial-and-error basis, which will be described below.

The time resolution of events in the FITS event files is 2.6 s, which corresponds to the CCD readout period (Turner et al. (2001)). Thus the minimum possible value of  $T$  is 2.6 sec. If  $T$  is too short, we will not have enough statistics to detect soft protons. On the other hand, if  $T$  is too long, we will have two drawbacks. First, we will be insensitive to soft proton events on time scales shorter than  $T$ . Second, we need to discard longer exposure time intervals to keep a uniform bin length of  $T$  overall time bins when  $T$  becomes longer. We thus determined the value of  $T$  starting from a small value and gradually increasing it until we can clearly identify a gradual increase of counts in the time-history plot such as the upper panel of Figure 5.5. As a result, we decided to set  $T = 350$  sec. When we make count time histories, we aligned the time bins of the MOS1 and the MOS2 so that we can reject time bins for which at least one of the MOS1 or the MOS2 does not satisfy the acceptance criterion.

We applied the criteria of Equations (5.8) and (5.10) to all ObsIDs varying the value of  $P_{\text{Th}}$ , and checked the results by eyes. In the process, we would like to find a value of  $P_{\text{Th}}$  with which all anomalies which can be identified by eyes are discarded. We find  $P_{\text{Th}} = 0.05$  applied to the pair probability in Equation (5.10) gives reasonable results. We applied the criterion and the accepted exposure time is summarized in Table (5.2) and in Appendix A.2.

Table 5.2: Summary of exposure time after applied short time-scale filter.

| ObsIDs     | Exposure time† sec |           |
|------------|--------------------|-----------|
|            | MOS1               | MOS2      |
| 0108060401 | 13738.9            | 13742.3   |
| 0108060501 | 23124.7            | 23128.9   |
| 0108060601 | 44874.3            | 44889.7   |
| 0108060701 | 69221.0            | 69244.5   |
| 0108061801 | 31622.8            | 31613.7   |
| 0108061901 | 38594.4            | 38610.8   |
| 0108062101 | 35474.3            | 35506.0   |
| 0108062301 | 58748.6            | 58773.0   |
| 0555780101 | 65504.7            | 65528.3   |
| 0555780201 | 74703.0            | 74706.5   |
| 0555780301 | 80145.6            | 80175.9   |
| 0555780401 | 46696.0            | 46718.7   |
| 0555780501 | 80272.4            | 80297.3   |
| 0555780601 | 52635.4            | 52648.4   |
| 0555780701 | 76918.7            | 76948.9   |
| 0555780801 | 66517.6            | 66537.7   |
| 0555780901 | 55747.6            | 55770.2   |
| 0555781001 | 80917.6            | 80932.5   |
| 0555782301 | 83166.0            | 83171.9   |
| 0604960101 | 69176.2            | 69188.7   |
| 0604960201 | 73497.6            | 73538.3   |
| 0604960301 | 79571.7            | 79617.5   |
| 0604960401 | 85330.0            | 85400.8   |
| 0604960501 | 45954.0            | 45979.7   |
| 0604960601 | 56769.1            | 56804.2   |
| 0604960701 | 34383.7            | 34394.0   |
| 0604960801 | 64045.3            | 64069.5   |
| 0604960901 | 62881.9            | 62899.1   |
| 0604961001 | 79317.5            | 79363.0   |
| 0604961101 | 94329.5            | 94378.9   |
| 0604961201 | 70895.8            | 70948.3   |
| 0604961301 | 7179.4             | 7188.3    |
| 0604961801 | 73356.1            | 73372.1   |
| Total      | 1975325.4          | 1976087.6 |

**Notes.**

†Threshold,  $P_{\text{Th}}$ , is 0.05

and  $u$  equals  $4\sqrt{\mu}$  for all observations.

## 5.5.2 Long time scales

The soft proton removal process applied in the previous Section does not remove contaminated time interval if data of whole one ObsID are contaminated continuously. There can be contamination on such long time scales. We thus tried to identify and remove residual soft proton contamination (RSPC) in this Section. For this purpose, we compared the counting rates of each ObsIDs. Because of the non X-ray background (NXB) exhibits long-term variations, its contribution must be subtracted before the comparison. As we will discuss in Section 6.2, in the energy range above 10 keV, the effective area of the X-ray telescope is extremely small, and thus all counts can be considered to arise from the NXB. We used the counting rate in 10–11 keV as an indicator of the NXB. On the other hand, we used the 2-5 keV band for checking whether the long time scale variation in the soft proton flux exists or not. Because we used 5-10 keV and the time variation take place due to the solar activity below 2 keV. We first estimate the counting rates per unit area of the detector for in and out of fields of view, respectively, as

$$R_{i,\text{ID}}(E_1, E_2) = \frac{C_{i,\text{ID}}(E_1, E_2)}{T_{\text{ID}}A_{i,\text{ID}}}, \quad (5.12)$$

where  $i$  is either inFOV or outFOV as defined in Section 5.4, ID is the ObsID, and  $E_1, E_2$  denote the energy range.  $T_{\text{ID}}$  is the exposure time of the ObsID,  $R_{i,\text{ID}}(E_1, E_2)$ ,  $C_{i,\text{ID}}(E_1, E_2)$ , and  $A_{i,\text{ID}}$  are the counting rate, the

total number of counts, and the detector area. The values of  $A_{i,\text{ID}}$  were estimated in Section 5.4. The background subtracted counting rate is then estimated by

$$z_{\text{ID}}(2 \text{ keV}, 5 \text{ keV}) = R_{\text{inFOV, ID}}(2 \text{ keV}, 5 \text{ keV}) - r_{\text{ID}} R_{\text{outFOV, ID}}(2 \text{ keV}, 5 \text{ keV}), \quad (5.13)$$

where

$$r_{\text{ID}} = \frac{R_{\text{inFOV, ID}}(10 \text{ keV}, 11 \text{ keV})}{R_{\text{outFOV, ID}}(10 \text{ keV}, 11 \text{ keV})}. \quad (5.14)$$

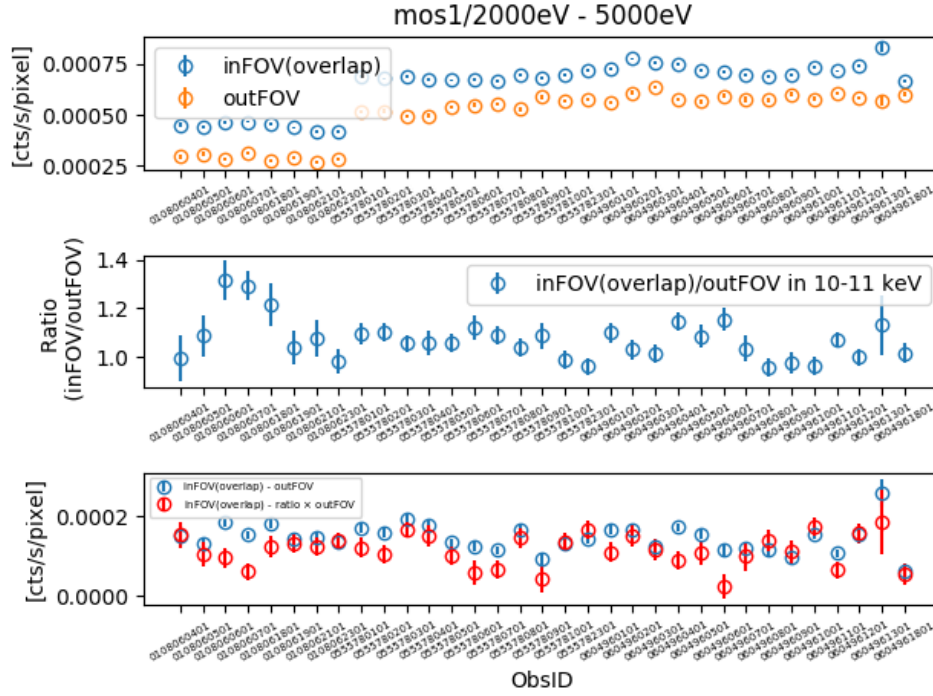
The correction by the  $r_{\text{ID}}$  factor is introduced to correct for the non-uniformity of the NXB. The statistical errors of  $z_{\text{ID}}(2 \text{ keV}, 5 \text{ keV})$  are estimated by propagating Poisson errors of each factor in the above equations. Namely,

$$\begin{aligned} (\delta z_{\text{ID}}(2 \text{ keV}, 5 \text{ keV}))^2 &= (\delta R_{\text{inFOV, ID}}(2 \text{ keV}, 5 \text{ keV}))^2 \\ &\quad + (\delta r_{\text{ID}})^2 R_{\text{outFOV, ID}}^2(2 \text{ keV}, 5 \text{ keV}), \\ &\quad + r_{\text{ID}}^2 (\delta R_{\text{outFOV, ID}}(2 \text{ keV}, 5 \text{ keV}))^2 \end{aligned} \quad (5.15)$$

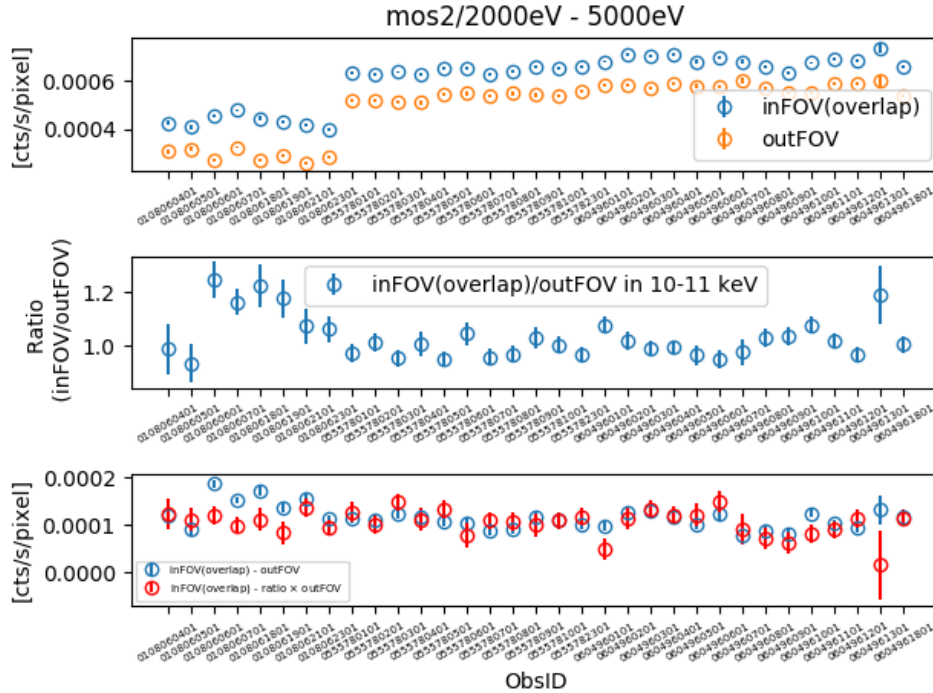
where

$$(\delta r_{\text{ID}})^2 = r_{\text{ID}}^2 \left[ \left( \frac{\delta R_{\text{inFOV, ID}}(10 \text{ keV}, 11 \text{ keV})}{R_{\text{inFOV, ID}}(10 \text{ keV}, 11 \text{ keV})} \right)^2 + \left( \frac{\delta R_{\text{outFOV, ID}}(10 \text{ keV}, 11 \text{ keV})}{R_{\text{outFOV, ID}}(10 \text{ keV}, 11 \text{ keV})} \right)^2 \right]. \quad (5.16)$$

In Figure 5.7, we show  $R_{\text{inFOV, ID}}(2 \text{ keV}, 5 \text{ keV})$  and  $R_{\text{outFOV, ID}}(2 \text{ keV}, 5 \text{ keV})$  (upper panels),  $r_{\text{ID}}$  (middle panels), and  $z_{\text{ID}}(2 \text{ keV}, 5 \text{ keV})$  (red data points in lower panels) as a functions of ObsID. The (a) and (b) of the plot show the MOS1 and the MOS2, respectively. We found jumps in the upper panels between ObsID 8 and ObsID 9. This is because there is a long time interval of the NXB count rates between ObsID 8 and ObsID 9. We found the background subtracted counting rate is more continuous in the lower panels.



(a)



(b)

Figure 5.7: Long time variation in 2-5 keV (a) for the MOS1 and (b) for the MOS2. (upper): Event rate of the MOS detectors in 2-5 keV for inFOV (overlapping region with Chandra observation) and for outFOV (non X-ray exposed region). (middle) Ratio of count rates of inFOV to outFOV regions in the 10-11 keV range. (lower): Background subtracted inFOV count rate in 2-5 keV (red data points). Another estimation of the same quantity without correction of  $r_{\text{ID}}$  is shown with blue data points for comparison.

In order to assess whether the counting rates,  $z_{\text{ID}}(2 \text{ keV}, 5 \text{ keV})$ , follow a Gaussian statistics, we calculated the deviation from the average normalized to the statistical deviation of each ObsID. That is

$$s_{\text{ID}} = \frac{z_{\text{ID}}(2 \text{ keV}, 5 \text{ keV}) - \bar{z}}{\delta z_{\text{ID}}(2 \text{ keV}, 5 \text{ keV})}, \quad (5.17)$$

where

$$\bar{z} = \frac{1}{N} \sum_{\text{ID}=1}^N z_{\text{ID}}(2 \text{ keV}, 5 \text{ keV}). \quad (5.18)$$

We then created an occurrence histogram of  $s_{\text{ID}}$ , which is shown in Figure 5.8 for the MOS1 and the MOS2 separately. Subsequently, we fitted the histogram with a Gaussian function with the mean and  $\sigma$  fixed to zero and unity, respectively. The best fit Gaussian function is shown with horizontal bars connected with a dotted broken line. We find that histogram of the MOS1 is more extended in the horizontal axis than the Gaussian function. On the other hand, the histogram of the MOS2 is more or less consistent with the Gaussian function. It is very unlikely that the counting rates decreased because of some additional effect, we consider that we likely have soft proton contamination in some of the MOS1 ObsIDs and the average counting rate was increased by this effect. With this assumption, if we remove the highest  $s_{\text{ID}}$  bin containing three occurrences and recalculate the histogram and fit it with a Gaussian as shown in Figure 5.9. As shown in Figure 5.9, we obtain a more consistent result. However, for safety, we decided to not to use the MOS1 data the spectral analysis in Chapter 7.

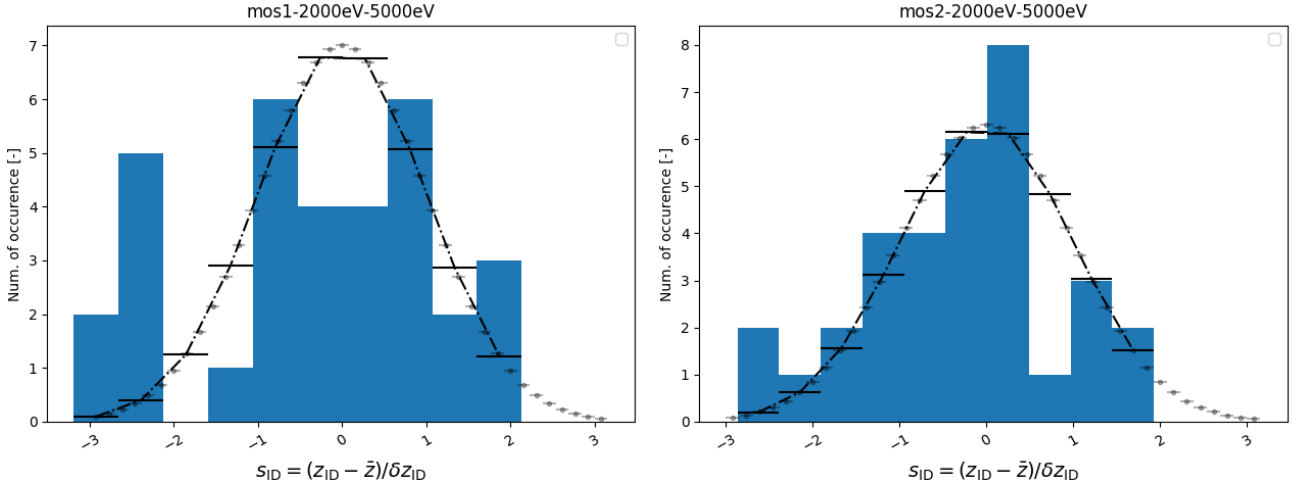


Figure 5.8: Occurrence histogram of  $s_{\text{ID}}$  (see Equation (5.17)), for the MOS1 and the MOS2 separately. Histogram of deviation from the average normalized to with statistical fluctuation of each ObsIDs. The MOS1 and the MOS2 are shown separately. The best fit Gaussian function is shown with horizontal bars connected with a dotted broken line. Distribution of the MOS1 is more extended than the Gaussian function.

### 5.5.3 Confirmation of soft proton removal

As explained previous Section 5.5.2, we are sure that the contaminated time intervals are completely discarded in the MOS2. We consider how much residual soft proton contamination (RSPC) includes in our final spectrum. The conceivable residual soft proton contamination makes us overestimate surface brightnesses of the X-ray background. Thus, the systematic errors are calculated in Appendix C. We show the results of the calculated systematic errors in Table 5.3.

## 5.6 Long-term variations in the soft band

The observations of the first eight ObsIDs were made near the solar maximum, while the others were done during less active phases. We thus expect a difference in the intensity of X-rays arising from solar wind charge exchange (SWCX). We can check this by applying the same method to the 0.4-1 keV energy range.

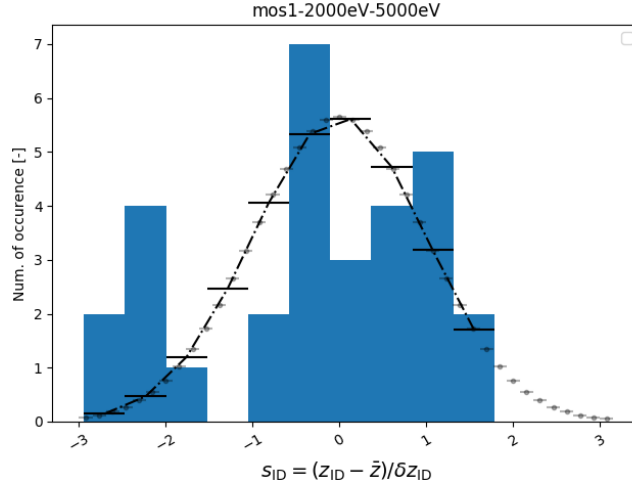


Figure 5.9: Same as Figure 5.8 for the MOS1. We remove the highest  $s_{ID}$  bin containing three occurrences in Figure 5.8 and recalculate the histogram and fit it with a Gaussian.

Table 5.3: Systematic errors due to conceivable residual soft proton contaminations

| Surface brightnesses | Systematic error of conceivable residual soft proton contamination (RSPC) |
|----------------------|---|
| Total (0.4-1 keV)    | +0%   |
|                      | -16%  |
| Total (0.5-1 keV)    | +0%   |
|                      | -12%  |
| Total (2-8 keV)      | +0%   |
|                      | -31%  |
| OVII                 | +6%   |
|                      | -6%   |
| OVIII                | +4%   |
|                      | -7%   |

The results are shown in Figure 5.10. We find that the NXB non-subtracted count rate in 0.4-1 keV is almost constant throughout all the observations. We consider this is just a chance coincidence. Namely, the increase of the NXB count rate is obvious from orange-color data points in the top panel of the Figure 5.10 and the increase of the NXB was compensated by the decrease of the 0.4-1 keV flux of the NXB subtracted count rate, which is shown in the lower panel of the Figure 5.10.

X-rays arising from SWCX is a kind of background emission in the present study and we would like to keep it as low as possible. Although we lose 8 ObsIDs out of the 33 ObsIDs in total, we consider that it is more beneficial for the present study to remove the eight ObsIDs from further study.

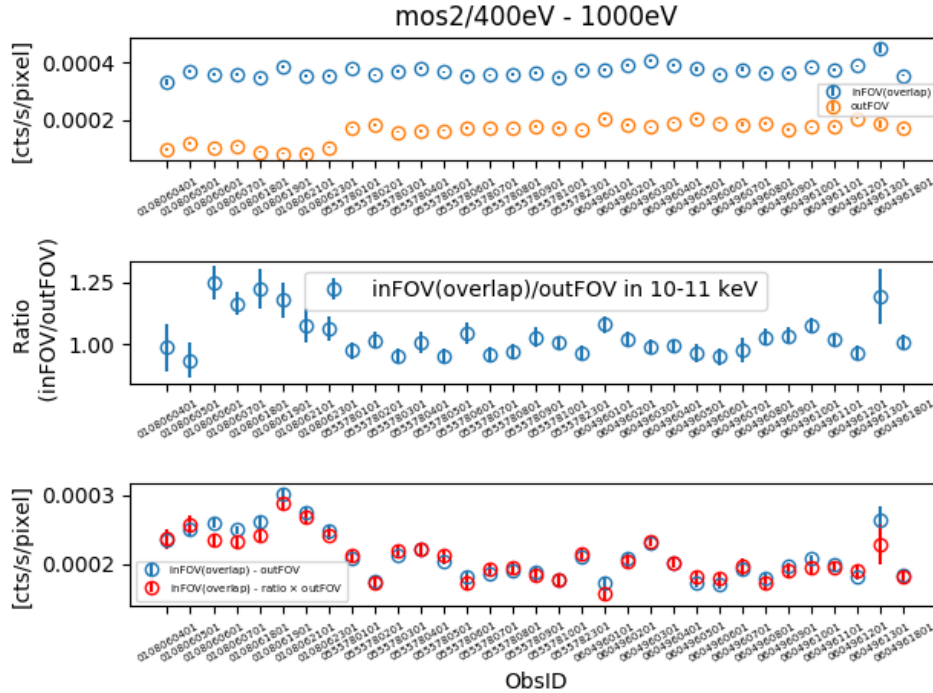
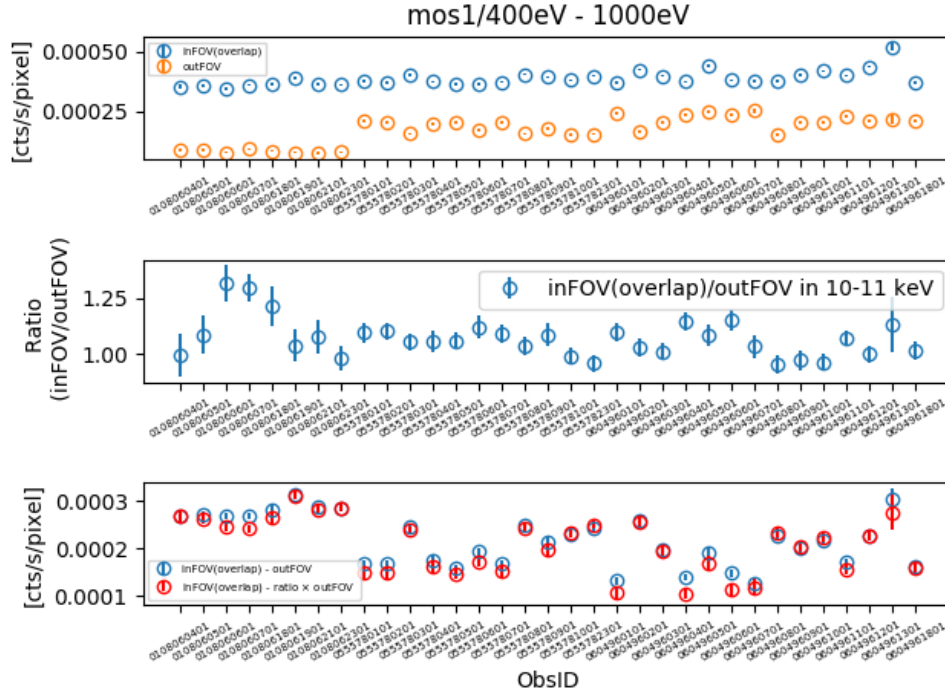


Figure 5.10: Long-term variability of count rate, (a) for the MOS1 and (b) for the MOS2, as a function of ObsID. (upper): Count rate of the MOS detector in the 0.4-1 keV range. The blue circle represents an inFOV count rate ( $R_{\text{inFOV}}$ ), while the orange circle represents an outFOV count rate ( $R_{\text{outFOV}}$ ). We see constant count rate of the  $R_{\text{inFOV}}$ . On the other hand, the count rate of  $R_{\text{outFOV}}$  suddenly goes up between 0108062301 and 0555780101 and stay higher after 0555780101. (middle): Ratio,  $r_{\text{ID}}$  in Equation 5.14 in the 10-11 keV range. (lower): The blue circle is  $R_{\text{inFOV}} - R_{\text{outFOV}}$  and the red circle is  $R_{\text{inFOV}} - r_{\text{ID}}R_{\text{outFOV}}$ .

Thus, we finally analyzed the X-ray background spectrum obtained by the MOS2 in the solar minimum period. The total exposure is 1.66 Msec. As shown in Table 5.4, the total exposures are reduced from 3.6 Msec to 1.66 Msec.

Table 5.4: Total exposure times

| Sections         | Filter   | Exposures    |                |
|------------------|--|--------------|----------------|
|                  |  | MOS1<br>Msec | MOS2<br>Msec   |
| Initial          | -  | 3.6          | 3.6            |
| Section 5.3      | Standard screening   | 2.4          | 2.4            |
| Subsection 5.5.1 | Soft proton contamination removal<br>(short time scale) in the 5-10 keV band | 2.0          | 2.0            |
| Subsection 5.5.2 | Soft proton contamination removal<br>(long time scale) in the 2-5 keV band   | 2.0          | 0 <sup>†</sup> |
| Section 5.6      | Long-term variability in the 0.4-1 keV band                                  | 1.66         | 0              |
|                  | Final  | 1.66         | 0              |

<sup>†</sup> the MOS1 data is not used because of the residual soft proton contamination (RSPC).

## 5.7 Sky region free from *Chandra* point sources

### 5.7.1 *Chandra* point-source list

The latest *Chandra* point sources catalog was published in Luo et al. (2017) using the  $\sim 7$  Ms the CDF-S observation data. The catalogue contains 1008 sources in total. Among them, 916 sources are resolved in the 0.5-7.0 keV band, while 84 and 8 sources are resolved only either in the 0.5-2 keV or the 2-7 keV band, respectively. We employ the positions and fluxes tabulated in Table 4 of Luo et al. (2017) in the following analysis. The systematic errors of the sky positions and the method to determine the X-ray fluxes in the 0.5-8 keV band are described in Sections 2.4.1 and 2.4.2.1 of Chapter 2.

### 5.7.2 Overview of point-source mask

In this thesis, we would like to remove the contribution of point sources resolved by *Chandra* from the *XMM-Newton* CDF-S X-ray background spectrum. For this purpose, we mask the *XMM-Newton* pixels which contain significant contributions of point sources, and we derive a diffuse background spectrum from the rest of the pixels. If the point spread function (PSF) of the X-ray telescope is ideally sharp, this removal would be straightforward. However, since the half power diameter (HPD) of the PSF is 15 arcsec at the center and it increases towards the edge of the field of view. If we simply remove circular image regions whose diameter is twice as large as HPD at the center, the total regions will be  $\pi \times (1/4 \text{ arcmin})^2 \times 1008 = 198 \text{ arcmin}^2$ . This number is significant compared to the total the CDF-S field of view,  $285 \text{ arcmin}^2$ , but still we are not sure twice HPD is enough or not. If we increase the mask diameter to 2.5 HPD then, we will lose most of the area because of  $\pi \times (1/4 * 1.25 \text{ arcmin})^2 \times 1008 = 309 \text{ arcmin}^2$ . Spill over of the point sources flux to the diffuse background spectrum will be smaller for a larger mask size, however, we lose photon statistics.

Obviously, we need to determine the size of mask adoptively taking the brightness of each point sources into account. We also need to estimate the X-ray fluxes from point sources which fell outside the mask and their effect on the remaining masked spectrum. In order to estimate the best mask size, we utilize image simulations. We create *XMM-Newton* observation images of *Chandra* point sources and compare them with the *XMM-Newton* image of the flat-field X-ray background.

### 5.7.3 *XMM-Newton* simulation images of resolved point sources

**Response files and point sources spectra** If we have point sources in the sky at spatial positions of  $\{(x_i, y_i), i = 1 \dots N\}$  emitting X-rays whose intensity and energy spectrum are described  $I_i(E)$  where  $E$  is the X-ray energy, the

image ( $V$ ) where we obtain with the *XMM-Newton*-Newton X-ray telescope system will be the

$$V(p_j, q_j, E) = \sum_{i=1}^N f_{\text{PSF}}(p_j, q_j, x_i, y_i, E) A(x_i, y_i, E) I_i(E), \quad (5.19)$$

where  $A(x_i, y_i, E)$  and  $f_{\text{PSF}}(p_j, q_j, x_i, y_i, E)$  are, respectively, the effective area and point spread function (PSF) of the telescope system in the direction of  $(x_i, y_i)$  at the and energy  $E$ ,  $(p_j, q_j)$  is the location of the  $j$ -th pixel in the detector coordinates.  $A(x_i, y_i, E)$  decreases from the bore sight direction to the edge of the field of view due to vignetting. Thus  $A(x_i, y_i, E)$  is also called a vignetting function. Integrating  $V(p, q, E)$  with  $E$ ,

$$V(p_j, q_j) = \int_{E_1}^{E_2} V(p_j, q_j, E) dE, \quad (5.20)$$

we obtain a simulation image in the energy band from  $E_1$  to  $E_2$ .

We can create both the PSF and the vignetting function for all *Chandra* point sources using the SAS software package and the *XMM-Newton* calibration database. We ignored the PSF region more distant than 3 arcmin from the source position. For the source spectrum, we assumed a power-law spectrum with the Galactic absorption in the column density  $N_{\text{H}}$ ,  $8.8 \times 10^{19} \text{ cm}^{-2}$ .

**Image maps** Using response functions and source spectra, we can create simulation images. The details of the tasks are shown in Figure 5.12. Examples of simulation images in the two different energy bands of 0.4-1 keV and 2-8 keV are shown in Figure 5.12.

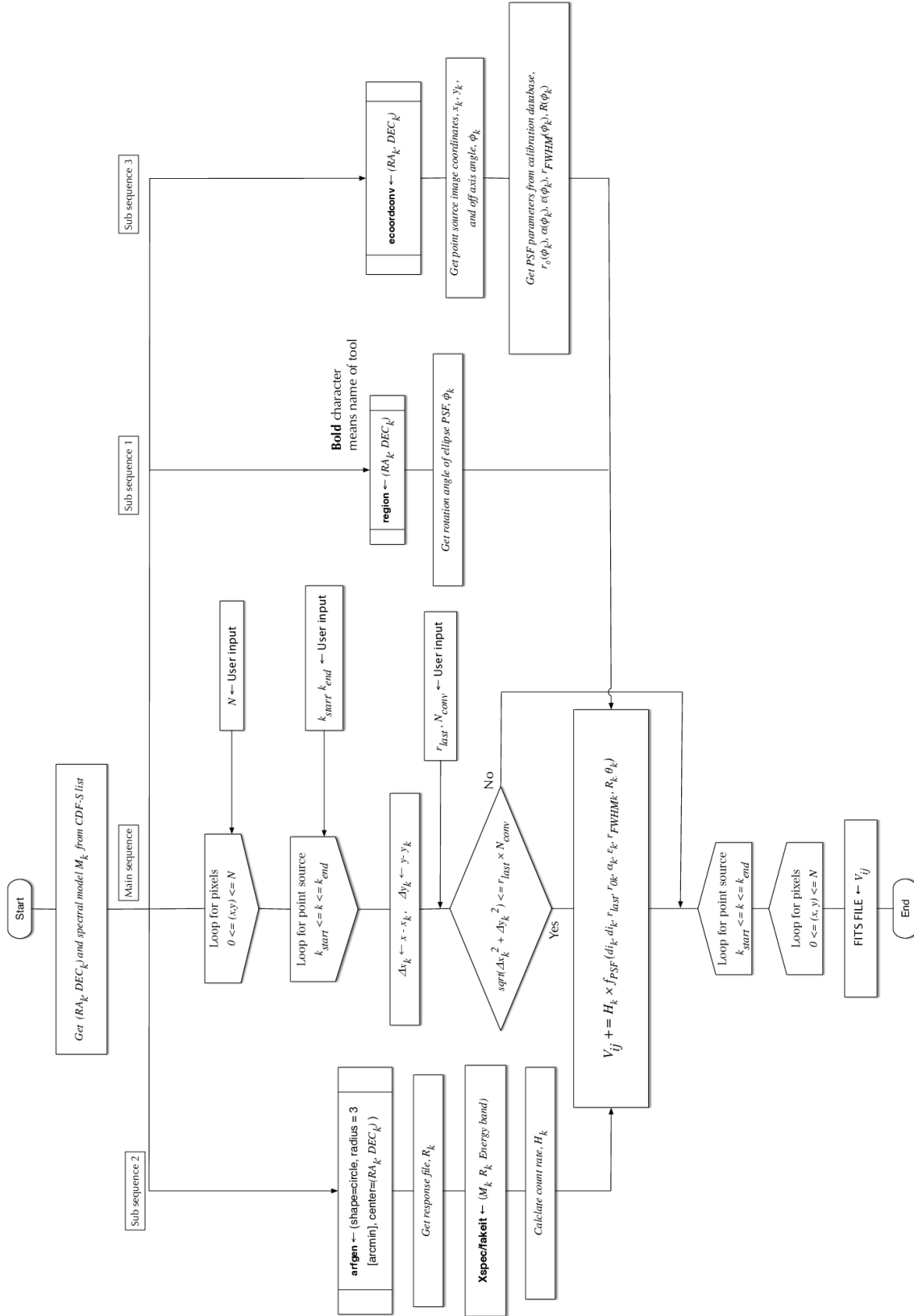


Figure 5.11: Flow chart for making simulation image. The name of a tool is expressed by black bold characters.  $V_{pq}$  indicates a simulation image.  $N_{conv}$  is a conversion factor for calculating pixel length,  $L$ .  $M_k$  and  $R_k$  are a spectral model and a response for a point source, respectively.

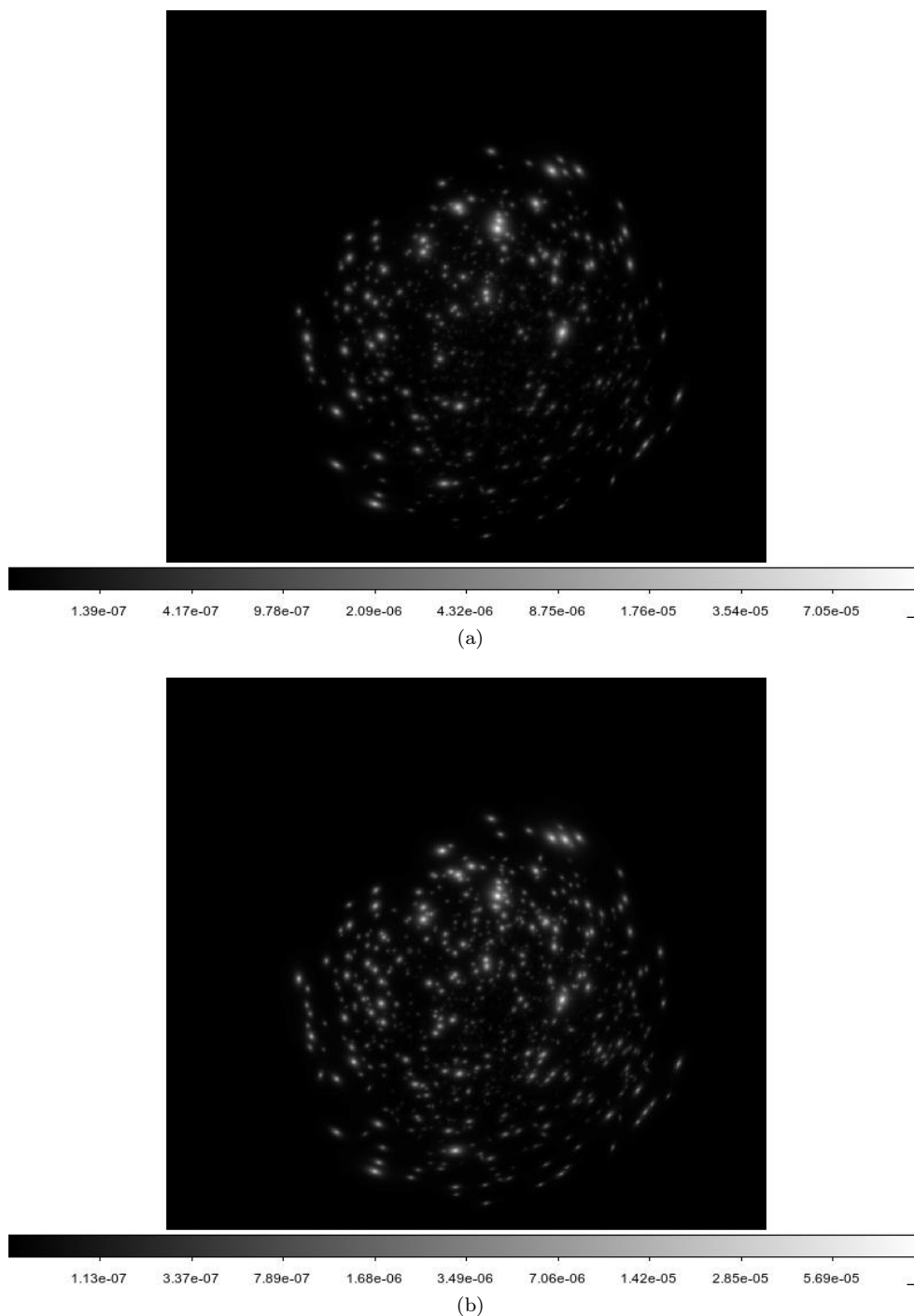


Figure 5.12: *XMM-Newton* simulation images of point sources in the CDF-S catalogue in Luo et al. (2017), (a) for the 0.4-1 keV band and (b) for the 2-8 keV band, respectively. These images are for the MOS1 in Observation ID:0604960101. The radius of the image is 9.5 arcmin and the spatial resolution is 2.5 arcsec/pixel. Underbar is in a unit of cts/s. Entire size is  $37.5 \times 37.5$  arcmin<sup>2</sup>. We calculated these images in the sky coordinate system.

#### 5.7.4 Comparisons of simulation image and the *XMM-Newton* real image

We checked the consistency of a simulation image with an *XMM-Newton* real image.

We first checked the locations of some bright sources. The comparisons between a simulation image and an *XMM-Newton* image of the brightest 10 sources are shown in Figure 5.13. Both images are consistent with each other. Subsequently, we defined the center of a point sources image by eyes and took out a circular image within 1 arcmin radius centered at the point source. Then we calculated the center of photon weighted gravity of the

*XMM-Newton* real image. In Table 5.5, a comparison for a source position between the *XMM-Newton* real image and the simulation image (the CDF-S list) is shown as an example. We see that the position of the simulation input is different from the *XMM-Newton* real image by 0.74 arcsec and 1.42 arcsec for the MOS1 and the MOS2, respectively. These values are consistent with the uncertainties in astrometry of *XMM-Newton* and *Chandra*.

Table 5.5: Comparison of a source position between the CDF-S list and the *XMM-Newton* real image

| Observation ID | XID | Inst. | Simulation image (CDF-S list) |            |              |              | <i>XMM-Newton</i> real image |                | Distance |                 |
|----------------|-----|-------|-------------------------------|------------|--------------|--------------|------------------------------|----------------|----------|-----------------|
|                |     |       | RA<br>deg                     | DEC<br>deg | $x$<br>pixel | $y$<br>pixel | $x_G$<br>pixel               | $y_G$<br>pixel | pixel    | $L_G$<br>arcsec |
| 0604960101     | 175 | MOS1  | 53.036                        | -27.792    | 594.01       | 381.85       | 594.3                        | 381.9          | 0.294    | 0.74            |
|                |     | MOS2  |                               |            |              |              | 593.5                        | 382.1          | 0.568    | 1.42            |

Pixel size corresponds to 2.5 arcsec/pixel. The XID means the CDF-S catalogue ID. We choices this source because independent from other sources. Source location is converted into  $(x, y)$  by using `ecordconv`.

We then compared the intensities of point sources. We extracted a spectrum of each point sources among the ten brightest ones from a circular region within 1 arcmin radius centered at the *Chandra* catalogue coordinates. For the *XMM-Newton* real observation, we need to subtract background, and we extracted it from the annular region between 1 arcmin and 2 arcmin radii centered at the source. The 1 arcmin corresponds to the encircled energy fraction of  $\sim 90\%$ . We fitted each source spectrum with a broken power law and calculated the Galactic-absorption corrected flux by a tool, `cflux`. The fluxes of the isolated three sources obtained from the simulation image in Figure 5.13 (b) together with those observed by *XMM-Newton* are shown in Figure 5.14. The vertical error bars show  $1.6\sigma$  single parameter errors. The sources ( $k = 1$  and 9) are not chosen because these two sources are closely located with each other and the flux cannot be estimated with the present simple analysis. The sources ( $k = 3, 4, 5, 7$  and 10) are outside the overlapping region. Thus the sources ( $k = 2, 6,$  and 8) are plotted in Figure 5.14. We find the simulation and the real observations are consistent with each other within the errors.

### 5.7.5 Determination of point-source mask

In order to set a point-source mask, we created one more simulation image, which is the flat-field image ( $B$ ) whose intensity is adjusted to match the real *XMM-Newton* observation;

$$B(p_j, q_j, E) = \sum_{i=1}^N f_{\text{PSF}}(p_j, q_j, x_i, y_i, E) A(x_i, y_i, E) I(E), \quad (5.21)$$

where the entire region is divided into  $N$  ( $37.5/(2.5/60) \times 37.5/(2.5/60)$ ) cells in the sky coordinates,  $I(E)$  is the surface brightness per cell,  $A(x_i, y_i, E)$  and  $f_{\text{PSF}}(p, q, x_i, y_i, E)$  are, respectively, the effective area and point spread function (PSF) of the telescope system,  $(x_i, y_i)$  is the location of  $i$ -th cell in the sky coordinates,  $(p_j, q_j)$  is the location of  $j$ -th pixel in the detector coordinates. In Equation (5.21), the PSF can be approximated by a delta function and the following is a good approximation:

$$B(p_j, q_j, E) = \sum_{i=1}^N A(p_j(x_i, y_i), q_j(x_i, y_i), E) I(E). \quad (5.22)$$

Then integrating with  $E$ , we obtain

$$B(p, q) = \int_{E_1}^{E_2} A(p, q, E) I(E) dE. \quad (5.23)$$

Then introducing one adjustable parameter  $b$ , we define the point sources mask,

$$M(p, q) = \begin{cases} 0 & \text{for } V(p, q) > bB(p, q) \\ 1 & \text{for } V(p, q) \leq bB(p, q) \end{cases}, \quad (5.24)$$

where  $V(p_j, q_j)$  is defined in Equation (5.19).  $M(p_j, q_j) = 0$  means that the  $j$ -th pixel  $(p_j, q_j)$  is masked and will not be used to extract the diffuse background spectrum.

We determine the value  $b$ , taking two factors into account; (1) larger  $b$  will make the masked region smaller so that we have better photon statistics for the diffuse background spectrum, (2) but at the same time the spill over

from point sources becomes larger. Suppose  $C(p_j, q_j)$  is the real *XMM-Newton* image. We apply the point sources mask to it as  $C(p_j, q_j)M(p_j, q_j)$ . Then we will calculate the background subtracted surface brightness of the image as we have done in Section 5.5.2, but here we simplify it by not correcting by the 10-11 keV intensities. Then, setting in count image in the field of view (inFOV)

$$C_{\text{inFOV}} = \sum_j C(p_j, q_j)M(p_j, q_j), \quad (5.25)$$

and the count image out of the field (outFOV) to be  $C_{\text{outFOV}}$  and the detector areas of those as  $A_{\text{inFOV}}$  and  $A_{\text{outFOV}}$ , the background subtracted average surface brightness ( $z$ ) will be

$$z = \frac{C_{\text{inFOV}}}{A_{\text{inFOV}}} - \frac{C_{\text{outFOV}}}{A_{\text{outFOV}}}. \quad (5.26)$$

Then the relative statistical error of  $z$  is given by

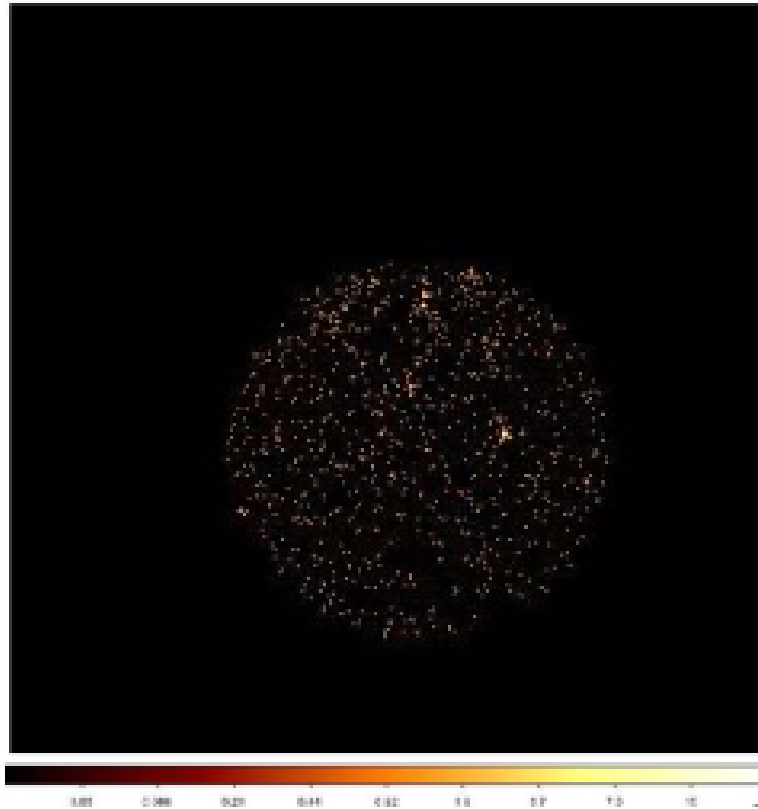
$$\delta_{\text{stat}} \equiv \frac{\delta z}{z} = \frac{\left(\frac{\sqrt{C_{\text{inFOV}}T}}{TA_{\text{inFOV}}}\right)^2 + \left(\frac{\sqrt{C_{\text{outFOV}}T}}{TA_{\text{outFOV}}}\right)^2}{z}, \quad (5.27)$$

where  $T$  is the exposure time. The ratio of spill over to the total counts are estimated by

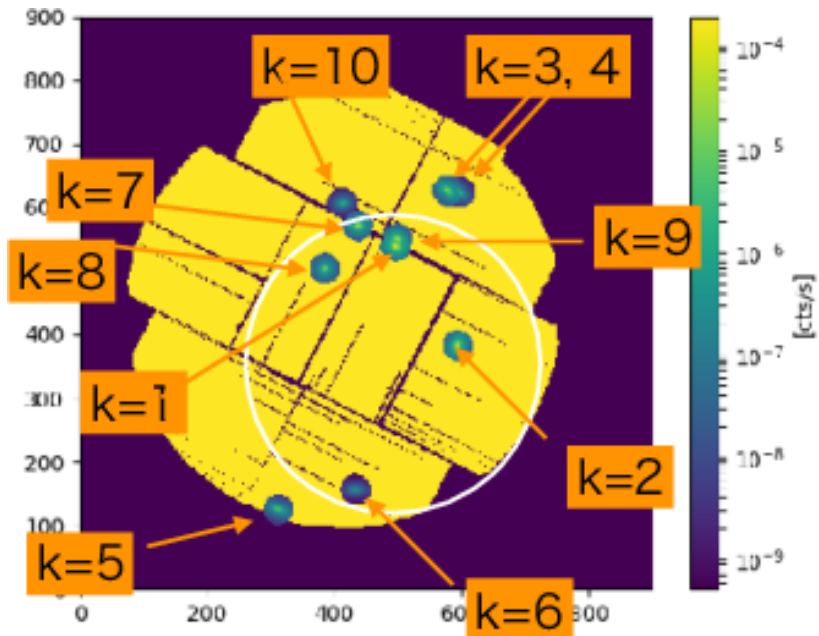
$$\delta_{\text{PS}} = \frac{\sum_j M(p_j, q_j)V(p_j, q_j)/A_{\text{inFOV}}}{z}. \quad (5.28)$$

We show  $\delta_{\text{stat}}$  and  $\delta_{\text{PS}}$  as functions of  $b$  in the 0.4-1.0 keV energy band in Figure 5.15. We calculated these values for one ObsID and scaled  $\delta_{\text{stat}}$  depending on exposure time for all ObsIDs:  $\delta_{\text{stat}}$  for the ObsID is plotted with circles connected with solid lines, while that expected for all data is plotted with broken lines. We find that  $\delta_{\text{stat}}$  rapidly increases and  $\delta_{\text{PS}}$  rapidly decreases with increasing  $b$  for  $b < 2$ , while the slopes are mild for  $b > 2$ , and that two quantities ( $\delta_{\text{PS}}$  of the one ObsID and  $\delta_{\text{stat}}$  for all ObsIDs) cross at  $b = 1.7$  and  $\delta_{\text{stat}}$  for all ObsID and  $\delta_{\text{PS}}$  is 4.5%. Therefore, at  $b = 1.7$  we can make the effect of spill over comparable to the statistical error, which is  $\sim 5\%$ . We consider 5% is a good number for the present analysis, thus we decided to adopt  $b = 1.7$ .

We created and applied a mask function ( $M(p_j, q_j)$ ) for each ObsID. In Figure 5.16, we show *XMM-Newton* real images after the mask was applied step by step for ObsID=0604960101. In Table 5.6, we show the detector area without the mask (i.e. including the *Chandra* point sources) and with the mask (i.e. excluding the *Chandra* point sources) for the MOS1 and the MOS2 for all ObsIDs. The detector area out of field view is also shown. We find that only about 10% of the detector area survives after masking.



(a)



(b)

Figure 5.13: Comparison between (a) simulation image and (b) actual *XMM-Newton* real image within *Chandra* and *XMM-Newton* overlapping region indicated inside a white circle. We show the simulation image including 10 bright sources in the CDF-S. Note that the vertical color scale bar shows the surface brightness only around these point sources. The yellow region is not related to the vertical color scale bar.

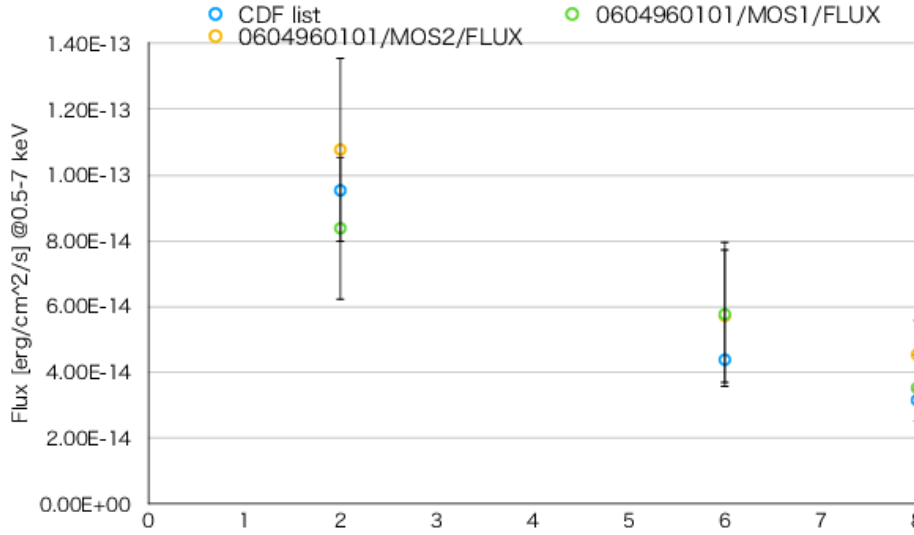


Figure 5.14: Comparison between observed fluxes and the CDF-S catalogue fluxes. Errors are  $1.6\sigma$  single parameter errors. The sources,  $k = 2, 6$  and  $8$  are employed, as they are isolated and inside the overlapping region between *XMM-Newton* and *Chandra*.

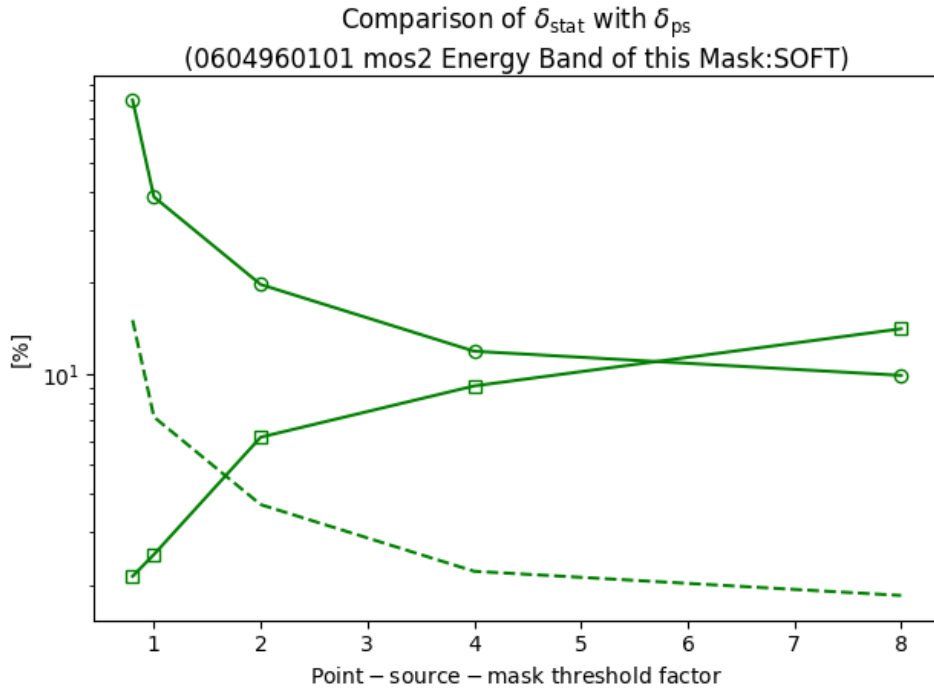


Figure 5.15: Expected statistical error ( $\delta_{stat}$ ) and spill over of point sources in the background spectrum ( $\delta_{ps}$ ) as a function of factor  $b$  which determines the threshold of the point sources mask (see Equation 5.24). We calculated  $\delta_{stat}$  and  $\delta_{ps}$  for an ObsID, 0604960101, and we scaled  $\delta_{stat}$  for all ObsIDs by  $\sqrt{T_1/T_{all}} = 0.035$ , where  $T_1$  and  $T_{all}$  are the exposure times of the ObsID and all ObsIDs, respectively.

Table 5.6: Summary of the detector areas before and after applying the point sources mask for the MOS1 and the MOS2.

| Detector area arcmin <sup>2</sup> |                    |       |           |       |                     |       |
|-----------------------------------|--------------------|-------|-----------|-------|---------------------|-------|
| ObsID                             | $A_{\text{inFOV}}$ |       |           |       | $A_{\text{outFOV}}$ |       |
|                                   | without mask       |       | with mask |       | -                   |       |
|                                   | MOS1               | MOS2  | MOS1      | MOS2  | MOS1                | MOS2  |
| 0108060401                        | 268.8              | 267.9 | 27.29     | 28.95 | 155.6               | 162.2 |
| 0108060501                        | 268.4              | 266.9 | 27.35     | 30.21 | 155.4               | 162.7 |
| 0108060601                        | 250.8              | 266.8 | 15.22     | 31.24 | 121.5               | 162.3 |
| 0108060701                        | 250.3              | 266.3 | 14.86     | 29.68 | 121.6               | 162.0 |
| 0108061801                        | 247.3              | 267.5 | 14.24     | 29.41 | 121.6               | 162.5 |
| 0108061901                        | 247.1              | 267.4 | 20.24     | 30.16 | 121.6               | 162.1 |
| 0108062101                        | 247.2              | 267.2 | 12.52     | 29.57 | 121.2               | 162.6 |
| 0108062301                        | 245.8              | 266.1 | 13.86     | 29.74 | 124.5               | 161.9 |
| 0555780101                        | 259.7              | 251.7 | 24.85     | 24.81 | 106.7               | 128.8 |
| 0555780201                        | 255.4              | 256.1 | 25.18     | 26.03 | 106.7               | 128.9 |
| 0555780301                        | 251.1              | 254.1 | 25.16     | 26.08 | 111.3               | 128.8 |
| 0555780401                        | 260.0              | 249.0 | 24.80     | 25.59 | 106.7               | 128.8 |
| 0555780501                        | 231.7              | 247.9 | 19.76     | 29.67 | 106.1               | 128.4 |
| 0555780601                        | 238.3              | 245.3 | 21.71     | 29.15 | 108.1               | 128.5 |
| 0555780701                        | 247.5              | 267.6 | 22.84     | 29.99 | 106.5               | 162.3 |
| 0555780801                        | 227.0              | 267.9 | 20.66     | 31.53 | 108.2               | 162.5 |
| 0555780901                        | 226.8              | 249.8 | 19.53     | 29.84 | 74.9                | 128.4 |
| 0555781001                        | 237.3              | 266.4 | 21.02     | 30.63 | 75.6                | 161.9 |
| 0555782301                        | 237.3              | 266.6 | 21.02     | 30.53 | 75.5                | 162.4 |
| 0604960101                        | 255.3              | 266.8 | 25.34     | 25.34 | 106.7               | 162.5 |
| 0604960201                        | 255.9              | 254.1 | 25.66     | 26.12 | 75.5                | 128.8 |
| 0604960301                        | 243.8              | 264.0 | 24.71     | 27.51 | 73.7                | 162.3 |
| 0604960401                        | 249.1              | 267.5 | 26.19     | 28.76 | 106.3               | 161.8 |
| 0604960501                        | 229.3              | 267.5 | 20.28     | 30.57 | 108.9               | 161.9 |
| 0604960601                        | 239.5              | 244.4 | 22.08     | 28.78 | 106.7               | 128.8 |
| 0604960701                        | 232.7              | 249.5 | 20.73     | 29.48 | 106.9               | 128.2 |
| 0604960801                        | 235.0              | 267.9 | 21.79     | 30.40 | 75.6                | 162.1 |
| 0604960901                        | 231.2              | 267.6 | 20.56     | 30.82 | 73.9                | 162.2 |
| 0604961001                        | 223.0              | 267.4 | 19.94     | 30.72 | 73.9                | 162.2 |
| 0604961101                        | 223.8              | 266.1 | 18.57     | 31.46 | 106.7               | 162.0 |
| 0604961201                        | 219.7              | 266.9 | 20.44     | 32.36 | 108.6               | 161.9 |
| 0604961301                        | 230.9              | 268.3 | 20.79     | 30.96 | 109.3               | 163.2 |
| 0604961801                        | 230.7              | 267.9 | 21.44     | 30.80 | 73.6                | 162.6 |

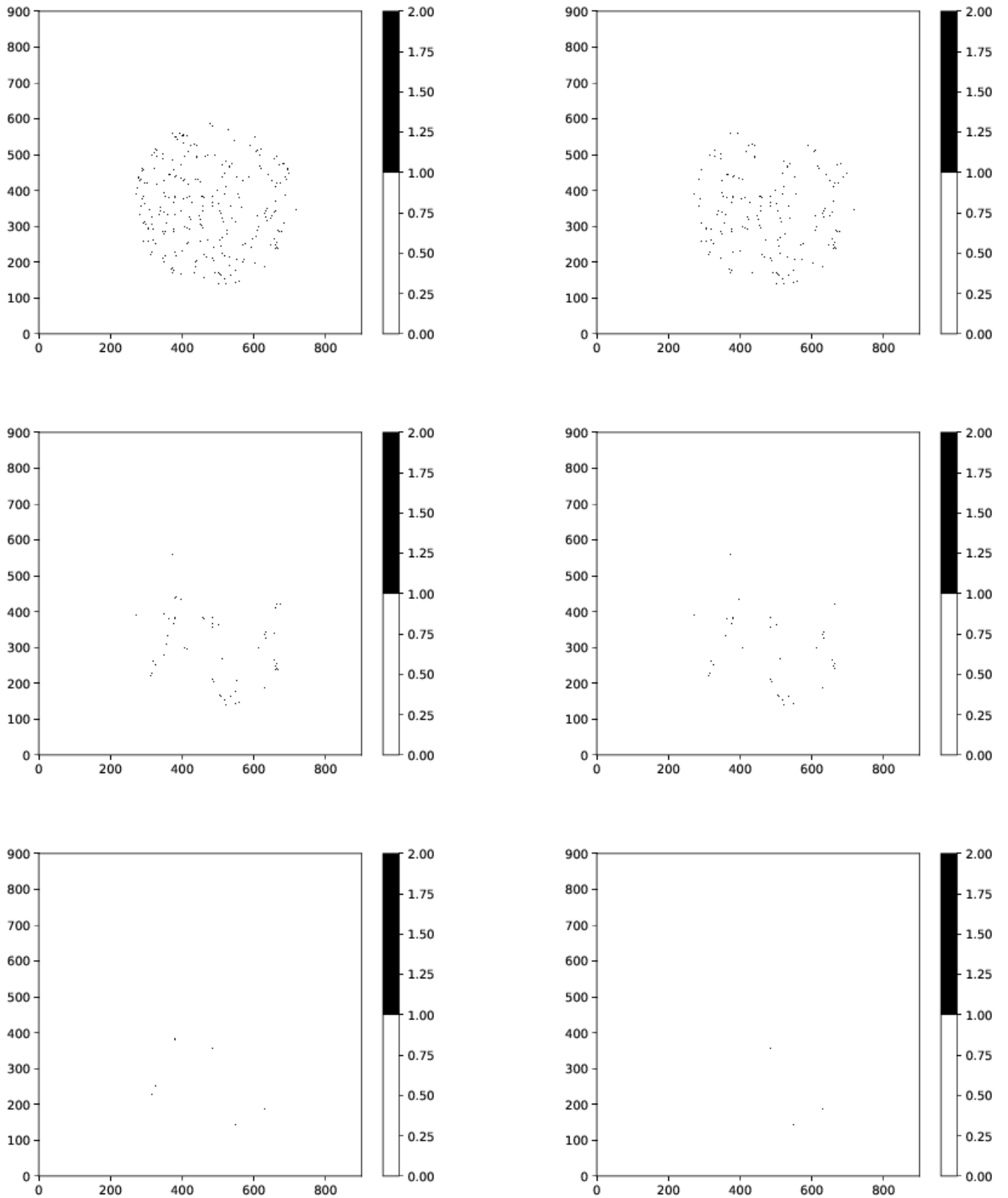


Figure 5.16: *XMM-Newton* real images after the mask was applied step by step for ObsID=0604960101. The color bar is in unit of cts/s. From top-left, (top-left), (top-right), (middle-left), (middle-right), (bottom-left), (bottom-right), we set  $b$  to 8, 4, 2, 1.7, 1, 0.8, respectively.

## Chapter 6

# Analysis 2: Estimation of non X-ray background and Response functions

In order to analyze the spectrum, we need the background spectrum, the telescope+detector effective area and the pulse-height redistribution matrix. These three must be estimated for each extracted spectrum. Among the three, estimation of the effective area requires special care for spatially extended emission. We need to take into account two effects: vignetting and point spread function of the telescope. We assume a flat surface brightness as the model emission and estimate the grasp (effective area multiplied with the solid angle of the observation) using the vignetting function and position-dependent point spread function of the telescope.

### 6.1 Spectral fits

An X-ray photon absorbed in the CCD X-ray detector of *XMM-Newton* produces electron charges and they are collected in CCD pixels. The charges may spread over multiple pixels of the CCD as shown in Figure 4.11. The pulse-height-analyzer value (PHA value) of the event is given by the sum of each pulse height value of the pixels. Then the PHA value is converted to a Pulse Invariant (PI) value,  $p$ , according to the calibration database. In PI, the non-linearity of the detector response is corrected for in the first order, and the PI value is approximately proportional to the X-ray energy. Thus, the abscissa of the PI spectrum plot is often labeled as "Energy" or "Channel energy". Suppose the energy spectrum coming from the sky is described with a model function,  $M(E)$ , where  $E$  is the X-ray energy. For spatially diffuse emission, we adopt photons  $\text{s}^{-1} \text{cm}^{-2} \text{keV}^{-1} \text{str}^{-1}$  as the unit of  $M(E)$ . Then the expected value of the observed PI spectrum,  $f(p)$  will be,

$$f(p) = \int dER(p, E)S(E)M(E) + b(p), \quad (6.1)$$

where  $S(E)$ ,  $R(p, E)$ , and  $b(p)$  are, respectively, the effective area of the X-ray telescope + the detector, the pulse height redistribution matrix, and the background PI spectrum. The unit of  $f(p)$  is counts  $\text{s}^{-1} \text{keV}^{-1}$ , and  $R(p, E)$  is dimensionless. Thus the unit of  $S(E)$  is  $\text{cm}^2 \text{str}$ . For spatially diffuse emission,  $S(E)$  is not a simple effective area but is equivalent to so-called grasp. Please note that for point sources, the units will be different and photons  $\text{s}^{-1} \text{cm}^{-2} \text{keV}^{-1}$  for  $M(E)$  and  $\text{cm}^2$  for  $S(E)$ .

The X-ray counts are accumulated in a PI bin. The number of counts is a statistical function obeying a Poisson distribution:

$$P(\bar{C}(p_i), C(p_i)) = \exp\{-\bar{C}(p_i)\} \frac{\bar{C}(p_i)^{C(p_i)}}{C(p_i)!}, \quad (6.2)$$

where  $C(p_i)$  is the observed number of counts in the  $i$ -th PI bin, while  $\bar{C}(p_i)$  is its expectation value:

$$\bar{C}(p_i) = \int_{p_{i,b}}^{p_{i,e}} dp f(p)T, \quad (6.3)$$

and  $T$  is the observation integration time and integration over  $p$  is made from  $p_{i,b}$  to  $p_{i,e}$ .

In a spectral model fit, the model function is described with a set of free parameters,  $\{m_j, j = 1 \dots N\}$ . The spectral fit will be performed by maximizing the likelihood defined with,

$$\mathcal{L} = \prod_i P(\bar{C}(p_i), C(p_i)). \quad (6.4)$$

In the actual procedure, we minimize,

$$\mathcal{C} = -2 \ln \mathcal{L}. \quad (6.5)$$

The statistics which  $\mathcal{C}$  follows are often called C-statistics in X-ray astronomy. When the number of counts in each spectral bin is large, e.g.  $C(p_i) > 100$ , the Poisson distribution approaches to the Gaussian distribution and  $\mathcal{C}$  approaches to  $\chi^2$  statistics, respectively:

$$\chi^2 = \sum_i \frac{1}{\sqrt{2\pi}\sigma} \exp \left\{ -\frac{(C(p_i) - \bar{C}(p_i))^2}{2\sigma^2} \right\}, \quad (6.6)$$

$$\sigma = \sqrt{C(p_i)}. \quad (6.7)$$

For all the spectra we treat in this thesis,  $C(p_i) > 100$  is satisfied, thus we use  $\chi^2$  statistics throughout this thesis.

The background ( $B(p_i)$ ) will be estimated from the observation data, which have statistical errors independent of  $C(p_i)$ . In  $\chi^2$  fitting, we take them into account in the spectral fits. We conduct a spectral fit to a background subtracted spectrum:

$$C'(p_i) = C(p_i) - B(p_i), \quad (6.8)$$

with a model function

$$\bar{C}'(p_i) = \int_{p_{i,b}}^{p_{i,e}} dp \int dE R(p, E) S(E) M(E) T, \quad (6.9)$$

by minimizing

$$\chi^2 = \sum_i \frac{1}{\sqrt{2\pi}\sigma} \exp \left\{ -\frac{(C'(p_i) - \bar{C}'(p_i))^2}{2\sigma^2} \right\}, \quad (6.10)$$

where  $\sigma$  is estimated as

$$\sigma = \sqrt{C(p_i) + \sigma_B^2}, \quad (6.11)$$

with  $\sigma_B$  as corresponding to 1- $\sigma$  error of the background spectrum.

The statistical errors of the model parameters are estimated by utilizing the difference between the  $\chi^2$  value for the true parameter values and that for the best-fit parameters,

$$\Delta\chi^2 = \chi_{\text{true}}^2 - \chi_{\text{min}}^2, \quad (6.12)$$

obeys a  $\chi^2$  statistics of  $N$  degrees of freedom. Note that the same is true for C-statistics,

$$\Delta\mathcal{C} = \mathcal{C}_{\text{true}} - \mathcal{C}_{\text{min}}, \quad (6.13)$$

although  $\mathcal{C}$  does not obey  $\chi^2$  statistics.

In the rest of this chapter, we will show how we derive the background  $B(p_i)$ , effective are  $S(E)$ , and  $R(p_i, E)$ , then we will apply the model fit to the spectra during the three steps of the soft proton removal process.

## 6.2 Non X-ray background

Present understandings of the *XMM-Newton* non X-ray background (NXB) were reviewed in Section 4.2. Both of the MOS cameras are equipped with a filter wheel system, which has a filter called a closed position. The filter is 1.05 mm thick Al plate, and the transmission is  $< 1\%$  for X-rays below 10 keV. Among the seven CCD Chips of the MOS camera, six CCD Chips have a pixel region which is blocked from X-rays from the X-ray telescope (out-of-field-of-view pixels). The non X-ray background has been studied using filter-wheel-closed (FWC) data and out-of-field-of-view (outFOV) pixels.

The NXB intensity has time variations as shown in Figure 4.16 ( Gastaldello et al. (2017)). Thus Kuntz & Snowden (2008) proposed to estimate the NXB from the spectra of outFOV pixels during the same observation time. Suppose that  $C_{\text{inFOV}}(E)$ ,  $A_{\text{inFOV}}$ ,  $T_{\text{inFOV}}$  are the number of counts per energy integrated over the pixel area inside the field of view (inFOV), the pixel area inside the field of view and an exposure time, and that  $C_{\text{outFOV}}(E)$ ,  $A_{\text{outFOV}}$ ,  $T_{\text{outFOV}}$  are the number of counts per energy integrated over the pixel area outside the field of view (outFOV), the pixel area outside the field of view and an exposure time. Here we allowed that  $T_{\text{inFOV}}$  and  $T_{\text{outFOV}}$  can be different because of some observation conditions. Kuntz & Snowden (2008) proposed to estimate the NXB counts ( $C_{\text{NXB}}$ ) for  $C_{\text{inFOV}}$  by scaling  $C_{\text{outFOV}}(E)$  as,

$$C_{\text{NXB}}(E) = C_{\text{outFOV}}(E) \frac{A_{\text{inFOV}} T_{\text{inFOV}}}{A_{\text{outFOV}} T_{\text{outFOV}}}, \quad (6.14)$$

giving a good approximation for the NXB expectation at and near the energies of instrumental emission lines of Si (1.49 keV), Al (1.74 keV), Au (2.12 keV, 9.71 keV and 11.4 keV), Cr (5.4 keV), and Fe (6.4 keV).

However as seen in Figure 4.13, emission lines are highly non-uniform spatially, the scaling with a pixel area and exposure time can not reproduce the line intensities.

Also, Salvetti et al. (2017) reported a small but statistically significant difference in count rate between the inFOV pixels and the outFOV pixels when the filter wheel is in the closed position. As all the events detected inFOV when the filter wheel is in the closed position are supposed to be due to the NXB, the difference in the count rate should exist between inFOV in the real observation (filter wheel is in the open position) and outFOV in real observation.

Furthermore, we should consider the energy dependence of the count-rate ratios between inFOV and outFOV. Therefore, we will improve the analysis method to estimate the NXB spectrum by taking the three points into account.

### 6.2.1 Treatment of instrumental lines

As there is no good way to estimate the NXB by these instrumental emission lines of Si (1.49 keV), Al (1.74 keV), Au (2.12 keV, 9.71 keV and 11.4 keV), Cr (5.4 keV), and Fe (6.4 keV). Presently, we simply excluded the energy ranges at and near instrumental emission lines from the spectral analysis.

### 6.2.2 NXB estimation considering count rate between inFOV and outFOV, and energy dependence of count-rate ratio between inFOV and outFOV

Considering the difference in the counting rate between inFOV and outFOV, we estimate the NXB spectrum. We introduce a factor  $r$  to correct for this difference and propose to determine the value using in the 10-11 keV energy range. The throughput of the X-ray telescope is virtually zero above 10 keV, thus the spectrum in this energy range represents the NXB even when the filter wheel is open. The *XMM-Newton* spectrum covers up to 12 keV, however, we did not use it above 11 keV to avoid instrumental Au lines which exist in the 9.5-10 keV and the 11-12 keV energy bands.

We thus adopt the following spectrum as the NXB;

$$C_{\text{NXB}}(E) = r C_{\text{outFOV}}(E) \frac{A_{\text{inFOV}} T_{\text{outFOV}}}{A_{\text{outFOV}} T_{\text{inFOV}}} \quad (6.15)$$

where

$$r = \frac{R_{\text{inFOV}}(10 - 11 \text{ keV})}{R_{\text{outFOV}}(10 - 11 \text{ keV})}. \quad (6.16)$$

These are equivalent to Equations (5.13) and (5.14). We compare estimated the NXB spectrum according to Equation 6.15 with the inFOV spectrum in the CDF-S *Chandra* overlapping region before resolved point sources removal in Figure 6.2 and that after resolved point sources removal in Figure 6.3, respectively.

Generally, all of the detected events outside the field of view are considered as the NXB. On the other hand, all of the detected events in the field of view when the filter wheel is closed can be considered as the NXB, because the filter wheel blocks the X-rays. A  $C_{\text{FWCinFOV}}(E)$  indicates all of the detected events inside the field of view when the filter wheel is closed. A  $C_{\text{FWCoutFOV}}(E)$  indicates all of the detected events outside the field of view when the filter wheel is closed (FWC). A ratio of the FWC count rate inside the field of view to the FWC count rate outside the field of view,  $b(E)$ , is defined as follows,

$$b(E) = \frac{C_{\text{FWCinFOV}}(E) / A_{\text{FWCinFOV}} / T_{\text{FWCinFOV}}}{C_{\text{FWCoutFOV}}(E) / A_{\text{FWCoutFOV}} / T_{\text{FWCoutFOV}}} = \frac{R_{\text{FWCinFOV}}(E)}{R_{\text{FWCoutFOV}}(E)}, \quad (6.17)$$

where  $T_{\text{FWCinFOV}}$  and  $T_{\text{FWCoutFOV}}$  are exposure times inside and outside the field of view,  $A_{\text{FWCinFOV}}$  and  $A_{\text{FWCoutFOV}}$  are the numbers of pixels inside and outside the field of view. We plot an energy dependence of  $b(E)$  as shown in the lower panel of Figure 6.1. Although we see  $b(E)$  does not seem to have any significant energy dependence below 1 keV, we use this ratio as the correction factor to translate the  $R_{\text{outFOV}}$  to the  $R_{\text{inFOV}}$ .

We correct  $C_{\text{outFOV}}(E)$  with using  $b(E)$ . As a result, we change  $C_{\text{outFOV}}$  to  $bC_{\text{outFOV}}$ . The counts of the corrected NXB ( $C'_{\text{NXB}}$ ) is expressed as follows,

$$C'_{\text{NXB}} = r' (bC_{\text{outFOV}}) \frac{A_{\text{inFOV}} T_{\text{inFOV}}}{A_{\text{outFOV}} T_{\text{outFOV}}}, \quad (6.18)$$

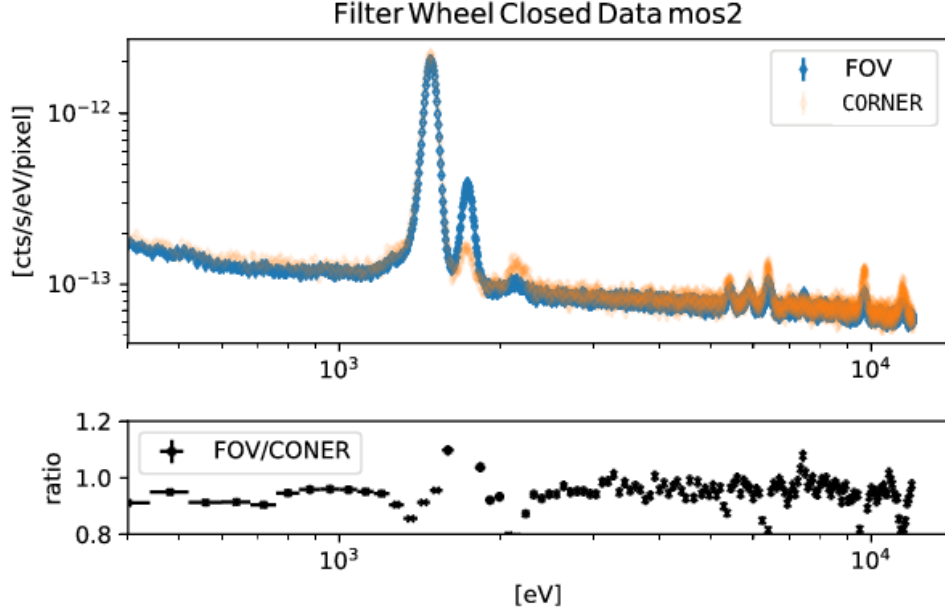


Figure 6.1: (upper): All of the detected events in the MOS2 when the filter wheel is closed. The extended source analysis team of *XMM-Newton* proved this data. Blue points are count rates inside the field of view ( $R_{\text{FWCinFOV}}$ ). Orange points are count rates outside the field of view ( $R_{\text{FWCoutFOV}}$ ). This data detected from 2001 to 2017. (lower): The total exposure is 1.9 Msec. Events detected in all chips are stacked. Black points are the ratio ( $b(E)$ ) of the count rate of inside to outside.

with

$$r' = \frac{R_{\text{inFOV}}(10 - 11 \text{ keV})}{R_{\text{outFOV}}(10 - 11 \text{ keV})}, \quad (6.19)$$

where  $R'_{\text{outFOV}}$  is equal to  $bC_{\text{FWCoutFOV}}(E)/A_{\text{FWCoutFOV}}/T_{\text{FWCoutFOV}}$ . We subtract the corrected the NXB ( $C'_{\text{NXB}}$ ) from the total detected events ( $C_{\text{inFOV}}$ ). We show the spectra of  $C_{\text{inFOV}}$ ,  $C_{\text{NXB}}$ , and  $C'_{\text{NXB}}$  in Figure 6.2 and Figure 6.3. The NXB of  $C_{\text{NXB}}$  and  $C'_{\text{NXB}}$  are roughly half of  $C_{\text{inFOV}}$  below 200 ch (1 keV).  $\sqrt{C_{\text{inFOV}}}$  indicates a Poisson statistical error of the detected events inside the field of view. The Poisson statistical error of the NXB ( $\delta C'_{\text{NXB}}$ ) are as follows,

$$\delta C'_{\text{NXB}} = \sqrt{(b\sqrt{C_{\text{outFOV}}})^2 + (\delta b C_{\text{outFOV}})^2 T_{\text{inFOV}} A_{\text{inFOV}} / T_{\text{outFOV}} A_{\text{outFOV}}}, \quad (6.20)$$

where  $\delta b$  is an error of  $b$ .

The correction factor,  $r'$ , was estimated by  $\chi^2$  fit to be  $1.043 \pm 0.009$  with resolved point sources and  $1.054 \pm 0.015$  without resolved point sources, respectively. The errors are  $1\sigma$  confidence limit. This does not contradict the previous study shown in Figure 4.18, because the blue shaded offset is  $(4 \pm 10)\%$ . We show  $C_{\text{inFOV}}$ ,  $C_{\text{NXB}}$   $C'_{\text{NXB}}$  in Figure 6.2 (c) and Figure 6.3 (c). The Au lines (9.71 keV and 11.4 keV) are corrected, which does not contradict the spatial distribution of the Au lines as shown in Figure 4.13.

In the low energy band  $< 2$  keV where fifty percents of events detected in the CDF-S overlapping region are the NXB we vary the value of  $r'$  within the  $2\sigma$  range, the spectral shape is not affected very much. On the other hand, systematic uncertainties in the NXB estimation can affect the spectral analysis results in the 2-5 keV band where roughly eighty percents of events detected in the CDF-S overlapping region are the NXB. We estimated the NXB systematic uncertainties in 0.4-5 keV due to the statistical error in the correction factor  $r'$ , varying  $r'$  within  $\pm 2\sigma$ . Practically, we replace  $r'$  with  $r' + n_b \sigma$  with  $n_b = \pm 2$ , to estimate the NXB systematic uncertainties.

### 6.3 Effective area

For a point source, the definition of the effective area,  $S(E)$  in Equations (6.1) and (6.9) are straightforward. For a point source,  $M(E)$  is the X-ray photon flux from the source at the entrance of the X-ray detector system. Thus

its typical unit will be photons  $\text{s}^{-1} \text{cm}^{-2}$ , and then the unit of  $S(E)$  is simply  $\text{cm}^2$ . In this case, the value of  $S(E)$  depends on the size of the detector image area from which X-ray events are retrieved.

For spatially extended emission, the story is more complicated. The model spectrum will be dependent on not only the X-ray energy  $E$ , but also the sky position, which we represent with a vector  $\mathbf{k}$ . Thus the model spectrum must be written as  $M(E, \mathbf{k})$ . As the observed spectrum,  $f(p)$ , is also a function of the detector position  $\mathbf{d} = \mathbf{d}(x, y)$ , we introduce  $f(p, \mathbf{d})$  instead of  $f(p)$ . Then the Equation (6.9) will be modified to

$$f(p, \mathbf{d}) = \int dE \int d\Omega_{\mathbf{k}} R(p, E) P(\mathbf{d}, \mathbf{k}, E) \eta(E, \mathbf{d}) S(E, \mathbf{k}) M(E, \mathbf{k}) + b(p, \mathbf{d}), \quad (6.21)$$

where  $P(\mathbf{d}, \mathbf{k}, E)$ , is the point spread function of the telescope,  $\eta(E, \mathbf{d})$  represents the detector detection efficiency whose non-uniformity is taken into account,  $\Omega_{\mathbf{k}}$  is the solid angle. To obtain the expectation value of the observed PI spectrum,  $f(p)$ , we integrate events over the pixel area represented by  $x$  and  $y$  on the detector. Thus, we finally obtain,

$$f(p) = \int dE R(p, E) \iint dxdy \int d\Omega_{\mathbf{k}} P(\mathbf{d}, \mathbf{k}, E) \eta(E, \mathbf{d}) S(E, \mathbf{k}) M(E, \mathbf{k}) + b(p). \quad (6.22)$$

In most of the coupled analysis of spectrum and image, we assume that the energy spectrum and spatial structures are independent of each other. Thus we assume that we can express the emission model with multiples of image and energy parts,

$$M(E, \mathbf{k}) = M_1(E) M_2(\mathbf{k}). \quad (6.23)$$

Then, we have

$$f(p) = \int dE R(p, E) S'(E) M(E) + b(p), \quad (6.24)$$

where

$$S'(E) = \iint dxdy \int d\Omega_{\mathbf{k}} P(\mathbf{d}, \mathbf{k}, E) M_2(\mathbf{k}) \eta(E, \mathbf{d}) S(E, \mathbf{k}). \quad (6.25)$$

The telescope effective area is often divided into two factors; the effective area at bore sight,  $S_N(E)$ , and vignetting function  $V(E, \mathbf{k})$ . Then

$$S'(E) = S_N(E) \iint dxdy \int d\Omega_{\mathbf{k}} P(\mathbf{d}, \mathbf{k}, E) M_2(\mathbf{k}) \eta(E, \mathbf{d}) V(E, \mathbf{k}). \quad (6.26)$$

If the point spread function is infinitely sharp for all energies, the PSF can be represented with a delta function:

$$P(\mathbf{d}, \mathbf{k}, E) = \delta(\mathbf{d} - \mathbf{k}), \quad (6.27)$$

Then we have

$$S'(E) = \int d\Omega_{\mathbf{k}} M_2(\mathbf{k}) \eta(E, \mathbf{k}) S(E, \mathbf{k}). \quad (6.28)$$

Therefore  $S'(E)$  has a dimension of grasp, i.e. the effective area times solid angle.

In our analysis, we may not be able to assume the point spread function to be infinitely sharp. However, we assume that the emission is spatially uniform over the spatial scale of the *XMM-Newton* telescope field of view. Thus we assume  $M_2(\mathbf{k})$  constant, then we have

$$S'(E) = \iint dxdy \int d\Omega_{\mathbf{k}} P(\mathbf{d}, \mathbf{k}, E) B_1 S(E, \mathbf{k}) \eta(E, \mathbf{d}), \quad (6.29)$$

where  $B_1$  represents a unit surface brightness. We call this ( $S'(E)$ ) a flat-field arf. Since

$$\iint dxdy P(\mathbf{d}, \mathbf{k}, E) = 1, \quad (6.30)$$

the delta-function approximation, i.e. Equation (6.28) will hold well, if the perimeter area is much smaller than the total area of the X-ray image region. For a flat field, this will be simply,

$$S'(E) = B_1 \int d\Omega_{\mathbf{k}} S(E, \mathbf{k}) \eta(E, \mathbf{k}). \quad (6.31)$$

### 6.3.1 Calculating effective area using arfgen

We can calculate the effective area (arf),  $S'(E)$ , numerically using an arf generator tool, **arfgen**, provided in the standard *XMM-Newton* data analysis package. According to the *XMM-Newton* data analysis handbook, **arfgen** will calculate the effective area as

$$S'(E) = S_N(E) \sum_{d=1}^m \sum_{k=1}^n P_{d,k}(E) \eta_d(E) V_k(E) M_k \quad (6.32)$$

where  $\{M_k, k = 1..n\}$  are the source image where they are normalized as  $\sum_{k=1}^n M_k = 1$ ,  $S_N(E)$  is an overall normalization factor of the effective area as a function of energy  $E$  and  $P_{d,k}(E)$  is the point spread function of the telescope and the summation over  $d$  will be done from 1 to  $m$  for the detector area from which X-ray events are retrieved. Equation (6.32) is equivalent to Equation (6.26).

For the present analysis, the effective area  $S'(E)$  is calculated for each ObsID and for the MOS1 and the MOS2 separately.

**Box size of the point-source masked image** The accuracy of the numerical calculation depends on mesh numbers  $m$  and  $n$ , or equivalently the mesh size which is proportional to an inverse of  $m$  or  $n$ . With a finer mesh size, we can obtain better numerical accuracy. However, more computation time is required. Thus the mesh size must be determined with a balance between accuracy and computation time. **arfgen** adopts the same mesh which is common to the detector and the sky map.

The mesh size on the detector must be determined also taking into account the resolution of the image mask. The point-source masked image we employ for removing resolved point sources consists of a number of rectangular boxes. Actually, acceptance regions are described with the part of the rectangular boxes. The **arfgen** calculates Equation (6.32) box by box and then sum them up together. Since the **arfgen** requires the mesh size to be smaller than the box size by some factor to obtain reasonable computation accuracy, an appropriate box size must be selected. To make computation time small, we would like to adopt a large box size so that we can adopt a large mesh size. However, if the box size is too large, we cannot represent the complicated shapes of the point sources mask, and in order to avoid accepting unwanted regions, we may need to throw away a significant part of the detector area. Thus we first studied the maximum acceptable box size.

Table 6.1: Relation between box size and the accepted region of the point-source masked mask

| Re-binning factor                | 1   | 2  | 3   | 4  |
|----------------------------------|-----|----|-----|----|
| Mask box size (arc sec)          | 2.5 | 5  | 7.5 | 10 |
| Accepted region <sup>1</sup> (%) | 100 | 81 | 64  | 50 |

Value for re-binning factor =1 is defined as 100%.

In Table 6.1, we show the accepted region when we re-binned the boxes in the point-source masked image. The initial bin size of the point-source masked image is 2.5 arcsec. We find the acceptable area already drops to 81% by re-binning by a factor of two. We consider that 64% is small and not acceptable. In order to make computation time short, we selected 5 arcsec for the box size. The 5 arcsec accepted regions and the observed images in the 0.4-1 keV band are listed in Appendix A.3.

**Mesh size** Then we searched for the mesh size to use. It takes more than a day to calculate the effective area for the whole the point-source-removal mask for a mesh size smaller than 3.5 arcsec. Then it is impossible to test the convergence of the calculation as a function of the mesh size. Therefore, we picked up several boxes spreading over the mask as shown in Figure 6.4 for ObsID 0604960101. We checked the dependence of the calculation on the mesh size for each box separately. In what follows we describe the results for sample 0 as an example. Then we will compare the results of different samples.

In Figure 6.5 (a), we show the effective area calculated for the box 0 for different energies as a function of the mesh size. In Figure 6.5 (b), we show the derivatives of the curves. The absolute value of the derivative decreases as a function of the mesh size, but it has non-zero values even with the mesh size of 1 arcsec. The overall dependency on the mesh size is linear and it seems to converge to 0 when the mesh size approaches at 0. This suggests that the effective area ( $S'_{\text{arf}}(m)$ ) can be represented with a parabolic function ( $S'_{\text{parabolic}}(m)$ ) of the mesh size ( $m$ ). We thus fitted the relations with parabolic functions,

$$S'_{\text{parabolic}}(m) = am^2 + S'_0, \quad (6.33)$$

where  $a(< 0)$  and  $S'_0$  are free parameters. The best-fit curves are shown in Figure 6.6 (a).  $S'_0$  is an effective area when the mesh size is infinitely small. Then in the lower panel, we plotted  $(S'_0 - S'_{\text{arf}}(m))/S'_{\text{arf}}(m)$  as functions of energy for different values of  $m$ . We may calculate  $S'_{\text{arf}}(m)$  and then multiply it by  $S'_0/S'_{\text{arf}}(m)$  to obtain a value for the lower mesh-size limit. We would like to keep the correction factor itself small in order to make the systematic error introduced by the correction small. Since the calculation for whole the unmasked image is estimated to take a few days for a mesh size of the 3.75 arcsec, we would like to use it. Since we will use only the energy range below 5 keV in the fit, the correction factor can be kept  $< 4\%$ . We consider this is a good number.

Then we need to check if the correction factor  $(S'_0 - S'_{\text{arf}}(m))/S'_{\text{arf}}(m)$  satisfies  $< 4\%$  for the other boxes. In Figure 6.7 (a), we show the  $(S'_0 - S'_{\text{arf}}(m))/S'_{\text{arf}}(m)$  curve for the box 9. Essentially the plot is similar to that of the box 0. In Figure 6.7 (b), we show  $S'_0/S'_{\text{arf}}$  for  $m = 3.75$  arc sec as a function of energy for different the other boxes. We averaged these curves and fitted it with a model function,

$$S'_0/S'_{\text{arf}}(3.75 \text{ arcsec}) = (E/c_1)^{c_2}, \quad (6.34)$$

in the energy range 2.3-5 keV, together with the best fit curve. In the energy range below 5 keV, the deviation of all the data points from the best fit curve in Figure 6.7 (b) is at the most 1%. In the energy region below 2.3 keV, the deviation becomes much smaller. Thus the systematic error in  $S'_0$  is estimated to be smaller than 1% if we correct the effective area ( $S'_{\text{arf}}$ ) calculated with  $m = 3.75$  arc sec with the best fit model. Thus we decided to employ this method to calculate the effective area ( $S'_{\text{arf}}$ ). To calculate the effective areas of all ObsIDs for the MOS1 and the MOS2, it took more than a month.

### 6.3.2 Comparison of effective area between without and with Delta-Function approximation of the PSF

Effective area can be easily calculated if we assume a delta function for the telescope the PSF (see Equation 6.28). This can be done with the tool **arfgen**. In Figure 6.8, we compare the two effective areas. From Figure 6.8, we find the effective area with delta-function approximation the PSF is larger. The average ratio is about 1.04, but it is larger for higher energies. This is consistent with the fact that the real the PSF is more extended in higher energies. From this comparison, we can confirm that the systematic error of the effective area is smaller than  $\sim 5\%$ .

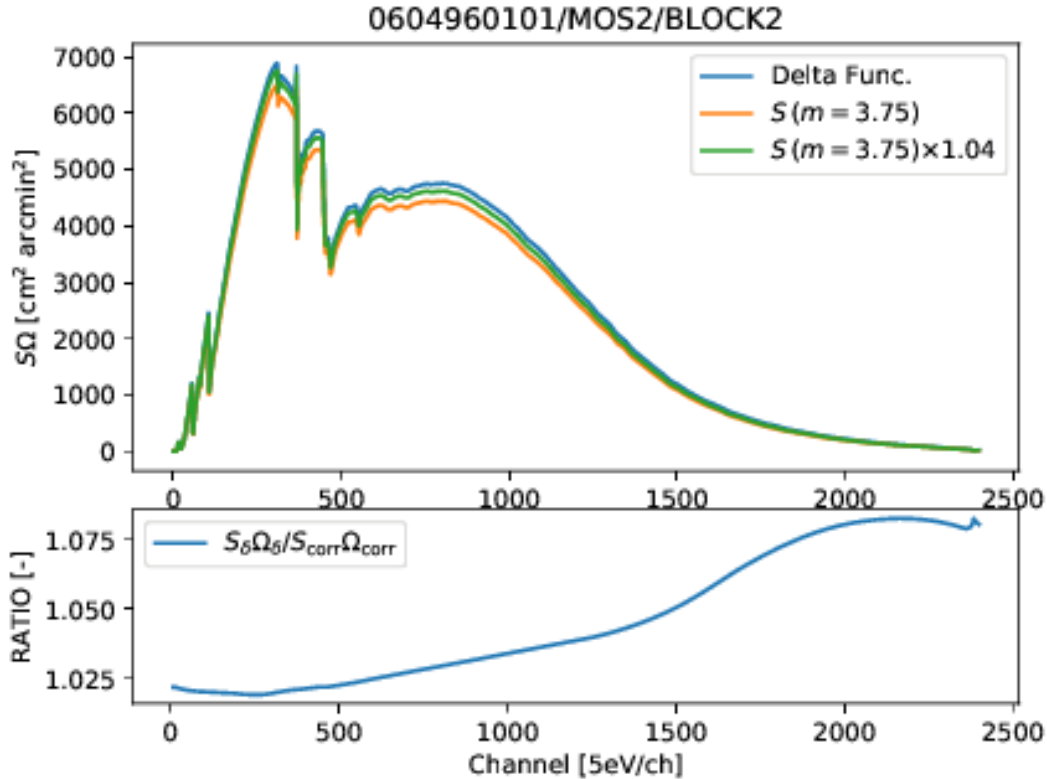


Figure 6.8: Comparison of calculated effective area between without and with Delta-Function approximation of the PSF as a function of Channel (5eV/ch).

## 6.4 Pulse height redistribution matrix

The pulse height redistribution matrix of the EPIC-MOS is dependent on pixels we used to extract spectra. The tool `rmfgen` will calculate the average matrix over the pixel region used to extract the spectra, using the spatial dependence data stored in the calibration database. We can set weight on each pixel when we calculate the average. We set all weight equivalently 1.0. The bin size of the PHA spectrum was set to be 5 eV/ch equivalent. Figure 6.9 shows one column of the pulse height redistribution matrix which is the response of the MOS2 for monochromatic X-rays of 0.56 keV. The energy resolution at this energy is 125 eV FWHM.

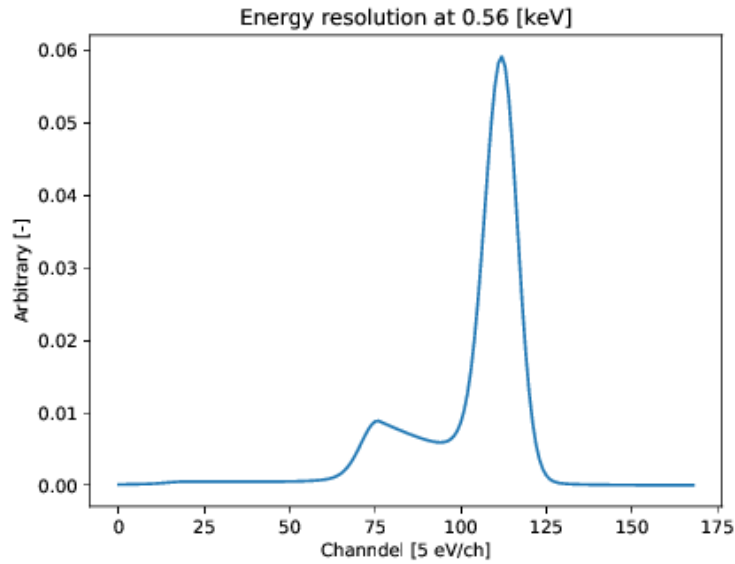


Figure 6.9: One column of the pulse height redistribution matrix, which shows the PHA response to the MOS2 for monochromatic X-rays of 0.56 keV. This is calculated for ObsID 0555780101. The input X-ray energy corresponds to the OVII line. There is a significant low energy tail which is a feature of the *XMM-Newton* MOS detectors. The FWHM is 25 ch. It is equivalent corresponding to 125 eV.

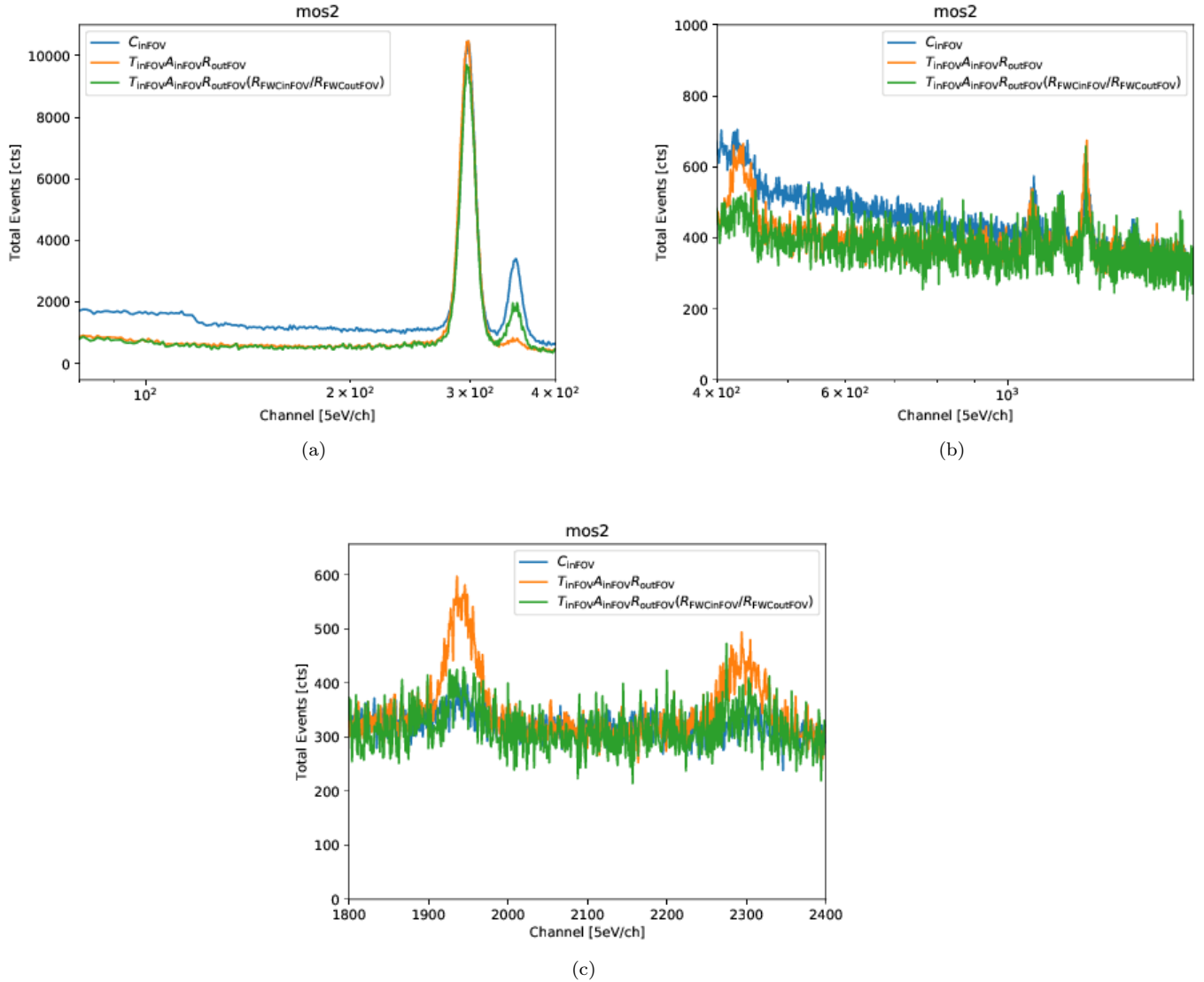


Figure 6.2: In field of view spectrum in the CDF-S *Chandra* overlapping region with resolved point sources ( $C_{\text{inFOV}}$ ) (blue), estimated the NXB spectrum ( $C_{\text{NXB}}$ ) (orange) and corrected the NXB spectrum ( $C'_{\text{NXB}}$ ) (green) for all ObsIDs from 0555780101 to 0604961801. The panel (a) and (b) show the spectra for the 0.4-2 keV energy range and for the 2-9 keV energy range of *XMM-Newton*, respectively, while the panel (c) shows a close-up view from 9 to 12 keV. The abscissa is linearly plotted with the channel number where one channel corresponds to 5 eV. The NXB correction factor  $r'$  is determined by using the spectrum in 10-11 keV (ch 2000 to 2200). Note that strong instrumental lines in ch 280 (Al), ch 340 (Si) and ch 420 (Au) are very different between orange and blue spectra. The energy ranges at and near the instrumental emission lines must be excluded from the spectral analysis.

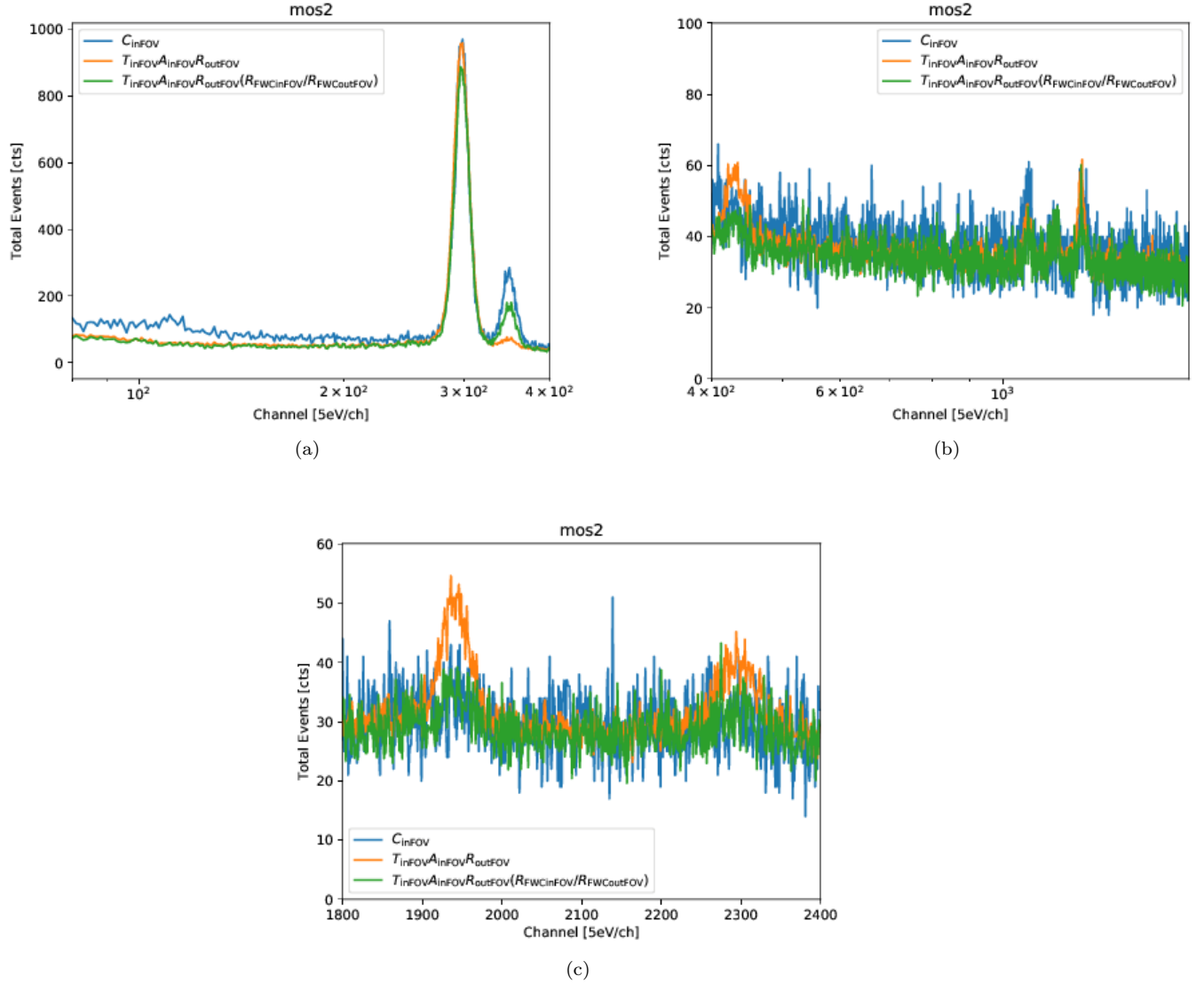


Figure 6.3: In field of view spectrum in the CDF-S *Chandra* overlapping region without resolved point sources ( $C_{\text{inFOV}}$ ) (blue), estimated the NXB spectrum ( $C_{\text{NXB}}$ ) (orange) and corrected the NXB spectrum ( $C'_{\text{NXB}}$ ) (green) for all ObsIDs from 0555780101 to 0604961801. The panel (a) and (b) show the spectra for the 0.4-2 keV energy range and for the 2-9 keV energy range of *XMM-Newton*, respectively, while the panel (c) shows a close-up view from 9 to 12 keV. The abscissa is linearly plotted with the channel number where one channel corresponds to 5 eV. The NXB correction factor  $r'$  is determined by using the spectrum in 10-11 keV (ch 2000 to 2200). Note that strong instrumental lines in ch 280 (Al), ch 340 (Si) and ch 420 (Au) are very different between orange and blue spectra. The energy ranges at and near the instrumental emission lines must be excluded from the spectral analysis.

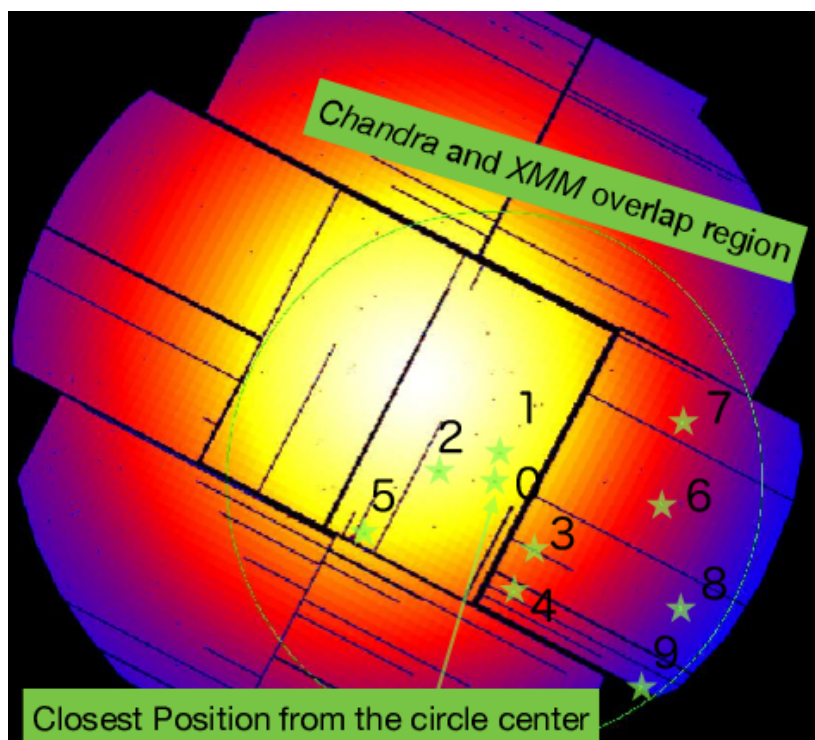
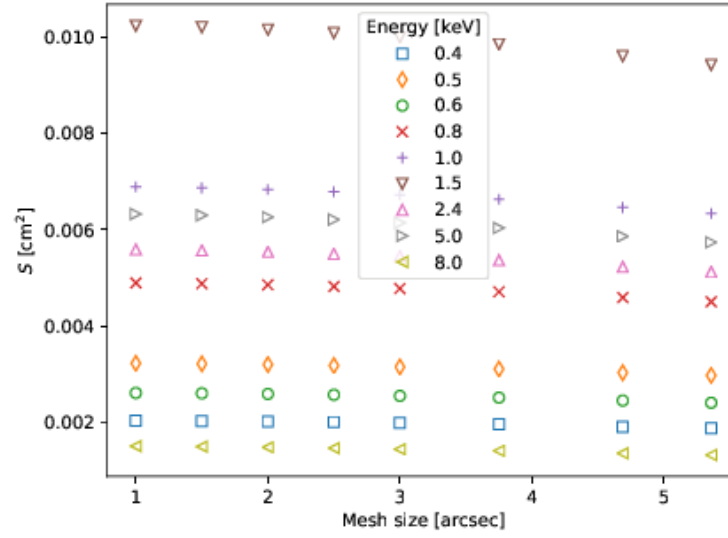
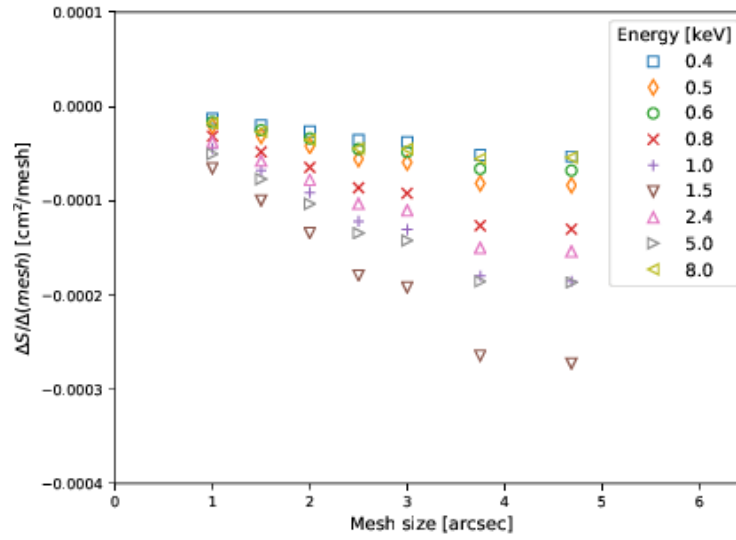


Figure 6.4: The box samples used to determine the mesh size and determination method.

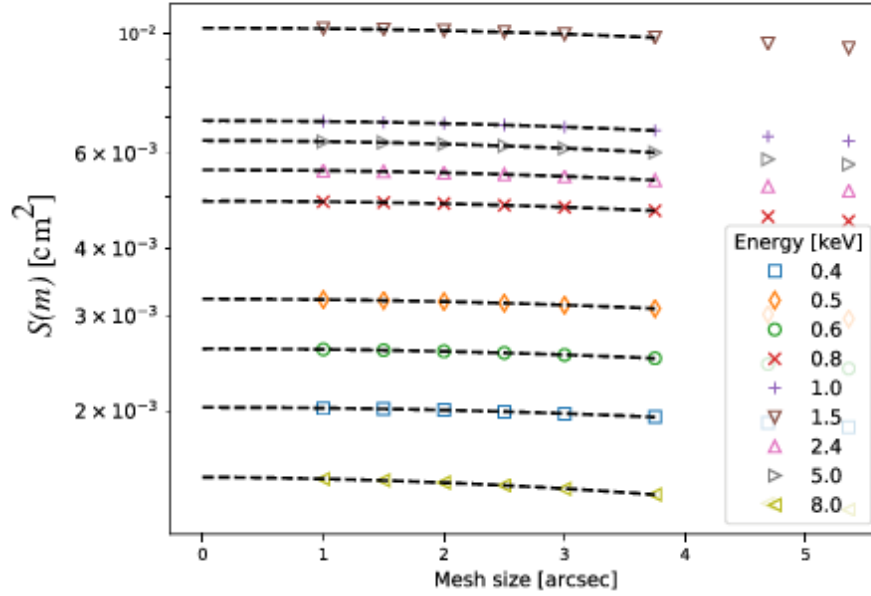


(a)

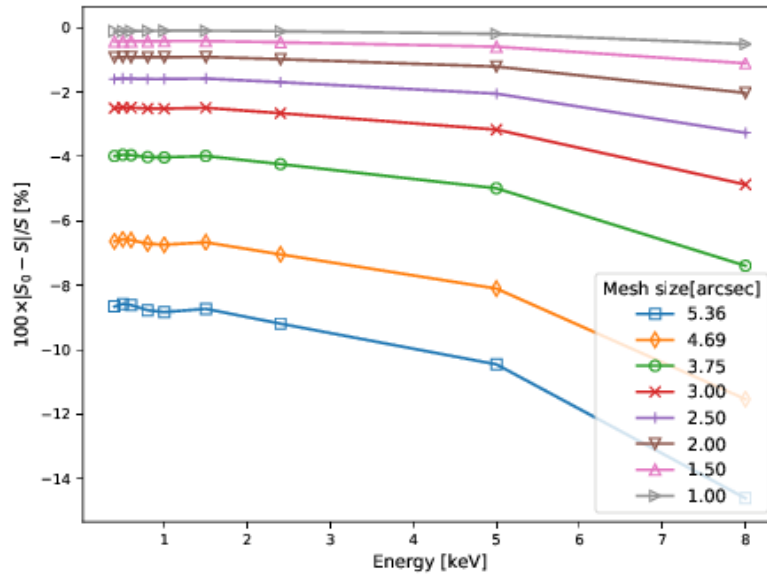


(b)

Figure 6.5: Effective area calculated with **arfgen** for box 0 shown in Figure 6.4 plotted as a function of mesh sizes for different energies (a). Derivative of the effective area as a function of mesh size (b).

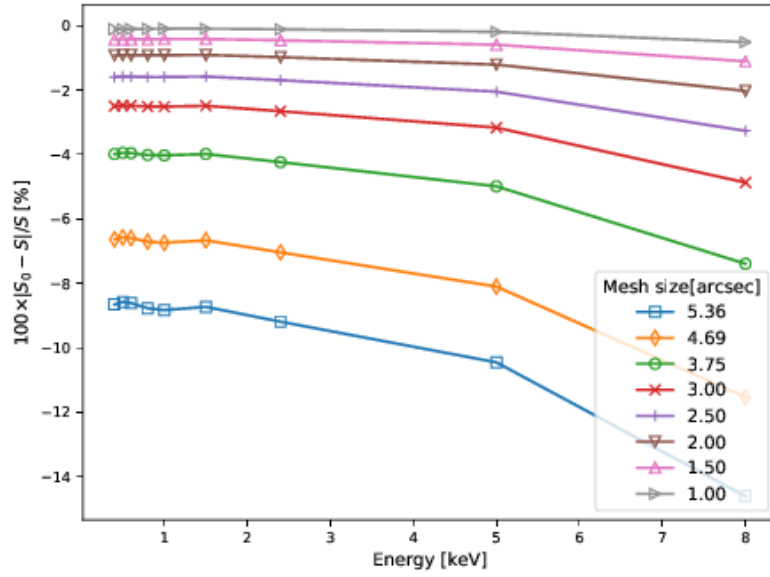


(a)

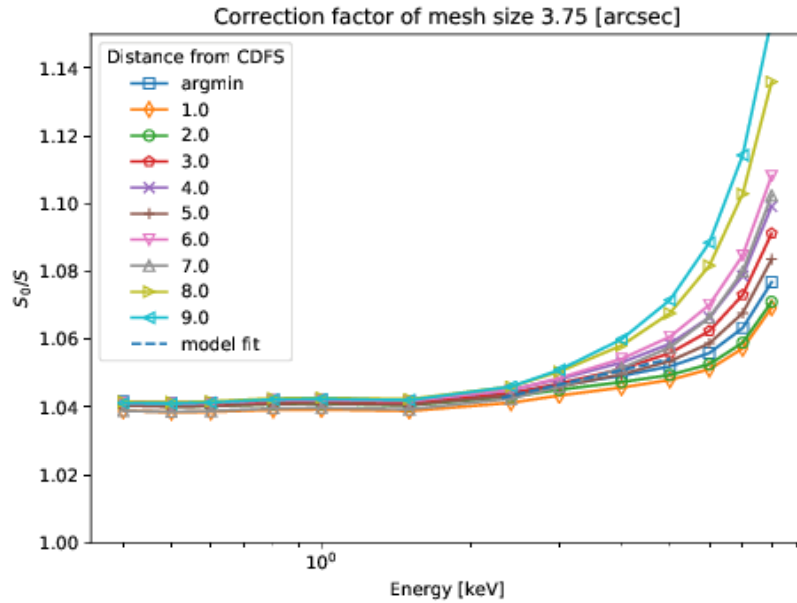


(b)

Figure 6.6: (a): Same as Figure 6.5 (a) but with best-fit parabolic model functions. (b): Relative difference in the effective  $(S'_0 - S'_{\text{arr}}(m))/S'_{\text{arr}}(m)$  for the box 0 shown in Figure 6.4 as a function of  $E$ , where  $S'_{\text{arr}}$  is the effective area calculated by **arfgen**, the best fit  $S'_{\text{palabora}}$  and  $S'_0$  are defined in Equation 6.33, for various mesh sizes  $m$ .



(a)



(b)

Figure 6.7: (a): Relative difference in the effective  $(S'_0 - S'_{\text{arf}}(m))/S'_{\text{arf}}(m)$  for the box 9 shown in Figure 6.4 as a function of  $E$ , where  $S'_{\text{arf}}$  is the effective area calculated by **arfgen**, the best fit  $S'_{\text{palabora}}$  and  $S'_0$  are defined in Equation 6.33. (b): The ratio of  $S'_0/S'_{\text{arf}}(m)$  as a function of  $E$ , where  $S'_{\text{arf}}$  is the effective area calculated by **arfgen**,  $S'_{\text{palabora}}$  and  $S'_0$  are defined in Equation 6.33 for various mesh sizes  $m$ .

## Chapter 7

# Surface brightnesses in two energy bands and of O lines and other remaining emission

In this chapter, we will derive the surface brightnesses of the X-ray background in two energy bands, 0.4-1 keV (soft band) and 2-8 keV (hard band) for two cases with and without *Chandra* point sources separately. We will also try to divide the 0.4-1 keV surface brightness into two components, the OVII and the OVIII emission lines and the rest. For these purposes, we utilize spectral fits. We thus use the X-ray background spectra with and without *Chandra* point sources, the detector response functions, and the non X-ray background spectra which we derived in the previous two chapters. All of these were derived for each ObsID and the MOS1 and the MOS2 separately. However, in the spectral fits, we will add spectra of different ObsIDs together. From Equation 6.9, the model PI spectrum of the  $j$ -th ObsID will be written as,

$$\bar{C}'_j(p_i) = \int_{p_{i,b}}^{p_{i,e}} dp \int dE R_j(p, E) S_j(E) M(E) T_j, \quad (7.1)$$

where we added the suffix  $j$  to a factor dependent on ObsID,  $R$  and  $S$  are the detector response and the telescope effective area, respectively, as explained in Section 6.9,  $M(E)$  is a spectrum model of X-rays coming from the sky. The  $M(E)$  is explained in Subsection 7.1.1 and Section 7.2. Then, the summed spectrum will be

$$\bar{C}'(p_i) = \int_{p_{i,b}}^{p_{i,e}} dp \int dE \sum_j R_j(p, E) S_j(E) T_j M(E). \quad (7.2)$$

The non X-ray background spectra for different ObsIDs are also added together. As we discussed in Section B, we will use only the MOS2 data.

### 7.1 X-ray background spectrum with *Chandra* resolved point sources

We first analyze the X-ray background spectrum with *Chandra* resolved point sources. In next Section 7.2, we analyze the X-ray background spectrum without *Chandra* resolved point sources. We show the X-ray background spectrum with *Chandra* resolved point sources which is obtained by subtracting the corrected the NXB spectrum (green) from the total events spectrum (blue) shown in Figure 6.2.

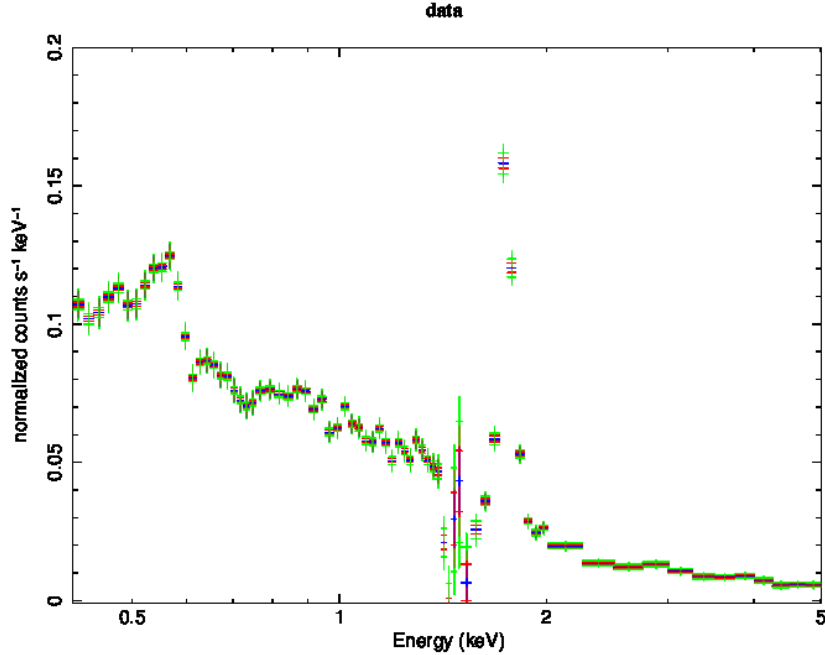


Figure 7.1: NXB-subtracted MOS2 spectra of the CDF-S overlapping region with point sources. The spectra with different colors show uncertainties of the NXB. The spectrum with  $n_b = 0$  is plotted in blue, while those for  $n_b = \pm 1$  and  $n_b = \pm 2$  are plotted in red and green, respectively, where for the definition of  $n_b$ , see Subsection 6.2.2. In the energy range 1.3-2.4 keV, the NXB is not properly subtracted because of position dependence of instrumental emission lines.

### 7.1.1 Spectral models and fitting results

We would like to estimate the value of  $M(E)$  integrated over the two energy ranges from the observation. For this purpose, we utilize a model fitting. Thus, we first consider the model used in the previous researches (see Yoshino et al. (2009), Henley & Shelton (2013), for example),

$$M_1(E) = A(E; N_1, T_1, \mathbf{Z}_1) + \exp(-\sigma_g(E)N_H) [A(E; N_2, T_2, \mathbf{Z}_2) + P_b(E; N_b, \alpha_1, \alpha_2, E_b)]. \quad (7.3)$$

$A(E; N, T, \mathbf{Z})$  is a thermal emission model of optically-thin plasma in collisional equilibrium with temperature  $T$ . The normalization parameter  $N$  is given as an emission-measure column density for diffuse emission,

$$N = \frac{1}{4\pi} \int_{\ell} dl n_e n_H, \quad (7.4)$$

where  $l$  is a depth of line of sight,  $n_e$  is the electron density and  $n_H$  is the hydrogen density.  $\mathbf{Z}$  specifies abundances of elements other than H and He relative to the solar values. As solar values we adopt Anders & Grevesse (1989). As the emission model, we adopt the APEC (Astrophysical Plasma Emission Code) which is developed at Smithsonian Astrophysical Observatory (SAO) of Harvard University.  $P_b(E; N_b, \alpha_1, \alpha_2, E_b)$  is a broken power function given by

$$P_b(E; N_b, \alpha_1, \alpha_2, E_b) = \begin{cases} N_b \left(\frac{E}{E_b}\right)^{-\alpha_1} & \text{for } E < E_b \\ N_b \left(\frac{E}{E_b}\right)^{-\alpha_2} & \text{for } E \geq E_b \end{cases}. \quad (7.5)$$

The term  $-\sigma_g(E)N_H$  represents the absorption by the neutral medium in our Galaxy. We fixed the column density,  $N_H$ , to the value obtained with 21 cm radio observations,  $8.8 \times 10^{-19} \text{ cm}^{-2}$ . The same column density was used in the previous CDF-S analyses, e.g. Luo et al. (2017). According to the previous researches, the first thin-thermal emission component in Equation 7.3 represents a sum of emission from the heliosphere and the local bubble.

They consider the former is dominant in the energy range above  $\sim 0.5$  keV. The second thin-thermal emission component is considered to arise from the halo of our Galaxy. The emission spectra of components are overlapped at OVII emission, and it is impossible to determine them from the spectral model fits without placing any boundary conditions. Yoshino et al. (2009) argued that when solar activity is low, the surface brightness of OVII is 2 LU for all directions of the sky (see review Subsection 2.5.4). And they fixed both the normalization factor and the temperature of this component to appropriate values so that the component produces OVII but not OVIII lines and so that OVII line surface brightness is 2 LU. We follow this approach but modify it slightly. The thermal model produces also CV and NeVI lines and recombination continuum whose intensities are not known in the model. There is also ambiguity in the *XMM-Newton* MOS effective area below 0.5 keV due to contamination in orbit. In order to avoid the fitting results to be affected by these ambiguities, we replaced the model with

$$M'_1(E) = G(E; N_1, E_{\text{OVII}}, \sigma_1) + \exp(-\sigma_g(E)N_{\text{H}}) [A(E; N_2, T_2, \mathbf{Z}_2) + P_b(E; N_b, \alpha_1, \alpha_2, E_b)], \quad (7.6)$$

where  $G(E, N, E_c, \sigma)$  is a Gaussian function expressing an emission line in solar-wind charge exchange (SWCX)

$$G(E, N, E_c, \sigma) = \frac{N}{\sqrt{2\pi}\sigma} \exp\left[-\frac{(E - E_c)^2}{2\sigma^2}\right]. \quad (7.7)$$

As the most probable origin of an emission line in SWCX is OVII, we set  $E_c$  to the energy of OVII forbidden line 0.561 keV. We set  $\sigma = 0.01$  keV, which is small enough compared to the energy resolution of the detector. The normalization is also set to 2 LU surface brightness of the OVII line in the SWCX.

We adopted the solar abundance for the thin-thermal emission, thus all elements in the  $\mathbf{Z}$  vector are set to unity. The break energy of the broken power-law spectrum is also fixed to 1.3 keV. In Figure 7.2 and the second column of Table 7.1, we show the result. Although the  $\chi^2$  value is acceptable Table, we notice a systematic excess of data over the model. Therefore, we added a Gaussian function to the model to represent the excess. Then, the model function becomes

$$M''_1(E) = G(E; N_1, E_{\text{OVII}}, \sigma_1) + \exp(-\sigma_g(E)N_{\text{H}}) [A(E; N_2, T_2, \mathbf{Z}_2) + P_b(E; N_b, \alpha_1, \alpha_2, E_b)] + G(E; N_u, E_{\text{Cu}}, \sigma_u), \quad (7.8)$$

where the width of the added Gaussian was set to 0.01 keV which is small enough compared to the energy resolution of the detector. The best fit model and spectral parameters are shown in Figure 7.2 and the third column of Table 7.1. The  $\chi^2$  value decreased significantly.

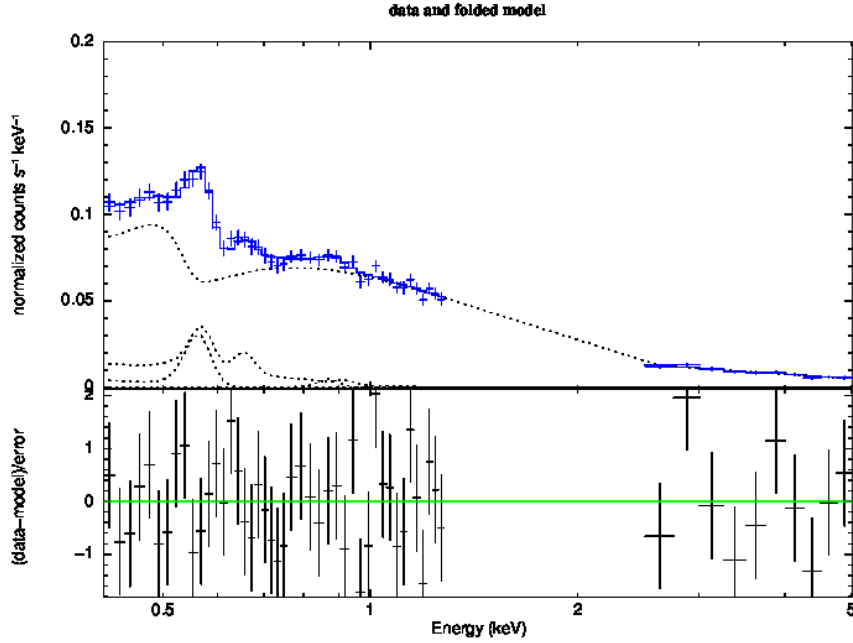


Figure 7.2: Fitting results of the X-ray background with *Chandra* resolved point sources without considering systematic uncertainty of the NXB (for the definition of  $n_b = 0$ , see Subsection 6.2.2). The best fit models (defined in Equation 7.8) are plotted in the dashed lines.

Table 7.1: Results of the spectral fits before removing *Chandra* point sources

| Component  | Before <i>Chandra</i> point sources removed |                              |
|--|---|------------------------------|
| Parameter  | model $M'_1(E)$                             | model $M'_2(E)$              |
| Correction for the Non X-ray Background                                  | ✓   | ✓                            |
| SWCX Gaussian  |   |                              |
| $N_1$ (LU)   | 2 (fixed)                                   | -                            |
| $E_c$ (keV)  | 0.561 (fixed)                               | -                            |
| Galactic halo APEC   |   |                              |
| $N_2$ ( $\text{cm}^{-5} \text{str}^{-1}$ )                               | $2.96 \pm 0.46$                             | $3.36^{+1.64}_{-1.67}$       |
| $T_2$ (keV)  | $0.178^{+0.010}_{-0.012}$                   | 0.178(fixed)                 |
| Broken Power Law   |   |                              |
| $N_b$ ( $\text{cm}^{-2} \text{s}^{-1} \text{keV}^{-1} \text{str}^{-1}$ ) | $13.1^{+0.3}_{-0.3}$                        | $13.3 \pm 0.29$              |
| $\alpha_1$   | $2.06 \pm 0.06$                             | 2.06(fixed)                  |
| $\alpha_2$   | $1.46 \pm 0.06$                             | 1.46(fixed)                  |
| Unknown Gaussian   |   |                              |
| $N_{\text{Gu}}$ (LU)   | $0.10 \pm 0.08$                             | $0.10 \pm 0.08$              |
| $E_{\text{cu}}$ (keV)  | $0.870^{+0.040}_{-0.044}$                   | 0.870 (fixed)                |
| OVII Gaussian  |   |                              |
| $N_{\text{G1}}$ (LU)   | -   | $3.43 \pm 0.27$              |
| $E_{c1}$ (keV)   | -   | $0.5650^{+0.0002}_{-0.0002}$ |
| OVIII Gaussian   |   |                              |
| $N_{\text{G2}}$ (LU)   | -   | $0.70 \pm 0.15$              |
| $E_{c2}$ (keV)   | -   | $0.650^{+0.005}_{-0.010}$    |
| $\chi^2/\text{d.o.f.}$ (d.o.f.)  | 0.82(47)                                    | 0.82(47)                     |

$n_b$  for the NXB correction is 0 for all fits above.  
Errors are  $1.6\sigma$  (90% confidence level).

We calculated the surface brightnesses in the two energy bands from the best fit model. For this calculation, we excluded the unknown Gaussian ( $G(E; N_u, E_{cu}, \sigma_u)$ ). The surface brightness is calculated as

$$S_B(E1, E2) = \int_{E_1}^{E_2} E dE \{G(E; N_1, E_{OVII}, \sigma_1) + \exp(-\sigma_g(E)N_H) [A(E; N_2, T_2, \mathbf{Z}_2) + P_b(E; N_b, \alpha_1, \alpha_2, E_b)]\} \quad (7.9)$$

We estimated the statistical errors by  $\chi^2$  values. We calculated the surface brightness for all combinations of parameters near the  $\chi^2$  minimum. Then we searched for the minimum and the maximum values within the parameter combinations which satisfies  $\chi^2 - \chi_{\min}^2 < \chi_1^2(90\%)$  (see data reduction Section 6.1). Here  $\chi_1^2(90\%) = 2.7$  is the 90% upper  $\chi^2$  value for 1 degree of freedom. We performed the calculations for  $n_b = 0$  and  $n_b = \pm 2$  (see Equation 6.19 in Subsection 6.2.2 for the definition) separately and finally determined the error range which covers all the 90% error ranges of  $n_b = 0$  and  $n_b = \pm 2$ . The systematic errors are the difference between the center values.

It is well known that the energy spectrum is represented with a power-law model in the hard band (2-8 keV). Therefore, we calculated the hard-band (2-8 keV) surface brightness with the power-law model determined by the X-ray background spectrum in 2-5 keV.

Table 7.2: Surface brightness before removing *Chandra* point sources

| $n_b$        | 2-8 keV                      | 0.4-1 keV                       | OVII                     | OVIII                           | 0.4-1 keV - lines                |
|--------------|------------------------------|---------------------------------|--------------------------|---------------------------------|----------------------------------|
| 2            | $17.7^{+0.5}_{-0.4}$         | $7.37^{+0.05}_{-0.05}$          | $0.95^{+0.06}_{-0.06}$   | $0.22^{+0.05}_{-0.05}$          | $6.17^{+0.10}_{-0.11}$           |
| 0            | $16.3^{+0.5}_{-0.6}$         | $7.29^{+0.04}_{-0.05}$          | $0.95^{+0.07}_{-0.07}$   | $0.22^{+0.05}_{-0.05}$          | $6.08^{+0.09}_{-0.11}$           |
| -2           | $14.9^{+0.5}_{-0.3}$         | $7.21^{+0.05}_{-0.05}$          | $0.95^{+0.06}_{-0.06}$   | $0.21^{+0.05}_{-0.05}$          | $6.06^{+0.15}_{-0.10}$           |
| Final result | $16.3^{+0.5}_{-0.6} \pm 1.4$ | $7.29^{+0.04}_{-0.05} \pm 0.08$ | $0.95 \pm 0.07 \pm 0.01$ | $0.22^{+0.05}_{-0.05} \pm 0.01$ | $6.08^{+0.09+0.09}_{-0.11-0.08}$ |

All units are  $10^{-12}$  erg  $s^{-1}$   $cm^{-2}$   $deg^{-2}$

Statistical error  $1.6\sigma$  and systematic error due to the NXB subtraction are shown.

We then determined the surface brightnesses of the OVII and the OVIII emission lines. For this, we also follow the procedure by Yoshino et al. (2009). We set the Oxygen abundance of the thermal-emission component to 0, i.e.  $Z(O) = 0$ , and instead included another Gaussian function. Thus the model is now,

$$M_2''(E) = G(E; N_{G1}, E_{c1}, \sigma_{G1}) + G(E; N_{G2}, E_{c2}, \sigma_{G2}) + \exp(-\sigma_g(E)N_H) [A(E; N_2, T_2, \mathbf{Z}_2(O=0))] + P_b(E; N_b, \alpha_1, \alpha_2, E_b) + G(E; N_u, E_{cu}, \sigma_u), \quad (7.10)$$

We fixed the centroid energies of the two Gaussians to 0.574 keV (OVII) and 0.654 keV (OVIII), respectively and set their  $\sigma$  values to 0.1 eV. The Gaussian with the centroid energy of 0.574 keV now represents the total OVII emission. In the fit, we fixed the shapes of all components, i.e.  $T_2$  and  $\alpha_1, \alpha_2$ , to the best-fit value of the previous fit and set only the normalization factors free. The results for  $n_b = 0$  are shown in Figure 7.3 and in the last column of Table 7.1. To estimate the systematic uncertainty of the surface brightnesses, the fit results ( $n_b = \pm 2$ ) are also shown in Figure 7.4.

The surface brightness of an emission line can be estimated from the normalization factor of the Gaussian model,

$$S_B = E_c N_G. \quad (7.11)$$

The results are tabulated in the fourth and fifth columns of Table 7.2. The surface brightness of total minus the OVII emission line and the OVIII emission lines are tabulated in six column of Table 7.2

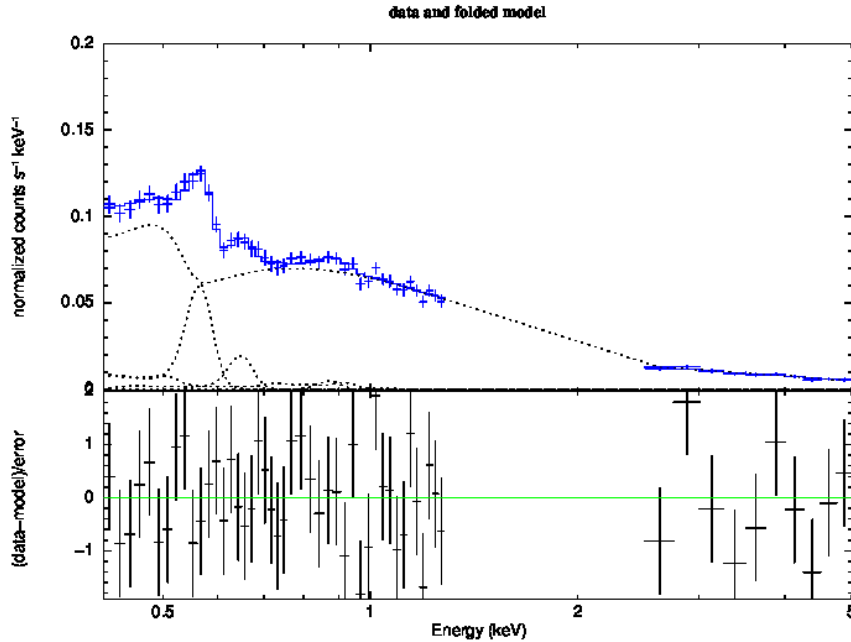


Figure 7.3: Fitting results of the X-ray background with *Chandra* resolved point sources without considering systematic uncertainty of the NXB (for the definition of  $n_b = 0$ , see Equation 6.19 in Subsection 6.2.2). The best fit models (defined in Equation 7.10) are plotted in the dashed lines.

## 7.2 X-ray background spectrum without *Chandra* resolved point sources

In Figure 7.5, we show the NXB subtracted spectrum after the *Chandra* resolved point sources are removed. This spectrum was analyzed with the same procedures as described in previous Subsection 7.1.1, except that we did not include the unknown Gaussian component.

### 7.2.1 Spectral models and fitting results

We employed two models,  $M'_1(E)$  (Equation (7.6) ) and  $M'_2(E)$ ,

$$M'_2(E) = G(E; N_{G1}, E_{c1}, \sigma_{G1}) + G(E; N_{G2}, E_{c2}, \sigma_{G2}) + \exp(-\sigma_g(E)N_H) [A(E; N_2, T_2, \mathbf{Z}_2(O=0)) + P_b(E; N_b, \alpha_1, \alpha_2, E_b)] \quad (7.12)$$

Then, the surface brightnesses and their errors were estimated from the model fits. We show the results for  $n_b = 0$  in Table 7.6, Figure 7.7. The fitting results of  $n_b = \pm 2$  are shown in 7.8. We show the surface brightnesses in Table 7.4 for  $n_b = -2, 0, +2$ .

## 7.3 Components of Soft X-ray Diffuse Background

By excluding *Chandra* resolved point sources, we reduced surface brightnesses both in the soft and the hard bands. Figure 7.9 shows the contributions of spectral components to the surface brightness based on our spectral analysis. The hard band was modeled only with a power law component. In the soft band, two emission lines are clearly detected. Although we modeled the spectrum with a Gaussian function representing the SWCX OVII, a thin-thermal-emission component, and a (soft part of broken) power-law component, we considered that the break down into thermal emission other than the O lines, namely emission lines of the other elements, recombination and

Table 7.3: Results of the spectral fits after *Chandra* point sources removed

| Component<br>Parameter   | After <i>Chandra</i> point sources removed |                           |
|--|--|---------------------------|
|  | model $M'_1(E)$                            | model $M'_2(E)$           |
| SWCX Gaussian  |  |                           |
| $N_1$ (LU)   | 2 (fixed)                                  | -                         |
| $E_c$ (keV)  | 0.561 (fixed)                              | -                         |
| Galactic halo APEC   |  |                           |
| $N_2$ ( $\text{cm}^{-5} \text{str}^{-1}$ )                               | $2.85 \pm 0.87$                            | $3.86 \pm 2.60$           |
| $T_2$ (keV)  | $0.196^{+0.023}_{-0.018}$                  | 0.196(fix)                |
| Broken Power Law   |  |                           |
| $N_b$ ( $\text{cm}^{-2} \text{s}^{-1} \text{keV}^{-1} \text{str}^{-1}$ ) | $4.53 \pm 0.53$                            | $4.58 \pm 0.59$           |
| $\alpha_1$   | $2.31^{+0.26}_{-0.30}$                     | 2.31(fix)                 |
| $\alpha_2$   | $1.56^{+0.35}_{-0.29}$                     | 1.56(fix)                 |
| OVII Gaussian  |  |                           |
| $N_{G1}$ (LU)  | -  | $3.50 \pm 0.55$           |
| $E_{c1}$ (keV)   | -  | $0.565 \pm 0.005$         |
| OVIII Gaussian   |  |                           |
| $N_{G2}$ (LU)  | -  | $0.91 \pm 0.32$           |
| $E_{c2}$ (keV)   | -  | $0.640^{+0.014}_{-0.016}$ |
| $\chi^2/\text{d.o.f}$ (d.o.f.)   | 0.70(26)                                   | 0.69(25)                  |

$n_b$  for the NXB correction is 0 for all fits above.  $n_b$   
(see Subsection 6.2.2 for definition of  $n_b$ )  
Statistical errors are  $1.6\sigma$ (90% confidence level.)

Table 7.4: Surface brightness after *Chandra* point sources removed

| $n_b$ | 2-8 keV                     | 0.4-1 keV             | OVII                     | OVIII                    | 0.4-1 keV excl. lines            |
|-------|-----------------------------|-----------------------|--------------------------|--------------------------|----------------------------------|
| 2     | $7.8^{+0.9}_{-1.0}$         | $4.1 \pm 0.1$         | $0.99 \pm 0.17$          | $0.29^{+0.11}_{-0.12}$   | $2.83 \pm 0.26$                  |
| 0     | $4.7 \pm 0.9$               | $3.9 \pm 0.1$         | $0.98 \pm 0.17$          | $0.28 \pm 0.10$          | $2.65^{+0.22}_{-0.27}$           |
| -2    | $2.0^{+1.0}_{-0.6}$         | $3.7 \pm 0.1$         | $0.98 \pm 0.17$          | $0.28 \pm 0.10$          | $2.45^{+0.25}_{-0.30}$           |
|       | $4.7 \pm 0.9^{+3.1}_{-2.7}$ | $3.9 \pm 0.1 \pm 0.2$ | $0.98 \pm 0.17 \pm 0.01$ | $0.28 \pm 0.10 \pm 0.01$ | $2.47^{+0.22+0.18}_{-0.27-0.20}$ |

All units are  $10^{-12} \text{erg s}^{-1} \text{cm}^{-2} \text{deg}^{-2}$

Statistical errors are  $1.6\sigma$ (90% confidence level.)

thermal-bremsstrahlung continuums, and power-law component are model dependent. For example, the SWCX of the other elements may contribute to the emission. Thus in Figure 7.9, we just denoted sum of them as "the others". For the spectrum before *Chandra* point sources removal, we introduced an additional Gaussian component. Although the origin of this component is not well known it can be instrumental. The surface brightness is only  $0.04^{+0.02}_{-0.02}$  [ $10^{-12} \text{erg cm}^{-2} \text{s}^{-1} \text{deg}^{-2}$ ]. This is very small compared to the other components. We thus ignore it in Chapter 8. The systematic errors are tabulated in Table 7.5 and Table 7.6.

Table 7.5: Budgets of systematic errors for surface brightnesses with *Chandra* resolved point sources

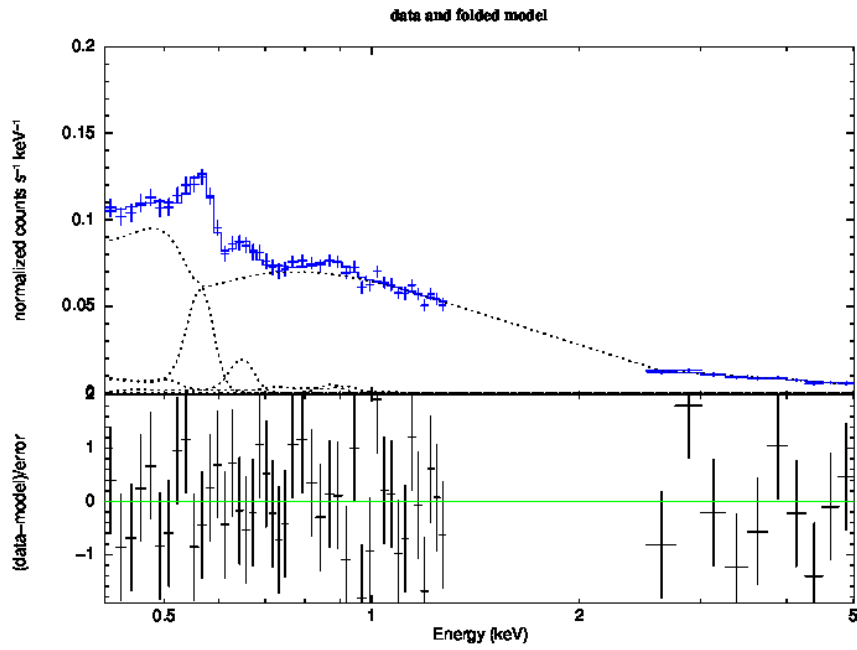
| Causes  | Total<br>in 2-8 keV | Total<br>in 0.4-1 keV | OVII           | OVIII          | 0.4-1 keV excl. lines<br>(The other) | Table       |
|---|---------------------|-----------------------|----------------|----------------|--------------------------------------|-------------|
| Uncertainty of the NXB                            | +1.4<br>-1.4        | +0.08<br>-0.08        | +0.01<br>-0.01 | +0.01<br>-0.00 | -                                    | 7.2 and 7.4 |
| Conceivable residual soft<br>proton contamination | +0.0<br>-5.0        | +0.0<br>-1.22         | +0.06<br>-0.06 | +0.01<br>-0.02 | -                                    | 5.3         |
| Total   | +1.4<br>-6.4        | +0.08<br>-1.30        | +0.07<br>-0.09 | +0.02<br>-0.02 | +0.12<br>-1.30                       |             |

All of the surface brightness values are given in the unit of  $10^{-12}$  erg s $^{-1}$ cm $^{-2}$ deg $^{-2}$ .

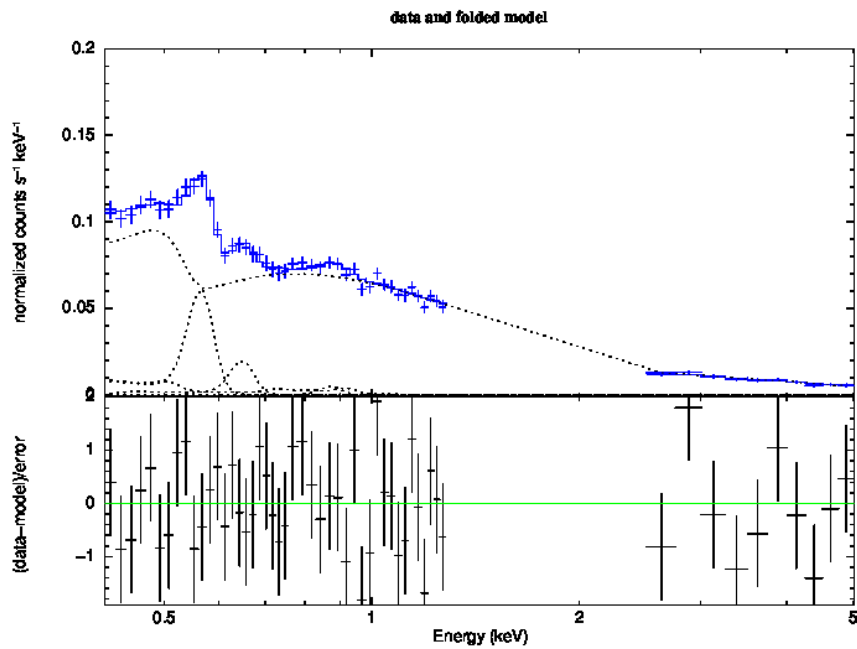
Table 7.6: Budgets of systematic errors for surface brightnesses without *Chandra* resolved point sources

| Causes  | Total<br>in 2-8 keV | Total<br>in 0.4-1 keV | OVII           | OVIII          | 0.4-1 keV excl. lines<br>(The other) | Table       |
|---|---------------------|-----------------------|----------------|----------------|--------------------------------------|-------------|
| Uncertainty of the NXB                            | +3.1<br>-2.7        | +0.3<br>-0.3          | +0.01<br>-0.01 | +0.01<br>-0.00 | -                                    | 7.2 and 7.4 |
| Conceivable residual soft<br>proton contamination | +0.0<br>-1.0        | +0.0<br>-0.6          | +0.06<br>-0.06 | +0.01<br>-0.02 | -                                    | 5.3         |
| Total   | +3.1<br>-3.7        | +0.3<br>-0.9          | +0.07<br>-0.09 | +0.02<br>-0.02 | +0.34<br>-0.91                       |             |

All of the surface brightness values are given in the unit of  $10^{-12}$  erg s $^{-1}$ cm $^{-2}$ deg $^{-2}$ .



(a)  $n_b = +2$



(b)  $n_b = -2$

Figure 7.4: Fitting results of the X-ray background with *Chandra* resolved point sources considering systematic uncertainty of the NXB (for the definition of  $n_b = \pm 2$ , see Subsection 6.2.2). The best fit models (defined in Equation 7.10) are plotted in the dashed lines.

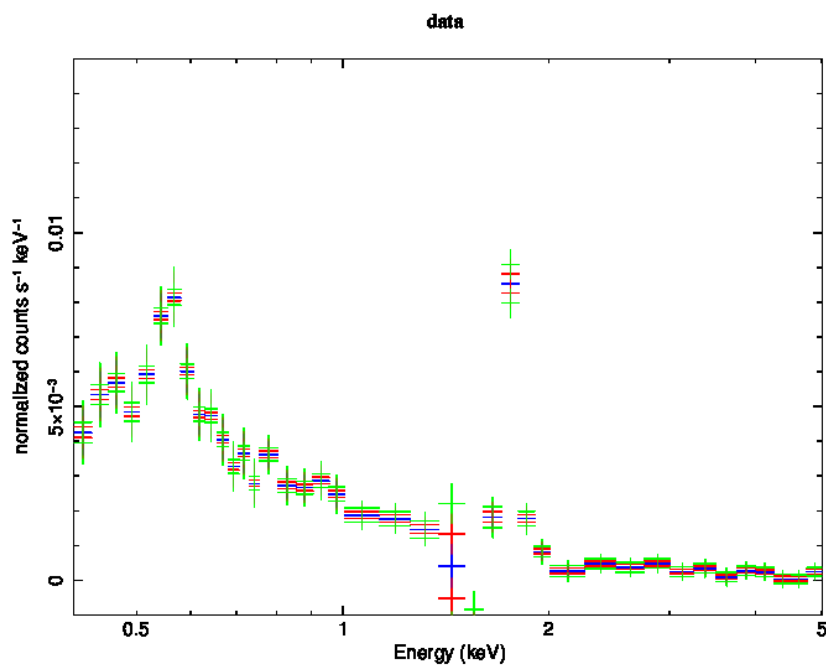


Figure 7.5: NXB-subtracted MOS2 spectra of the CDF-S overlapping region with resolved point sources. The spectra with different colors show uncertainties of the NXB. The spectrum with  $n_b = 0$  is plotted in blue, while those for  $n_b = \pm 1$  and  $n_b = \pm 2$  are plotted in red and green, respectively, where for the definition of  $n_b$ , see Subsection 6.2.2. In the energy range 1.3-2.4 keV, the NXB is not properly subtracted because of position dependence of instrumental emission lines.

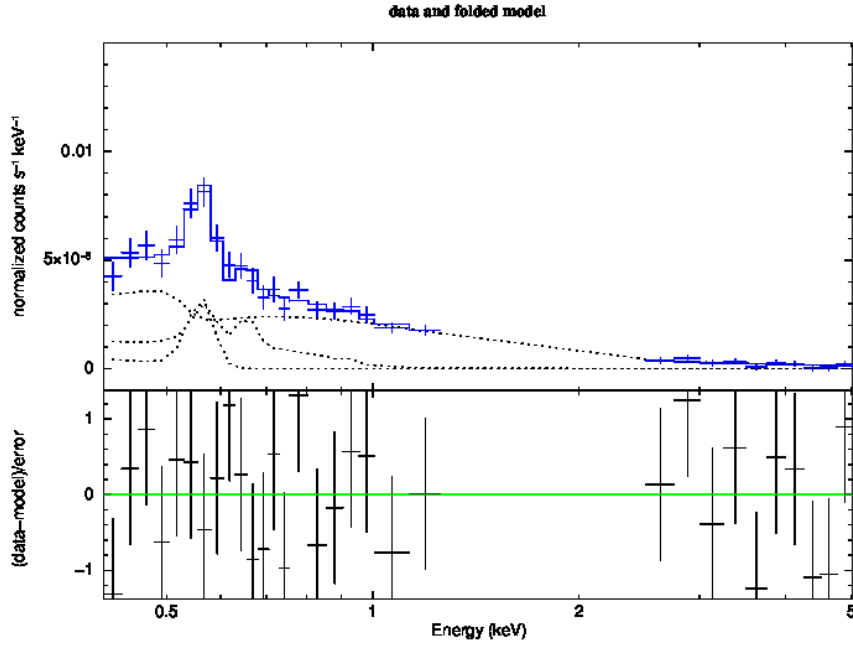


Figure 7.6: Fitting results of the X-ray background without *Chandra* resolved point sources without considering systematic uncertainty of the NXB (for the definition of  $n_b = 0$ , see Subsection 6.2.2). The best fit models (defined in Equation 7.8) are plotted in the dashed lines.

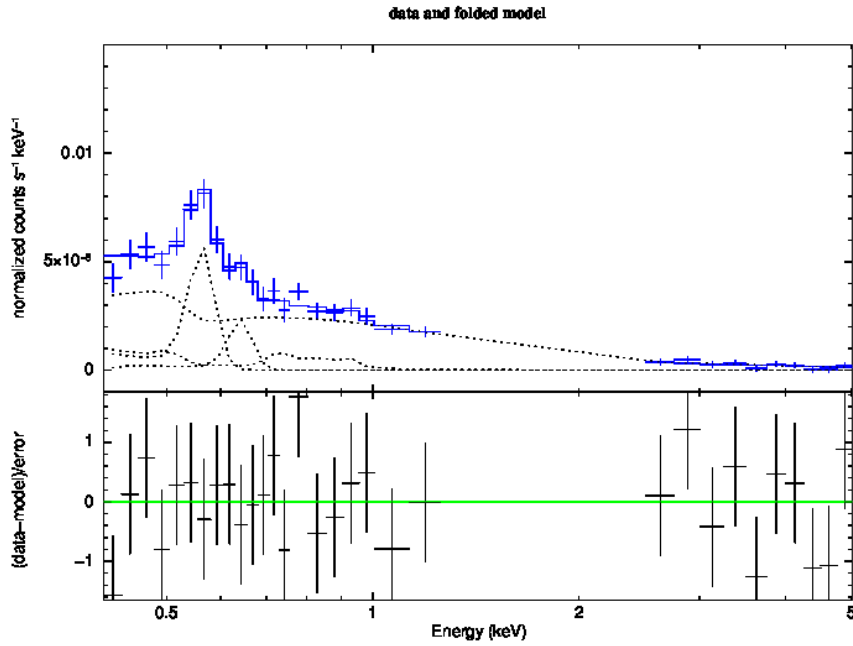
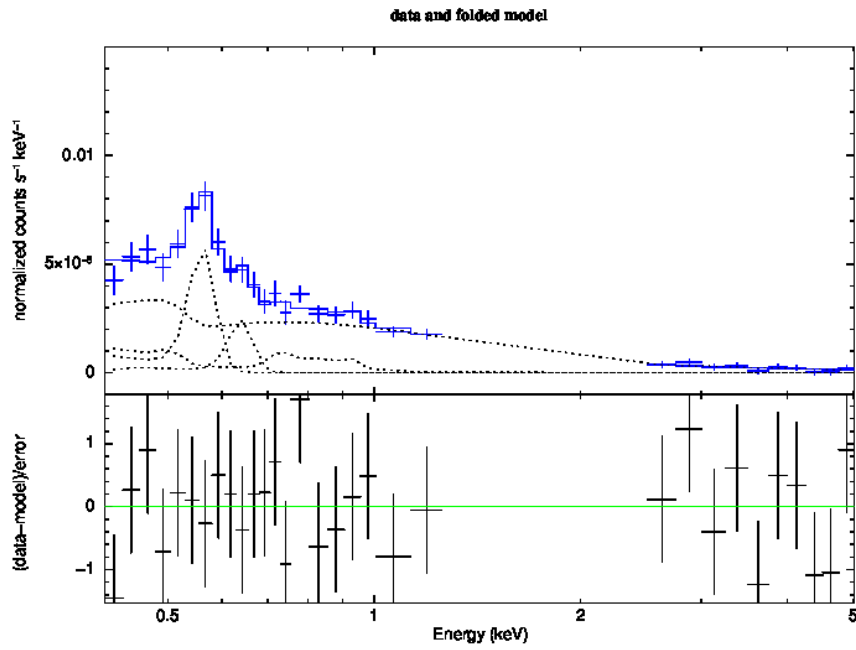
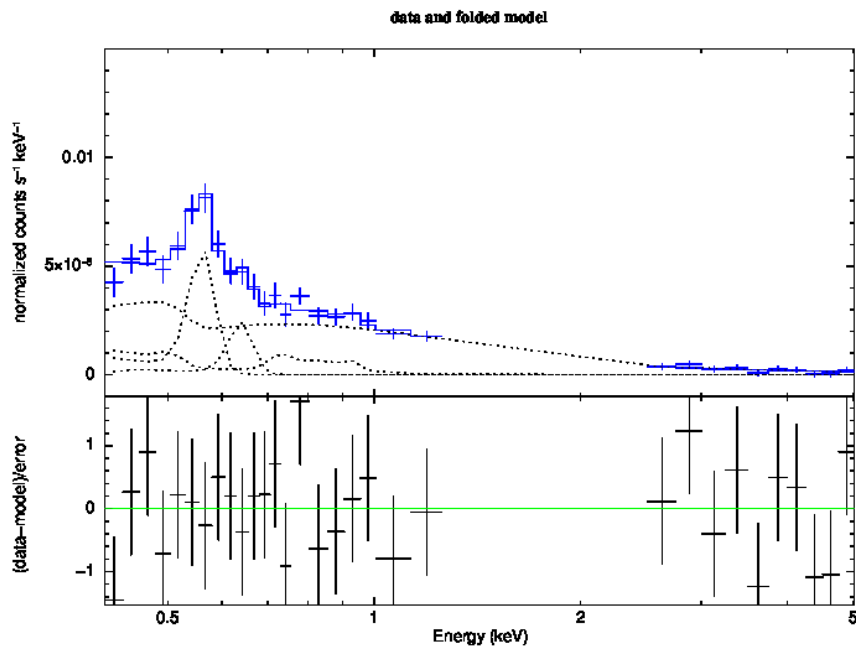


Figure 7.7: Fitting results of the X-ray background without *Chandra* resolved point sources without considering systematic uncertainty of the NXB (for the definition of  $n_b = 0$ , see Equation 6.19 in Subsection 6.2.2). The best fit models (defined in Equation 7.12) are plotted in the dashed lines.



(a)  $n_b = +2$



(b)  $n_b = -2$

Figure 7.8: Fitting results of the X-ray background without *Chandra* resolved point sources considering systematic uncertainty of the NXB (for the definition of  $n_b = \pm 2$ , see Subsection 6.2.2). The best fit models (defined in Equation 7.10) are plotted in the dashed lines.

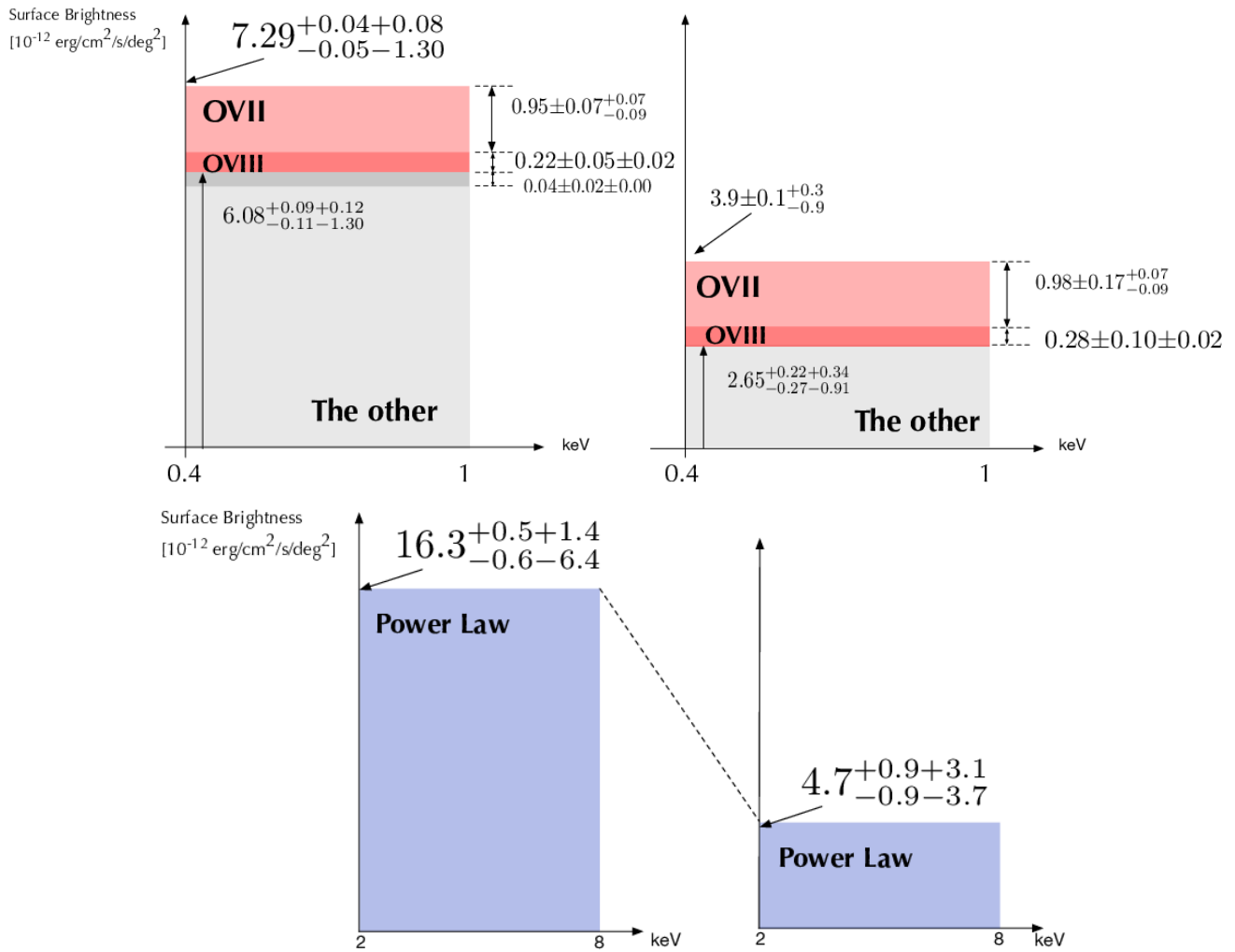


Figure 7.9: Surface brightnesses in two energy bands, 0.4-1 keV (top panels) and 2-8 keV (bottom panels) before (left panels) and after (right panels) *Chandra* resolved point sources removal. The contributions of emission components are also shown. The errors quoted are for statistical errors at 90% ( $1.6\sigma$ ) confidence and systematic error. The systematic errors are calculated in Table 7.5 and Table 7.6.

# Chapter 8

## Discussion

### 8.1 Summary of Results

In the previous chapters, we have obtained two different kinds of the *XMM-Newton* CDF-S X-ray spectra; one for the total field of view overlapped with the *Chandra* deep observations, the other for which the detector area where X-ray photons from the *Chandra* point sources contribute are removed. After the removal, the spill out of photons from point sources due to the point spread function of the X-ray telescope is controlled to be smaller than 5% of the remaining spectrum. We carefully removed time intervals for which the data are contaminated with soft protons from the Sun. As a result, for the first time by the *XMM-Newton* observation, we obtained the soft-proton-free X-ray background spectrum in the CDF-S and the spectrum without *Chandra* resolved point sources. We estimated the surface brightnesses in the 0.4-1 keV bands and the 2-8 keV bands, and the surface brightnesses of the OVII and the OVIII emission lines, separately.

In this chapter, we will first compare our results with the previous studies, and discuss the origins of the X-ray background.

### 8.2 Comparison with previous studies

There are two previous studies: One is Hickox & Markevitch (2006). And the other is Luo et al. (2017).

Hickox & Markevitch (2006) analyzed the 0.5 Msec *Chandra* data of the X-ray background in 0.5-8 keV during 2000-2001 with the 1 Msec the CDF-S point sources catalogue to remove point sources. On the other hand, we used the 1.66 Msec *XMM-Newton* data of the X-ray background in 0.4-8 keV during 2000-2010 with the 7 Msec CDF-S point source catalogue to remove point sources. Thus, we compared our results with Hickox & Markevitch (2006).

Luo et al. (2017) estimated the *Chandra* point-source removal fraction in 2-8 keV, based on the 7 Msec the CDF-S point sources catalogue.

#### 8.2.1 Figure of Merit

The figure of merit is essential to observe a weak emission line in case that equivalent width of the weak emission line is narrower than the detector energy resolution. The *XMM-Newton* MOS detectors have a large effective area and slightly better energy resolution than *Chandra* ACIS below 1 keV. Therefore, the figure of merit of *XMM-Newton* is higher than *Chandra*, as shown in Figure 8.1.

#### 8.2.2 Spectra without point sources in 2-8 keV

We summarized the results in 2-8 keV in comparison with the previous study by Hickox & Markevitch (2006) in Table 8.1. We found both the surface brightness and the power-law index after point source removal were consistent with *Chandra* by Hickox & Markevitch (2006) within the errors. From the surface brightnesses, we found the point-source removal fraction is  $71_{-5}^{+6+20}$  % (the statistical 90% error and the NXB systematic errors).

This number is consistent within the errors with  $92.7 \pm 13.3$  % based on the  $\log N$ - $\log S$  relation of a point source by Luo et al. (2017). We also found both the surface brightness and the power-law index without *Chandra* resolved point sources are consistent with *Chandra* by Hickox & Markevitch (2006)(within the errors).

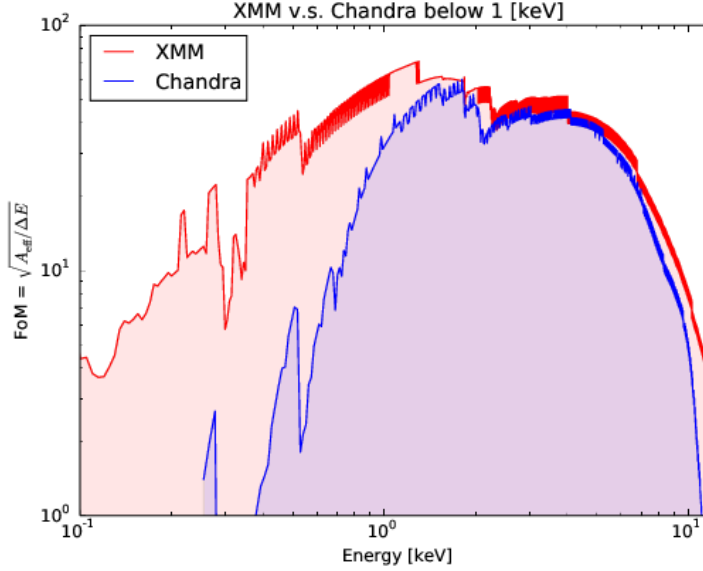


Figure 8.1: Figure of Merits (FoM) below 1 keV. Red curve indicates the *XMM-Newton* MOS2 detector. Blue curve shows the *Chandra* ACIS-I.

Table 8.1: 2-8 keV surface brightness and power-law index

|                       | This work                        | <i>Chandra</i> (Hickox & Markevitch (2006))* |
|-----------------------|----------------------------------|--|
| Total spectrum        |                                  |  |
| Surface brightness    | $16.3^{+0.5+1.4}_{-0.6-6.4}$     | $14.1 \pm 2.2$                               |
| Power-law index       | $1.44^{+0.05+0.10}_{-0.04-0.06}$ | (1.4)  |
| Point sources removed |                                  |  |
| Surface brightness    | $4.7^{+0.9+3.1}_{-0.9-3.7}$      | $3.6 \pm 1.45 \pm 1.63$                      |
| Power law index       | $1.56^{+0.35+0.63}_{-0.29-0.30}$ | $1.5^{+0.5}_{-0.4}$                          |

\* the CDF-S only

Error is statistical  $1.6\sigma$  error and total systematic error for this work.

Error is statistical  $1.0\sigma$  error and total systematic error for *Chandra*.

### 8.2.3 Spectra without point sources below 2 keV

In Table 8.2, we compared the surface brightnesses without *Chandra* resolved point sources in 0.5-1 keV. We should note that these values are not directly compared because the observation periods are different. *Chandra* observed the X-ray background around solar maximum period, 2000. Fortunately, our observation ranged from 2000 to 2010. Thus, we compared two surface brightnesses between the solar maximum period (2000-2001) and the solar minimum period (2008-2010). The spectrum in the solar maximum epoch is shown in Figure 8.2. The surface brightness in the 2000-2001 interval is  $(6.48^{+0.08+0.10}_{-0.10-0.11}) \times 10^{-12} \text{ erg cm}^{-2} \text{ s}^{-1} \text{ deg}^{-2}$  (the statistical  $1.6\sigma$  error and the NXB systematic error) in 0.5-1 keV. On the other hand, The surface brightness in the 2008-2010 interval is  $(5.74^{+0.12+0.05}_{-0.12-0.05}) \times 10^{-12} \text{ erg cm}^{-2} \text{ s}^{-1} \text{ deg}^{-2}$  (the statistical  $1.6\sigma$  error and the NXB systematic error) in 0.5-1 keV. We note that these values include resolved point sources. The difference in observed surface brightness between 2000-2001 and 2008-2010 was  $(0.74^{+0.13+0.12}_{-0.16-0.12}) \times 10^{-12} \text{ erg cm}^{-2} \text{ s}^{-1} \text{ deg}^{-2}$ . Assuming that this difference is the same as in the X-ray background data in 0.5-1 keV without *Chandra* resolved point sources, we estimated the surface brightness without resolved point sources in 0.5-1 keV during 2008-2010 to be  $(3.19 + 0.74)^{+0.16+0.28}_{-0.19-0.28} = 3.93^{+0.16+0.28}_{-0.19-0.28}$  (the statistical  $1.6\sigma$  error and the NXB systematic error), by adding  $(0.74^{+0.13+0.12}_{-0.16-0.12}) \times 10^{-12} \text{ erg cm}^{-2} \text{ s}^{-1} \text{ deg}^{-2}$  to the observed surface brightness in 0.5-1 keV during 2008-2010. Thus, our surface brightness  $3.93^{+0.16+0.28}_{-0.19-0.28} \times 10^{-12} \text{ erg cm}^{-2} \text{ s}^{-1} \text{ deg}^{-2}$  (the statistical  $1.6\sigma$  error and the NXB systematic error) is consistent with the *Chandra* surface brightness  $(5.0 \pm 0.4) \times 10^{-12} \text{ erg cm}^{-2} \text{ s}^{-1} \text{ deg}^{-2}$  (the statistical  $1.0\sigma$  error and the systematic error) within  $2\sigma$ . As previously mentioned in Section 5.6, we discarded the X-ray background data around the solar maximum period during 2000-2001.

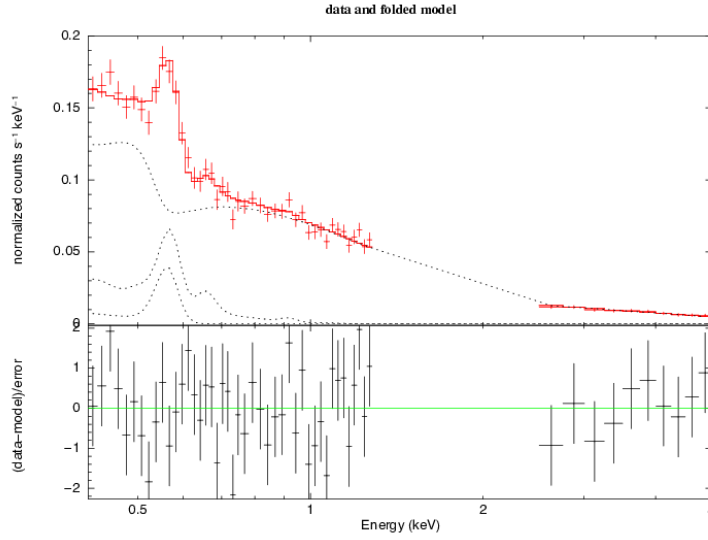


Figure 8.2: Spectrum in the solar maximum epoch observed by the MOS2.

Hickox & Markevitch (2006) used a single power-law model. The *Chandra* index was in the middle of the soft and hard indices of this work.

Hickox & Markevitch (2006) did not separate the OVIII line from the OVII line, as shown in Figure 8.3 (right) and (left). On the other hand, as shown in Figure 7.7, we succeeded in separating the OVIII line from the OVII line, where the significance of the OVIII line is  $3.4\sigma$ . This is the first detection of the OVIII line in the X-ray background without *Chandra* resolved point sources. For comparison, we overlay the *Chandra* spectrum on the spectrum in this work in Figure 8.4.

Table 8.2: Spectra without resolved point sources (Hickox & Markevitch (2006)). See text about difference in surface brightness between this work and .

| Component   | This work                       | <i>Chandra</i> (Hickox & Markevitch (2006))* |
|---|---------------------------------|--|
| Total surface brightness in 0.5-1 keV<br>( $10^{-12}$ erg $s^{-1}$ $cm^{-2}$ $deg^{-2}$ ) | $3.19 \pm 0.10^{+0.25}_{-0.61}$ | $5.0 \pm 0.4$                                |
| (Broken) Power Law  |                                 |  |
| $\alpha_1$  | $2.31^{+0.26}_{-0.30}$          | $1.84^{+0.48}_{-0.35}$                       |
| $\alpha_2$  | $1.56^{+0.35}_{-0.29}$          | (single PL)                                  |

\* the CDF-S only

Error is statistical  $1.6\sigma$  error and total systematic error for this work.

Error is statistical  $1.0\sigma$  error and total systematic error for *Chandra*.

## 8.3 Total surface brightness of X-ray background in 0.5-1 keV

As mentioned in Subsection 7.2.1, the energy range, 1-2 keV, where instrumental lines are dominant is not included in the further discussion. We also decided not to include the energy range, 0.4-0.5 keV. as is explained in the next Subsection 8.3.1. Therefore, we will study the X-ray background in 0.5-1 keV in the following discussion.

### 8.3.1 Treatment of surface brightness in 0.4-0.5 keV

In the 0.4-0.5 keV band, emission lines of the SWCX are important, as shown in Figure 2.11. The spectrum of the SWCX is determined with the following quantities/processes

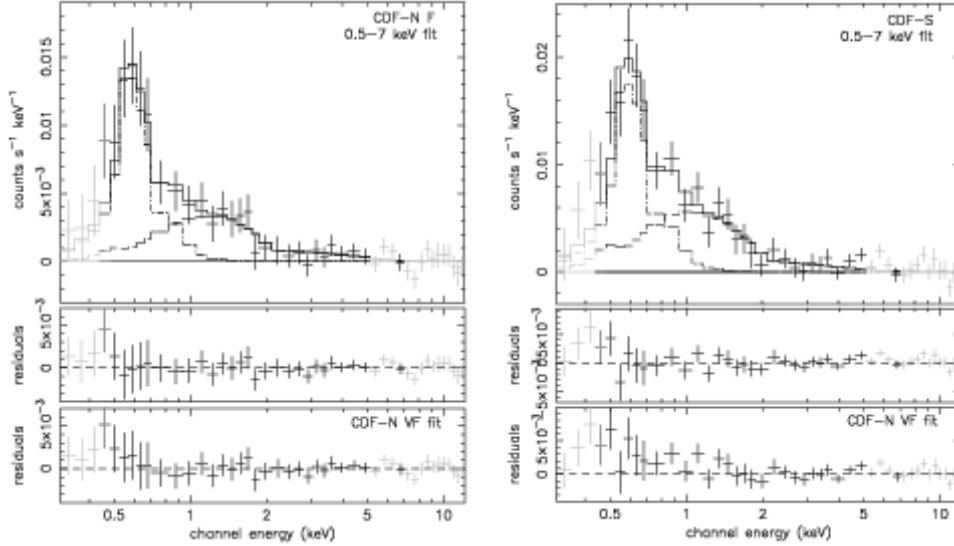


Figure 8.3: Two spectra without resolved point sources (a) in CDF-N and (b) in the CDF-S observed by *Chandra* cited from Hickox & Markevitch (2006). Fitting models for these spectra are a simple power-law model and a thermal emission model (APEC). These models convolve the response of *Chandra*. The OVII plus OVIII emission lines are not separated in 0.5-0.7 keV.

- (1) Ionization fraction of plasma in the Sun which is a seed of solar wind
- (2) Selection probability of ions for acceleration process of solar wind
- (3) Cross section of charge-exchange-induced X-ray emission

Since the plasma is considered to be in collisional thermal equilibrium, (1) is determined by the temperature and the element abundance of the plasma. The element abundance can be assumed to be the solar abundance. Process (2) is known to be related to the first ionization potential of the ion. (3) is known to be dependent on the collision velocity and ions. The ionization fraction and velocity of the solar wind have been measured with interplanetary space missions, such as ACE (from 1997 at Lagrangian point 1), Ulysses (1990-2009, high inclination interplanetary orbit). Ulysses observations clearly showed that both the velocity and the ion temperatures change drastically at ecliptic latitude  $\beta$  of  $\pm 20^\circ$ . Two different kinds of solar wind are, respectively, called fast wind ( $\beta > 20^\circ$ ,  $T \sim 0.07$  keV, and  $v = 750$  km/s) and slow wind ( $\beta < 20^\circ$ ,  $T \sim 0.13$  keV, and  $v = 400$  km/s). In the line of sight towards the CDF-S direction, both slow and fast winds will contribute to the SWCX.

There is still not enough experimental data on the charge exchange cross sections in the velocity range of 400 to 750 km/s. Thus a precise prediction of the SWCX spectrum is still not possible. Nevertheless, several SWCX spectral models have been proposed. In this subsection, we will use the simulation code by Smith et al. (2012). As the velocity is assumed to be a fixed value in their simulation, the velocity dependence of cross sections is ignored. The abundance and the ion temperature are free parameters.

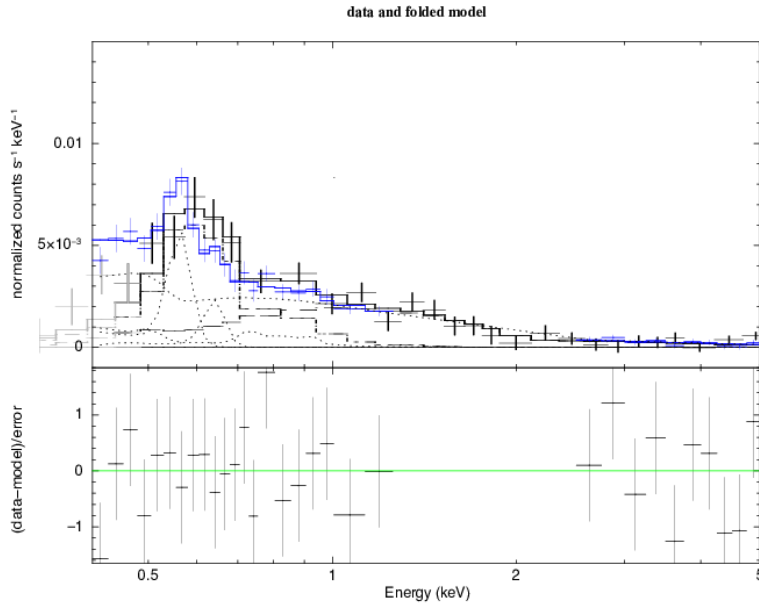


Figure 8.4: Comparison between two spectra below 1 keV. This work is indicated by the blue crosses with error bars, which is the same as Figure 7.7. The *Chandra* spectrum in the CDF-S is indicated by the black crosses cited from Hickox & Markevitch (2006). This work separates the OVIII line from the OVII line.

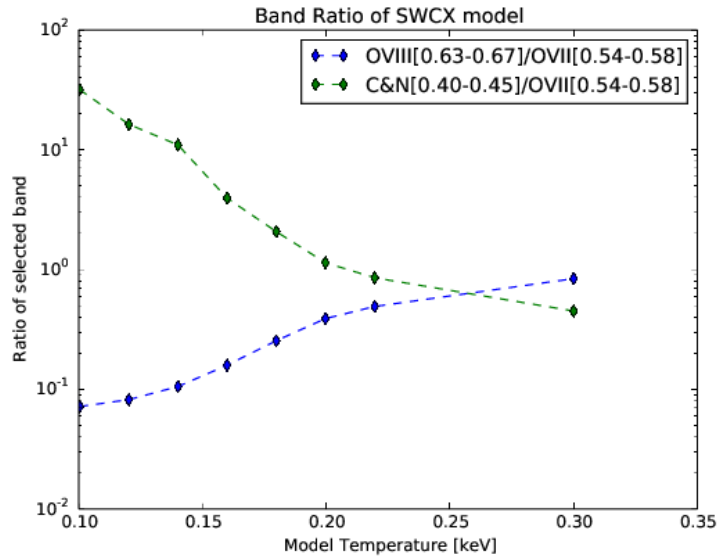


Figure 8.5: Intensity ratio of solar wind emission lines to the OVII emission line as a function of ion temperature. The ratios of C+N emission lines to OVII, and of OVIII to OVII are calculated using the simulation code by Smith et al. (2012).

In Figure 8.5, we found that the OVIII emission line is negligible compared to the OVII emission line. However, the CV and NVI emission lines are not negligible. Taking the difference in the photon energy (between OVII and CV or NVI) and the Galactic absorption into account, the surface brightness ratio will be smaller than that plotted in Figure 8.5. The correction factor was estimated to be 0.45. As the SWCX ion temperature is within the range of 0.1 to 0.13 keV according to the *Ulysses* observation, the surface brightness of CV and NVI emission will be larger

than that of OVII ( $(0.98 \pm 0.17_{-0.09}^{+0.07}) \times 10^{-12} \text{ erg s}^{-1} \text{ cm}^{-2} \text{ deg}^{-2}$ ) by a factor of 4 to 15 after the correction. The surface brightness of CV and NVI is 4 to 15  $\times 10^{-12} \text{ erg s}^{-1} \text{ cm}^{-2} \text{ deg}^{-2}$  which was even larger than the total surface brightness after *Chandra* point source removal ( $(3.9 \pm 0.1_{-0.9}^{+0.3}) \times 10^{-12} \text{ erg s}^{-1} \text{ cm}^{-2} \text{ deg}^{-2}$ ). We thus considered this estimation of the (C+N)/OVII ratio is too large and that there must be problems in the model calculation of the SWCX. As this discrepancy may prevent us from studying the yet-unknown components, we ignored the energy range 0.4 to 0.5 keV in the further discussion. On the other hand, emission lines in the SWCX other than OVII were considered to be negligibly small above 0.5 keV. Furthermore, we can subtract the OVII and OVIII lines from the observed X-ray background in 0.5-1 keV to study the yet-unknown components without depending on SWCX model calculations.

### 8.3.2 Total surface brightness in 0.5-1 keV

In Chapter 7, we calculated the surface brightnesses in the 0.4-1 keV band. However, we decided not to include the energy range, 0.4-0.5 keV in previous Subsection 8.3.1. Thus, the re-calculated surface brightnesses in 0.5-1 keV are tabulated in Table 8.3. We considered the origins of the total surface brightness are the OVII line, the OVIII line, thermal emissions other than the OVII and OVIII lines and the contribution of the unresolved point sources which were not resolved by *Chandra* in 2-8 keV. We will discuss the origins of the surface brightness of the X-ray background other than the OVII and OVIII emission lines in the following subsections.

Table 8.3: Re-calculation for 0.5-1 keV band.

| Item                                     | value <sup>(1)</sup>            |
|--|---------------------------------|
| Surface brightness with point sources    |                                 |
| 0.5-1 keV                                | $5.74 \pm 0.04_{-1.02}^{+0.08}$ |
| 0.5-1 keV - line                         | $4.57 \pm 0.09_{-1.02}^{+0.10}$ |
| Surface brightness without point sources |                                 |
| 0.5-1 keV                                | $3.19 \pm 0.10_{-0.61}^{+0.25}$ |
| 0.5-1 keV - line                         | $1.9 \pm 0.2_{-0.61}^{+0.25}$   |

<sup>(1)</sup>: in unit of  $10^{-12} \text{ erg s}^{-1} \text{ cm}^{-2} \text{ deg}^{-2}$ .

Error is statistical  $1.6\sigma$  error and total systematic error

### 8.3.3 Thermal hot plasma emission other than OVII and OVIII emission lines

The thermal emission contains emission lines other than OVII and OVIII and thermal bremsstrahlung and recombination continuum. We can constrain the emission measure of the thermal plasma by the OVII and OVIII line intensities as well as the temperature of the thermal plasma by the OVIII/OVII ratio, if we assume the Oxygen abundance. Then, we can estimate the surface brightness of the thermal emission other than OVII and OVIII lines from the emission measure and the temperature. The surface brightness increases with decreasing O abundance.

The emission measure ( $N_2$ ) and the temperature ( $T_2$ ) of the thermal emission model ( $A$ ) in Equation 7.12 were already determined as shown in Table 7.3. By using these parameters, we estimated the surface brightness of the thermal emission other than OVII and OVIII lines for abundance ( $Z_2$ ) values of 0.3, 0.5, and 1.0 and found the best estimates are 0.42, 0.40,  $0.38 \times 10^{-12} \text{ erg s}^{-1} \text{ cm}^{-2} \text{ deg}^{-2}$ , for  $Z=0.3, 0.5,$  and 1.0 respectively. Thus, the variation is by an order of magnitude smaller than the systematic errors of the total surface brightness.

### 8.3.4 Surface brightness of unresolved point sources which were not resolved by *Chandra* in 2-8 keV

*Chandra* determined a power-law index in the two energy bands, 0.5-2 keV and 2-8 keV. The power-law index is shown in Figure 8.6 where we focus on the index for all stacked point sources in cyan crosses. The faintest source has a power-law index of 2.0. Thus, we assumed that the unresolved point sources have a spectral index of 2.0.

To estimate the unresolved power-law surface brightness in 0.5-1 keV, we used the following equations,

$$\frac{1 - \xi}{\xi} = \frac{S_{2-8}}{\Delta S_{2-8}} = \eta \frac{S_{0.5-1}}{\Delta S_{0.5-1}}, \quad (8.1)$$

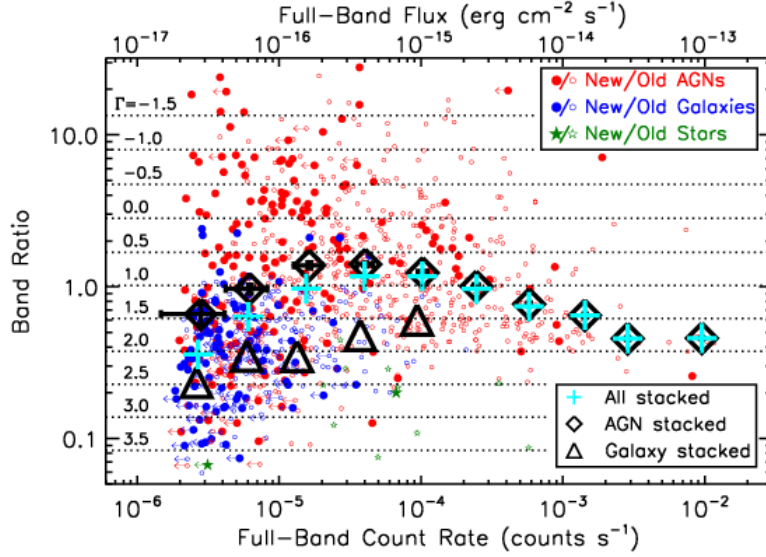


Figure 8.6: Relation between power-law index and point-source flux determined by *Chandra* in the two energy bands, 0.5-2 keV and 2-8 keV cited from Luo et al. (2017).

with

$$\eta = \frac{\Delta S_{0.5-1}/\Delta S_{2-8}}{S_{0.5-1}/S_{2-8}}, \quad (8.2)$$

where  $\xi$  is the point-source removal fraction,  $\Delta S_{0.5-1}$  is the surface brightness of the resolved point sources in 0.5-1 keV,  $\Delta S_{2-8}$  is the surface brightness of the resolved point sources in 2-8 keV,  $S_{0.5-1}$  is surface brightness of the unresolved point sources in 0.5-1 keV and  $S_{2-8}$  is surface brightness of the unresolved point sources in 2-8 keV. We employed a coefficient,  $\eta$ , because of the difference of power-law index between the resolved sources and the unresolved point sources. We determined  $\Delta S_{0.5-1}$  and  $\Delta S_{2-8}$  from the difference in the surface brightness between with resolved point sources and without resolved point sources. We obtained surface brightnesses,  $\Delta S_{0.5-1} = (2.56 \pm 0.11 \pm 0.13) \times 10^{-12} [\text{erg cm}^{-2} \text{s}^{-1} \text{deg}^{-2}]$  (the statistical  $1.6\sigma$  error and the NXB systematic error) and  $\Delta S_{2-8} = (11.7_{-0.9-3.6}^{+1.0+4.0}) \times 10^{-12} [\text{erg cm}^{-2} \text{s}^{-1} \text{deg}^{-2}]$  (the statistical  $1.6\sigma$  error and the NXB systematic error). Therefore, we obtained a power-law index  $1.6 \pm 0.3$  determined by  $\Delta S_{0.5-1}/\Delta S_{2-8}$ , which is consistent with the power-law index of the resolved point sources,  $1.47 \pm 0.04$ , observed by *Chandra* cited from Hickox & Markevitch (2006). We calculated the surface brightness ( $S_{0.5-1}$ ) to be  $(0.20 \pm 0.10 \pm 0.10) \times 10^{-12} [\text{erg cm}^{-2} \text{s}^{-1} \text{deg}^{-2}]$  (the statistical  $1.6\sigma$  error and the NXB systematic error) assuming the power-law index 1.6 ( $\eta = 1$ ). However, the power-law index of  $1.6 \pm 0.3$  (the statistical  $1.6\sigma$  error and the NXB systematic error) is flatter than a power-law index of the unresolved point sources, 2.0 for the faintest sources detected by *Chandra*. Meanwhile, the power-law index  $1.6 \pm 0.3$  is steeper than the power-law index of  $1.42 \pm 0.02$  in 2-8 keV (Revnivtsev et al. (2003)). Therefore, we set the upper limit of the power-law index to 2.0 ( $\eta = 2.174$ ) and we set the lower limit of the power-law index 1.4 ( $\eta = 0.753$ ) to estimate systematic uncertainty of the surface brightness due to the uncertainty of power-law index. Table 8.4 shows the estimated surface brightnesses of the unresolved point sources which were not resolved by *Chandra* in 2-8 keV, together with the systematic errors. In this work, we estimated the systematic uncertainty of the surface brightness of the unresolved point sources ( $S_{0.5-1}$ ) due to the uncertainty of the power-law index for the first time.

### 8.3.5 Break down of X-ray background without resolved point sources in 0.5-1 keV

The total surface brightness of the X-ray background was described in Subsection 8.3.2. Subsequently, we considered the origins of the total surface brightness are the OVII line, the OVIII line, thermal emissions other than the OVII and OVIII lines and the contribution of the unresolved point sources which were not resolved by *Chandra* in 2-8 keV. The budget of the 0.5-1 keV X-ray background is shown in Table 8.5. The budget of the systematic errors is shown in Table 8.6.

The OVII and OVIII emission lines were explained in Figure 7.9. The thermal emission other than the OVII and OVIII emission lines was described in Subsection 8.3.3. The contribution of the unresolved point source which were

Table 8.4: Surface brightness of the unresolved point sources which were not resolved by *Chandra* in 2-8 keV.

| Resolved fraction<br>$\xi$ % | Power-law index of the<br>unresolved point sources. | Softness ratio<br>$S_{0.5-1}/S_{2-8}$ | $\eta$ | Surface brightness ( $S_{0.5-1}$ )<br>$10^{-12} \text{erg cm}^{-2} \text{s}^{-1} \text{deg}^{-2}$ |
|------------------------------|---|---------------------------------------|--------|---|
| 92.7                         | 1.4   | 0.165                                 | 0.753  | 0.152   |
| ↓                            | 1.6   | 0.224                                 | 1.023  | 0.204   |
| ↓                            | 2.0   | 0.476                                 | 2.174  | 0.438   |
| 79.4                         | 1.4   | 0.165                                 | 0.753  | 0.500   |
| ↓                            | 1.6   | 0.224                                 | 1.023  | 0.679   |
| ↓                            | 2.0   | 0.476                                 | 2.174  | 1.444   |
| 100                          | -   | -                                     | -      | 0   |

not resolved in 2-8 keV was discussed in Subsection 8.3.4. To make a breakdown of the X-ray background emission in 0.5-1 keV, we subtracted these surface brightnesses from the total surface brightness as shown in Table 8.5.

In Table 8.5, we show the result assuming  $92.7 \pm 13.3\%$  removal of point sources, because the value  $(92.7 \pm 13.3)\%$  is relatively a firm number from the log  $N$ -log  $S$  analysis by *Chandra*, while the value,  $71_{-5}^{+6+20}\%$  (the statistical 90% error and the total systematic errors), obtained by this work contains large systematic errors. We finally obtained the yet-unknown components,  $1.33 \pm 0.46_{-0.62}^{+0.35} \times 10^{-12} \text{ erg s}^{-1} \text{cm}^{-2} \text{deg}^{-2}$  (statistical  $1.6\sigma$  error and total systematic error) for point-source resolved fraction 92.7 %,  $2.32 \pm 0.45_{-0.19}^{+0.78} \times 10^{-12} \text{ erg s}^{-1} \text{cm}^{-2} \text{deg}^{-2}$  (statistical  $1.6\sigma$  error and total systematic error) for point-source resolved fraction 79.4 % and  $1.66 \pm 0.45_{-0.09}^{+0.08} \times 10^{-12} \text{ erg s}^{-1} \text{cm}^{-2} \text{deg}^{-2}$  (statistical  $1.6\sigma$  error and total systematic error) for point-source resolved fraction 100 %.

The error bars added in the yet-unknown components are too large to claim detection. The surface brightness of the yet-unknown components is consistent with zero within the errors for the point-source resolved fraction 79.4 % case. Therefore, we set a  $1.6\sigma$  statistical + systematic upper limit of  $2.3 \times 10^{-12} \text{ erg cm}^{-2} \text{s}^{-1} \text{deg}^{-2}$  on the yet-unknown components.

 Table 8.5: Budget of the X-ray background in 0.5-1 keV after *Chandra* point sources removal.

| Item                               | Value <sup>(1)</sup>            | Rationale  | Grade <sup>(2)</sup> |
|------------------------------------|---------------------------------|--|----------------------|
| Total Surface brightness           | $3.19 \pm 0.10_{-0.61}^{+0.25}$ | Table 8.3  | A                    |
| Components resolved/inferred       |                                 |  |                      |
| (1) OVII emission                  | $0.98 \pm 0.17 \pm 0.01$        | Table 7.4  | A                    |
| (2) OVIII emission                 | $0.28 \pm 0.10 \pm 0.02$        | Table 7.4  | A                    |
| (3) Thermal other than OVII, OVIII | $0.4 \pm 0.4 \pm 0.02$          | Subsection 8.3.3                                 | B <sup>(3)</sup>     |
| (4a) Sources in 2-8 keV            | $0.20 \pm 0.01_{-0.05}^{+0.24}$ | If 92.7% was removed in 2-8 keV<br>(Table 8.3.4) | C                    |
| (4b)                               | $0.66 \pm 0.03_{-0.16}^{+0.78}$ | If 79.4% was removed in 2-8 keV                  | C                    |
| (4c)                               | 0.00                            | If 100% was removed in 2-8 keV                   | C                    |
| Sum                                |                                 |  |                      |
|                                    | $1.86 \pm 0.45_{-0.05}^{+0.24}$ | For 92.7% removal in 2-8 keV                     |                      |
|                                    | $2.32 \pm 0.45_{-0.19}^{+0.78}$ | For 79.4% removal in 2-8 keV                     |                      |
|                                    | $1.66 \pm 0.45_{-0.09}^{+0.08}$ | For 100% removal in 2-8 keV                      |                      |
| Components yet-unknown             |                                 |  |                      |
|                                    | $1.33 \pm 0.46_{-0.62}^{+0.35}$ | For 92.7% removal in 2-8 keV                     |                      |
|                                    | $0.87 \pm 0.46_{-0.70}^{+0.82}$ | For 79.4% removal in 2-8 keV                     |                      |
|                                    | $1.53 \pm 0.46_{-0.68}^{+0.26}$ | For 100% removal in 2-8 keV                      |                      |

<sup>(1)</sup> All surface brightness are given in unit of  $10^{-12} \text{ erg s}^{-1} \text{cm}^{-2} \text{deg}^{-2}$ .

Error is statistical  $1.6\sigma$  (90 % confidence level) error and total systematic error

<sup>(2)</sup> Grade A: estimated directly from observations.

Grade B: estimated from observations with reasonable assumptions.

Grade C: estimated from observations with assumptions without any evidence.

<sup>(3)</sup> The values with abundance = 0.3, 0.5 and 1.0 are well within the error quoted.

### 8.3.6 Comparisons with pre-expectation prior to the analysis in 0.5-1 keV

We then compare the pre-expectation discussed in Chapter 3 to the final breakdown shown in Figure 8.5. Figure 8.7 (a) shows the pre-expectation values. The OVII emission line (6.4 LU) in Figure 8.7 (a) is different from what

Table 8.6: Budget of the systematic errors

| Causes  | Total        |       | (1)   |       | (2)   |       | (3)   | (4a)  | (4b)  | Sum <sup>†</sup> | yet-unknown <sup>†</sup> |
|---|--------------|-------|-------|-------|-------|-------|-------|-------|-------|------------------|--------------------------|
|   | in 0.5-1 keV |       | OVI   | OVI   | OVI   | OVI   | (3)   | (4a)  | (4b)  |                  |                          |
| Uncertainty of the NXB  | +0.25        | -0.01 | +0.01 | +0.01 | +0.01 | -     | -     | -     | -     | -                | -                        |
| Conceivable residual  | -0.25        | -0.01 | -0.01 | -0.00 | -0.00 | -     | -     | -     | -     | -                | -                        |
| soft proton contamination (RSPC)  | +0.00        | +0.06 | +0.06 | +0.01 | +0.01 | -     | -     | -     | -     | -                | -                        |
| Uncertainty on the abundance of the thermal emission                                  | -0.36        | -0.06 | -0.06 | -0.02 | -0.02 | -     | -     | -     | -     | -                | -                        |
| Difference of indices between the resolved point sources and unresolved point sources | -            | -     | -     | -     | -     | +0.02 | -0.02 | -     | -     | -                | -                        |
| Total   | +0.25        | -0.61 | +0.07 | +0.02 | +0.02 | +0.02 | +0.24 | +0.78 | +0.25 | +0.25            | +0.35                    |
|   |              |       | -0.09 | -0.02 | -0.02 | -0.02 | -0.05 | -0.16 | -0.11 | -0.11            | -0.62                    |

All surface brightness are given in unit of  $10^{-12}$  erg  $s^{-1}$   $cm^{-2}$   $deg^{-2}$ .

<sup>†</sup> In the case of (4a).

we obtained in the present analysis (3.4 LU). This is likely due to spatial intensity variations of emission from the halo of our Galaxy. We thus corrected for this in Figure 8.7 (a') where we assumed that the "remaining thermal emission" can be linearly scaled with the OVII line intensity. The final breakdown is also shown in Figure 8.7 (A), (B) and (C). The yet-unknown components of the final breakdown do not contradict the pre-expectation, because of the large systematic error of the yet-unknown components.

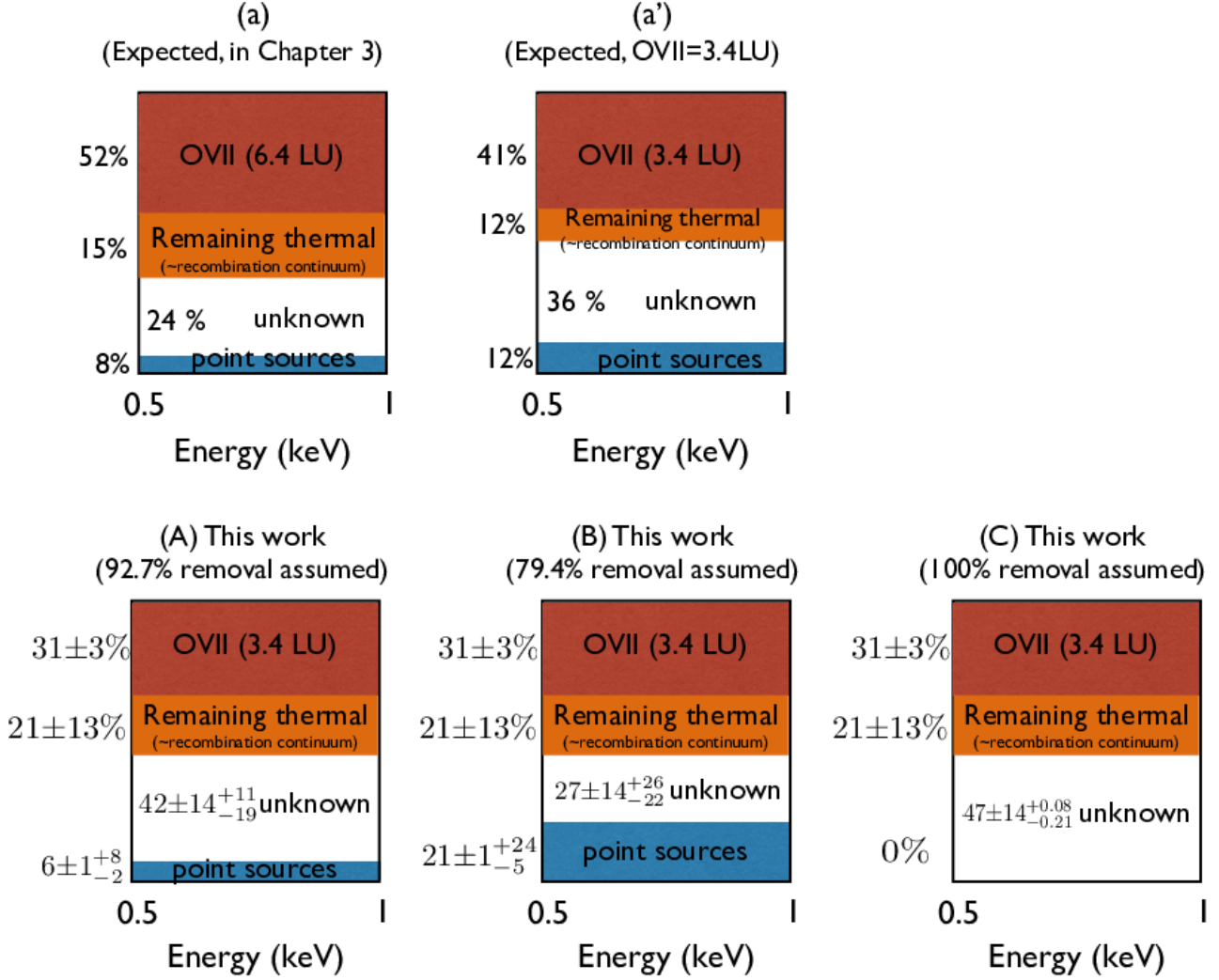


Figure 8.7: Contents of the X-ray background in 0.5-1 keV based on previous observations ((a) and (a')) and based on this work ((A), (B) and (C)). The panel (a) is the same as Figure 3.1 (c), while the OVII line intensity is corrected to the value obtained with this work in the panel (a'). The (A), (B) and (C) panels show the estimation based on this work.

### 8.3.7 Comparisons with WHIM and re-ionizing photons

Several authors performed simulations of cosmological structure formation including the WHIM (e.g. Cen & Ostriker (1999), Yoshikawa et al. (2004)). The emission spectra of the WHIM have been investigated (e.g., Takei et al. (2007) and Cappelluti et al. (2012b)), using the results of these simulations. Takei et al. (2007) claimed the surface brightness of the WHIM was  $(0.36 \pm 0.03) \times 10^{-12} \text{ erg cm}^{-2} \text{ s}^{-1} \text{ deg}^{-2}$  in 0.5-1 keV. On the other hand, Cappelluti et al. (2012b) claimed that the surface brightness of the WHIM was  $0.57 \times 10^{-12} \text{ erg cm}^{-2} \text{ s}^{-1} \text{ deg}^{-2}$  in 0.5-1 keV.

The relic of re-ionization photons in the soft X-ray bands has been studied by Fialkov et al. (2017) and Cappelluti et al. (2012b). Cappelluti et al. (2012b) claimed the surface brightness of the re-ionizing Quasar was  $< 0.35 \times 10^{-12} \text{ erg cm}^{-2} \text{ s}^{-1} \text{ deg}^{-2}$  in 0.5-2 keV.

We found that the upper limit of  $2.3 \times 10^{-12} \text{ erg cm}^{-2} \text{ s}^{-1} \text{ deg}^{-2}$  on the yet-unknown components has been room to include these surface brightnesses.

### 8.3.8 Possible further improvements

We had a significant systematic error in the contribution of the unresolved point sources which were not resolved by *Chandra* in 2-8 keV. To estimate the surface brightness of the yet-unknown components we need more knowledge on the unresolved point sources. Currently, *Chandra* continues the observation to resolve the unresolved point sources in the 2-8 keV band. However, we need an X-ray telescope which has a better spatial resolution than *Chandra* and hopefully a larger effective area than *XMM-Newton*. Unfortunately, such an X-ray observatory is not planned in twenty-year time scales.

On the other hand, we successfully obtained the OVII emission line and the OVIII emission line, separately. However, we could not measure the redshift of the two emission lines because of the detector energy resolution (125 eV@0.56 keV). Thus, to detect and unveil the filament structure of the WHIM in the future, a higher energy-resolution (a few eV) imaging camera is needed to measure the redshift of the two emission lines.

# Chapter 9

## Summary and Conclusions

To study the nature and the origins of the X-ray background below about 2 keV, we analyzed the *XMM-Newton* observation data towards the Chandra Deep Field-South (CDF-S) direction. We obtained the X-ray spectra in the direction before and after all the *Chandra* spatially resolved point sources were removed. While we made efforts to obtain reliable spectra, we encountered the following problems and solved them:

- (a) Contamination of soft protons, which varies on a wide variety of time scales and amplitudes.

To remove it, utilizing the counting rates in the 5-10 keV energy band, we checked the time variability on short ( $\sim 100$  sec) and long ( $\sim 10$  ksec) time scales and eliminated the time intervals when such variability was found. We obtained soft-proton free *XMM-Newton* spectra of the X-ray background for the first time. After removing the time intervals suspected to be contaminated with soft protons, the remaining exposure time amounted to 1.6 Msec.

- (b) Determination of detector area to exclude the spatially resolved point sources.

If the area is too small, the spectra will be contaminated with the spill over of point sources due to the blur of the X-ray telescope image. If we make the area too large, the X-ray background spectra will not be very statistically significant. We created *XMM-Newton* simulation images of spatially resolved point sources by *Chandra*. Utilizing the images, we determined the best threshold for the point-source removal. We set the threshold at which the spill over is at the most 5% of the X-ray background spectrum without spatially resolved point sources in the 0.4-1 keV band, while the statistical significance of the surface brightness in the 0.4-1 keV band is also 5%.

- (c) Spatial non-uniformity of the non X-ray background (NXB) and its time variation.

It was already known that the NXB estimated by using the standard recipes can have a percent level offset, because of the non-uniformity. We estimated it by comparing the NXB and the X-ray background spectra in the 10-11 keV energy range, where the *XMM-Newton* X-ray telescope has a very small effective area and the X-ray photons are negligible compared to the NXB. The correction is small but significant for the spectrum in the 2-5 keV energy range. The statistical errors in the correction factor introduced systematic uncertainties in the spectral fit results. We took the correction factor and its statistical errors in the spectral analysis. Furthermore, we checked the 1.9 Msec filter wheel closed (FWC) data to investigate the difference in energy dependence of the count rate between inside and outside the field of view. The difference turned out to be smaller than the statistical error.

- (d) Effective area of the telescope to use in the spectral fit to the X-ray background spectra.

Because of the complex shape of the detector regions, we have to conduct computation-time-consuming calculations. We found that the calculation does not converge to the expected value within a few % levels even with a fine mesh of 1 arcsec and that it will take more than a month to complete the calculation with the 1 arcsec mesh size. To complete the computation on a time scale of a week (corresponding to 3.8 arcsec mesh), keeping the accuracy less than 1 % we estimated the expected value from the mesh size dependence of the convergence value and established the relationship between the expected value and the convergence value with 3.8 arcsec mesh. We confirmed that the deviation of the estimated value with this method from the expected value is less than 1% in the 0.4-5 keV range.

We then performed spectral fits. Both the spectra before and after removal of the *Chandra* spatially resolved point sources can be represented with a model consisting of (1) a Gaussian function which represents 2 LU of OVII emission from the Heliospheric SWCX, (2) thin-thermal emission of temperature  $\sim 0.2$  keV affected by the Galactic absorption, (3) a broken-power-law function with the Galactic absorption. In the previous researches, the component (2) was considered to arise from the hot gas in the Galactic halo, while the component (3) was considered to arise from distant unresolved faint point sources. We fixed the break energy at 1.3 keV cited from Gilli et al. (2001), since we had to mask the spectra in 1.3 to 2.4 keV because the instrumental lines in the NXB cannot be subtracted properly. The photon index of the broken power-law function above 1.3 keV was consistent with the canonical value, 1.4, within the errors, while that in the soft band below 1.3 keV was steeper than 1.4;  $2.06 \pm 0.06$  and  $2.31^{+0.26}_{-0.30}$  with and without the spatially resolved point sources, respectively.

Even though we obtained acceptable fits, we considered that the interpretation of the model components is arbitrary and decided not to discuss the model components. And we used the model only to estimate the surface brightnesses. Because the OVII and OVIII lines are resolved, we also estimated each surface brightness of the OVII line and the OVIII line from the model fits. The results of the spectral fits are:

(A) Before *Chandra* resolved spatially point sources are removed:

- (a) Total surface brightness was  $(5.74 \pm 0.04^{+0.08}_{-1.02}) \times 10^{-12}$  erg cm $^{-2}$  s $^{-1}$  deg $^{-2}$  in 0.5-1 keV
- (b) OVII emission line was  $(0.95 \pm 0.07^{+0.07}_{-0.09}) \times 10^{-12}$  erg cm $^{-2}$  s $^{-1}$  deg $^{-2}$
- (c) OVIII emission line was  $(0.22 \pm 0.05 \pm 0.02) \times 10^{-12}$  erg cm $^{-2}$  s $^{-1}$  deg $^{-2}$

(B) After *Chandra* resolved spatially point sources are removed:

- (a) Total surface brightness was  $(3.19 \pm 0.10^{+0.25}_{-0.61}) \times 10^{-12}$  erg cm $^{-2}$  s $^{-1}$  deg $^{-2}$  in 0.5-1 keV
- (b) OVII emission line was  $(0.98 \pm 0.17^{+0.07}_{-0.09}) \times 10^{-12}$  erg cm $^{-2}$  s $^{-1}$  deg $^{-2}$
- (c) OVIII emission line was  $(0.28 \pm 0.10 \pm 0.02) \times 10^{-12}$  erg cm $^{-2}$  s $^{-1}$  deg $^{-2}$

These errors are the statistical  $1.6\sigma$  error (90% confidence level) and the systematic error. We successfully separated the OVII line and the OVIII line for the first time in the X-ray background spectrum without the *Chandra* spatially resolved point sources, which was not possible with the *Chandra* data. The detection significance of the OVIII line was  $3.4(= 0.28/(0.10/1.6 + 0.02))\sigma$ .

After the *Chandra* spatially resolved point sources are removed, we performed break down of the surface brightness of the X-ray background,  $(3.19 \pm 0.10^{+0.25}_{-0.61}) \times 10^{-12}$  erg cm $^{-2}$  s $^{-1}$  deg $^{-2}$  in 0.5-1 keV. We considered the origins of the total surface brightness are the OVII line, the OVIII line, thermal emissions other than the OVII and OVIII lines and the contribution of the unresolved point sources which were not resolved by *Chandra* in 2-8 keV.

(I) Break down of the X-ray background in 0.5-1 keV after *Chandra* spatially resolved point sources are removed:

- (a) Thermal emissions other than the OVII and OVIII lines
  - i.  $(0.4 \pm 0.4 \pm 0.02) \times 10^{-12}$  erg cm $^{-2}$  s $^{-1}$  deg $^{-2}$
- (b) Contribution of the unresolved point sources which were not resolved by *Chandra* in 2-8 keV
  - i.  $(0.20 \pm 0.01^{+0.24}_{-0.05}) \times 10^{-12}$  erg cm $^{-2}$  s $^{-1}$  deg $^{-2}$  if 92.7% was removed in 2-8 keV
  - ii.  $(0.66 \pm 0.03^{+0.78}_{-0.16}) \times 10^{-12}$  erg cm $^{-2}$  s $^{-1}$  deg $^{-2}$  if 79.4% was removed in 2-8 keV
  - iii.  $0.00 \times 10^{-12}$  erg cm $^{-2}$  s $^{-1}$  deg $^{-2}$  if 100% was removed in 2-8 keV
- (c) Yet-unknown components (Total – OVII – OVIII – Thermal emission other than OVII and OVIII – Unresolved point sources which were not resolved by *Chandra* in 2-8 keV)
  - i.  $(1.33 \pm 0.46^{+0.35}_{-0.62}) \times 10^{-12}$  erg cm $^{-2}$  s $^{-1}$  deg $^{-2}$  for 92.7% removal in 2-8 keV
  - ii.  $(0.87 \pm 0.46^{+0.82}_{-0.70}) \times 10^{-12}$  erg cm $^{-2}$  s $^{-1}$  deg $^{-2}$  for 79.4% removal in 2-8 keV
  - iii.  $(1.53 \pm 0.46^{+0.26}_{-0.68}) \times 10^{-12}$  erg cm $^{-2}$  s $^{-1}$  deg $^{-2}$  for 100% removal in 2-8 keV

This is the first quantitative breakdown of the X-ray background emission in 0.5-1 keV, taking various systematic errors into account. As we found no significant evidence for the yet-unknown components, we set a  $1.6\sigma$  statistical + systematic upper limit of  $2.3 \times 10^{-12}$  erg cm $^{-2}$  s $^{-1}$  deg $^{-2}$ . The upper limit was roughly 70% of the observed X-ray background, and it did not contradict the expected surface brightness of the WHIM from the cosmological

simulations.

We had a significant systematic error in the contribution of the unresolved point sources which were not resolved by *Chandra* in 2-8 keV. To estimate the surface brightness of the yet-unknown components we need more knowledge on the unresolved point sources. Currently, *Chandra* continues the observation to resolve the unresolved point sources in the 2-8 keV band. However, we need an X-ray telescope which has a better spatial resolution than *Chandra* and hopefully a larger effective area than *XMM-Newton*. Unfortunately, such an X-ray observatory is not planned in twenty-year time scales. On the other hand, we successfully obtained the OVII emission line and the OVIII emission line, separately. However, we could not measure the redshift of the two emission lines because of the detector energy resolution (125 eV@0.56 keV). Thus, to detect and unveil the filament structure of the WHIM in the future, a higher energy-resolution (a few eV) imaging camera is needed to measure the redshift of the two emission lines.

# Appendix A

## Figures employed to eliminate bad data

### A.1 All of out of FOV spectra for all ObsIDs to determine the anomalously bright CCD chips

In Subsection 5.3.2, we checked the following spectra for all ObsIDs. These spectra are chip by chip basis. The feature of an anomalously bright CCD chip indicates a high count rate only in the soft band below 1 keV.

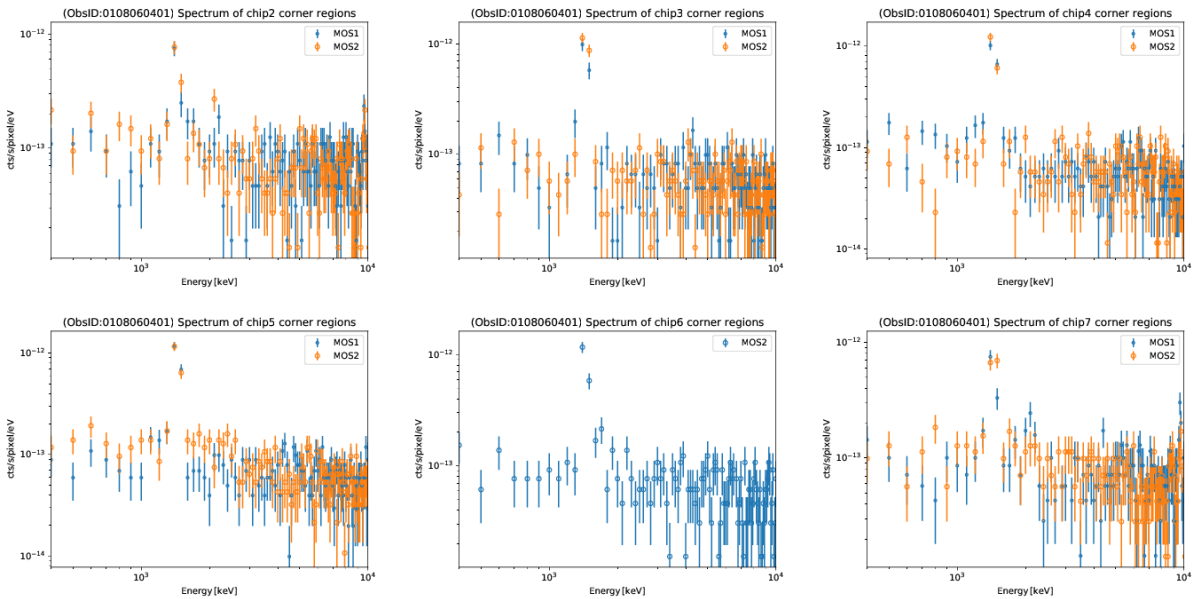


Figure A.1: Out field of view spectra for MOS1 (blue) and for MOS2 (orange) for 0108060401.

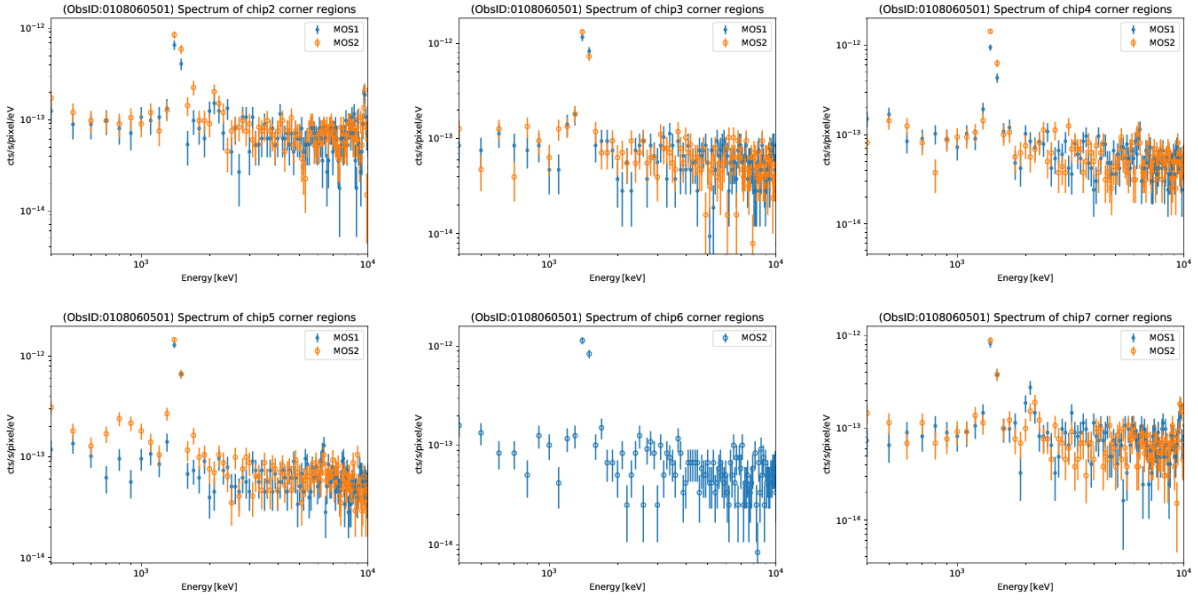


Figure A.2: Same as the previous figure but for 0108060501

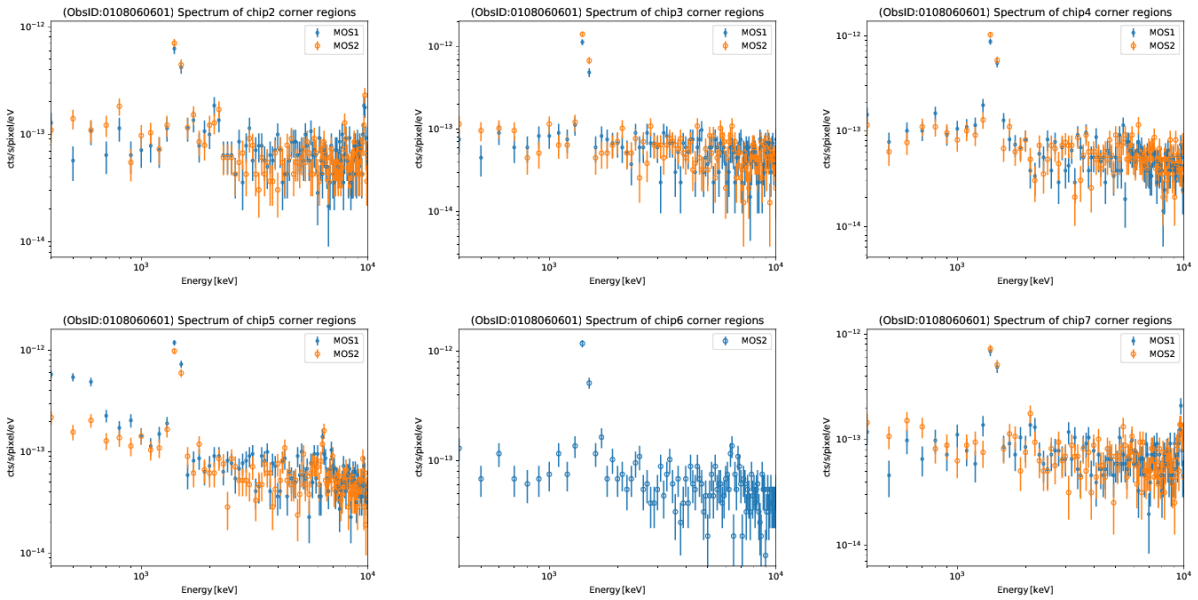


Figure A.3: Same as the previous figure but for 0108060601

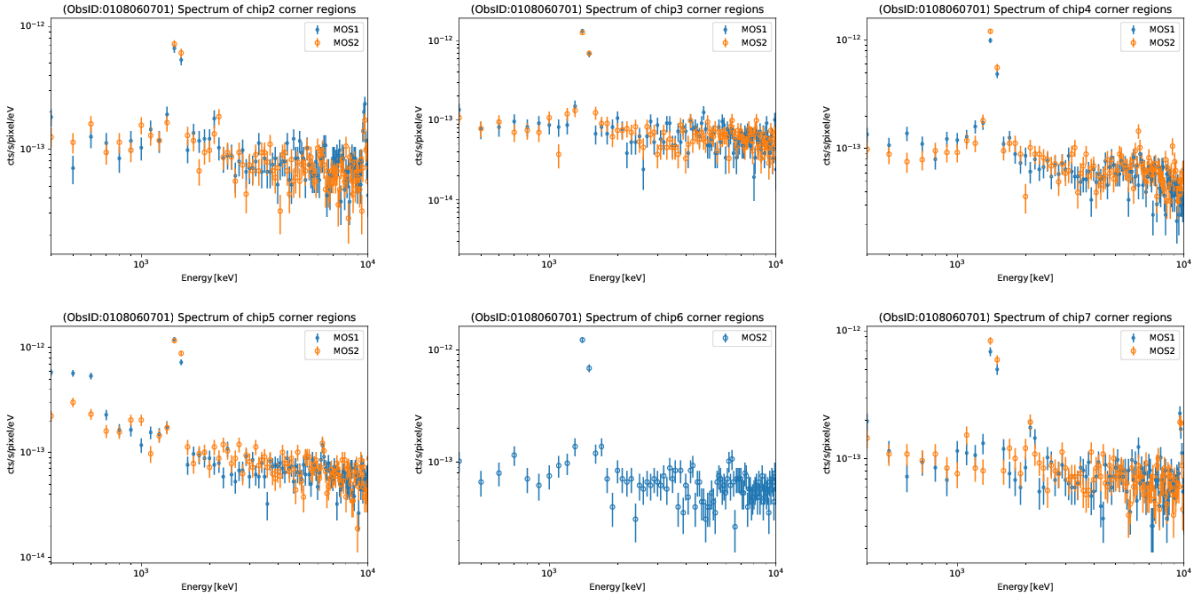


Figure A.4: Same as the previous figure but for 0108060701

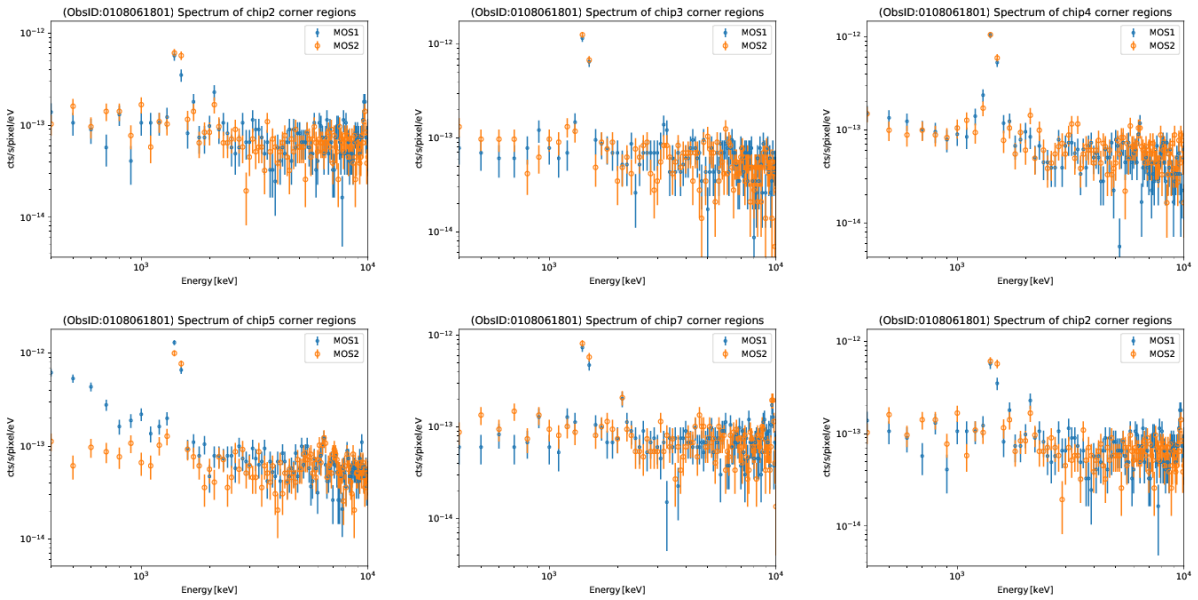


Figure A.5: Same as the previous figure but for 0108061801

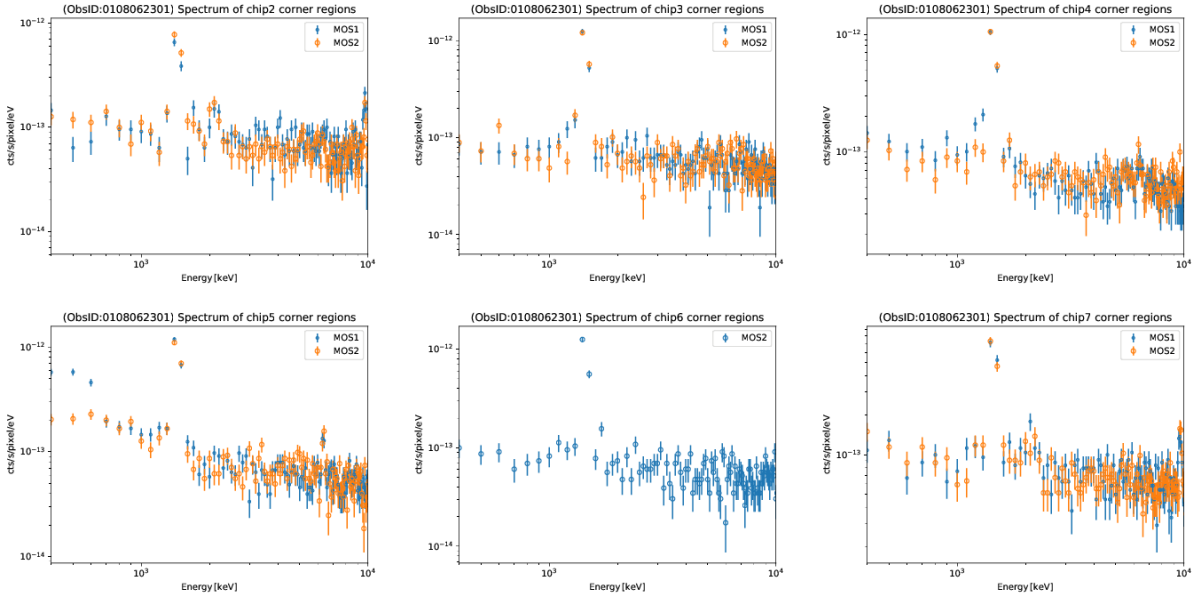


Figure A.6: Same as the previous figure but for 0108062301

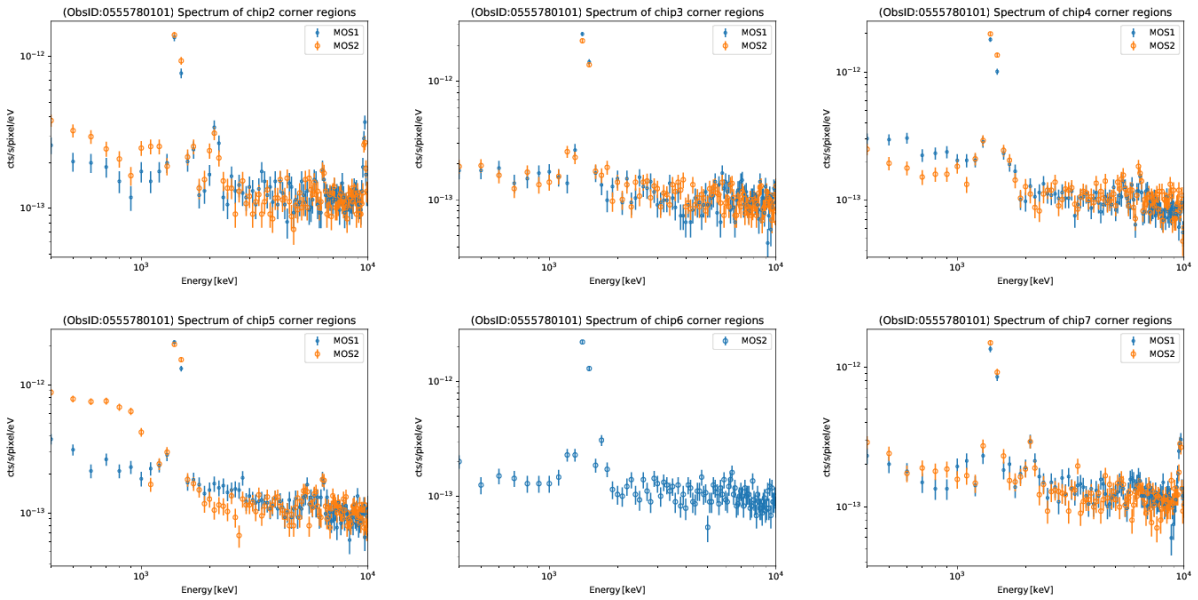


Figure A.7: Same as the previous figure but for 0555780101

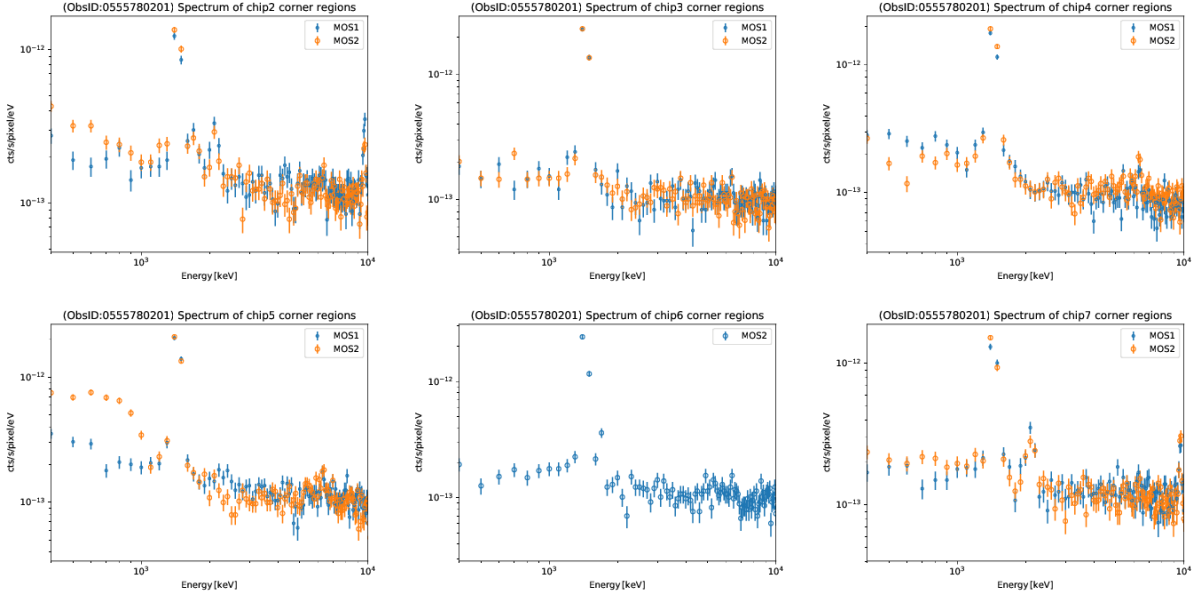


Figure A.8: Same as the previous figure but for 0555780201

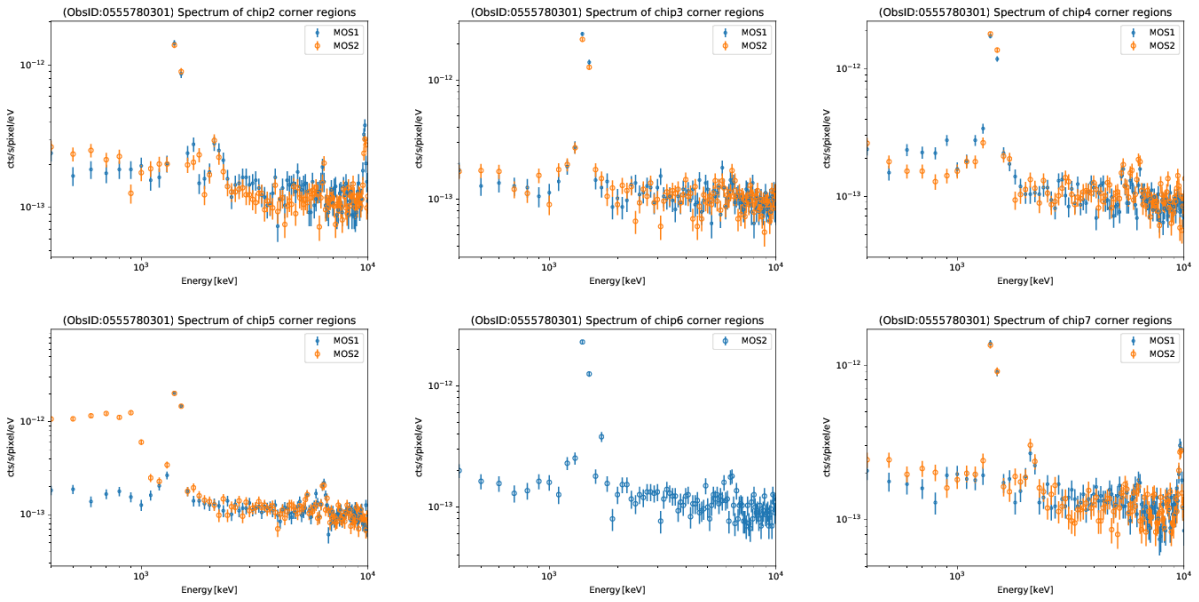


Figure A.9: Same as the previous figure but for 0555780301

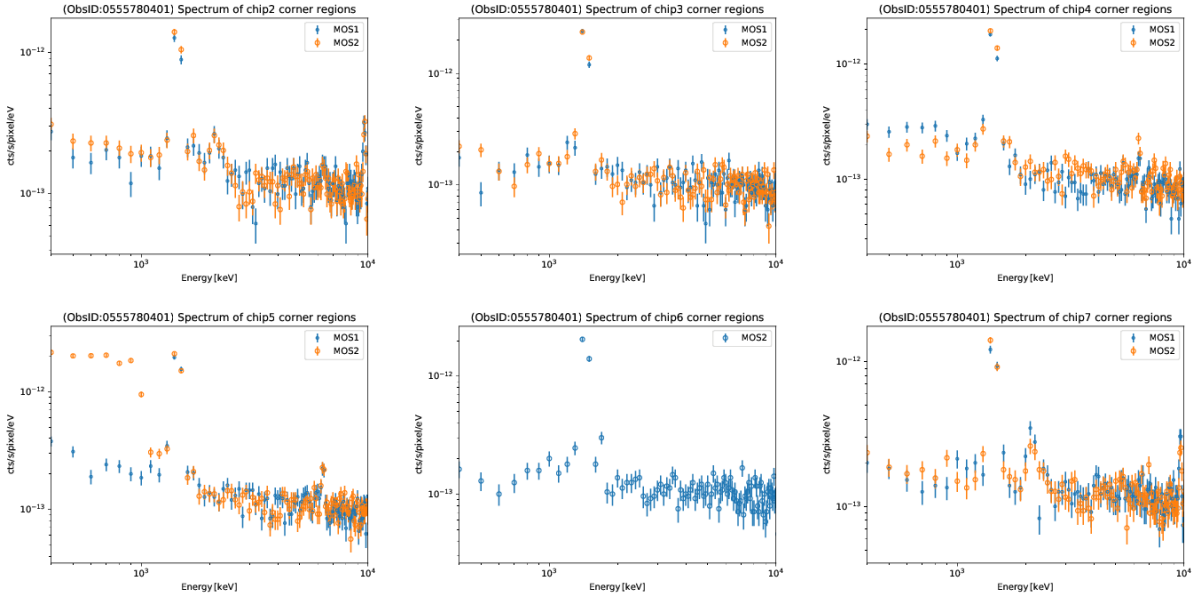


Figure A.10: Same as the previous figure but for 0555780401

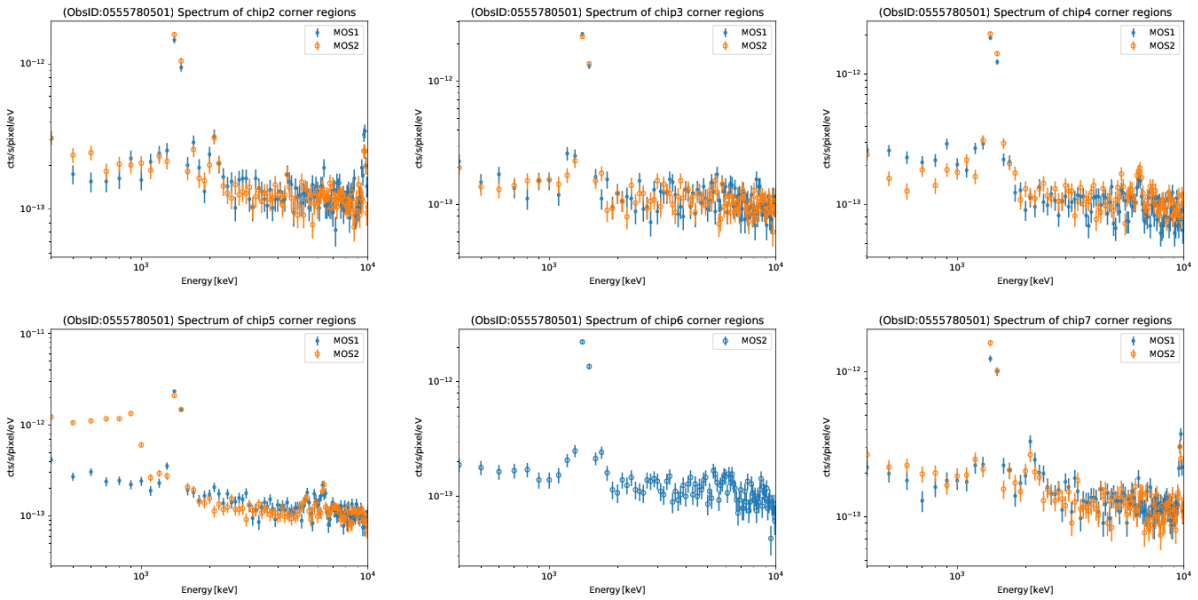


Figure A.11: Same as the previous figure but for 0555780501

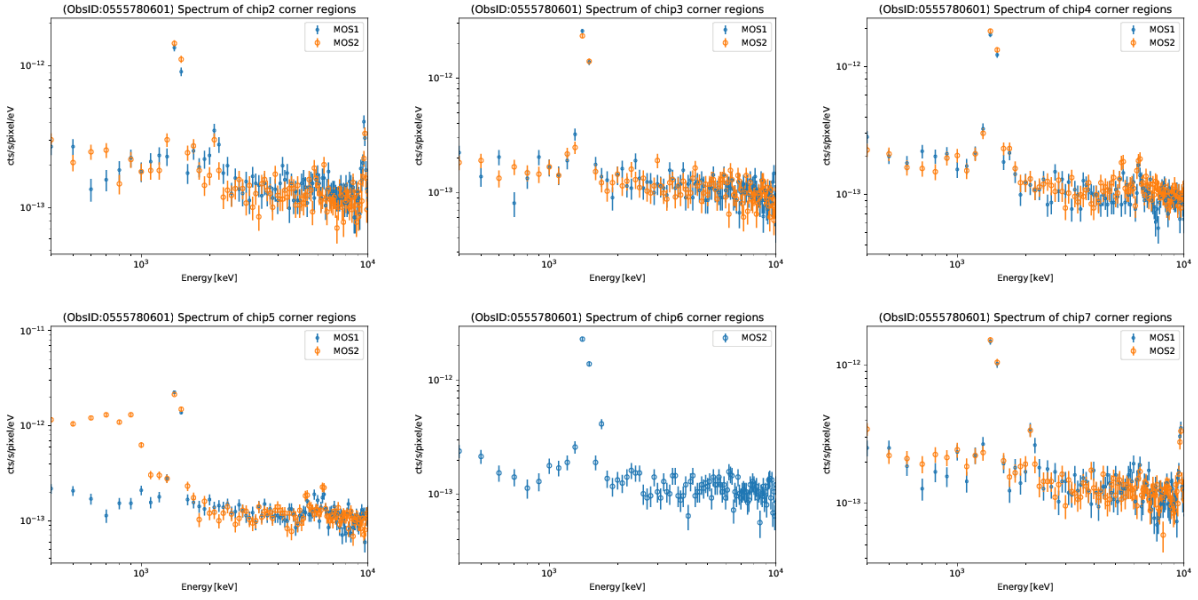


Figure A.12: Same as the previous figure but for 0555780601

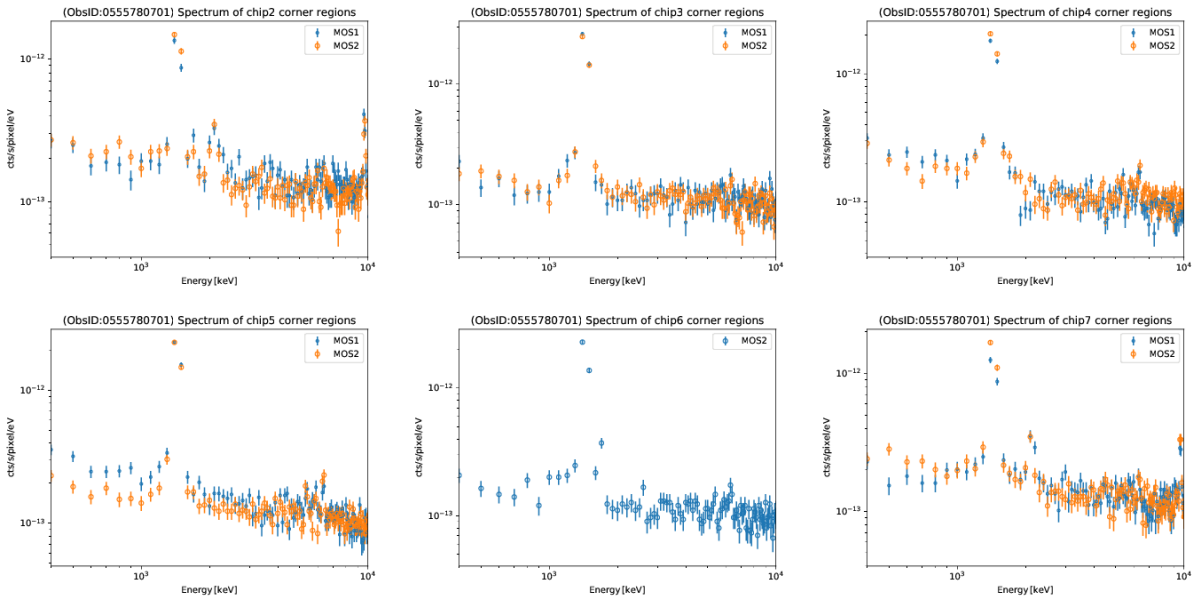


Figure A.13: Same as the previous figure but for 0555780701

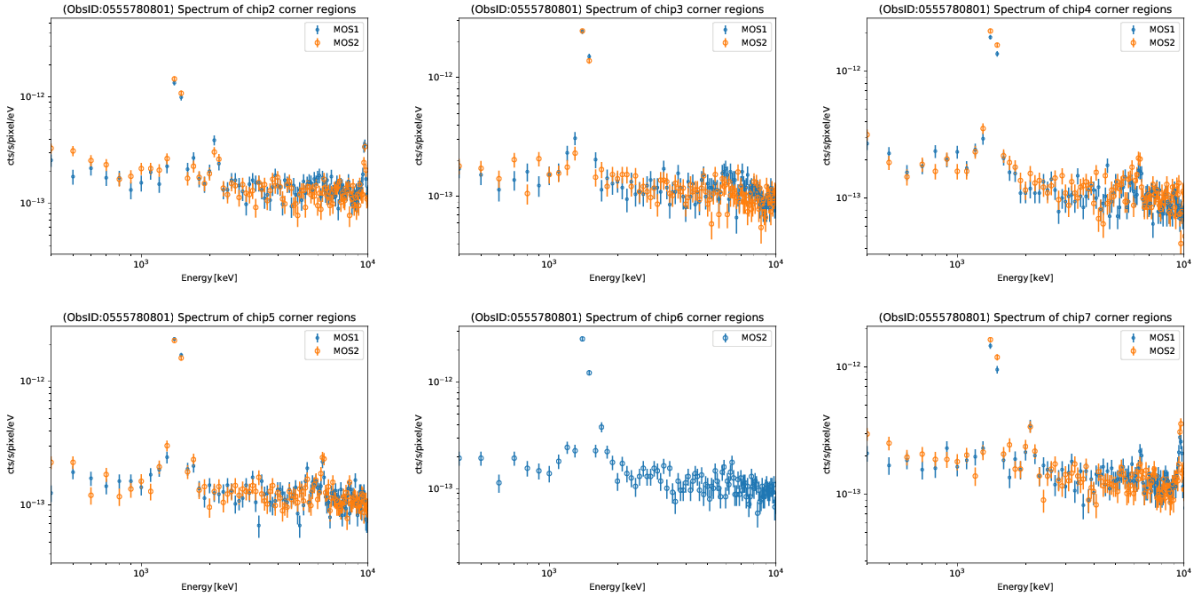


Figure A.14: Same as the previous figure but for 0555780801

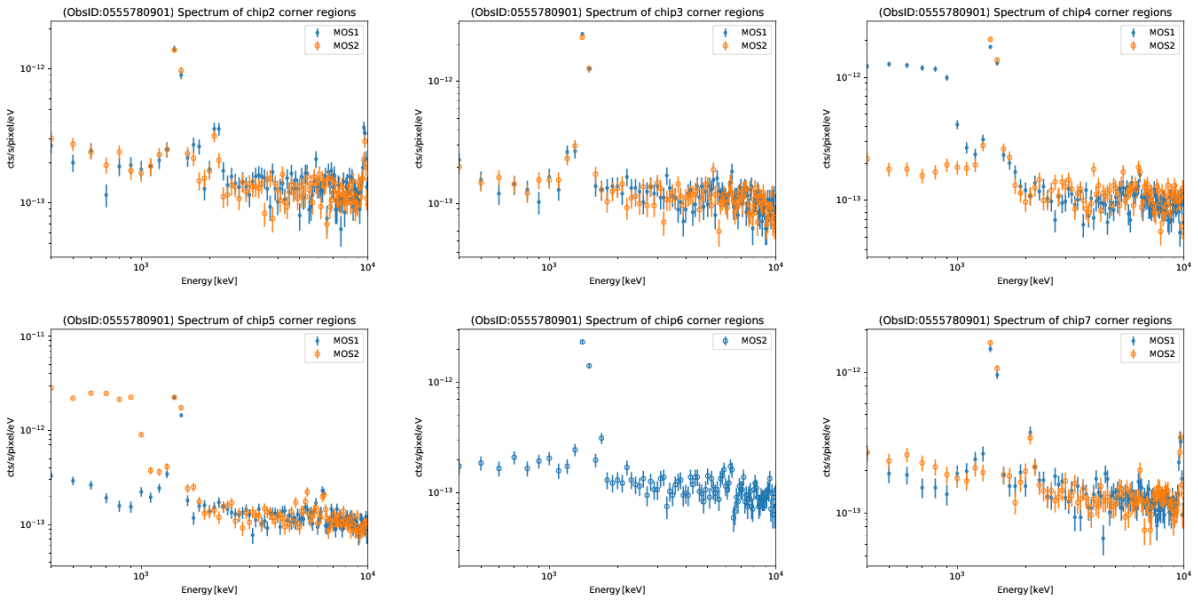


Figure A.15: Same as the previous figure but for 0555780901

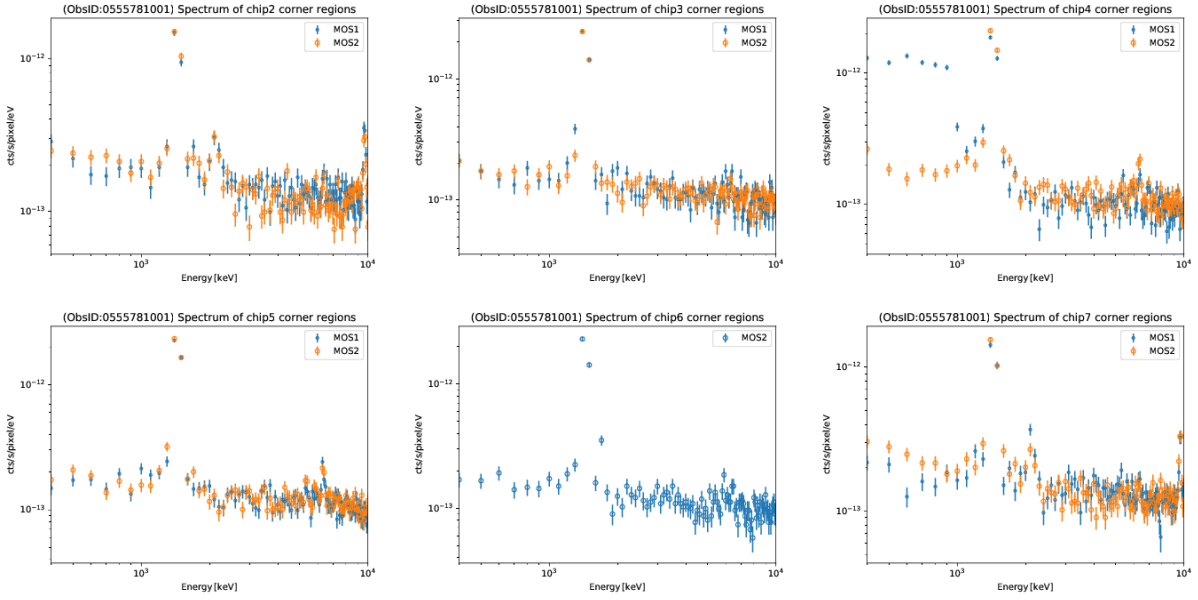


Figure A.16: Same as the previous figure but for 0555781001

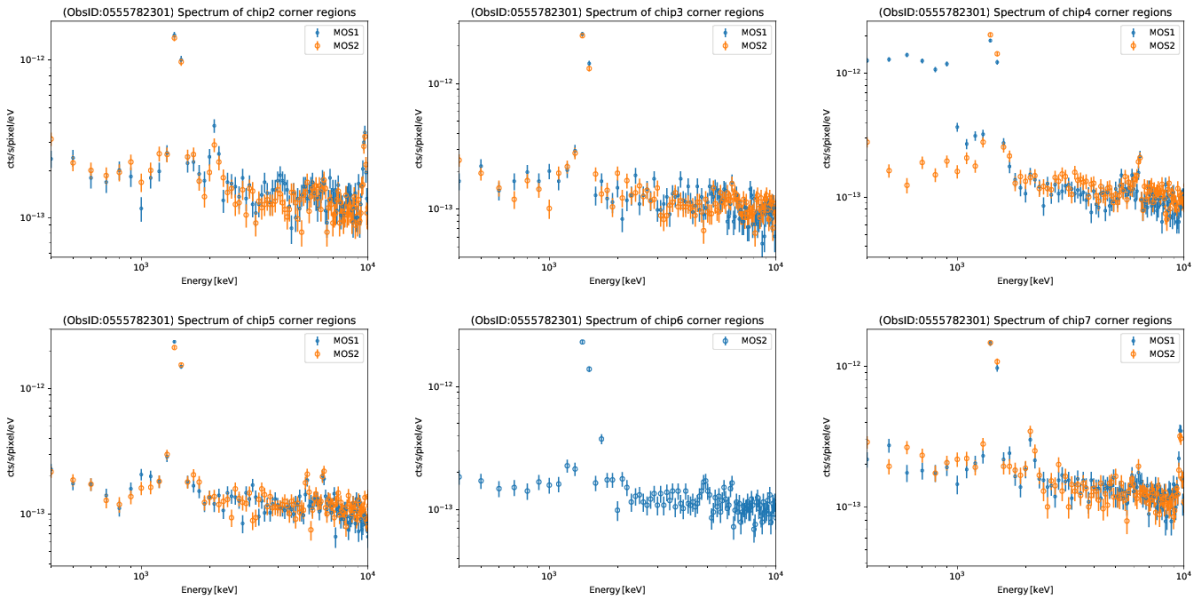


Figure A.17: Same as the previous figure but for 0555782301

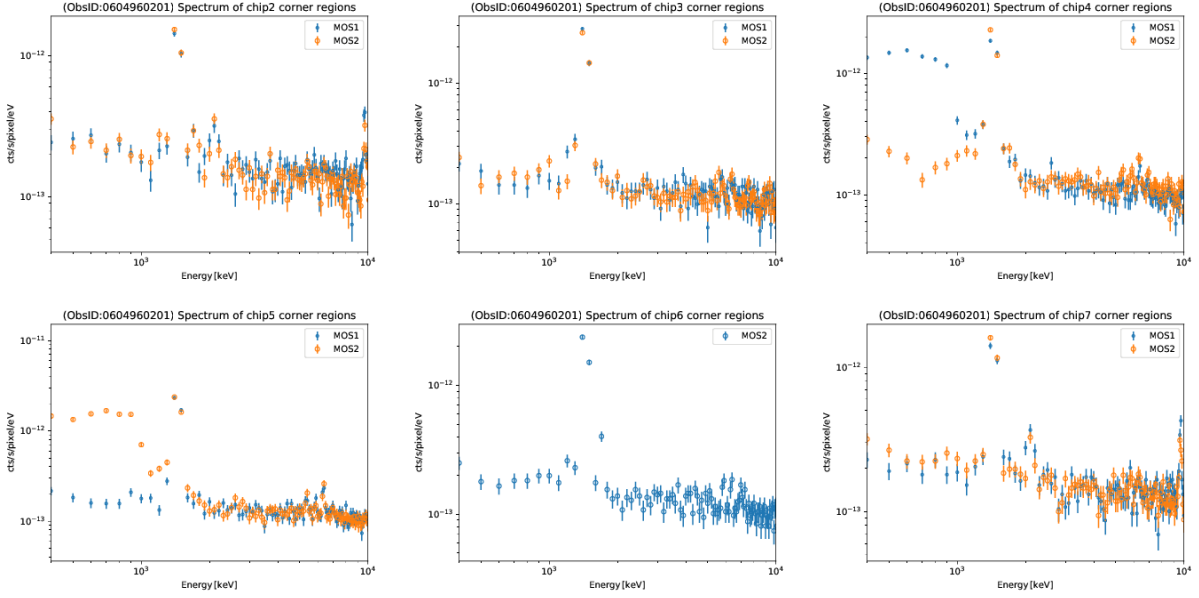


Figure A.18: Same as the previous figure but for 0604960201

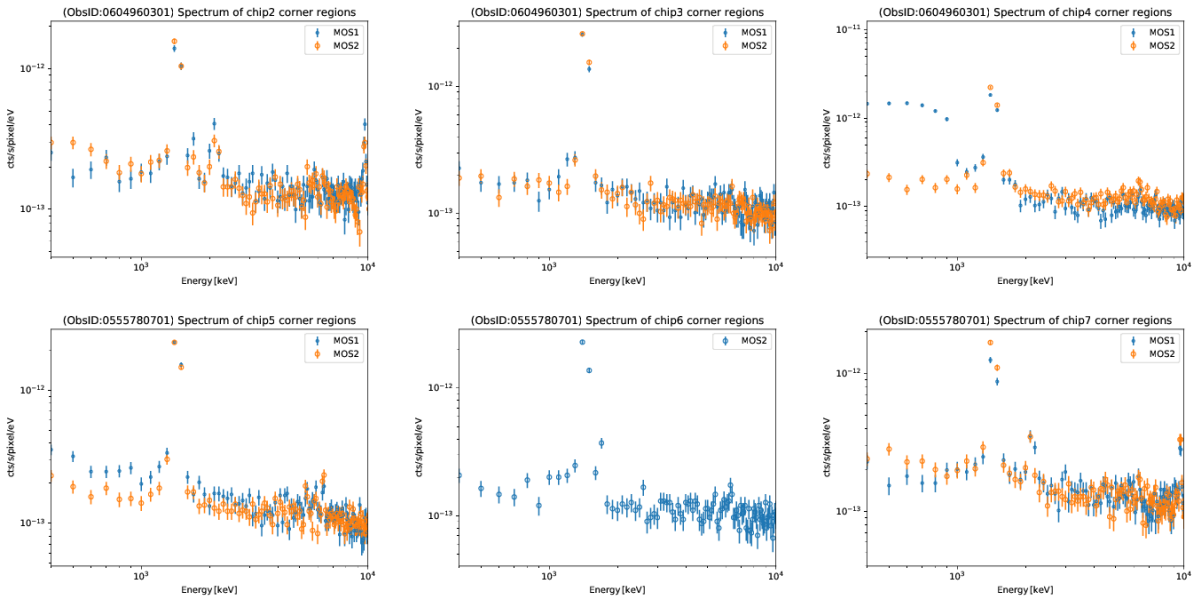


Figure A.19: Same as the previous figure but for 0604960301

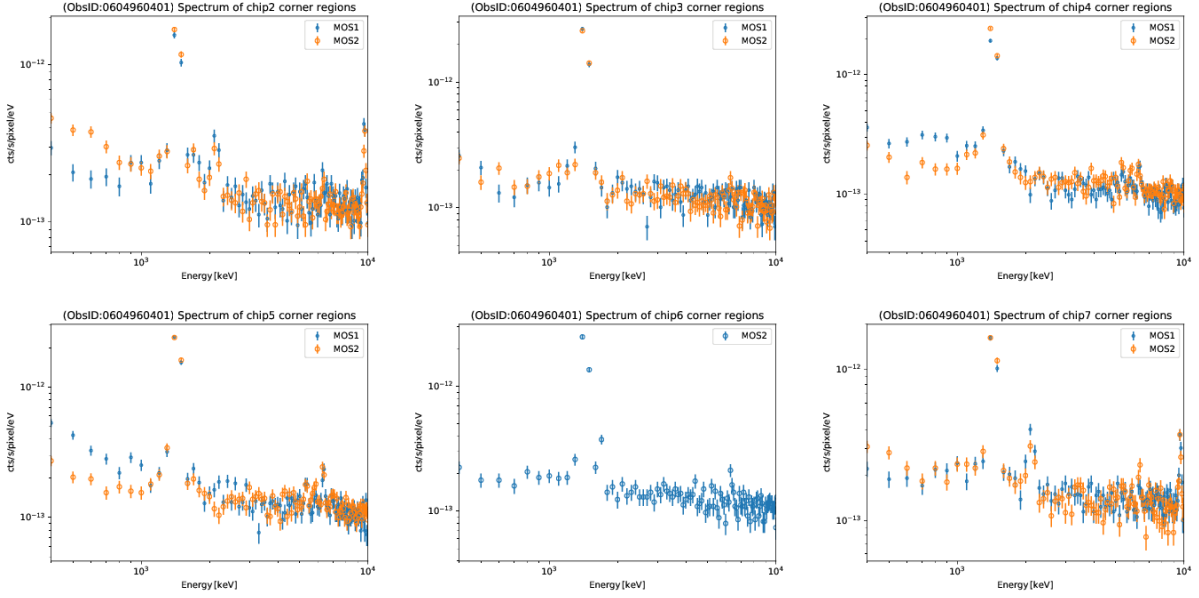


Figure A.20: Same as the previous figure but for 0604960401

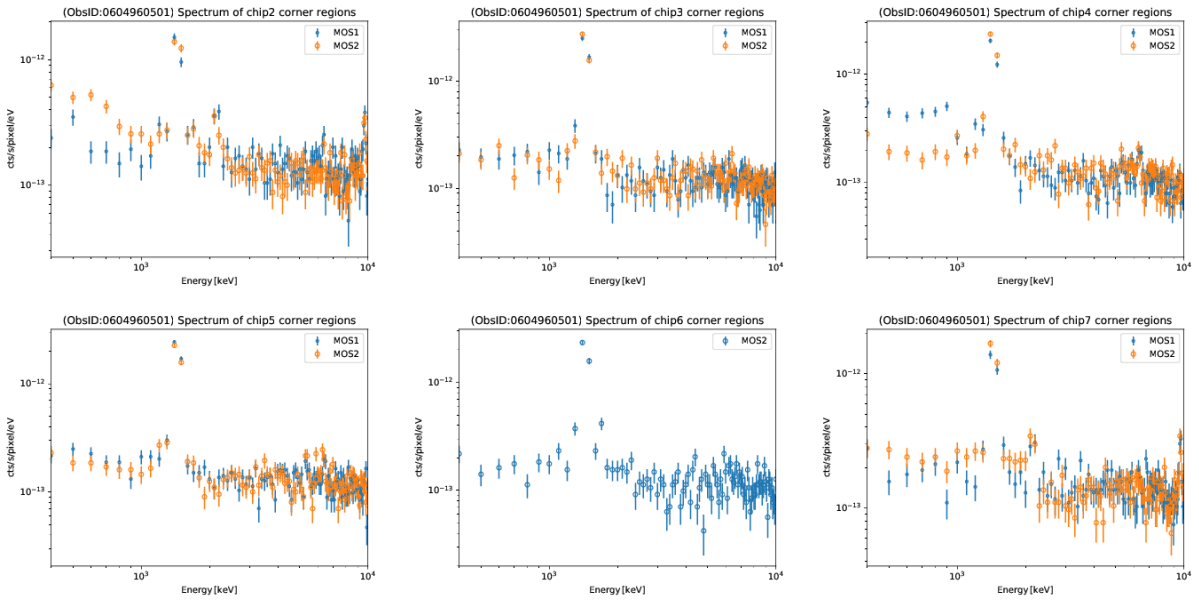


Figure A.21: Same as the previous figure but for 0604960501

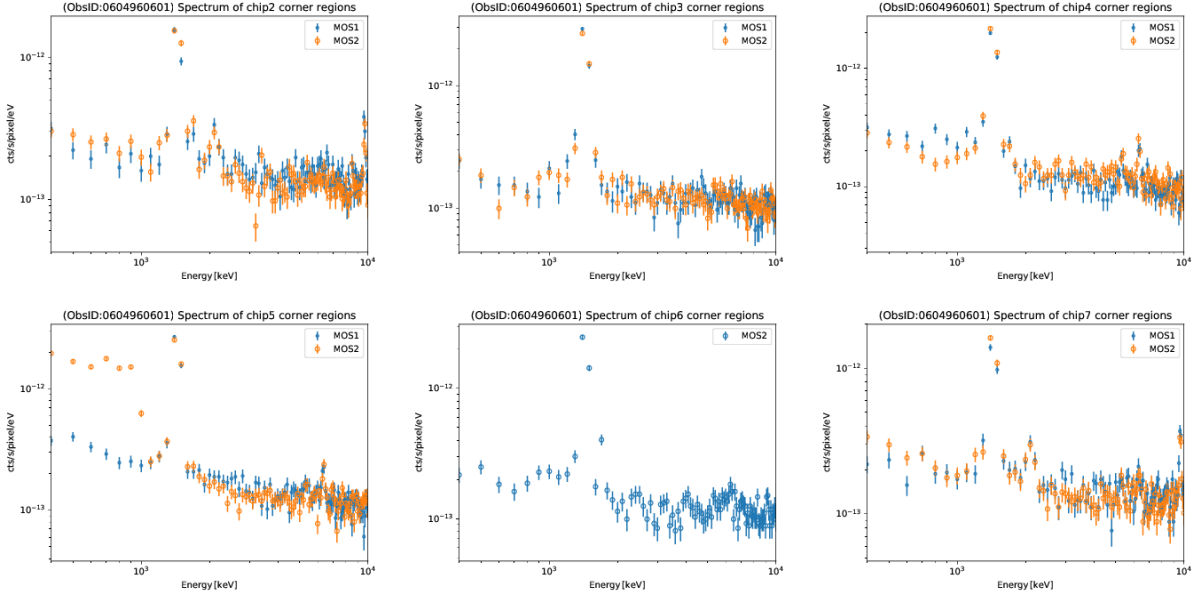


Figure A.22: Same as the previous figure but for 0604960601

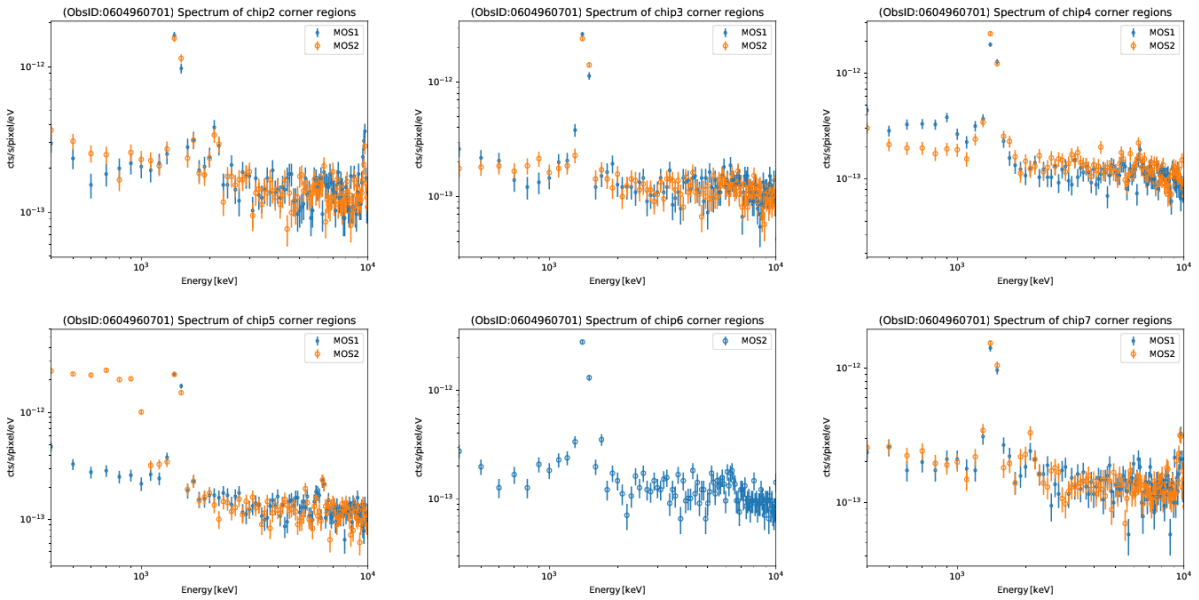


Figure A.23: Same as the previous figure but for 0604960701

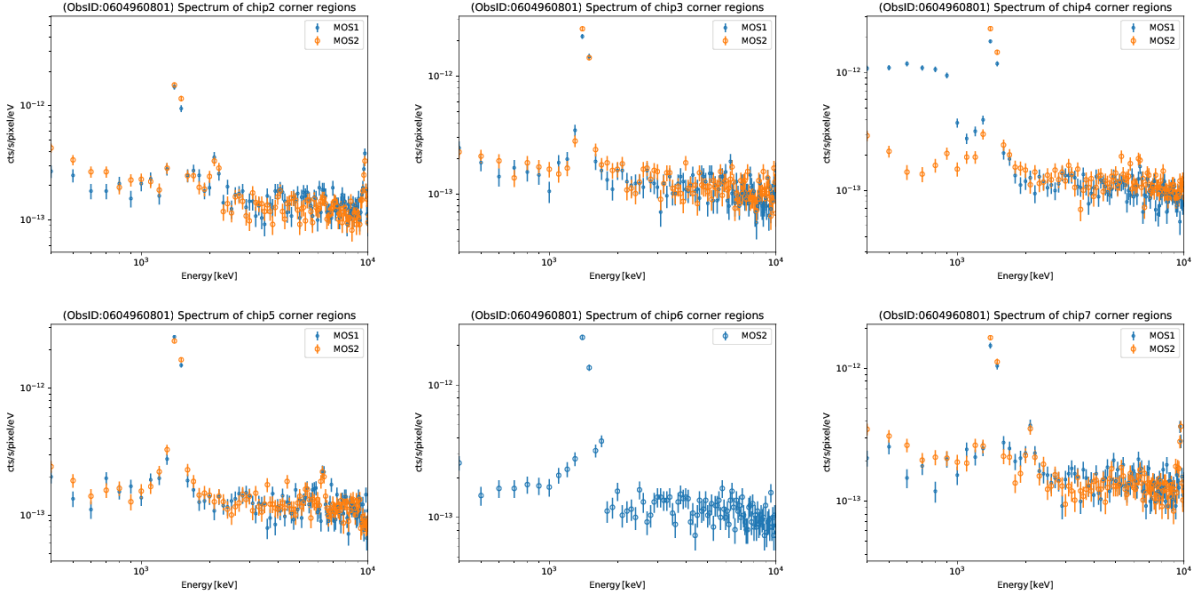


Figure A.24: Same as the previous figure but for 0604960801

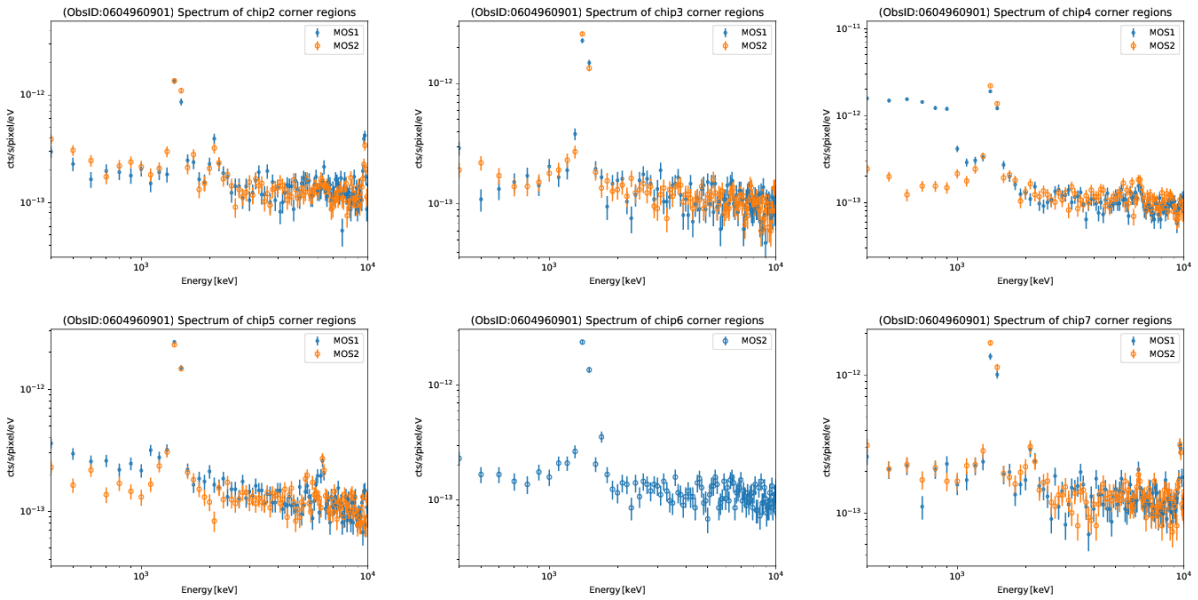


Figure A.25: Same as the previous figure but for 0604960901

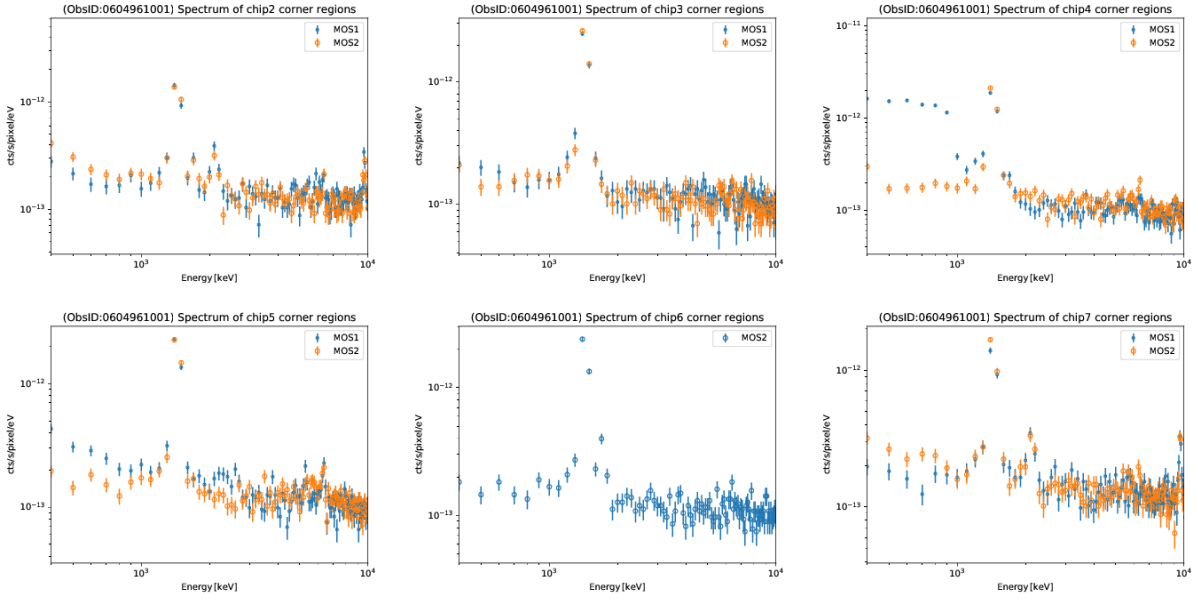


Figure A.26: Same as the previous figure but for 0604961001

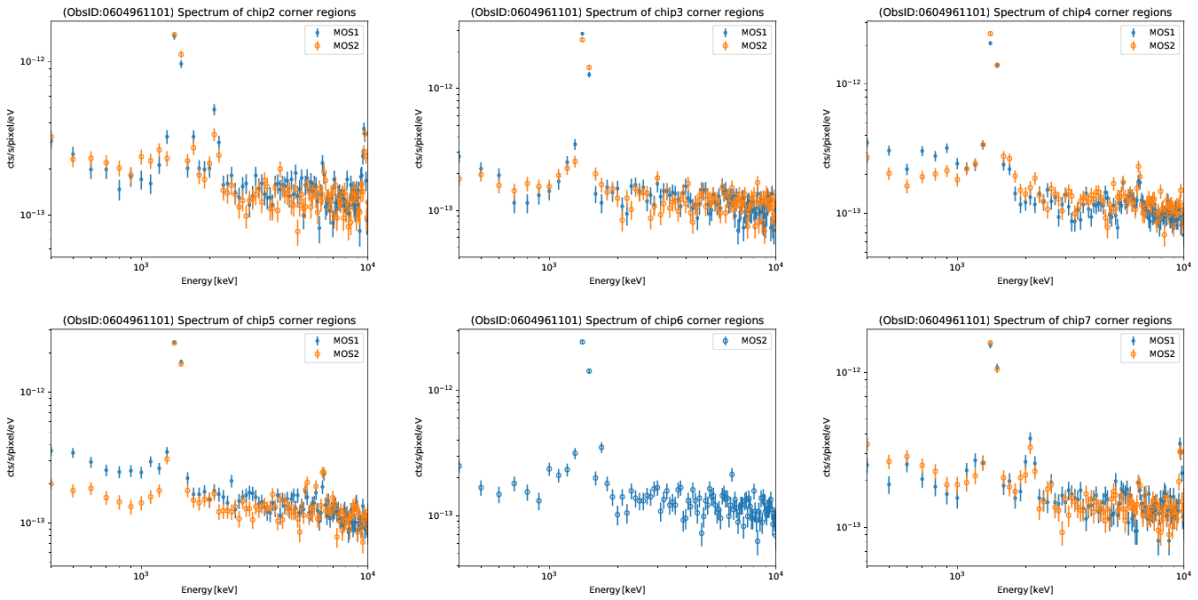


Figure A.27: Same as the previous figure but for 0604961101

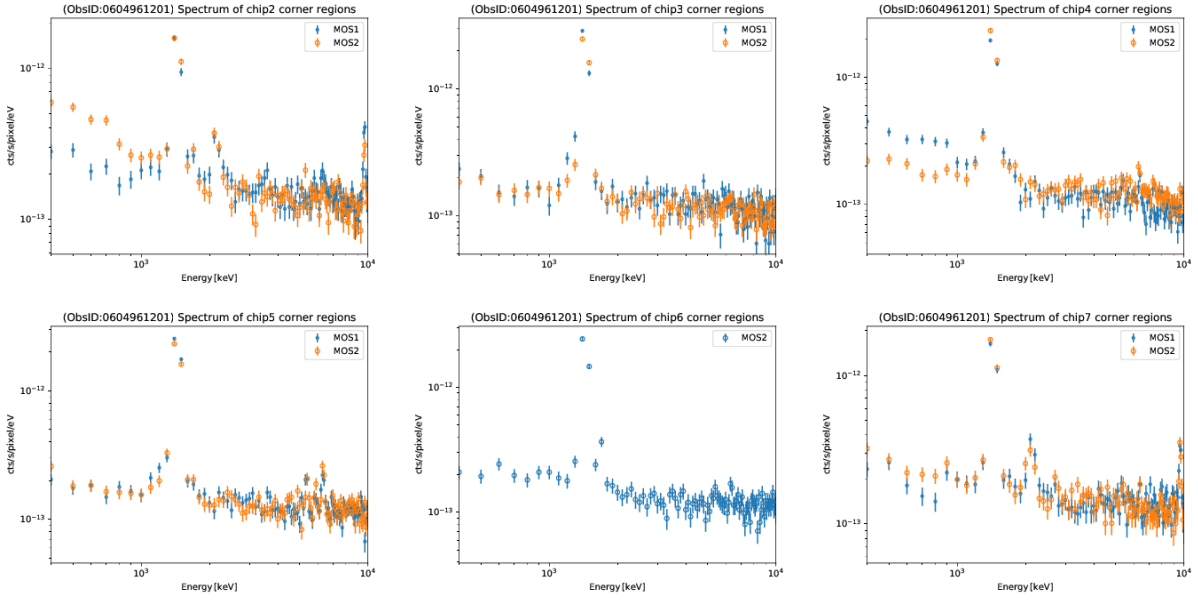


Figure A.28: Same as the previous figure but for 0604961201

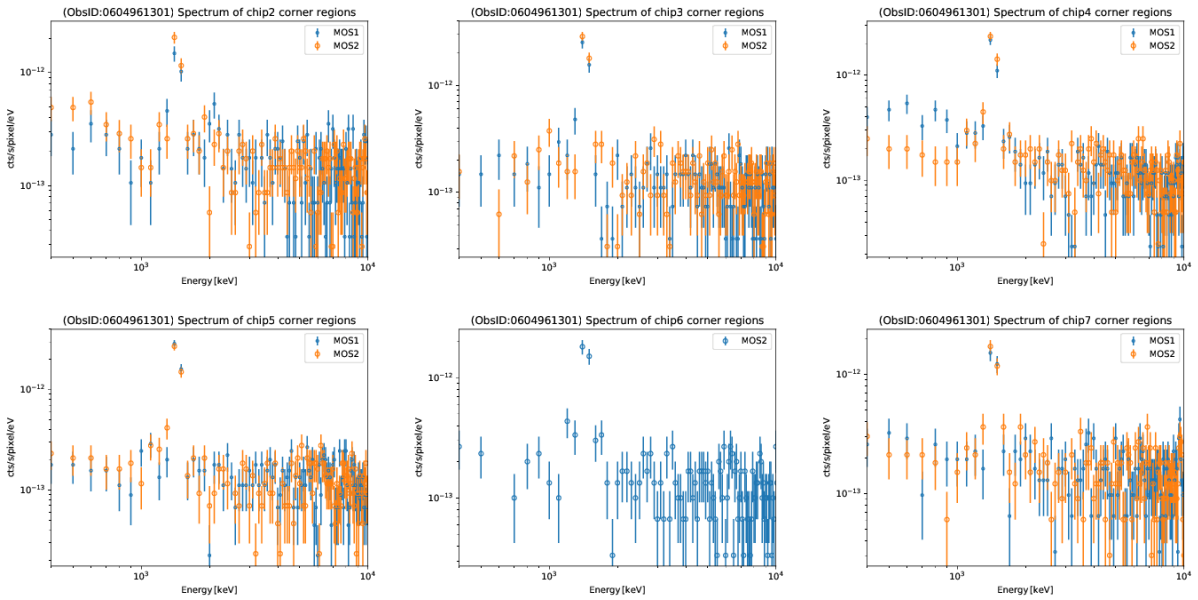


Figure A.29: Same as the previous figure but for 0604961301

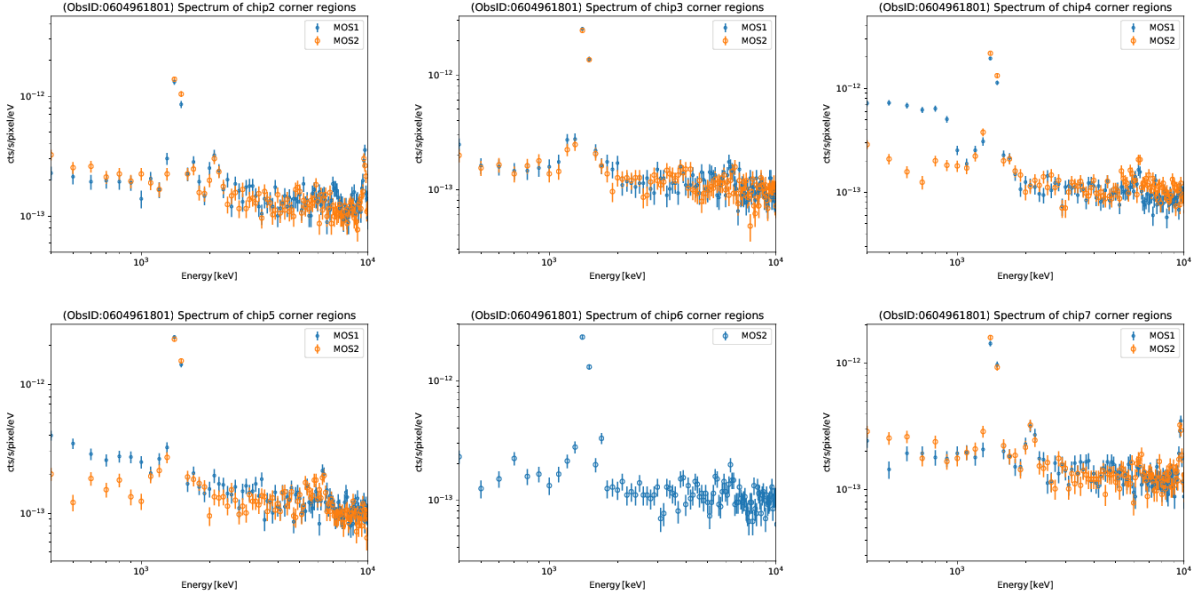


Figure A.30: Same as the previous figure but for 0604961801

## A.2 Light curve and good time interval

In Section 5.5, we investigated all light curves for filtering short-term variation of the soft proton contamination.

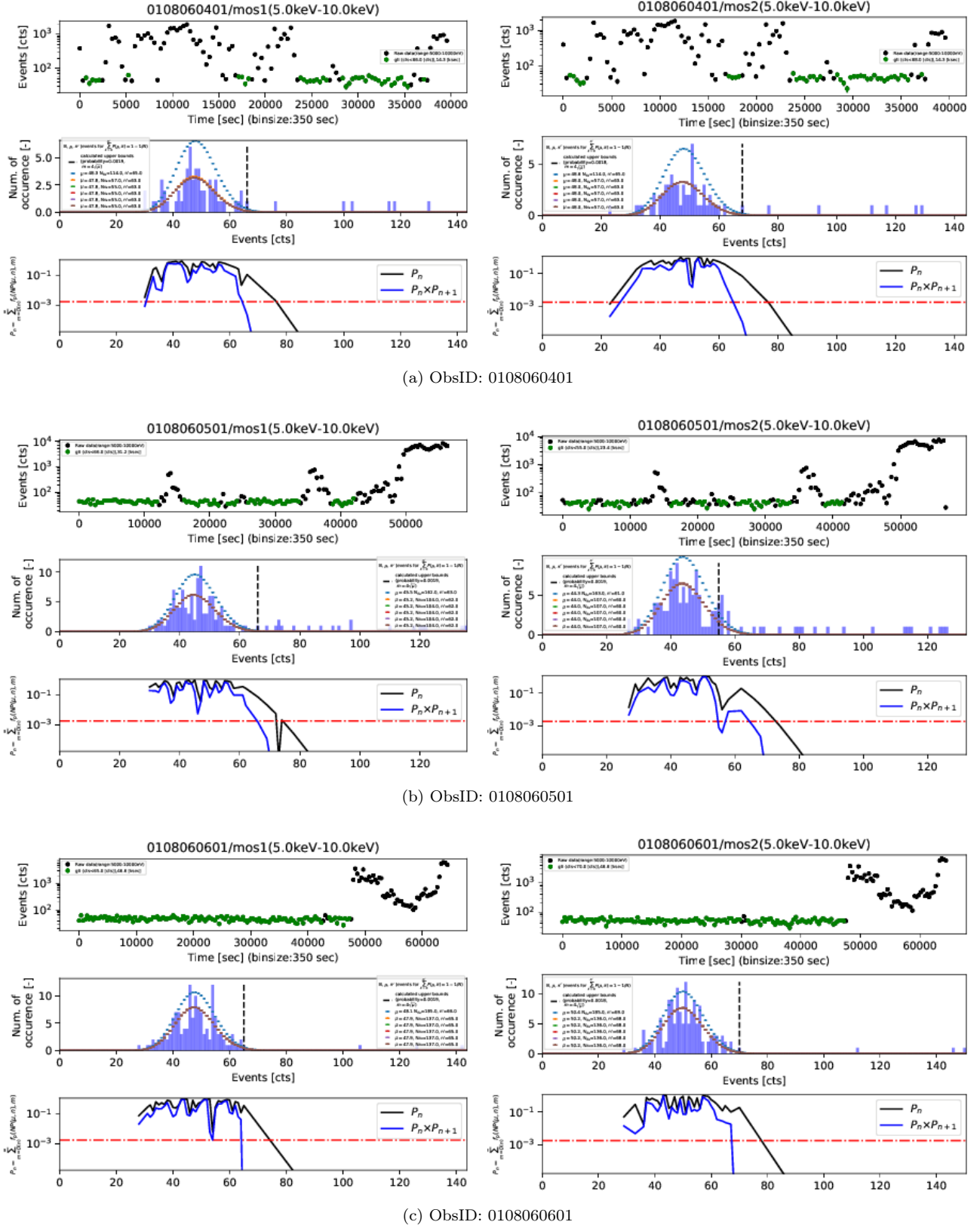


Figure A.31: The left figures are for MOS1 and the right figures are for MOS2, respectively, for different ObsIDs (a), (b) and (c). (upper): Time variation of count rates (light curve) in actual observation in the energy range of 5-10 keV. The accepted time bins are shown in green. (middle): Number of occurrence of time bins ( $D(n)$ ) as a function of number of counts per 350 sec. Results of model fits to the histogram are shown with blue and red curves, Blue curve is for the initial model of the iteration, while red curve for the converged model. (lower): Cumulative probability ( $P_c(n, D(n))$ ) for obtaining the number of occurrence of time bins larger than  $D(n)$  and the product of the two probabilities in the successive two bins,  $P_c(n, D(n))P_c(n+1, D(n+1))$ . The red horizontal dotted corresponds to  $P_{Th} = 0.05$  according to Equation (5.11).

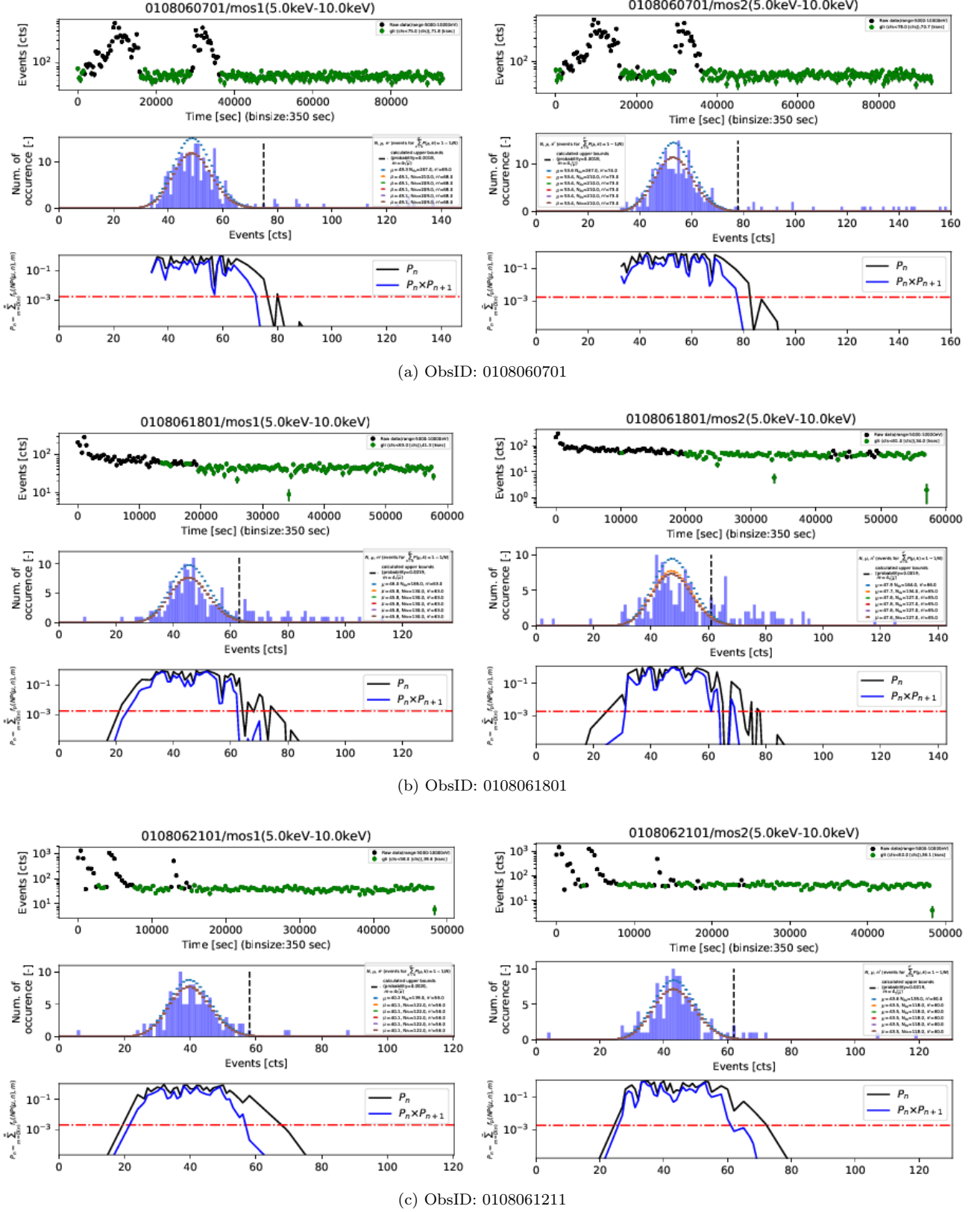


Figure A.32: Same as the previous figure for different ObsIDs

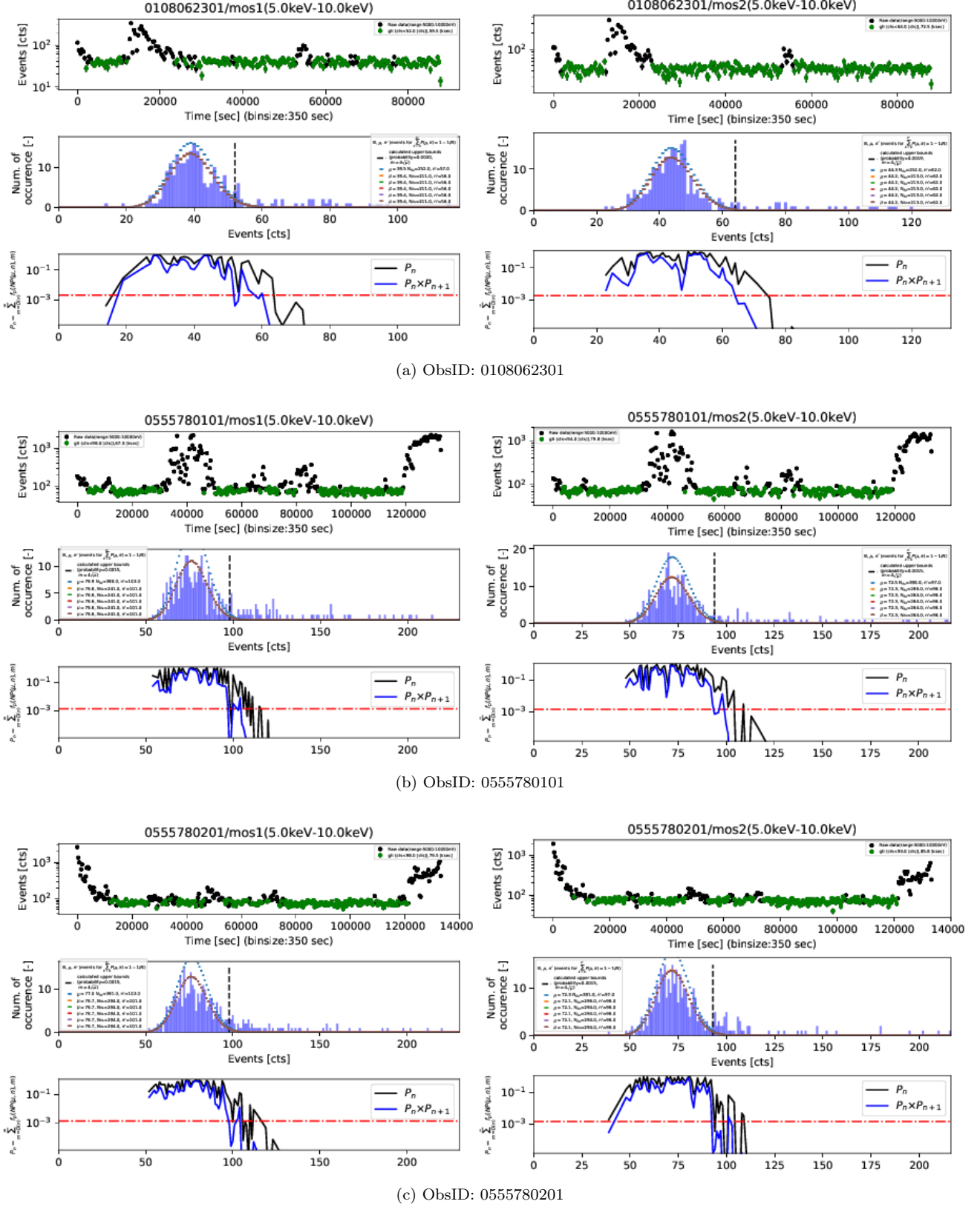


Figure A.33: Same as the previous figure for different ObsIDs

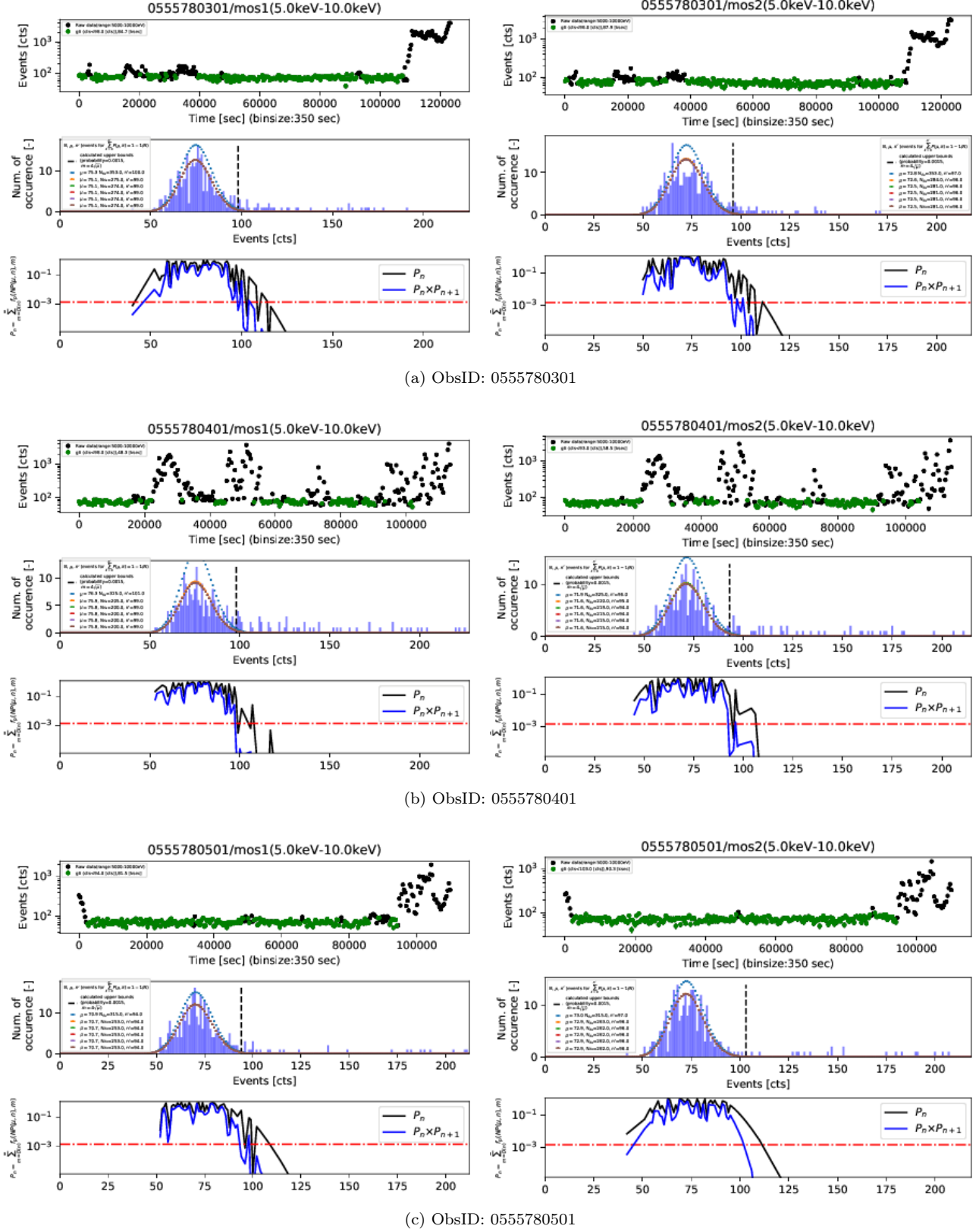


Figure A.34: Same as the previous figure for different ObsIDs

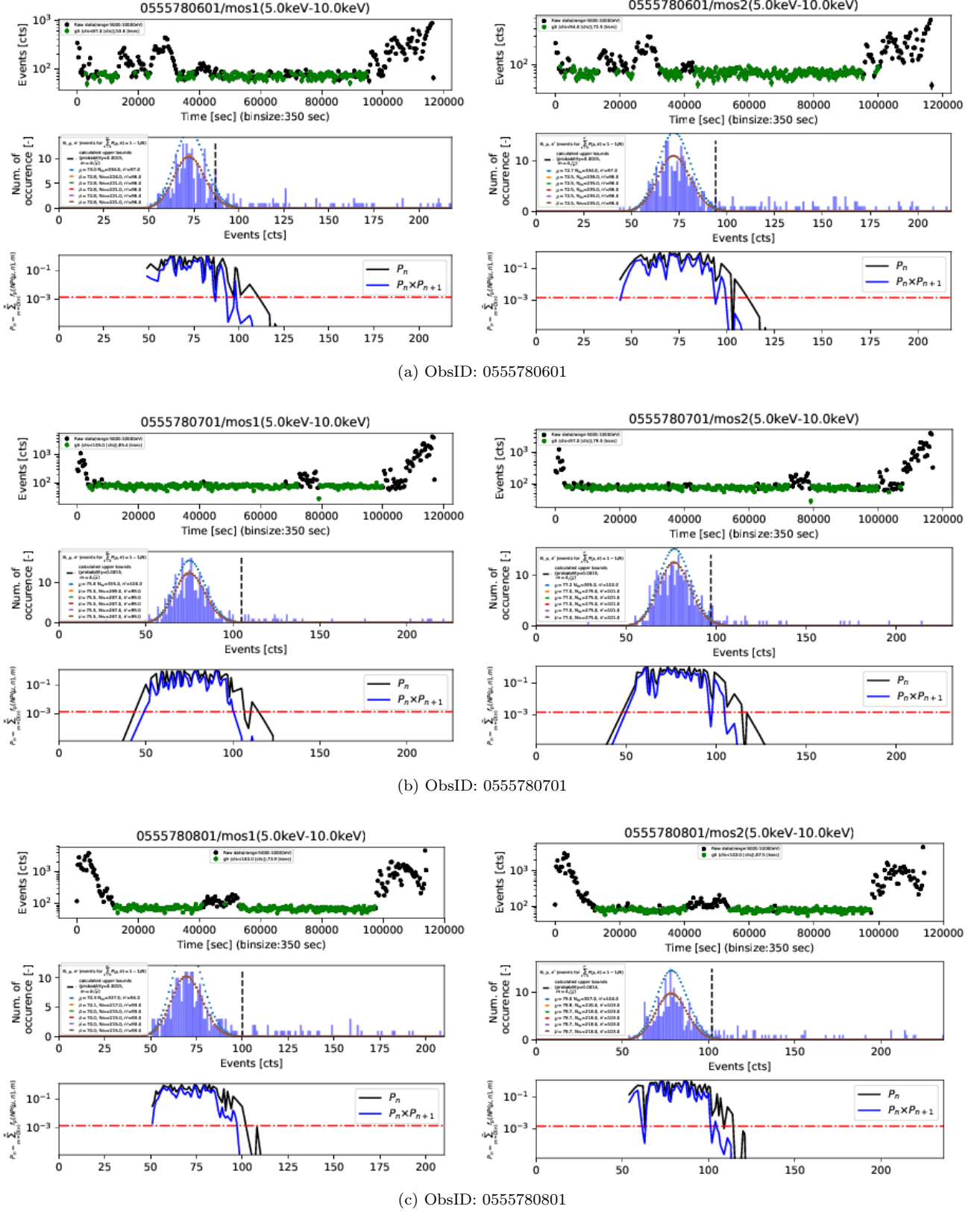


Figure A.35: Same as the previous figure for different ObsIDs

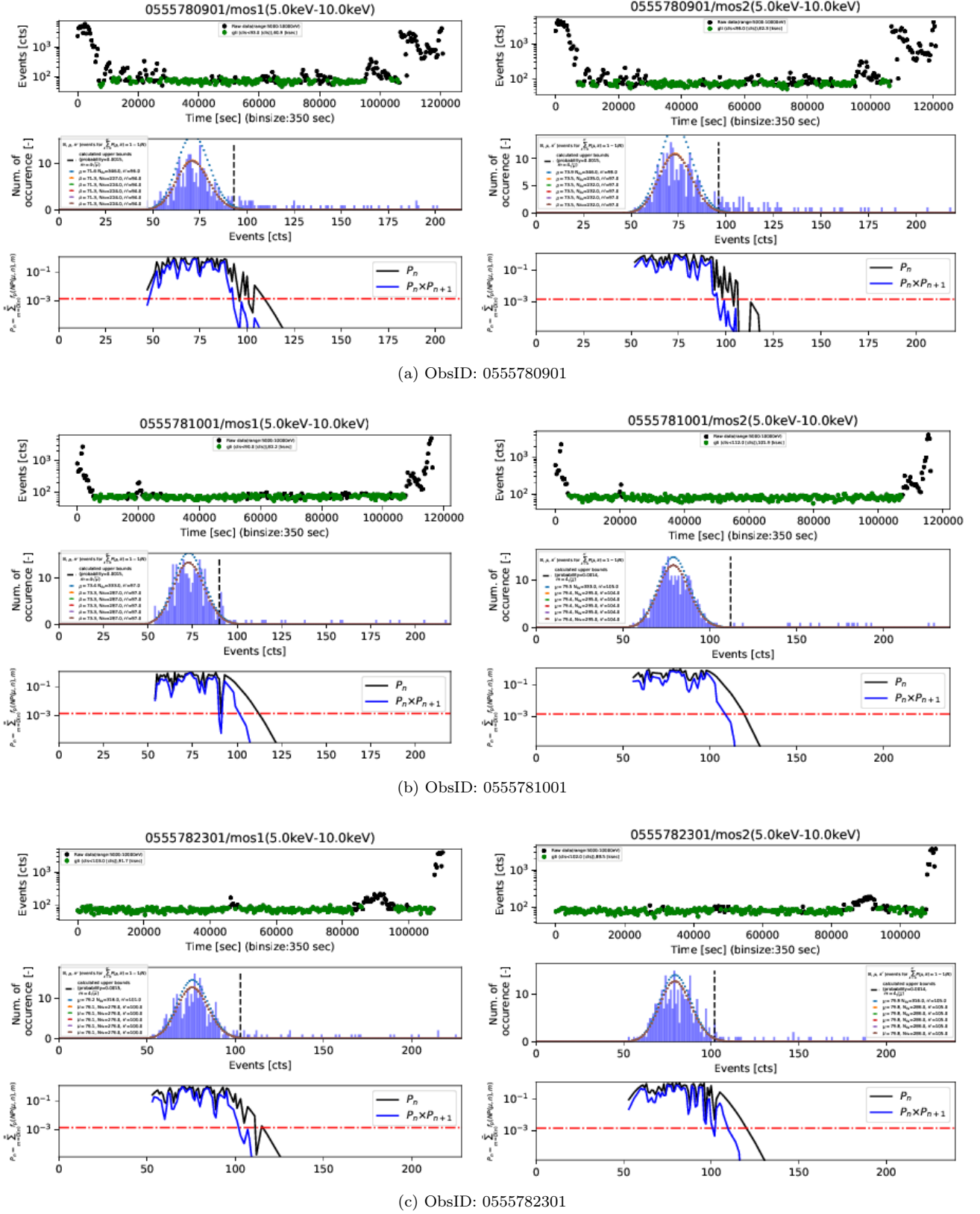


Figure A.36: Same as the previous figure for different ObsIDs

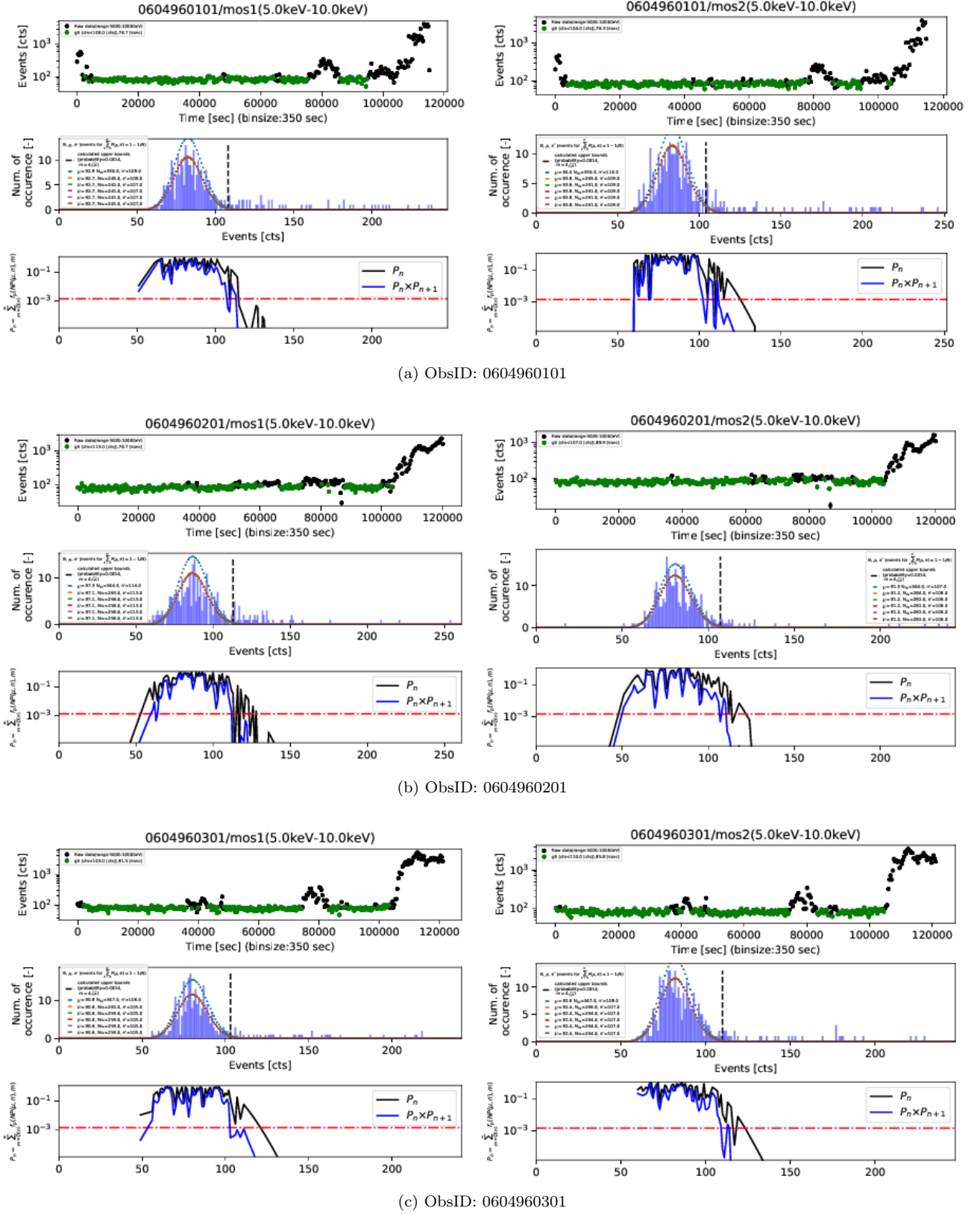


Figure A.37: Same as the previous figure for different ObsIDs

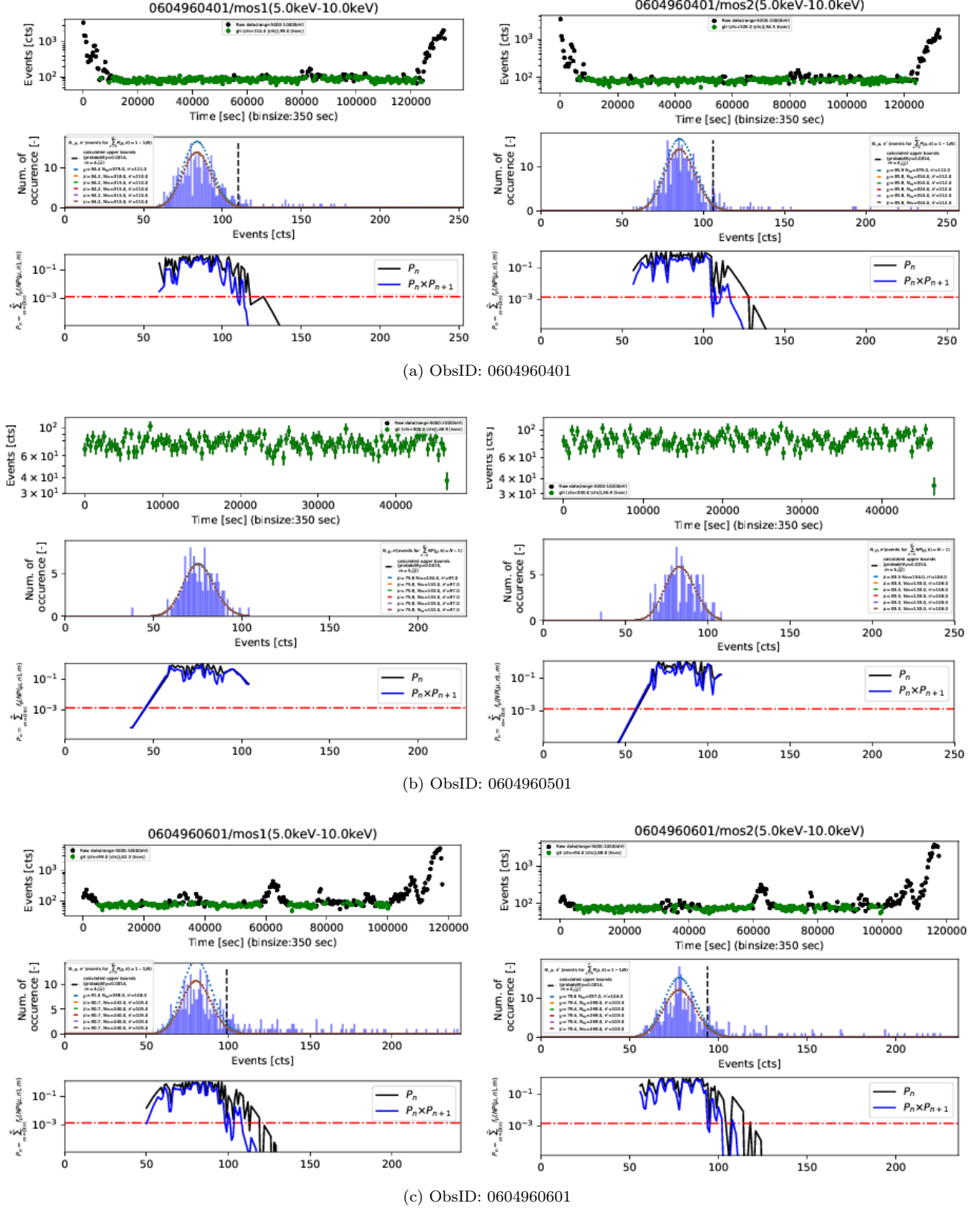


Figure A.38: Same as the previous figure for different ObsIDs

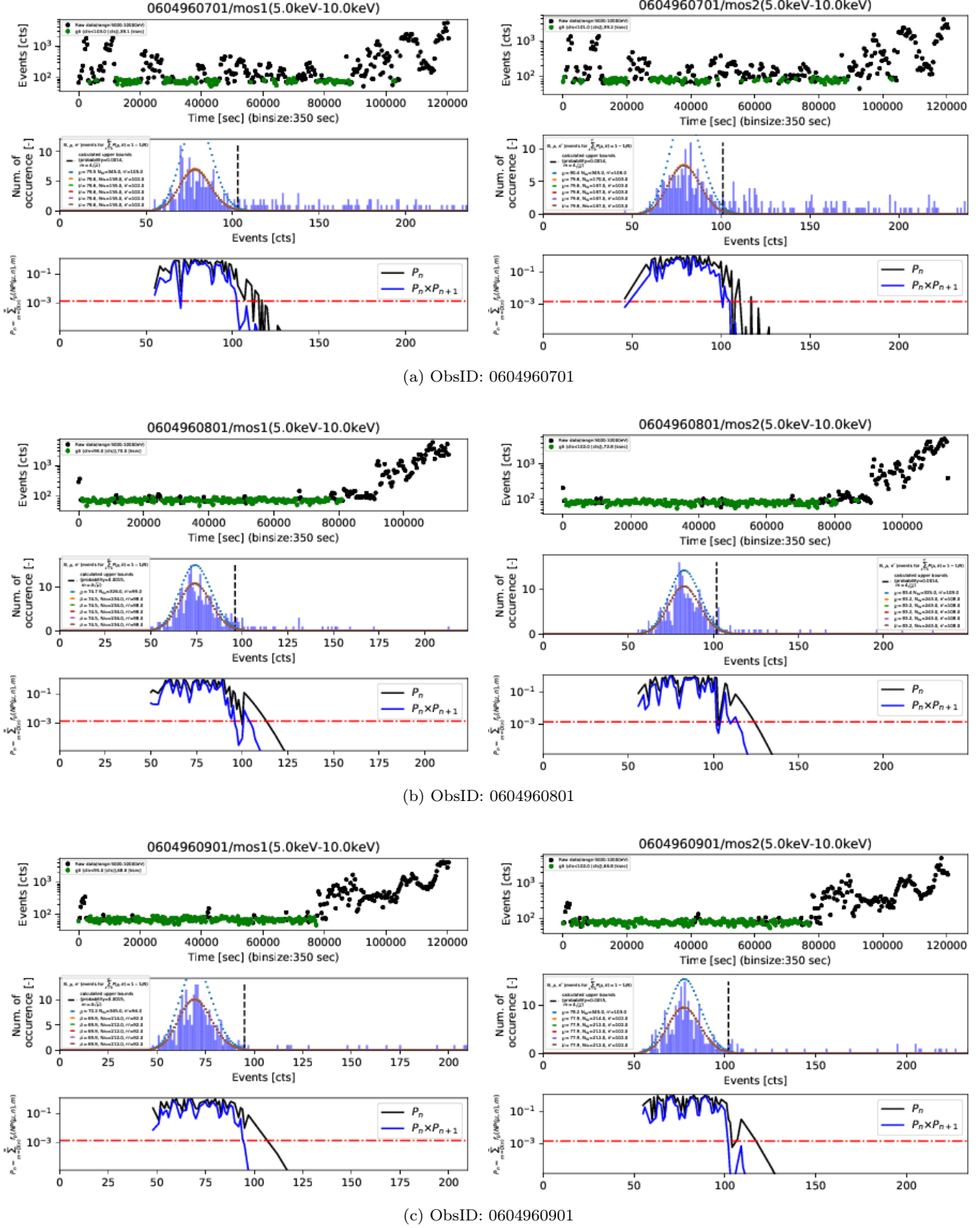


Figure A.39: Same as the previous figure for different ObsIDs

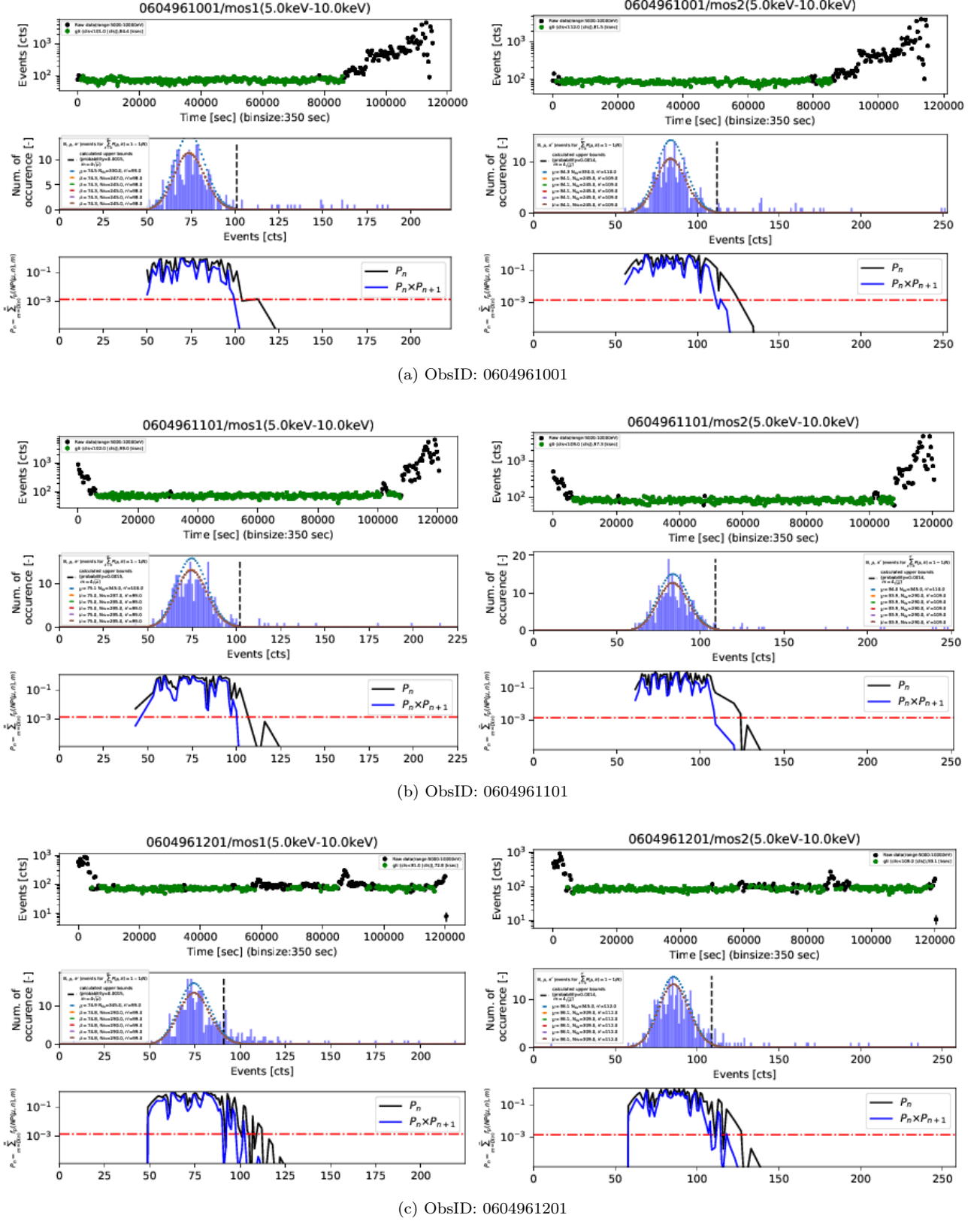
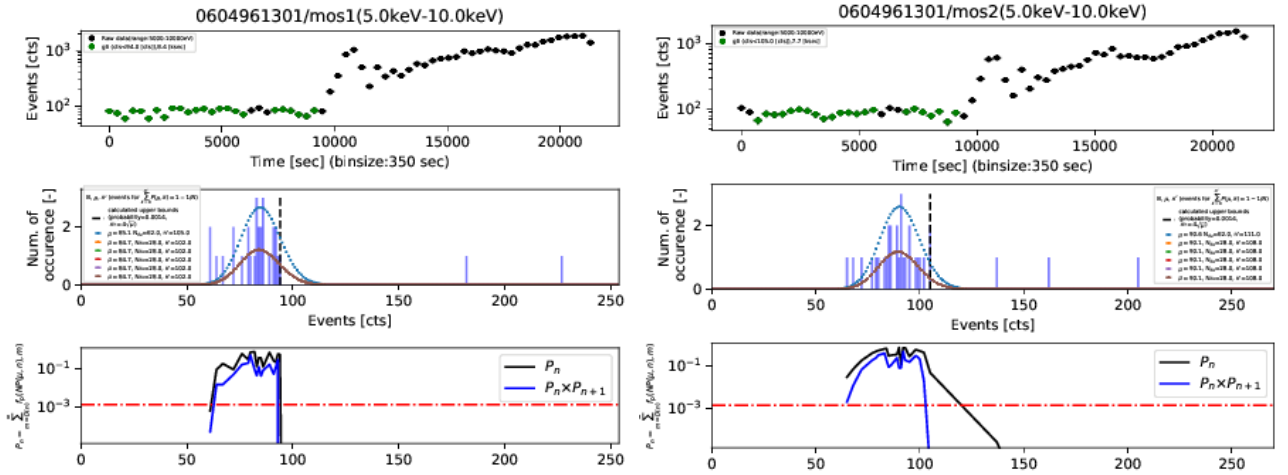
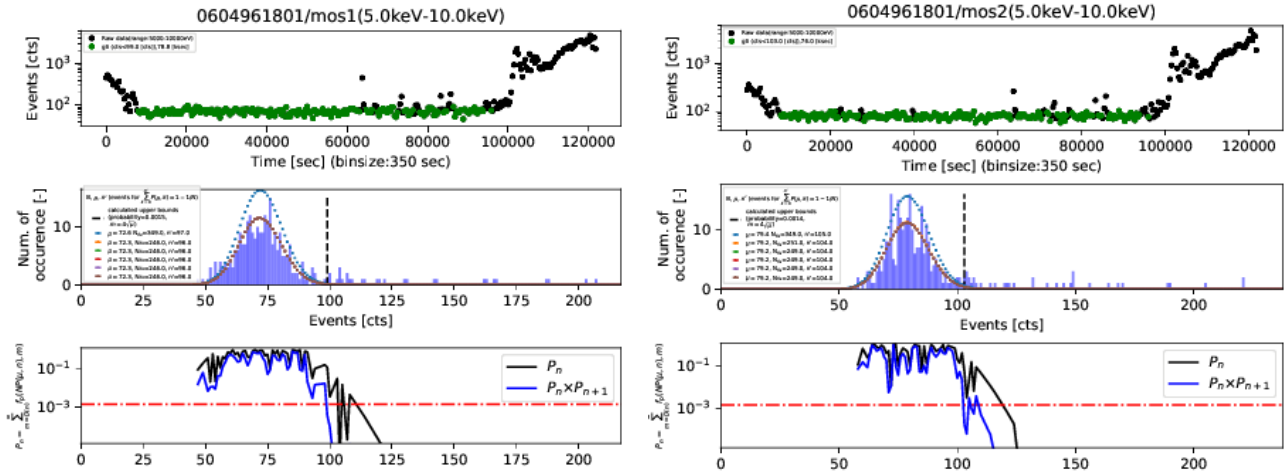


Figure A.40: Same as the previous figure for different ObsIDs



(a) ObsID: 0604961301



(b) ObsID: 0604961801

Figure A.41: Same as the previous figure for different ObsIDs

### A.3 Observed images in 0.4-1 keV and region for extracting spectrum for MOS2

In Subsection 5.7.5, we discussed the masked region. In this section, the observed images in 0.4-1 keV and the point-source free regions are shown for all ObsIDs. The *Chandra* and *XMM-Newton* overlapping region is also indicated in the figures.

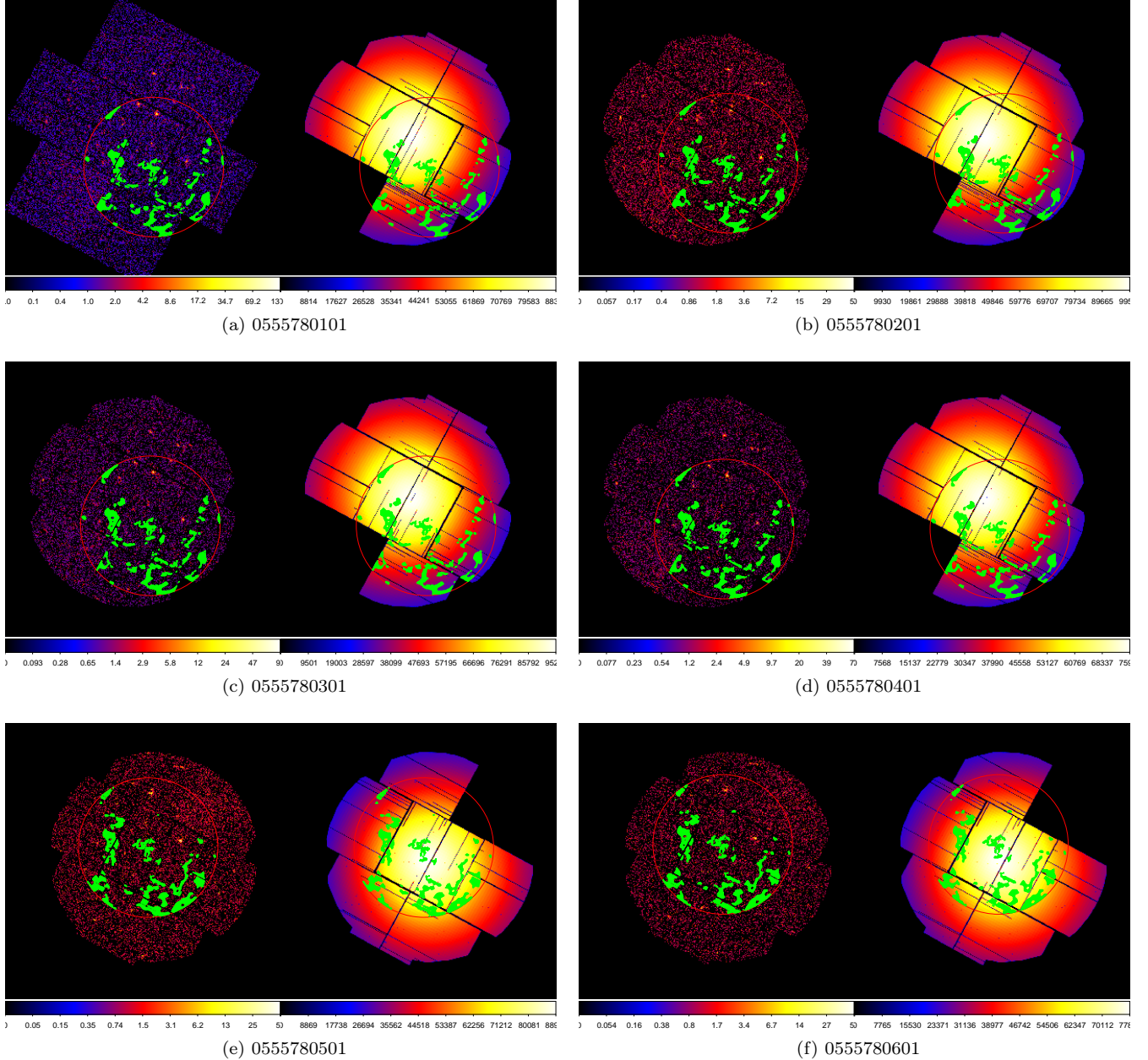


Figure A.42: The observed image (left) and exposure map (right) by MOS2 in 0.4-1 keV for different ObsIDs from (a) to (f). The green boxes indicate point-source free regions used to extract spectrum for MOS2. The red circle indicates the overlapping region between *XMM-Newton* and *Chandra*. The radius is 9.54 arcmin. The green boxes are regions used to extract the spectra.

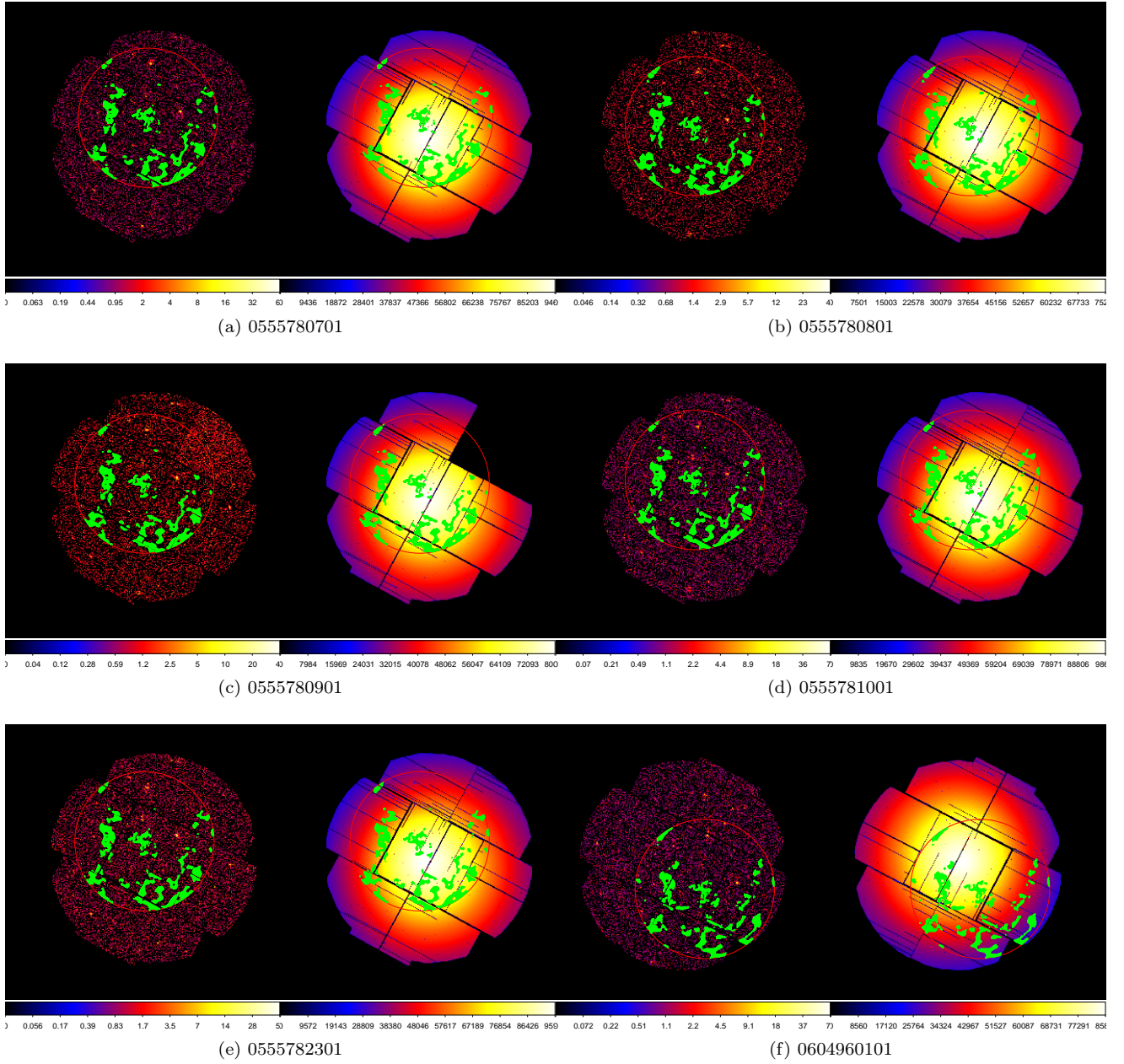


Figure A.43: The observed images and exposure maps by MOS2 in 0.4-1 keV for different ObsIDs from (a) to (f).

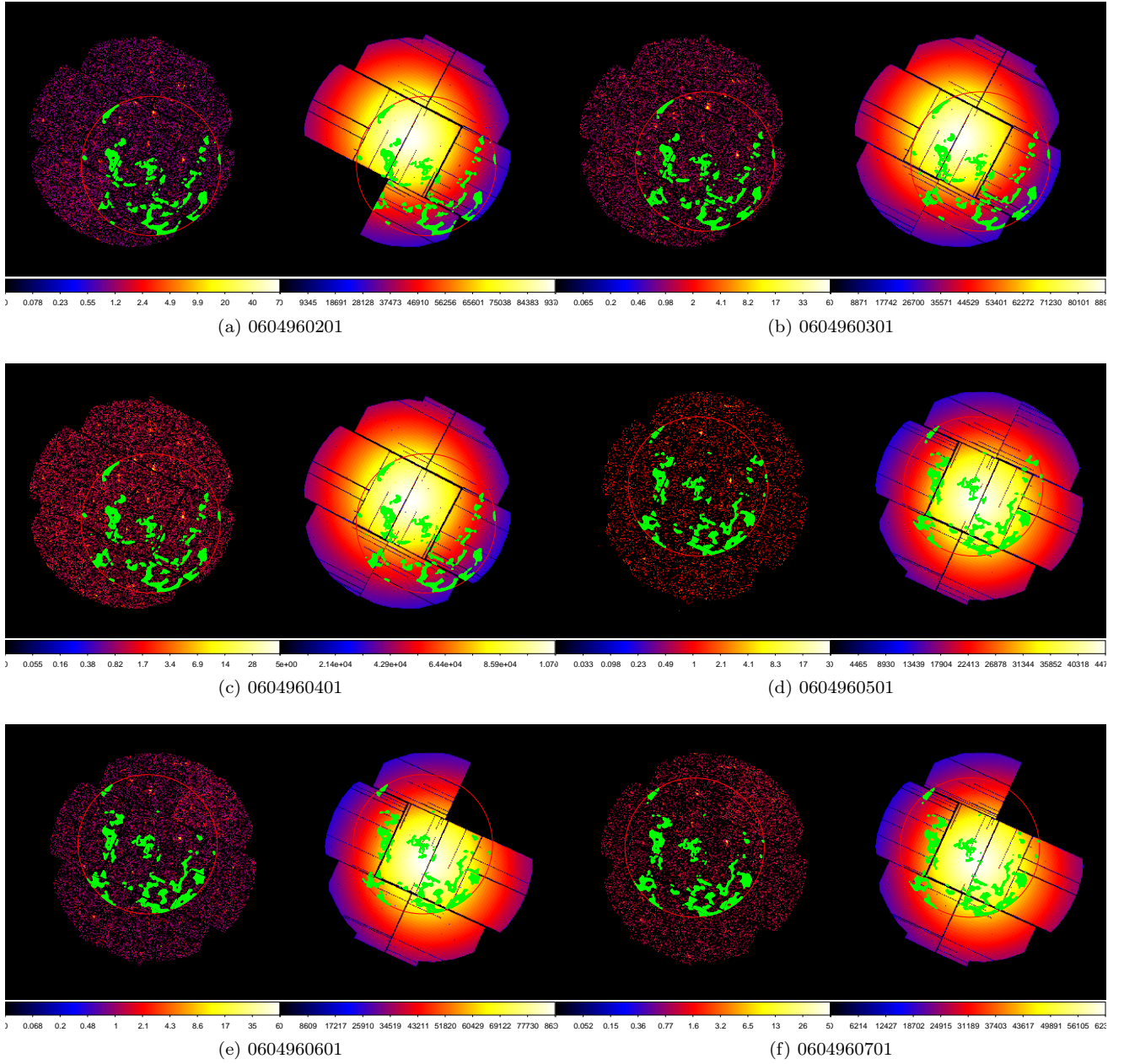


Figure A.44: The observed images and exposure maps by MOS2 in 0.4-1 keV for different ObsIDs from (a) to (f).

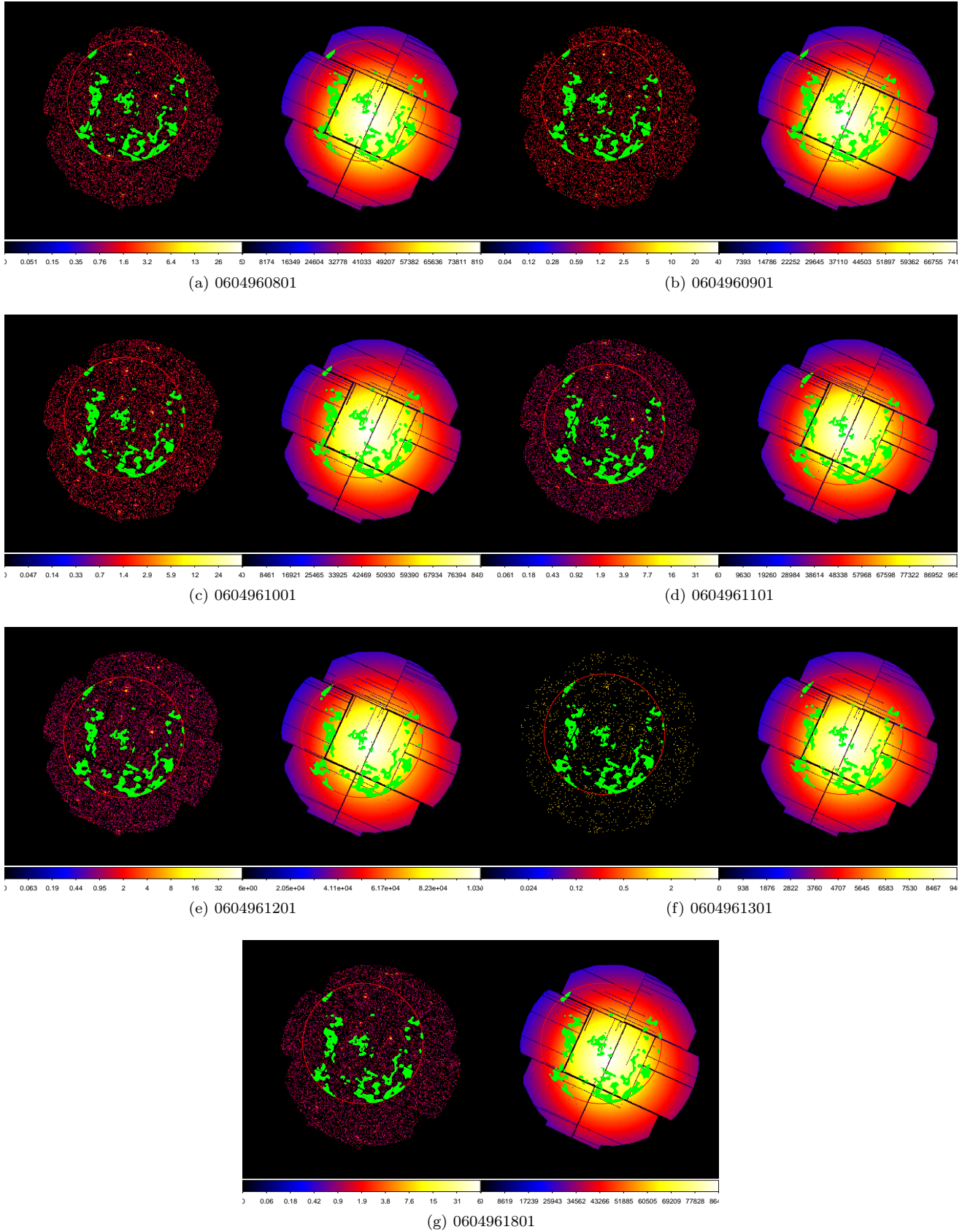


Figure A.45: The observed images and exposure maps by MOS2 in 0.4-1 keV for different ObsIDs from (a) to (g).

## Appendix B

# Examination of soft proton contamination in X-ray background

The power-law index above 2 keV can be modeled by a canonical value,  $1.42 \pm 0.02$  (Revnivtsev et al. (2003)). However, the spectrum was flatter than the canonical value above 2 keV, if the residual soft proton contamination (RSPC) existed. We utilized this fact in order to check that the RSPC existed or not. Thus, we fitted the spectra before and after soft-proton removal. The fit results are shown in Figure B.1 for the MOS1 and in Figure B.2 for the MOS2. The best fit parameters are tabulated in Table B.1(a) and Table B.1(b). Before soft-proton removal (before filtering short-term variation),  $r$  (see definition in Equation 6.16 in Subsection 6.2.2) for the MOS1 ( $r_{\text{MOS1}}$ ) was  $1.069 \pm 0.007$  and  $r_{\text{MOS2}}$  was  $1.045 \pm 0.006$ . Exposure time was 2.3 Msec for the MOS1 and 2.4 Msec for the MOS2. After soft-proton removal (after filtering short-term variation), the  $r_{\text{MOS1}}$  was  $1.125 \pm 0.008$  and  $r_{\text{MOS2}}$  was  $1.017 \pm 0.010$ . Exposure time was 1.98 Msec for the MOS1 and 1.98 Msec for the MOS2. We saw  $r_{\text{MOS2}}$  is higher than  $r_{\text{MOS1}}$ . As shown in Figure 4.18, this may take place because the blue shaded offset is  $(4 \pm 10)\%$ . However, the power-law index in the hard band was  $1.31_{-0.17}^{+0.07}$  for the MOS1 data ( $1.6\sigma$  statistical error). It was slightly higher than the canonical value of  $1.42 \pm 0.02$  (Revnivtsev et al. (2003)). Thus, we can not exclude the possibility that the MOS1 data contains the residual soft proton contamination (RSPC). On the other hand, the power-law index in the hard band was  $1.37_{-0.17}^{+0.13}$  ( $1.6\sigma$  statistical error) for the MOS2 data. It was consistent with the canonical value within  $1.6\sigma$  statistical error. Therefore, we used only the MOS2 data in the analysis.

Table B.1: Fit results for the MOS1 and the MOS2

(a) Before soft-proton removal (before filtering short-term variation)

| Inst. | APEC                      | S.B.†<br>in 0.4-1 keV  | Gaussian               | Power law              |                        | Break<br>keV           | S.B.†<br>in 2-8 keV  | $\chi^2$ /d.o.f (d.o.f.) |
|-------|---------------------------|------------------------|------------------------|------------------------|------------------------|------------------------|----------------------|--------------------------|
|       | Temp.<br>keV              |                        | Center<br>keV          | Index<br>soft          | hard                   |                        |                      |                          |
| MOS1  | $0.142^{+0.006}_{-0.005}$ | $7.56^{+0.04}_{-0.05}$ | $1.11^{+0.02}_{-0.03}$ | $2.15^{+0.05}_{-0.05}$ | $1.32^{+0.05}_{-0.07}$ | $1.17^{+0.11}_{-0.07}$ | $20.9^{+0.4}_{-0.4}$ | 1.03(25)                 |
| MOS2  | $0.145^{+0.004}_{-0.004}$ | $7.34^{+0.04}_{-0.04}$ | $0.88^{+0.02}_{-0.03}$ | $1.94^{+0.04}_{-0.04}$ | $1.44^{+0.05}_{-0.12}$ | $1.24^{+0.27}_{-0.11}$ | $18.0^{+0.7}_{-0.3}$ | 1.48(25)                 |

**Notes.**

† Surface brightness not corrected by the Galactic absorption in unit of  $10^{-12}\text{erg cm}^{-2}\text{s}^{-1}\text{deg}^{-2}$ .

All of error bars are the  $1.6\sigma$  statistical error.

The gaussian is just for filling a residual with 0.1 eV width.

(b) After soft-proton removal (after filtering short-term variation)

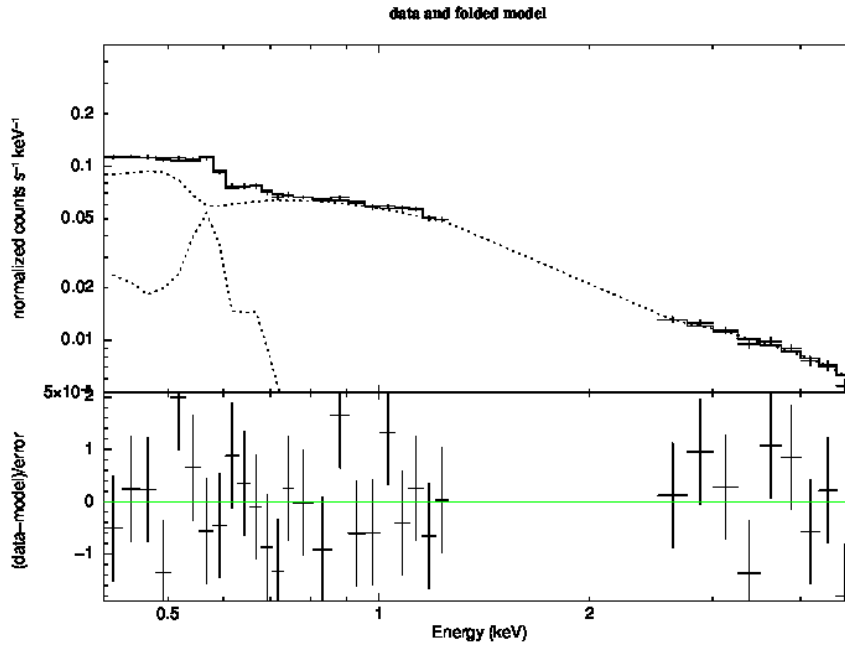
| Inst. | APEC                      | S.B.†<br>in 0.4-1 keV  | Gaussian               | Power law              |                        | Break<br>keV           | S.B.†<br>in 2-8 keV  | $\chi^2$ /d.o.f (d.o.f.) |
|-------|---------------------------|------------------------|------------------------|------------------------|------------------------|------------------------|----------------------|--------------------------|
|       | Temp.<br>keV              |                        | Center<br>keV          | Index<br>soft          | hard                   |                        |                      |                          |
| MOS1  | $0.138^{+0.006}_{-0.012}$ | $6.56^{+0.04}_{-0.05}$ | $1.05^{+0.07}_{-0.03}$ | $2.15^{-0.06}_{+0.07}$ | $1.31^{+0.07}_{-0.17}$ | $1.22^{+0.24}_{-0.13}$ | $17.5^{+0.6}_{-0.4}$ | 1.10(25)                 |
| MOS2  | $0.146^{+0.005}_{-0.004}$ | $7.14^{+0.03}_{-0.05}$ | $0.89^{+0.02}_{-0.03}$ | $1.95^{+0.05}_{-0.05}$ | $1.37^{+0.13}_{-0.17}$ | $1.50^{-0.31}_{+0.32}$ | $16.7^{+0.4}_{-0.7}$ | 1.61(25)                 |

**Notes.**

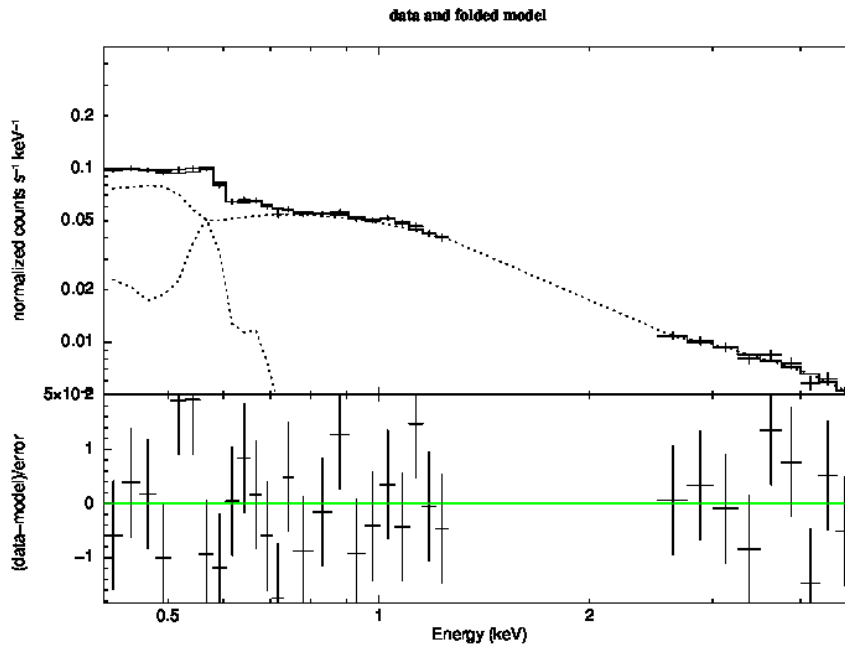
† Surface brightness not corrected by the Galactic absorption in unit of  $10^{-12}\text{erg cm}^{-2}\text{s}^{-1}\text{deg}^{-2}$ .

All of error bars are the  $1.6\sigma$  statistical error.

The gaussian is just for filling a residual with 0.1 eV width.



(a)



(b)

Figure B.1: Fit results for the MOS1 spectra, with the  $r$  (see definition Subsection 6.2.2) correction before soft-proton removal (before filtering short-term variation) (a), after soft-proton removal (after filtering short-term variation) (b). The best fit parameters are shown in Table B.1.

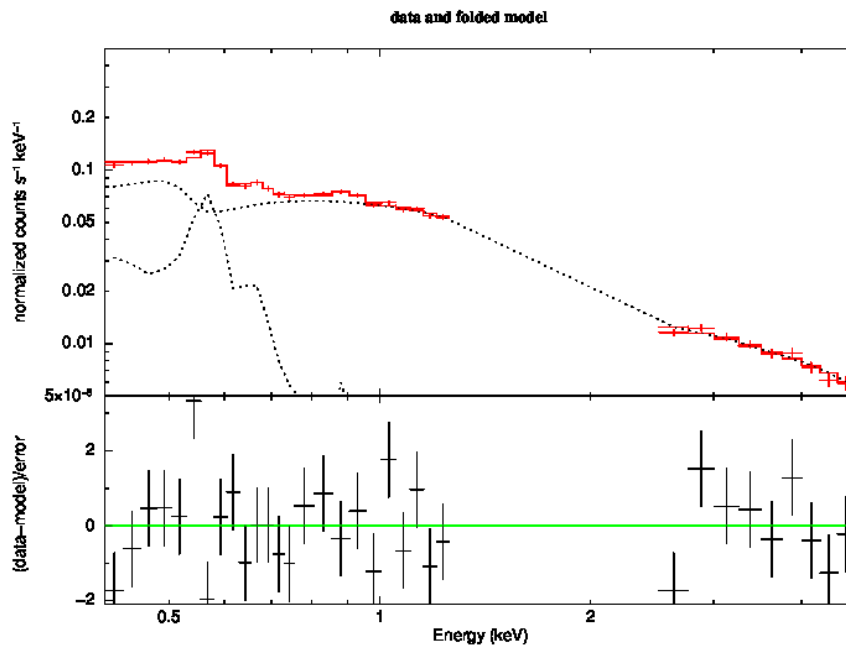
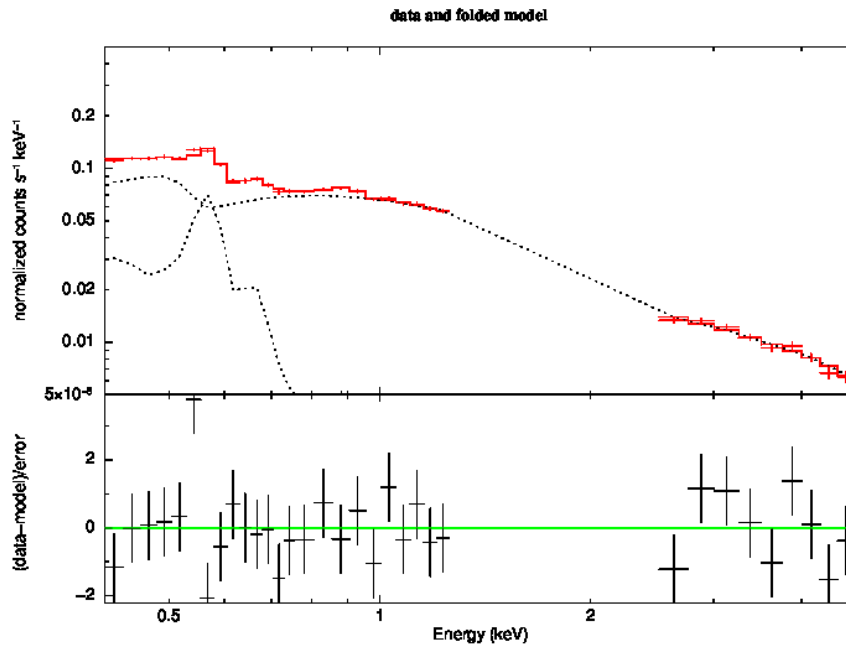


Figure B.2: Same as the previous Figure B.1 for the MOS2.

# Appendix C

## Estimation of conceivable residual soft proton contamination by Monte Carlo simulation

As described in Chapter 4 (Section 4.2.3), *XMM-Newton* often suffers from occasional enhancements of soft protons, whose time scale is hundreds of sec to several ksec or possibly be even longer.

### C.1 Example of observed time variability in count rate

The light curve observed by *XMM-Newton* in 5-10 keV is shown in Figure C.1. The close-up view is a time variable component. Therefore, we constructed a model of the time variable components.

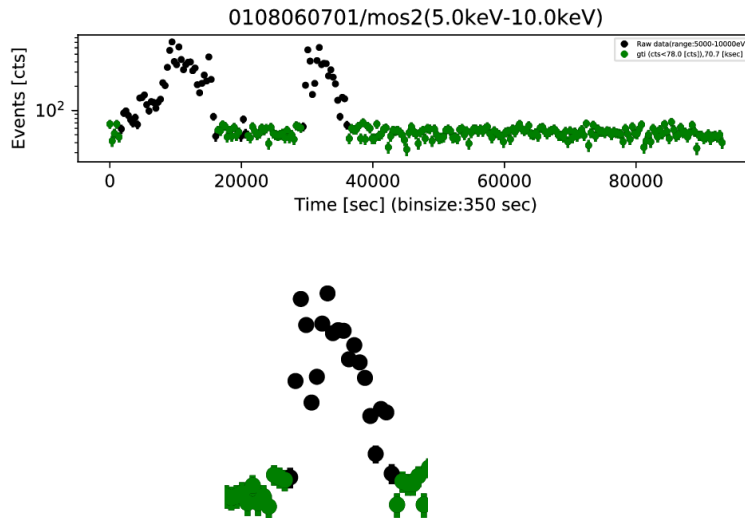


Figure C.1: Example of light curve observed by *XMM-Newton* and close-up view of the time variable component.

### C.2 Model of the time variable components

The time variable components which we call flare shown in Figure C.1 had an amplitude, a duration, a rise time, a fall time and a starting time. We constructed a flare as shown in Figure C.2. We used these flare models in the following analysis. According to Salvetti et al. (2017), the flares had a time scale of  $\sim 100$  sec to  $\sim 10$  ksec. The

amplitude had various strength. Thus, we considered the duration and the amplitude as variable parameters. For simplicity, we fixed the rise and fall time at 100 sec. A flare was assumed to randomly occur once in one observation ( $\sim 100$  ksec).

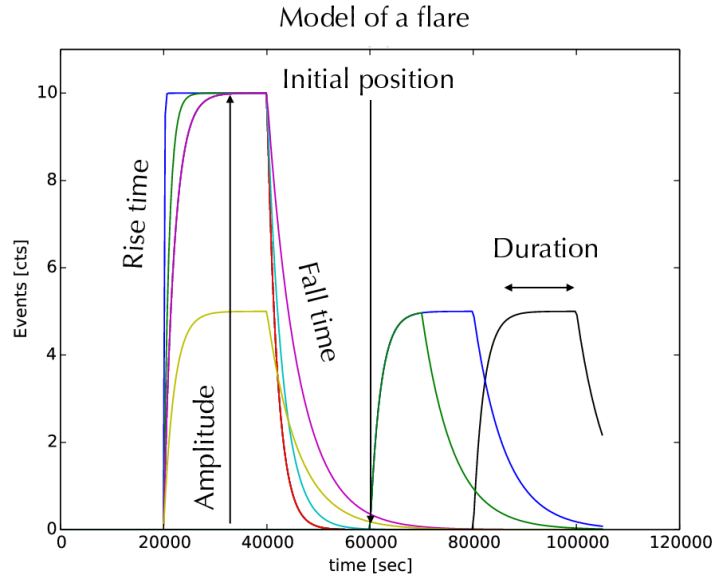


Figure C.2: Model of the time variable components which we call a flare. The amplitude and duration are treated as variable parameters. The rise time and the fall time are fixed at 100 sec. This flare is assumed to occur once in one observation ( $\sim 100$  ksec) randomly.

### C.3 Example of simulated flare

We showed an example of the simulation results in Figure C.3. Because the average count rate observed by *XMM-Newton* was 0.2 cts/s in 5-10 keV, we set the average count rate of the Poisson distribution to be the same value, 0.2 cts/s. Time bin size was set to 350 sec which was the same as in real analysis. Then, the center of the histogram of the Poisson distribution ( $\mu_{\text{true}}$ ) became 70 cts in the simulation which is an adequately reasonable number for approximation to a Gaussian distribution. In this example, the flare component had an amplitude of  $4\sigma$ , where  $\sigma \simeq \sqrt{\mu_{\text{true}}}$  is the width of the Gaussian distribution. The histogram of the flare events is clearly separated from the Poisson distribution because the flare amplitude ( $4\sigma$ ) was much higher than  $\sigma$ . Thus strong flares can be easily eliminated.

### C.4 Difference between true Poisson average and fit average

We showed fit results of the average of the Poisson distribution ( $\mu_{\text{fit}}$ ) in Figure C.4. The fit results ( $\mu_{\text{fit}}$ ) are slightly higher than  $\mu_{\text{true}}$  (= 70 cts).  $\mu_{\text{fit}}$  ranged from 70 cts to 76 cts. Therefore, the maximum difference was 6 cts.

### C.5 Residual soft proton contamination (RSPC) as a function of amplitude and duration

The flares with amplitudes as large as or smaller than the width of the Poisson distribution (e.g.,  $1\sigma$ ) are difficult to identify. Such weak flares may become residual soft proton contamination (RPSC). Based on our simulation, we obtained the residual soft proton contamination (RSPC) as a function of amplitude and duration as shown in Figure C.5. To estimate the RSPC, we defined the contamination rate in X-rays as follows,

$$C_{\text{SPC}} = C_{\text{total}} - C_{\text{poisson}}, \quad (\text{C.1})$$

$$C_{\text{Xray Background as a signal}} = \zeta C_{\text{total}}, \quad (\text{C.2})$$

$$\text{Contamination Rate} = \frac{C_{\text{SPC}}}{C_{\text{Xray Background as a signal}}}, \quad (\text{C.3})$$

where  $C_{\text{total}}$  is the total number of simulated counts in a good time interval,  $C_{\text{poisson}}$  is the number of simulated counts from the Poisson distribution in a good time interval,  $C_{\text{SPC}}$  is the number of the soft proton contamination counts in a good time interval and  $\zeta$  is a fraction of the X-ray background counts in the total simulated counts. A good time interval was defined by the same method as employed in the real analysis. We set  $\zeta$  to be 95% which was determined by the observation in 5-10 keV as shown in Figure 6.3 (b).

## C.6 Amounts of conceivable residual soft proton contamination

In this thesis, we checked that the power-law index in 2-5 keV was consistent with a canonical value,  $1.42 \pm 0.02$  (Revnivtsev et al. (2003)) after soft-proton removal (after removing short-term variation). However, conceivable residual soft proton contamination was not discussed. We assumed that the power-law index of the residual soft proton contamination (RSPC) to be 1.2 which is the same as in the previous X-ray background study (Henley & Shelton (2013)). We set the normalization of the soft proton contamination to be the count rate in 5-10 keV. Figure C.6 showed the power-law index in 2-5 keV v.s. the contamination rate in 5-10 keV. The fit results accommodated the canonical value, if the soft proton contamination was less than 23%. However, if more than 23%, the RSPC spectrum dominated the X-ray background spectrum. Thus, the amounts of maximum conceivable residual soft proton contamination were 23% of the count rate in 5-10 keV.

## C.7 Influence of conceivable residual soft proton contamination on X-ray background

We estimated the influence on the surface brightness of the X-ray background due to the maximum conceivable residual soft contamination, i.e., 23% of the count rate in 5-10 keV. Figure C.7 showed spectra by using the simulation model which included the residual soft proton contamination and the X-ray background. On the other hand, fit model assumed only the X-ray background. The ratio of the best fit parameters to the simulation parameters was shown in Table C.1 and Table C.2. The surface brightness of the X-ray background in 0.4-1 keV determined by the spectral fit was  $\sim +15\%$  higher than the surface brightness in the simulation. Thus, we estimated the systematic error in the surface brightness to be  $+15\%$ .

Table C.2 showed the results on the OVII and OVIII emission lines. Because the equivalent width of the OVIII emission line is smaller than the energy resolution,  $\sim 0.1$  keV, we performed this simulation many times for determining the amplitude of the OVIII emission line. Figure C.8 showed a scatter plot and histograms of the central value of the OVII and OVIII emission lines determined by spectral fit. The solid line is a parameter in the simulation model. The histograms of the OVII and OVIII emission lines are distributed around the solid line. We employed the width of the histogram as the systematic error.

Table C.1: Influence of maximum conceivable residual soft proton contamination rate on the total surface brightness of the X-ray background.

| Parameter  | Simulation            | model $M_1'(E)$            | model/Simulation  |
|--|-----------------------|----------------------------|-------------------|
| Soft Proton Contamination  |                       |                            |                   |
| index  | 1.21                  | -                          | -                 |
| Contamination rate in 5-10 keV                                     | 23%                   | -                          | -                 |
| Surface Brightness for X-ray Background                            |                       |                            |                   |
| in 0.4-1 keV ( $10^{-12}$ [erg cm $^{-2}$ s $^{-1}$ deg $^{-2}$ ]) | 3.82                  | 4.45 $\pm$ 0.10            | 1.165 $\pm$ 0.026 |
| in 0.5-1 keV ( $10^{-12}$ [erg cm $^{-2}$ s $^{-1}$ deg $^{-2}$ ]) | 3.14                  | 3.56 $\pm$ 0.10            | 1.133 $\pm$ 0.031 |
| in 2-8 keV ( $10^{-12}$ [erg cm $^{-2}$ s $^{-1}$ deg $^{-2}$ ])   | 5.75                  | 7.53 $\pm$ 0.34            | 1.310 $\pm$ 0.059 |
| X-ray Background   |                       |                            |                   |
| Galactic absorption  |                       |                            |                   |
| $N_H$ (cm $^{-2}$ )  | $8.8 \times 10^{-19}$ |                            |                   |
| SWCX Gaussian  |                       |                            |                   |
| $N_1$ (LU)   | 2                     | 2(fix)                     |                   |
| $E_c$ (keV)  | 0.561                 | 0.561(fix)                 |                   |
| Galactic halo APEC   |                       |                            |                   |
| $N_2$ (cm $^{-5}$ str $^{-1}$ )                                    | 2.80                  | 2.76 $\pm$ 0.56            |                   |
| $T_2$ (keV)  | 0.189                 | 0.186 $^{+0.013}_{-0.011}$ |                   |
| Broken Power Law   |                       |                            |                   |
| $N_b$ (cm $^{-2}$ s $^{-1}$ keV $^{-1}$ str $^{-1}$ )              | 4.71                  | 5.66 $\pm$ 0.26            |                   |
| $\alpha_1$   | 2.20                  | 2.38 $^{+0.12}_{-0.13}$    |                   |
| $\alpha_2$   | 1.45                  | 1.34 $^{+0.07}_{-0.07}$    |                   |
| $\chi^2$ /d.o.f (d.o.f.)   | -                     | 0.99(26)                   | -                 |

Errors are  $1.6\sigma$ (90%).

Table C.2: Influence of maximum conceivable residual soft proton contamination rate on the surface brightnesses of the each X-ray background component.

| Parameter   | Simulation            | model1 $M_1'(E)$           | model2 $M_2'(E)$        | model2/Simulation       |
|---|-----------------------|----------------------------|-------------------------|-------------------------|
| Soft Proton Contamination                             |                       |                            |                         |                         |
| index   | 1.21                  | -                          | -                       | -                       |
| Contamination rate in 5-10 keV                        | 23%                   | -                          | -                       | -                       |
| X-ray Background                                      |                       |                            |                         |                         |
| Galactic absorption                                   |                       |                            |                         |                         |
| $N_H$ (cm $^{-2}$ )                                   | $8.8 \times 10^{-19}$ | $8.8 \times 10^{-19}$      | $8.8 \times 10^{-19}$   |                         |
| SWCX Gaussian   |                       |                            |                         |                         |
| $N_1$ (LU)  | -                     | 2.0(fix)                   | -                       |                         |
| $E_c$ (keV)   | -                     | 0.561(fix)                 | -                       |                         |
| Galactic halo APEC                                    |                       |                            |                         |                         |
| $N_2$ (cm $^{-5}$ str $^{-1}$ )                       | 2.80                  | 2.57 $^{+0.82}_{-0.56}$    | 3.02 $^{+1.53}_{-1.62}$ | 1.08 $^{+0.53}_{-0.58}$ |
| Oxygen Abundance                                      | 0                     | 1(fix)                     | 0(fix)                  |                         |
| $T_2$ (keV)   | 0.189                 | 0.172 $^{+0.012}_{-0.018}$ | 0.172(fix)              |                         |
| Broken Power Law                                      |                       |                            |                         |                         |
| $N_b$ (cm $^{-2}$ s $^{-1}$ keV $^{-1}$ str $^{-1}$ ) | 4.71                  | 6.00 $^{+0.22}_{-0.26}$    | 6.05 $\pm$ 0.18         | 1.28 $\pm$ 0.03         |
| $\alpha_1$  | 2.20                  | 2.21 $^{+0.12}_{-0.13}$    | 2.21(fix)               |                         |
| $\alpha_2$  | 1.45                  | 1.43 $^{+0.07}_{-0.07}$    | 1.43(fix)               |                         |
| OVII Gaussian   |                       |                            |                         |                         |
| $N_{G1}$ (LU)   | 3.69                  | -                          | 3.64 $^{+0.37}_{-0.18}$ | 1.01 $^{+0.10}_{-0.05}$ |
| $E_{c1}$ (keV)  | 0.565                 | -                          | 0.560 $\pm$ 0.005       |                         |
| OVIII Gaussian  |                       |                            |                         |                         |
| $N_{G2}$ (LU)   | 0.84                  | -                          | 0.62 $^{+0.17}_{-0.16}$ | 0.73 $^{+0.19}_{-0.20}$ |
| $E_{c2}$ (keV)  | 0.643                 | -                          | 0.650 $\pm$ 0.010       |                         |
| $\chi^2$ /d.o.f (d.o.f.)                              | -                     | 0.923(26)                  | 1.022 (25)              | -                       |

Errors are  $1.6\sigma$ (90%).

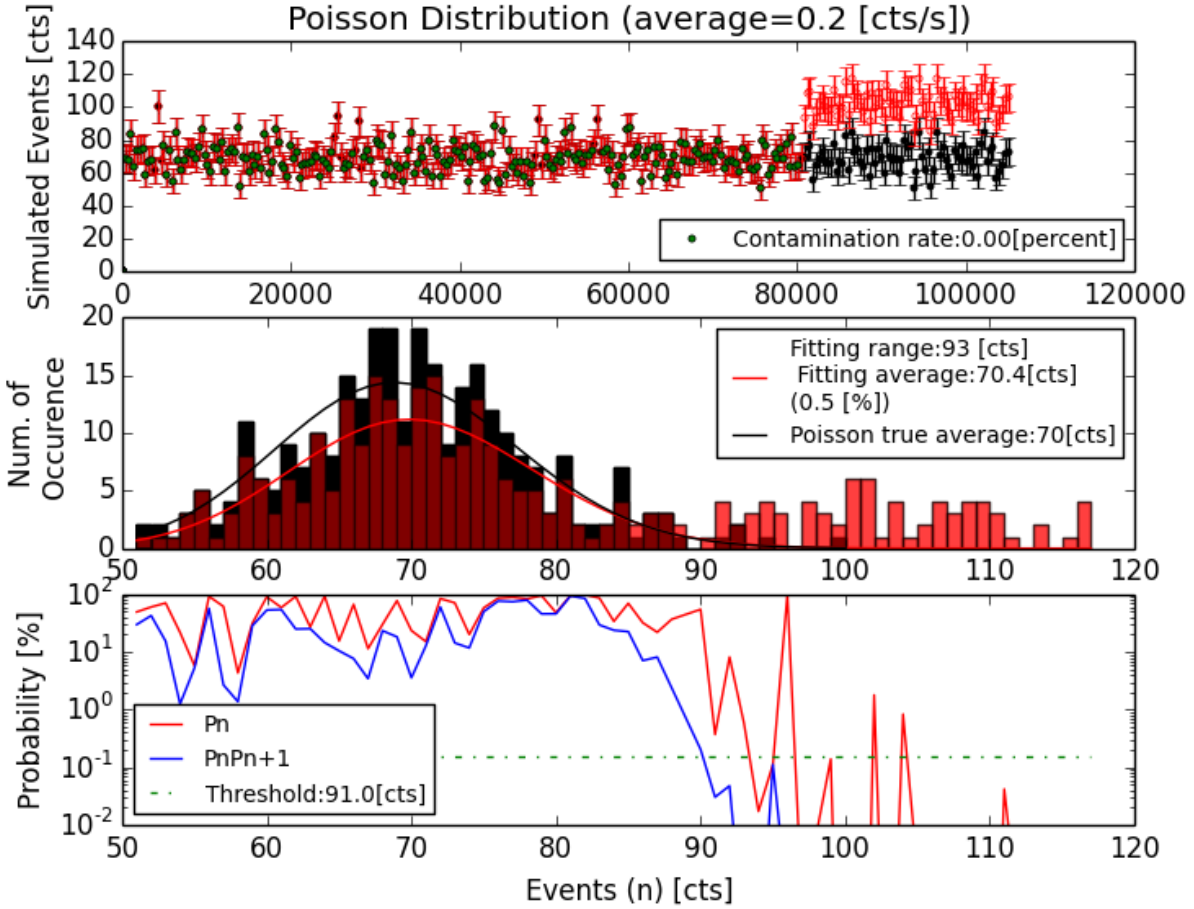


Figure C.3: Example of the simulation results for the strong amplitude ( $4\sigma$ ) and the long duration flare. The flare is assumed to be once in one observation ( $\sim 100$  ksec). Simulated light curve (upper). The x-axis is in a unit of sec and the time bins are 350 sec. The black points are reproduced by the Poisson distribution while the red points are reproduced by the flares and the Poisson distribution. The green points are good time intervals. The inset shows the contamination rate. The number of occurrence of time bins ( $D_{\text{sim}}(n)$ ) for the simulated light curve (middle). The black histogram is the Poisson distribution corresponds to the upper black light curve. Average of the Poisson distribution is 0.2 cts/s which is the same as observed count rate in 5-10 keV. Then, the center of the histogram of the Poisson distribution ( $\mu_{\text{true}}$ ) became 70 cts in the simulation. The solid red curve is the Poisson distribution determined by fit with a given range. The inset shows the fit range and the average of the Poisson distribution determined by fit ( $\mu_{\text{fit}}$ ). Cumulative probability ( $P_c(n, D_{\text{sim}}(n))$ ) for obtaining the number of occurrence of time bins larger than  $D_{\text{sim}}(n)$  (Equation (5.6)) and the product of the two probabilities in the successive two bins,  $P_c(n, D(n))P_c(n+1, D_{\text{sim}}(n+1))$ . The green horizontal dotted broken line corresponds to threshold probability ( $P_{\text{Th}}$  see Equation (5.11)) (lower).

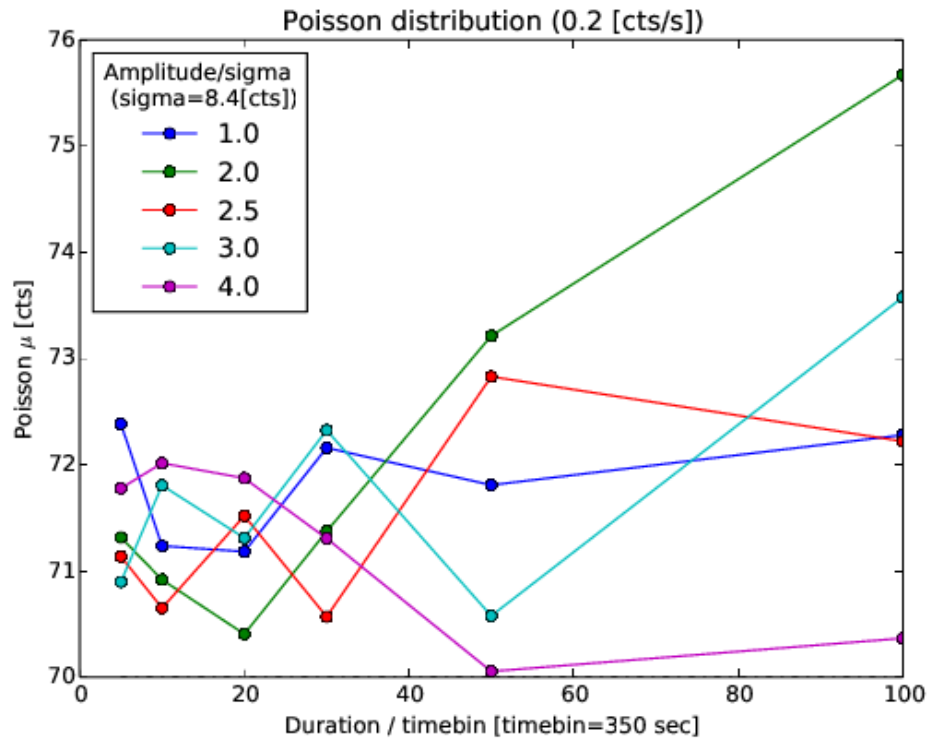


Figure C.4: Difference between  $\mu_{\text{true}}$  and  $\mu_{\text{fit}}$ . The  $\mu_{\text{true}}$  is 70 [cts]. Colors indicate the different amplitude of flares.

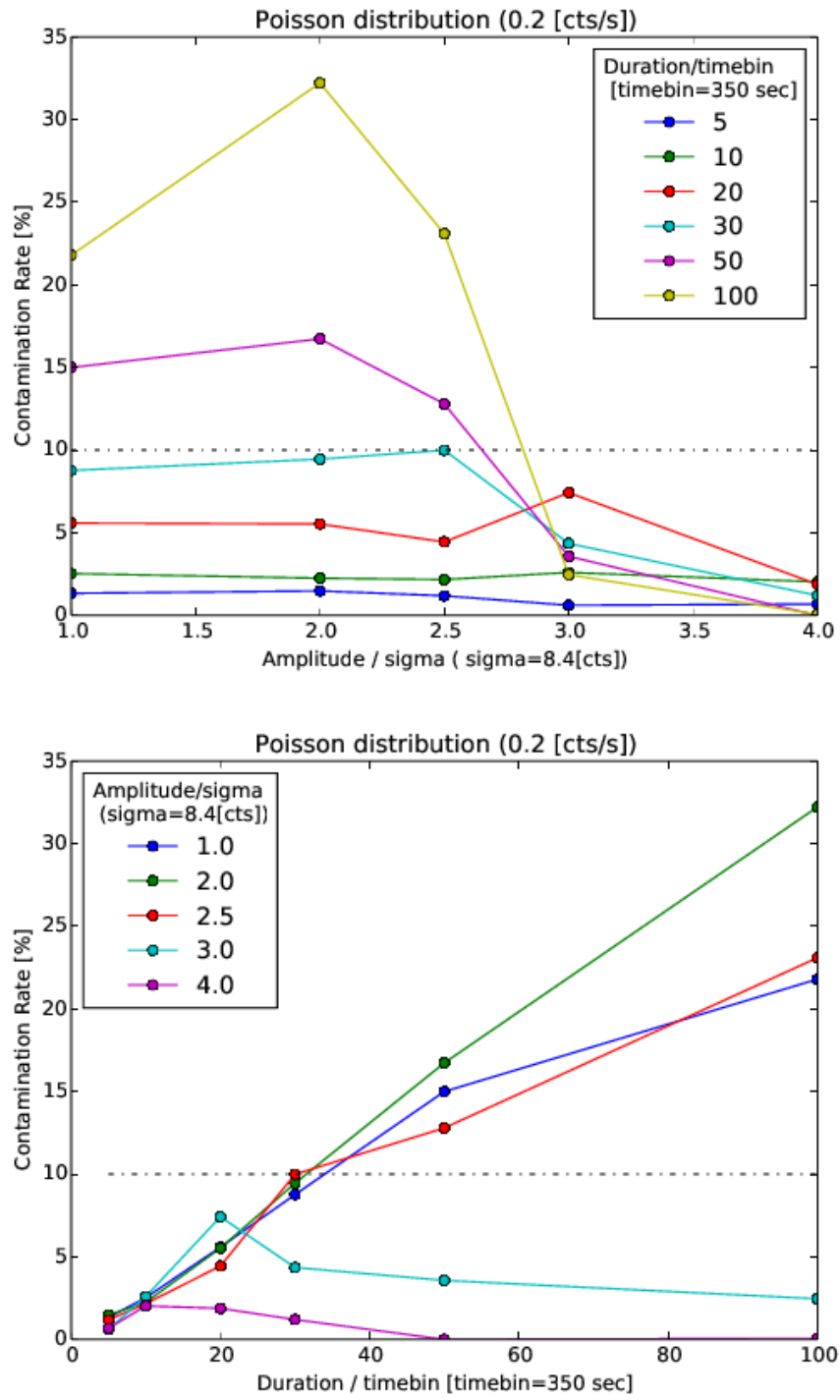


Figure C.5: Contamination rate as a function of amplitudes and durations.

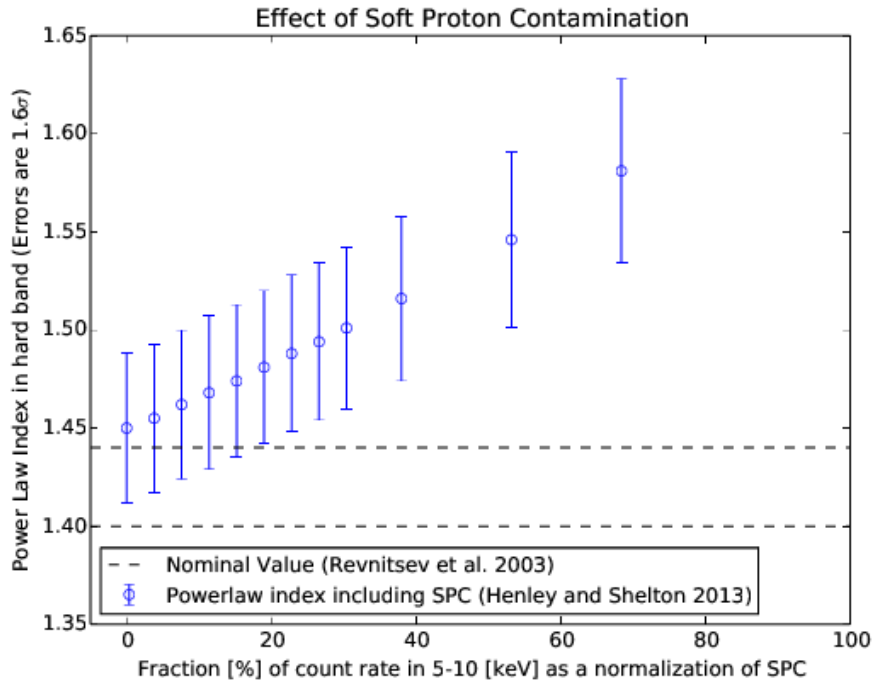


Figure C.6: Power-law index in 2-5 keV v.s. the contamination rate in 5-10 keV. The fit results (blue open circle) accommodated the canonical value (dashed line) if the soft proton contamination was less than 23%.

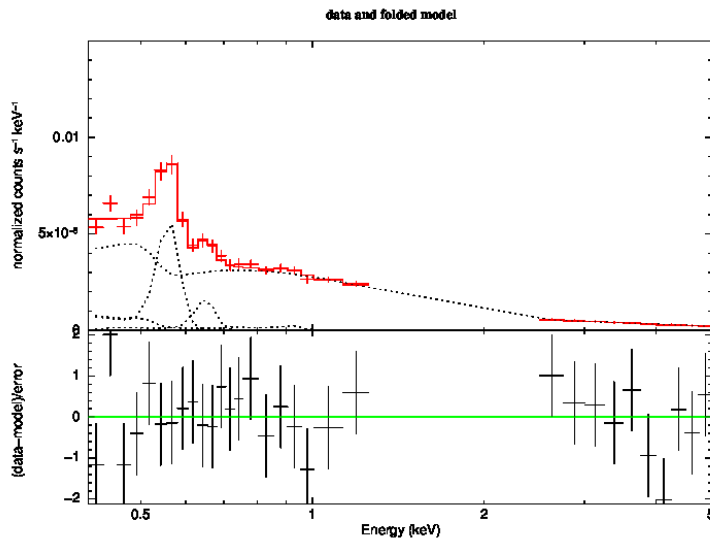


Figure C.7: Simulated spectrum and best fit models. Red crosses indicate the simulated spectrum by using the simulation model which included the residual soft proton contamination and the X-ray background. Dashed curved means fit model assumed only the X-ray background

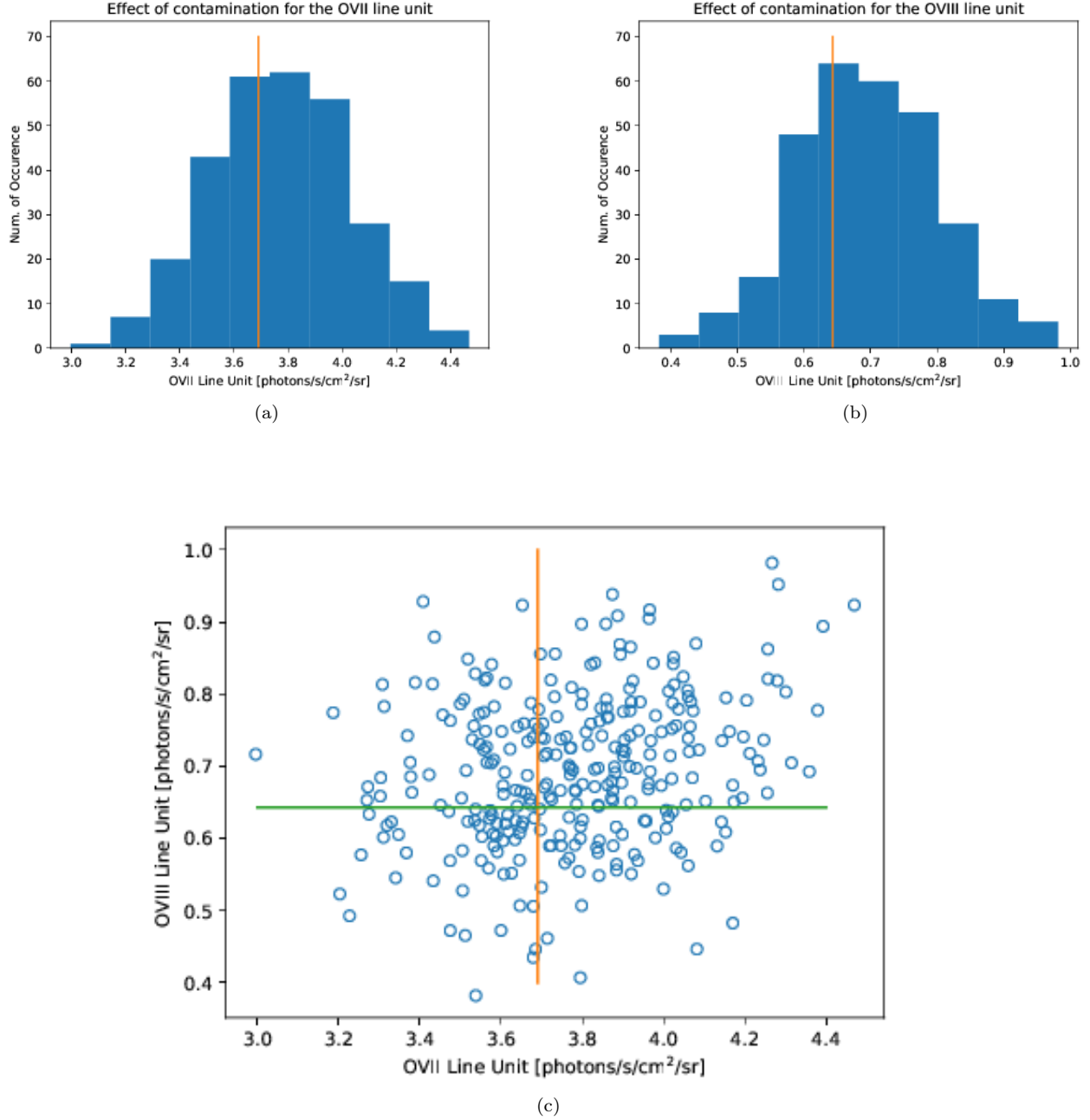


Figure C.8: Difference of the surface brightness due to the residual soft proton contamination between the simulation parameters and the best fit parameters for the OVII emission line (a) and for the OVIII emission line (b). The plot (c) indicates the relationship between the OVII emission line and the OVIII emission line. The orange and green lines are the simulation parameters.

# Bibliography

- Alexander, D. M., Bauer, F. E., Brandt, W. N., et al. 2003, *The Astronomical Journal*, 126, 539
- Anders, E., & Grevesse, N. 1989, *Geochimica Cosmochimica Acta*, 53, 197
- Bowyer, C. S., Field, G. B., & Mack, J. E. 1968, *Nature*, 217, 32
- Brandt, W. N., & Alexander, D. M. 2015, *Astronomy and Astrophysics Reviews*, 23, 1
- Cappelluti, N., Allevato, V., & Finoguenov, A. 2012a, *Advances in Astronomy*, 2012, 853701
- Cappelluti, N., Ranalli, P., Roncarelli, M., et al. 2012b, *Monthly Notices of the Royal Astronomical Society*, 427, 651
- Cen, R., & Ostriker, J. P. 1999, *Astrophysical Journal*, 514, 1
- Cravens, T. E. 2002, *Science*, 296, 1042
- Dijkstra, M., Gilfanov, M., Loeb, A., & Sunyaev, R. 2012, *Monthly Notices of the Royal Astronomical Society*, 421, 213
- Fialkov, A., Cohen, A., Barkana, R., & Silk, J. 2017, *Monthly Notices of the Royal Astronomical Society*, 464, 3498
- Freeman, P. E., Kashyap, V., Rosner, R., & Lamb, D. Q. 2002, *Astrophysical Journal Supplement Series*, 138, 185
- Fujimoto, R., Takei, Y., Tamura, T., et al. 2004, *Publications of the Astronomical Society of Japan*, 56, L29
- Fujimoto, R., Mitsuda, K., McCammon, D., et al. 2007, *Progress of Theoretical Physics Supplement*, 169, 71
- Galeazzi, M., Gupta, A., & Ursino, E. 2009, *Astrophysical Journal*, 695, 1127
- Gastaldello, F., Ghizzardi, S., Marelli, M., et al. 2017, *Experimental Astronomy*, 44, 321
- Ghizzardi, S., Marelli, M., Salvetti, D., et al. 2017, *Experimental Astronomy*, 44, 273
- Giacconi, R., & Gursky, H. 1965, *Space Science Reviews*, 4, 151
- Giacconi, R., Gursky, H., Paolini, F. R., & Rossi, B. B. 1962, *Physical Review Letters*, 9, 439
- Gilli, R., Salvati, M., & Hasinger, G. 2001, *Astronomy & Astrophysics*, 366, 407
- Gupta, A., Mathur, S., Galeazzi, M., & Krongold, Y. 2014, *Astrophysics & Space Science*, 352, 775
- Hagihara, T., Yamasaki, N. Y., Mitsuda, K., et al. 2011, *Publications of the Astronomical Society of Japan*, 63, S889
- Henley, D. B., & Shelton, R. L. 2013, *Astrophysical Journal*, 773, 92
- Hickox, R. C., & Markevitch, M. 2006, *Astrophysical Journal*, 645, 95
- Jansen, F., Lumb, D., Altieri, B., et al. 2001, *Astronomy & Astrophysics*, 365, L1
- Kim, M., Wilkes, B. J., Kim, D.-W., et al. 2007, *Astrophysical Journal*, 659, 29
- Kolodzig, A., Gilfanov, M., Hütsi, G., & Sunyaev, R. 2017, *Monthly Notices of the Royal Astronomical Society*, 466, 3035

- Koutroumpa, D., Lallement, R., Raymond, J. C., & Kharchenko, V. 2009, *Astrophysical Journal*, 696, 1517
- Kuntz, K. D., & Snowden, S. L. 2008, *Astronomy & Astrophysics*, 478, 575
- Kushino, A., Ishisaki, Y., Morita, U., et al. 2002, *Publications of the Astronomical Society of Japan*, 54, 327
- Lallement, R. 2015, in *Journal of Physics Conference Series*, Vol. 577, *Journal of Physics Conference Series*, 012016
- Lallement, R., Welsh, B. Y., Vergely, J. L., Crifo, F., & Sfeir, D. 2003, *Astronomy & Astrophysics*, 411, 447
- Lehmer, B. D., Xue, Y. Q., Brandt, W. N., et al. 2012, *Astrophysical Journal*, 752, 46
- Luo, B., Brandt, W. N., Xue, Y. Q., et al. 2017, *Astrophysical Journal Supplement Series*, 228, 2
- Marelli, M., Salvetti, D., Gastaldello, F., et al. 2017, *Experimental Astronomy*, 44, 297
- McCammon, D., & Sanders, W. T. 1990, *Annual Review of Astron and Astrophys*, 28, 657
- McCammon, D., Almy, R., Apodaca, E., et al. 2002, *Astrophysical Journal*, 576, 188
- Nicastro, F., Mathur, S., Elvis, M., et al. 2005, *Astrophysical Journal*, 629, 700
- Ranalli, P., Comastri, A., Vignali, C., et al. 2013, *Astronomy & Astrophysics*, 555, A42
- Read, A. M., Rosen, S. R., Saxton, R. D., & Ramirez, J. 2011, *Astronomy & Astrophysics*, 534, A34
- Revnivtsev, M., Gilfanov, M., Sunyaev, R., Jahoda, K., & Markwardt, C. 2003, *Astronomy & Astrophysics*, 411, 329
- Sakai, K., Yao, Y., Mitsuda, K., et al. 2014, *Publications of the Astronomical Society of Japan*, 66, 83
- Salvetti, D., Marelli, M., Gastaldello, F., et al. 2017, *Experimental Astronomy*, 44, 309
- Sanders, W. T., Kraushaar, W. L., Nousek, J. A., & Fried, P. M. 1977, *Astrophysical Journal Letters*, 217, L87
- Smith, R. K., Foster, A. R., & Brickhouse, N. S. 2012, *Astronomische Nachrichten*, 333, 301
- Smith, R. K., Bautz, M. W., Edgar, R. J., et al. 2007, *Publications of the Astronomical Society of Japan*, 59, 141
- Snowden, S. L., McCammon, D., & Verter, F. 1993, *Astrophysical Journal Letters*, 409, L21
- Snowden, S. L., Mushotzky, R. F., Kuntz, K. D., & Davis, D. S. 2008, *Astronomy & Astrophysics*, 478, 615
- Snowden, S. L., Egger, R., Freyberg, M. J., et al. 1997, *Astrophysical Journal*, 485, 125
- Takei, Y., Henry, J. P., Finoguenov, A., et al. 2007, *Astrophysical Journal*, 655, 831
- Tanaka, Y., & Bleeker, J. A. M. 1977, *Space Science Reviews*, 20, 815
- Turner, M. J. L., Abbey, A., Arnaud, M., et al. 2001, *Astronomy & Astrophysics*, 365, L27
- Yao, Y., Wang, Q. D., Hagihara, T., et al. 2009, *Astrophysical Journal*, 690, 143
- Yoshikawa, K., Dolag, K., Suto, Y., et al. 2004, *Publications of the Astronomical Society of Japan*, 56, 939
- Yoshino, T., Mitsuda, K., Yamasaki, N. Y., et al. 2009, *Publications of the Astronomical Society of Japan*, 61, 805
- Yoshitake, H., Mitsuda, K., Yamasaki, N. Y., & Takei, Y. 2012, in *American Institute of Physics Conference Series*, Vol. 1427, *American Institute of Physics Conference Series*, ed. R. Petre, K. Mitsuda, & L. Angelini, 263–264
- Yoshitake, H., Sakai, K., Mitsuda, K., et al. 2013, *Publications of the Astronomical Society of Japan*, 65, 32